Droplet-based Microfluidic Chip Design for High Throughput Screening Applications

by

Xiaoming Chen

A thesis
presented to the University of Waterloo
in fulfillment of the
thesis requirement for the degree of
Doctor of Philosophy
in
Mechanical Engineering

Waterloo, Ontario, Canada, 2015

AUTHOR'S DECLARATION

I hereby declare that I am the sole author of this thesis. This is a true copy of the thesis, including any required final revisions, as accepted by my examiners.

I understand that my thesis may be made electronically available to the public.

Abstract

Droplet-based microfluidics has been considered as a prospective tool for high throughput screening analysis, which is highly demanded in a wide range of areas including but not limited to life science research, drug discovery, material synthesis and environmental monitoring. Low sample consumption, reduced reaction time, high throughput manipulation, fast mixing, and prevention of cross contamination at channel walls are just some of the benefits of droplet-based microfluidics. Although extensive research efforts have been reported in the study of droplet-based microfluidics over the past decades, it has yet to be widely commercialized. One of the challenges that limit droplet microfluidic chips from being commercialized is the difficulty in integrating multiple functions robustly without increasing the device footprint. Major functionalities of interest include generating droplets with controlled volume and frequency, and precisely controlling and manipulating each individual droplet such as sorting, detecting, merging, splitting, pairing, mixing, trapping, releasing, long term and short term storing, etc. Since many of these functionalities rely on the accuracy of droplet generation which is the first step, it is crucial to investigate the droplet formation process and understand how to design microfluidic structures to manipulate each individual droplet effectively. To this end, this thesis started with a fundamental study of droplet generation in a flow focusing geometry based on extensive experimental data, from which a physical model was developed to describe droplet formation processes, then move on to study droplet generation in a geometry with two junctions in series, with the goal of improving single encapsulation (one particle per droplet) efficiency. Later, droplet merging towards whole genome amplification and drug screening applications was investigated, and finally a microfluidic chip integrated with multiple functionalities was developed, and its robustness was validated.

The first project studied the fundamental principles of liquid-liquid droplet generation in a flow focusing device. This work presents a 3D physical model with less fitting parameters than existing ones. The model describes droplet formation process in flow focusing devices operating in the squeezing regime, where droplet size is usually larger than the channel width, and was developed based on a systematic and extensive experimental study. In particular, it incorporates an accurate geometric description of the 3D droplet shape during the formation process, an estimation of the time period for the formation cycle based on the conservation of mass, and a semi-analytical model predicting the pressure drop over the 3D corner gutter between the droplet curvature and channel walls, which allows droplet size, spacing and formation frequency to be determined accurately. The

model takes into account change in channel geometry (height to width ratio), viscosity contrast, flow rate ratio and capillary number with a wide variety.

In the second project, liquid-liquid droplet generation in a flow focusing device with two junctions in series was investigated using experimental approach. Extra emphasis was placed on the device's ability to encapsulate single cell and particle. . This study employs glycerol solutions with different concentrations as the dispersed phase, which tends to form stratified flow at the first junction due to viscosity contrast. The stratified flow proceeds to form droplets in oil stream at the second junction. To obtain a comprehensive understanding of the droplet formation dynamics involving stratified flow, five different scenarios were considered. These include a single stream of 10%glycerol aqueous solution, a single stream of 80%glycerol aqueous solution, as well as the simultaneous flow of multiple streams of the above mentioned solution. Droplet size and formation period for these cases were compared and analyzed considering the same geometric and flow conditions. It is found that stratified flow structure strongly influences droplet formation dynamics such as droplet size and formation frequency and the scenario with 80%glyc surrounded by 10%glyc in the first junction generates the largest droplet size. Each structure finds its own applications. For the purpose of single encapsulation, the scenario with 80%glyc surrounded by 10%glyc in the first junction is most suitable because the high viscosity of 80%glyc allows particles to be focused into a thin stream and spaced out before entering droplets. On the other hand, the scenario with two fluids side by side in the first junction generates droplets with high monodispersity for a larger range of flow ratios, which is useful for high throughput reactions involving different reagents.

After understanding the fundamentals of the droplet generation process, several designs for practical use were proposed to generate or manipulate droplets. These designs include: i) a flow focusing device that improve droplet size uniformity through changing junction angle; ii) a system for droplet generation on demand, which is essential to controlling droplets of specific reagents; iii) a geometry for generating droplet pairs with uniform droplet sizes and controlled droplet spacing , and to study the interaction between two nearby droplets; iv) a simple droplet merging chamber for controlled reagent volume; and v) a droplet trapping and releasing on demand system for drug screening.

The final part of this thesis presents a complex microfluidic system that integrates multiple functionalities, including droplet generation, pairing, trapping, merging, mixing, and releasing. The criterion of this design was analyzed and verified by experiments. This design does not require any

synchronization of droplet frequency, spacing or velocity, which makes the microfluidic chip work robustly, and is controlled entirely by liquid flow eliminating the needs for electrodes, magnets or any other moving parts. This design can be applied to many chemical or biological reactions, such as drug screening, chemical synthesis, and cell culture, etc.

Acknowledgements

First of all, I would like to thank my supervisor, Dr. Carolyn Ren for giving me the opportunity to work under her supervision, when I was frustrated in another lab. I truly appreciate her passion for research and encouragement when I experienced difficulties during my study. She has also helped me to plan my research career, guiding me to be prepared for a professional researcher. The financial support from Dr. Carolyn Ren is gratefully acknowledged as well. I would also like to thank Prof. Songjing Li, who was my master's supervisor, for helping me always and introducing me to Dr. Carolyn Ren.

Next, I would like to thank Dr. Sean Peterson, Dr. Marios Ioannidis, and Dr. David Johnson for being my PhD comprehensive exam committee members. Their insightful thoughts and comments on my research topic are really helpful for my further study after the exam. I would like to give thanks to Dr. Derek Rayside and Dr. Francis Lin for serving as my PhD defense committee members. Their comments and suggestions are very valuable in improving my thesis.

My PhD study would not have been so fruitful and colorful without the help of other members of the Waterloo Microfluidics Laboratory. Special thanks to Dr. Tom Glawdel, who gave me lots of helpful training and insightful recommendations during my early stage of PhD study. I would also like to thank my collaborator, Dr. Esther Amstad, a postdoc from Harvard University, whose expertise in droplet microfluidics was truly appreciated. Many thanks to the Co-op undergraduate students Naiwen Cui, Matthew Courtney, and Sarah Chan, who finished any work I gave to them with outstanding results, and their strong research motivation is truly appreciated. I would also like to thank Alexander Brukson, who as a master student, provided valuable inputs with regard to the merging design. Great thanks to David Wong, who helped to improve the imaging process. In addition, I would like to thank other lab members, including but not limited to Pegah Pezeshk, Anna T. Nguyen, Ning Qin, Chao Jin, Gurkan Yesiloz, and Sahil Kashyap, who worked as a cooperative team to maintain our lab equipment and ensure everything runs smoothly in the lab. They are also my good friends who made my life more colorful and enjoyable during my time in Waterloo.

I would also like to thank my parents and parents in law for their love, encouragement and support of my PhD study. At last, Special thanks to my dear wife, Di Wang, who has been always loving, supporting, and accompanying me. Her true love is one of the greatest sources of strength to overcome any challenges during my PhD study.

Dedication

This dissertation is gratefully dedicated to my loving wife, Di Wang, who has been working hard to support the family and let me focus on completing this work, and also to my father Yuchang Chen, who chose to give me the best education he could.

Table of Contents

AUTHOR'S DECLARATION ii
Abstract iii
Acknowledgements vi
Dedication vii
Table of Contents viii
List of Figures xii
List of Tables xxii
Chapter 1 Introduction 1
1.1 Research Background 1
1.2 Thesis Outline 4
Chapter 2 Literature Review 6
2.1 Fundamentals of Two Phase Flow 6
2.1.1 Dimensionless Numbers 6
2.1.2 Surfactants, Carrier Fluids, and Chip Material 8
2.2 Droplet Generation 10
2.2.1 T-junction 11
2.2.2 Co-flowing 14
2.2.3 Flow Focusing 15
2.2.4 Step Emulsification 19
2.2.5 Active Techniques and Methods 21
2.2.6 Comparison of Droplet Generators 22
2.3 Droplet Manipulation 22
2.3.1 Droplet Sorting 23
2.3.2 Droplet Detecting and Sensing 26
2.3.3 Droplet Merging and Splitting 27
2.3.4 Droplet Pairing and Synchronization 30
2.3.5 Droplet Mixing 34
2.3.6 Droplet Trapping, Storing and Releasing 36
2.4 Dynamics of Droplet Transport 40
2.4.1 Droplet Velocity 40
2.4.2 Pressure Drop 42

2.5 Applications of Droplet Microfluidics 45
2.5.1 Chemical Applications 45
2.5.2 Biological Applications 47
2.5.3 Medical Applications 48
2.6 Summary 50
Chapter 3 Experimental Setup and Fabrication Techniques 51
3.1 Experimental Setup 51
3.1.1 Pressure-Driven System 52
3.1.2 Flow Sensors 52
3.1.3 Microscope and High-speed Camera 54
3.2 Soft Lithography Fabrication Method for Microfluidic Chips 55
3.3 Fluid Properties Used in Experiments 57
3.4 Microchannel Dimension Measurement 57
Chapter 4 Model of Droplet Generation in Flow Focusing Devices Operating in the Squeezing Regime 60
4.1 Introduction and Project Objectives 60
4.2 Experiments 63
4.2.1 Materials 63
4.2.2 Chip Design 64
4.2.3 Experimental Procedure 65
4.2.4 Experimental Data 67
4.3 Theoretical Model 69
4.3.1 Assumption of 3D Shape of Droplets 70
4.3.2 Filling Stage 72
4.3.3 Necking Stage 75
4.3.4 Calculation of Parameter W_{fill}^{*} 80
4.3.5 Calculation of Parameter L_{fill}^{*} 80
4.3.6 Calculation of Parameter W_{pinch}^{*} 87
4.3.7 Calculation of Parameter L_{pinch}^{*} 88
4.4 Model Validation 90
4.5 Model Error Analysis 92

4.6 Conclusions 97
4.7 List of symbols 98
Chapter 5 Experimental Study on droplet generation in a flow focusing device using stratified flow with viscosity contrast and its impact on single encapsulation 101
5.1 Introduction 102
5.2 Materials and Methods 104
5.3 Experimental Results and Discussions 106
5.3.1 Droplet generation with either pure 10%glyc or pure 80%glyc as the dispersed phase 106
5.3.2 Droplet generation with stratified flow as the dispersed phase 108
5.3.3 Stratified flow with a viscosity contrast and its impact on single encapsulation 114
5.4 Conclusion 117
5.5 List of Symbols 118
Chapter 6 Several Microfluidic Designs for Droplet Generation and Manipulation 120
6.1 Droplet Generation in Flow Focusing Devices with Various Junction Angles 120
6.2 A Droplet Generation on Demand System for Controlled Droplet Size 123
6.3 A Microfluidic Design for Droplet Pairs Generation 126
6.3.1 Introduction 126
6.3.2 Droplet Pair Generator Design 127
6.3.3 Experimental Results 132
6.3.4 Some Preliminary Results for Droplet Interaction Travelling in a Curved Microchannel 134
6.4 Droplet Merging Design for Controlled Reaction Volumes 138
6.4.1 Introduction 138
6.4.2 Design of the Merging Chamber 140
6.4.3 Working Principle of Trapping and Merging 141
6.4.4 Merging Performance 143
6.5 Design of a Microfluidic Device for Trapping and Releasing Droplets on Demand 145
6.5.1 Introduction 146
6.5.2 Design of the Trapping and Releasing Droplets on Demand System 146
6.5.3 Performance of the Design 148
6.6 Conclusion 149
6.7 List of Symbols 150

Chapter 7 A Microfluidic Chip Design Integrated Droplet Generating, Pairing, Trapping, Merging, Mixing and Releasing 153
7.1 Introduction 153
7.2 Working Principle and Design Criterion 154
7.2.1 Working Principle and Channel Structures 154
7.2.2 Design Criterion 161
7.3 Materials and Experimental Setup 169
7.4 Experiments 170
7.4.1 Droplet Generation 170
7.4.2 Droplet pairing and Trapping 171
7.4.3 Droplet Merging and Mixing 173
7.4.4 Droplet Releasing 177
7.4.5 Generating Sample Concentration Gradient 178
7.5 Conclusion 180
7.6 List of Symbols 182
Chapter 8 Conclusions and Recommendations for Future Work 185
8.1 Conclusions of this Thesis 185
8.2 Recommendations for Future Work 189
Appendix A Experimental Data Used in Chapter 4 191
Appendix B Flow Rates Applied for Each Experiment in Chapter 5 200
Appendix C Real Time Operating System (RTOS) Code for Microcontrollers in the Droplet on Demand System 201
Appendix D Matlab Code for Simulating Droplet Travelling in a Bypass Loop 216
Appendix E Experimental Results V.S. Calculated Results of a Droplet Pairs Generation Design Discussed in Chapter 6 223
Bibliography 226

List of Figures

Figure 2.1 (I) An emulsion stabilized with non-ionic surfactants remains stable and monodisperse throughout incubation off chip[68] ; (II) Surfactant structure and emulsion types in macroscale emulsion preparation corresponding to HLB values. O and W represent oil and water phases, respectively [55]. 9

Figure 2.2 (a)Microfabircated T-junction geometry to generate water-in-oil droplet first presented by Todd Thorsen *et al.* [93]. Dashed rectangle indicates area in photomicrograph; (b) Outline of the Y-junction presented by Steegmans *et al.* [94]; (c) schematic of the V-junction structure presented by Ding *et al.* [96]. 12

Figure 2.3 Co-flowing droplet generation device for (a) drop growth and (b) drop separation, which was first proposed by Umbanhowar *et al.* [121] 14

Figure 2.4 Left: first flow-focusing geometry implemented in a microfluidic device. Right: Experimental images of droplet breakup sequences (a) uniform-sized droplets are formed without visible satellites; (b) with small satellite droplets [126]. 16

Figure 2.5 (a) Schematic of a planar flow focusing geometry. (b) - (e) are representative of each of the different droplet breakup regimes, including (b) squeezing, (c) thread formation, (d) dripping and (e) jetting [130]..... 17

Figure 2.6 Typical capillary number based flow map in a flow focusing device with flow patterns (a) threading; (b) jetting; (c) dripping; (d) tubing; (e) viscous displacement [131]..... 17

Figure 2.7 (a) Schematic of step emulsification device. (b) Photos of droplet detachment via T-junction, step and jet breakup mechanisms. Step breakup occurs precisely at the step and jet breakup occurs downstream [150]. 19

Figure 2.8 (I): Channel design for controlling the dynamic separation of satellite droplets. It consists of a droplet generation region and a separation region. The separation region separates the satellite droplets according to their position across the width of the channel. (Bottom) Parent droplets are collected into the mid-collecting zone while the satellite droplets can be switched into either the top or bottom collecting zone [186]; (II): (a) Schematic of the sorting system. (b) Passive droplet separation module [188]; (III): Illustration of viscoelastic droplet sorting based on bi-modal equilibrium positions[189]. 24

Figure 2.9 (I): Schematic of the microfluidic device. The insets show the (a) droplet generation region and mixing region, (b) detection region[217]; (II): Schematic of microwave components for detecting droplets[218]..... 27

Figure 2.10 Geometries for passive coalescence of droplets. (I) Decompression merging by Bremond *et al.* [225]. (II) Pillar induced droplet merging by Niu *et al.* [228]. 29

Figure 2.11 Droplet breakup in a T-junction (I) provided by Link *et al.* [156] and in a Y-junction (II) provided by Abate *et al.* [157]. 30

Figure 2.12 (I): Schematic diagram of the microchannel pattern demonstrated by Hung *et al.* [250] ; (II): (a) Schematic of the double-step-emulsification device with

production units 1 and 2. (b) Time series of optical images displaying the droplet formation mechanism presented by Chokkalingam *et al.* [158]; (III): Schematic illustration of the systems of flow-focusing generators: a) a single flow-focusing generator; b, c) coupled flow-focusing generators reported by Hashimoto *et al.* [69]; (IV): Pairing module. Two aqueous phases are injected by the outer channels and synchronously emulsified by the central oil channel studied by Frenz *et al*. [251]; (V): Schematic diagrams of droplet-based microfluidic devices showed by Hong *et al*. [252]. The pressure oscillator is red and the oil regulator is yellow. 32

Figure 2.13 (I): A fluidic ladder network for bubble synchronization reported by Prakash and Gershenfeld[254]; (II) Microfluidic device for cell capture and pairing presented by Skelley *et al.* [258]..... 34

Figure 2.14 (I): Schematic illustration of droplets mixing rapidly by recirculation [261]; (II): The topology of the counter-rotating eddy pairs in front, behind and within the droplets moving in a channel [270]; (III): Serpentine type mixer with bumps on the microchannel walls proposed by Liau *et al.* [268]..... 35

Figure 2.15 (I): Trap-and-release mechanism and experimental setup proposed by Tan *et al.* [274]; (II): Droplet trapping arrays presented by Huebner *et al*. [277]; (III): Architecture of the metering trap demonstrated by Korczyk *et al.* [278]..... 37

Figure 2.16 State diagram showing the four different behaviors observed in experiments at three different oil flow rates: (a) $Q_o = 10\mu l/h$, (b) $Q_o = 20\mu l/h$, and (c) $Q_o = 50\mu l/h$. Images (d)-(g) are representative snapshots of these behaviors[279]..... 38

Figure 2.17 A modular approach to droplet-based screening system using off-the-shelf components demonstrated by Trivedi *et al*.[288]..... 39

Figure 2.18 Left: droplet train transporting in a carrier fluid; Right: cross-section view of a large moving droplet in a rectangular capillary with thin lubrication films and corner gutters. 40

Figure 2.19 Rough sketch of possible streamlines in a Taylor flow provided by Taylor [292]. (a) The flow is reduced to steady motion with only one stagnation point, when $m > 0.5$. (b) There is one stagnation point on the vertex and a stagnation ring on the meniscus, when $m < 0.5$. (c) There are two stagnation points on the axis, when $m < 0.5$ 41

Figure 2.20 (A) Sketch of the pressure drop along a microchannel containing a bubble train. (B) Crosse-section view of the bubble down the long axis of the channel. (C) A schematic diagram when the liquid does not flow past the bubble through the gutters. (D) A schematic diagram when liquid flows past the bubble through the gutters [309]..... 43

Figure 2.21 A qualitative plot of the pressure along a microchannel containing a droplet train in the case of (a) inviscid droplets ($\eta << 1$) and (b) viscous droplets ($\eta \sim 1$) [289] 45

Figure 2.22 (I): Droplet microfluidic system used to synthesize magnetochromatic microspheres reported by Kim *et al.*[322]. (II): Schematic of the microfluidic device for Janus droplet generation and produced Janus microparticles demonstrated by Marquis *et al.*[333]. 46

Figure 2.23 Microdroplet PCR workflow provided by Tewhey *et al.* [337]..... 48

Figure 2.24 Concentration gradient platforms. (I): Concentration gradient generator by controlling the flow rates of two samples reported by Yeh *et al.* [360]; (II) Concentration gradient generator by merging and mixing pre-formed droplets presented by Um *et al.*[367]. (III): Concentration gradient structures through diffusion between two samples, such as Y-junction by Bui *et al.* [363] and Radial distributor by Yang *et al.* [361]; 50

Figure 3.1 Photos of experimental setup. The central photo shows the whole connection of components 51

Figure 3.2 Calibration curve of flow rate vs 'tick' count for the SLG 1430 flow sensor. Linear regression profiles are: -6.4804x +104.96 (silicone oil), -4.3781x + 73.142 (10%glyc/water), -4.3282x + 66.894 (60%glyc/water), -4.4637x + 69.063 (80%glyc/water) with $R^2 > 0.997$ for all profiles. 53

Figure 3.3 Schematic of soft lithography fabrication procedure..... 56

Figure 3.4 Sketch of flow focusing equivalent hydrodynamic resistance measurements for calculating the junction height. The continuous phase is blocked and silicone is pumped from the inlet of disperse phase to the outlet of main channel. Pressure is controlled by the Fluigent system, and flow rate is measure by the flow sensor. 58

Figure 4.1 Sketch of global network design, the widths of the dispersed phase and continuous phase are the same at the flow focusing junction..... 65

Figure 4.2 Droplet speed over a formation cycle for the case where the dispersed phase is glyc/water 60% wt, height/width ratio $h^* = 0.58$, $Q_d = 1.69\mu l/min$, and $Q_c = 3.59\mu l/min$. 68

Figure 4.3 (a) Video captured from Exp #4 listed in Table 4.1. The flow rates of the continuous and dispersed phases are $Q_c = 3.74\mu l/min$ and $Q_d = 2.87\mu l/min$, respectively. V_d is the droplet volume, V_c the oil volume between two adjacent droplets, L_d the droplet length, f the frequency of droplet generation and s the spacing between two adjacent droplets. (b) Droplet generation cycle in the flow focusing generator with three stages: (i) filling stage (ii) necking stage, and (iii) pinch-off stage. The figures are not captured with the same Δt. 69

Figure 4.4 (a) The estimated 3D shape of droplet. The out of plane curvature is approximated as *h*/2. (b) The 2D shapes of droplet at the transitions between each stage, where V_{BF} and V_{EF} represent the droplet volume at the beginning and end of the filling stage, respectively, V_{BN} and V_{EN} the volume of the continuous phase in the V-

shape at the beginning and end of the necking stage, and V_{gutter} the volume of the continuous phase bypassing the gutter during the necking stage. 71

Figure 4.5 (a) Assumed configuration of the droplet cross-section; (b) Actual configuration of the droplet cross-section 71

Figure 4.6 (a) 2D top-view area A_1 of V_{BF}^* at the beginning of filling stage. (b) Cross-section area of the curved interface A_2 73

Figure 4.7 (a) 2D top-view area of V_{EF}^* and (b) 3D view of V_{BN}^* at the end of filling stage (also called "at the beginning of necking stage") 75

Figure 4.8 (a) Variations of the V-shape length, neck width and oil length during a droplet formation cycle for the case where the dispersed phase is glyc/water 60% wt, height/width ratio $h^* = 0.58$, $Q_d = 1.69\mu l/min$, and $Q_c = 3.59\mu l/min$. (b) Image of the V-shape length, neck width and oil length. 76

Figure 4.9 2D top-view area of the forming droplet at the end of necking stage. 78

Figure 4.10 (a) Sketch of the open rectangular channel (the gutter)with three walls and the forth being an arbitrary curved interface studied by Tchikanda *et al*. [377]; (b) Non-dimensional mean velocity $\overline{u}_g^*$ as a function of the gap aspect ratio $\lambda_{gap} = \frac{h}{w_{gap}}$ provided by Tchikanda *et al*. [377]. 82

Figure 4.11 Simulation domain of the 3D numerical model with, $L_{fill}^* = 0.7$, height/width ratio $h^* = 0.41$ and a fluid viscosity of 9.96 mPa.s (continuous phase). 83

Figure 4.12 Equivalent pressure drop length coefficient in the gutter region as a function of the penetrating drop length at the end of the filling stage with different height/width ratios, $h^* = 0.41$ (◇), $h^* = 0.58$ (○), and $h^* = 0.66$ (△). The fitting curve is an asymptote, $\left(1+0.2L_{fill}^{*\,-1.4}\right)^2$ 84

Figure 4.13 Relative pressure drop versus viscosity ratio. 85

Figure 4.14 Plots of non-dimensional L_{fill}^*. Experimental results VS. Calculated results in conditions of $h^* = 0.41$, $h^* = 0.58$, and $h^* = 0.66$, with the dispersed phase, glyc/water 10% by wt. (◇), glyc/water 60% by wt. (○) and glyc/water 80% by wt. (△), respectively. 87

Figure 4.15 Plot of non-dimensional W_{pinch}^*. Experimental results VS. Calculated results in conditions of $h^* = 0.41$, $h^* = 0.58$, and $h^* = 0.66$, with dispersed phase, glyc/water 10% by wt. (◇), glyc/water 60% by wt. (○) and glyc/water 80% by wt. (△), respectively. 88

Figure 4.16 Parity plot of the experimentally measured and model predicted non-dimensional L_{pinch}^* for the conditions with different channel heights ($h^* = 0.41$, $h^* = 0.58$,

and $h^* = 0.66$) and different dispersed phase (glyc/water 10% by wt. (◇), glyc/water 60% by wt. (○) and glyc/water 80% by wt. (△)), respectively. 90

Figure 4.17 Flow chart of the steps of calculating droplet volume, V_d^*, frequency , f^* and spacing, s^*. 91

Figure 4.18 Parity plot for the non-dimensional (a) droplet volume, (b) formation frequency and (c) droplet spacing for all the experimental data including different channel heights ($h^* = 0.41$, $h^* = 0.58$ and $h^* = 0.66$), and different dispersed phase (glyc/water 10% by wt. (◇), glyc/water 60% by wt. (○) and glyc/water 80% by wt. (△), respectively. 92

Figure 5.1 (a) Sketch of the microchannel design. The channel width is set to be 100μm, the height 40μm and the distance between the two junctions 300μm. Inlets 1 and 2 are for the dispersed phase and inlet 3 is for the continuous phase. (b) Sketch of flow combinations at the flow focusing junctions. 105

Figure 5.2 Droplet generation process. (i) Droplet pinches off; (ii) Dispersed phase returns back to semilunar shape due to the interfacial tension and starts filling the main channel; (iii) End of filling stage and the silicone oil starts squeezing the dispersed phase; (iv) The necking width reaches to a critical value and droplet starts pinching off; (v) Droplet pinches off and a new droplet is forming. (a) Pure 10%glyc as the dispersed phase with the flow rate of silicone oil and 10%glyc as $Q_{oil} = 4\mu l/min$ and $Q_{10\%glyc} = 1.62\mu l/min$, respectively; and (b) pure 80%glyc as the dispersed phase with flow rate of silicone oil and 80%glyc as $Q_{oil} = 4\mu l/min$ and $Q_{80\%glyc} = 1.62\mu l/min$, respectively. 107

Figure 5.3 Non-dimensional droplet volume under different flow ratios of 10%glyc/(10%glyc+80%glyc), with a fixed flow rate of $Q_{oil} = 4\mu l/min$ for the continuous phase and $Q_{10\%glyc+80\%glyc} = 1.62\mu l/min$ for the dispersed phases. Non-dimensional droplet volume is defined as $V_d^* = \frac{V_d}{w^2 h}$, where w is the channel width, h channel height. 109

Figure 5.4 Droplet generation process (i) Droplet pinches off; (ii) Dispersed phase returns back to semilunar shape due to the interfacial tension and starts filling the main channel; (iii) End of filling stage, and the silicone oil starts squeezing the dispersed phase; (iv) The necking width reaches a critical value and droplet starts pinching off; (v) Droplet pinches off, and a new droplet is forming. (a) $\lambda = 0.2$, $Q_{oil} = 4\mu l/min$, $Q_{10\%glyc} = 0.32\mu l/min$, $Q_{80\%glyc} = 1.3\mu l/min$; (b) $\lambda = 0.7$, $Q_{oil} = 4\mu l/min$, $Q_{10\%glyc} = 1.13\mu l/min$, $Q_{80\%glyc} = 0.49\mu l/min$; (c) $\lambda = 0.8$, $Q_{oil} = 4\mu l/min$, $Q_{10\%glyc} = 1.30\mu l/min$, $Q_{80\%glyc} = 0.32\mu l/min$ 111

Figure 5.5 Droplet generation process (i) Droplet pinches off; (ii) Dispersed phase returns back to semilunar shape due to the interfacial tension and starts filling the main channel; (iii) End of filling stage, and the silicone oil starts squeezing the dispersed phase; (iv) The necking width reaches a critical value, and the droplet

starts pinching off; (v) Droplet pinches off, and a new droplet forms. (a) $\lambda = 0.2$, $Q_{oil} = 4\mu l/min$, $Q_{10\%glyc} = 0.32\mu l/min$, $Q_{80\%glyc} = 1.3\mu l/min$; (b) $\lambda = 0.5$, $Q_{oil} = 4\mu l/min$, $Q_{10\%glyc} = 0.81\mu l/min$, $Q_{80\%glyc} = 0.81\mu l/min$; (c) $\lambda = 0.8$, $Q_{oil} = 4\mu l/min$, $Q_{10\%glyc} = 1.30\mu l/min$, $Q_{80\%glyc} = 0.32\mu l/min$ 112

Figure 5.6 Droplet generation process with (a) $\lambda = 0.5$, $Q_{oil} = 4\mu l/min$, $Q_{10\%glyc} = 0.81\mu l/min$, $Q_{80\%glyc} = 0.81\mu l/min$ and (b) $\lambda = 0.8$, $Q_{oil} = 4\mu l/min$, $Q_{10\%glyc} = 1.30\mu l/min$, $Q_{80\%glyc} = 0.32\mu l/min$ 113

Figure 5.7 Non-dimensional droplet volumes under different flow ratios and capillary numbers. Experiment #1~37 were performed for each case (i, ii, iii, 10%glyc only and 80%glyc only), within flow rate errors in $\pm 5\%$ 114

Figure 5.8 (a) Viscosity-stratified flow shapes when the dispersed phases start filling the main channel with flow rates $Q_{oil} = 4\mu l/min$, $Q_{10\%glyc} = 1.13\mu l/min$, $Q_{80\%glyc} = 0.49\mu l/min$ .Case I: 10%glyc is surrounded by 80%glyc, Case II: 10%glyc is parallel to 80%glyc, and Case III: 80%glyc is surrounded by 10%glyc. (b) Sketch of the velocity profile of viscous stratified flows in rectangular channel at the first junction for three cases..... 115

Figure 5.9 Images captured from experimental videos showing single particle encapsulation with a stratified flow of case (iii) (a ~ c) and without a stratified flow (d ~ e) 117

Figure 6.1 (a) ~(c) microfluidic flow focusing device geometries with different angles at the junction. The angle between the inlet of the dispersed phase and the continuous phase θ is (a) 45°, (b) 90° and (c) 135°. (d) ~ (f) Optical micrographs of drops produced in microfluidic devices with $\theta =$ (d) 45°, (e) 90° and (f) 135°. The viscosity of the dispersed phase is 8 mPas, that of the continuous phase is 1 mPas. The flow rate of the dispersed phase is 100 µl/h, that of the continuous phase 1 ml/h. The Experiments were done by Esther Amstad. 121

Figure 6.2 The size of drops produced in microfluidic flow focusing devices with $\theta = 45^\circ$ (●), 90° (▲), and 135° (■). The viscosity of the dispersed phase is 1 mPas, that of the continuous phase is 1 mPas (filled symbols) and 10 mPas (open symbols). (a) The flow rate of the continuous phase is 1 ml/h, that of the dispersed phase is varied between 100 µl/h and 1000 µl/h. (b-c) The drop size as a function of the (b) flow rate of the continuous phase and (c) the velocity component of the continuous phase in the inlet that is directed perpendicular to the main channel. The flow rate of the dispersed phase is 500 µl/h. 122

Figure 6.3 (a) Photograph of a droplet on demand system, consisting of a microcontroller, optical switches and two solenoid valves. (b) Sketch of valve connection to a T-junction droplet generator. The two solenoid valves are connected with the inlets of the continuous phase and the dispersed phase, respectively. 124

Figure 6.4 Droplet generation on demand captured from video using $4\times$ objective. Signals are sent from the digital outputs of microcontroller. Droplet length is determined by the opening time of valve 2. 125

Figure 6.5 Sketch of droplet pair generator consisting of one droplet generator, two diluting streams, and a droplet sorting structure. The droplet generator is used to generate monodispersed droplets. The continuous phase liquid is pumped through two diluting streams to control the droplet spacing. The sorting structure is used to guide droplets into two branches alternatively. 127

Figure 6.6 Sketch of bypass design for sorting droplets into two branches. The Y-junction angle is set to 90°. P_Y is the pressure at the Y-junction, P_{b1} is the pressure at the end of branch 1, P_{b2} is the pressure at the end of branch 2, s is the spacing between two droplets, r_1 is the length of branch 1, and r_2 is the length of branch 2. The pillars inside the bypass channel are used to prevent droplets from going into the bypass channel. 128

Figure 6.7 (a) Sketch of the bypass loop, 1 ~ 7 are the channel number; (b) Equivalent circuit network of the bypass loop. P_{in} is the pressure at the inlet of droplets, P_{out} is the pressure at the outlet of droplets, P_U is the pressure at the end of up branch, P_D is the pressure at the end of down branch, P_{j1} is the pressure at beginning of the loop, P_{j2} is the pressure at the end of the loop. $R_1 \sim R_7$ are the hydrodynamic resistances of each channel, respectively. 130

Figure 6.8 (a) Top view of the droplet sorting loop; (b) Droplet pairs are generated after the sorting loop. The pictures were captured from videos under experimental settings of $P_d = 945\text{mbar}$, $P_c = 960\text{mbar}$, and $P_{diluter1} = 860\text{mbar}$, where P_d is the pressure applied at the inlet of the dispersed phase, P_c is the pressure applied at the inlet of the continuous phase, and $P_{diluter1}$ is the pressure applied at the inlet of diluter 1. s is the initial spacing between droplets, f is droplet frequency, s_1 and s_2 are the spacing between two nearby droplets after the sorting loop, respectively. 134

Figure 6.9 (a) Picture of a curved microchannel with a diameter of ϕ=2000μm connected to the downstream channel of the droplet pair generator. The picture is captured using $4\times$ objective, and the droplet pairs are different from the one shown in (b) and (c); (b) A droplet pair before entering the curved channel captured using $20\times$ objective. s_{before} is the spacing between two droplets before entering the curved channel; (c) The same droplet pair as in (b) after leaving the curved channel captured using $20\times$ objective. s_{after} is the spacing between two droplets after leaving the curved channel; 136

Figure 6.10 Droplet spacing before entering the curved channel ($x-$ coordinate), and after leaving the curved channel ($y-$ coordinate) under experimental settings of viscosity ratio $\eta = 0.12$, capillary number $Ca = 0.81\times10^{-3}$, non-dimensional

droplet length $L_d / w = 1.18$. 100 Pairs of droplet were measured with an initial spacing range from 224 μm ~392 μm 137

Figure 6.11 Schematic of the merging chamber. L, W_{by}, W_c, W_p, W_s, and L_p represent the chamber length, bypass channel width, width of the central chamber, width of the pillars, inter-pillar spacing, and pillar lengths, respectively. 141

Figure 6.12 Sequential droplet merging captured using $10\times$ objective. (a) the first droplet enters the merging chamber, (b) the first droplet is trapped between the pillars allowing the next droplet to catch up, (c) the first two droplets merge and remain trapped within the pillar array and the length of the product droplet increases proportionally, (d) the product droplet blocks the exit of the bypass channel when the third droplet enters the central chamber, (e) the product droplet is fully merged and is forced out of the chamber by the continuous phase liquid. 143

Figure 6.13 (a) Microfluidic circuit design of the droplet trapping and releasing on demand system; (b) Flow focusing device for droplet generation; (c) Serpentine type channel for droplet mixing; (d) Design for droplet trapping and releasing on demand, where Q_B is the flow rate in the bypass channel and Q_T is the flow rate in the trapping well. 148

Figure 6.14 One example of droplet trapping sequence captured using $4\times$ objective with droplet velocity U_d =18.4mm/s. (a) Droplet trapping is triggered by stopping the pressure applied in the diluting stream; (b) A droplet is trapped in the first trapping well at time $t = 0.28$s ;(c) A droplet is trapped in the second trapping well at time $t = 0.40$s ;(d) A droplet is trapped in the third trapping well at time $t = 1.87$s 149

Figure 7.1 Sketch of the first version design for trapping two streams of droplets. A) Overview of the chip design. B) Droplet generator to generate two streams of droplets with channel height 60 μm , channel width of oil 240 μm , channel widths of reagent 1 and 2 120 μm . C) A regulator to adjust the spacing between two droplets. D) Trapping wells to trap two droplets from two different streams. An array of trapping wells can be integrated into the flow stream depending on requirements. Five trapping wells are integrated in this design to demonstrate the working principle. 155

Figure 7.2 A. Picture of droplet generation captured using $4\times$ magnification. B. Picture of trapped droplets captured using $10\times$ magnification. 156

Figure 7.3 Sketch of the second version design for trapping two streams of droplets. A) Overview of the chip design. B) Droplet generator to generate two streams of droplets alternatively with channel height 60 μm , channel width of oil 120 μm , channel widths of reagent 1 and 2 120 μm with a triangle pressure oscillator. C) A channel is added beside the trapping channel to dispose the sample waste, which has a rectangular pillar at the inlet. D) Trapping wells to trap two droplets from upstream. The channel of sample waste has the same dimensions

as the trapping channel. An array of trapping wells can be integrated into the flow stream depending on requirements. 157

Figure 7.4 (A) Picture of droplet generation alternatively captured using $4\times$ magnification. B. Droplet trapping process captured using $4\times$ magnification. 158

Figure 7.5 Sketch of the third version design for trapping two streams of droplets. A) Overview of the chip design. The design is symmetric and has two separate T-junction droplet generators with exactly the same channel dimensions. B) T-junction droplet generator for reagent 1 with channel height $60\,\mu m$, channel width of oil $120\,\mu m$, channel width of reagent 1 $120\,\mu m$. C) An intersection: the left channel is used to dispose sample waste; the right channel is used to remove dust inside the microfluidic chip, the downstream channel is used to trap droplets. D) Trapping design for trapping droplets from two droplet streams. The channel of sample waste has the same dimensions as the trapping channel. An array of trapping wells can be integrated into the flow stream depending on requirements. E) Dimensions of two trapping wells. Inlet channel width keeps the same as upstream channel $120\,\mu m$; trapping well diameter $85\,\mu m$; Distance between two centers $160\,\mu m$; gap width at the intersection of the two wells 57.4 μm; gap width between each pillar $25\,\mu m$. 160

Figure 7.6 (a) Definition of parameters of a trapping well unit. P_{up} and P_{down} are the pressures at the inlet and outlet of a trapping well unit, respectively; P_j and $P_j^{'}$ are the pressures at the T-junctions of each stream, respectively; P_{trap} and $P_{trap}^{'}$ are the pressures at the back tip of trapped droplets; Q_j and $Q_j^{'}$ are the flow rates in the main channels of each stream, respectively. Q_{bypass} and $Q_{bypass}^{'}$ are the flow rates in each bypass channel; Q_{trap} and $Q_{trap}^{'}$ are the flow rates in each trapping well; w the channel width; w_i the width of the intersection gap between two trapping wells; w_{gap} the width between each pillar; r the radius of the trapping well; L_1 length of the trapping well; L_2 length of gap between each pillar; L_{join} length of the junction that connects the two main channels of the two streams; and L_{main} length of the main channel. (b) Equivalent fluidic circuit of a trapping well unit with fluidic resistors. 163

Figure 7.7 Two streams of droplet generation captured from high-speed camera with $4\times$ objective under the setting conditions: $P_{oil1}=500\text{mbar}$, $P_{oil2}=500\text{mbar}$, $P_{water}=440\text{mbar}$, $P_{dye}=440\text{mbar}$, $P_{outlet1}=230\text{mbar}$, $P_{outlet2}=0\text{mbar}$. Silicone oil with a viscosity of 5cSt was used as the continuous phase. (a) Water droplets with droplet length about $2w$ and spacing $28w$. (b) Methylene blue dye droplets with droplet length $2w$ and spacing $19w$. 171

Figure 7.8 Droplet pairing and trapping process captured from high-speed camera using $4\times$ objective under the setting conditions: $P_{oil1}=500\text{mbar}$, $P_{oil2}=500\text{mbar}$,

$P_{water} = 440\text{mbar}$, $P_{dye} = 440\text{mbar}$, $P_{outlet1} = 0\text{mbar}$, $P_{outlet2} = 230\text{mbar}$. Silicone oil with a viscosity of 5cSt (5cSt silicone oil density 0.913g/ml) was used as the continuous phase. Droplets containing Methylene blue dye are on the left side branch, and Droplets full of water are on the right side branch. (a) Droplets reached in front of the first trapping well. The methylene blue droplet had an average velocity of $U_{d\_dye} = 13.9\text{mm/s}$, and the water droplet had an average velocity of $U_{d\_water} = 15.8\text{mm/s}$ before they got trapped in the first trapping well. Capillary number of the continuous phase were estimated as $Ca_{c\_dye} = 0.00118$, $Ca_{c\_water} = 0.00134$; (b) the first pair of droplets got trapped; (c) the second pair of droplets got trapped; (d) the third pair of droplets got trapped; (e) the forth pair of droplets got trapped. (f) Four pairs of droplets are fully mixed after 4.15s 172

Figure 7.9 Droplet merging and mixing process in the second trapping well captured from high-speed camera using $20\times$ objective under the setting conditions: $P_{oil1} = 500\text{mbar}$, $P_{oil2} = 500\text{mbar}$, $P_{water} = 440\text{mbar}$, $P_{dye} = 440\text{mbar}$, $P_{outlet1} = 0\text{mbar}$, $P_{outlet2} = 230\text{mbar}$. Silicone oil with a viscosity of 5cSt (5cSt silicone oil density 0.913g/ml) was used as the continuous phase. The darker droplet is methylene blue, and the brighter droplet is pure water. (a) The two droplets start merging. (b ~ h) Droplets mixing process after merging. 174

Figure 7.10 (a) Grayscale value measurement area, where the boundary was excluded. (b) Mixing index V.S. time under different droplet average velocities..... 177

Figure 7.11 Droplet releasing process captured from high-speed camera using $4\times$ objective under the setting conditions: $P_{oil1} = 500\text{mbar}$, $P_{oil2} = 500\text{mbar}$, $P_{water} = 0\text{mbar}$, $P_{dye} = 0\text{mbar}$, $P_{outlet1} = 1000\text{mbar}$, $P_{outlet2} = 0\text{mbar}$. Silicone oil with a viscosity of 5cSt (5cSt silicone oil density 0.913g/ml) was used as the continuous phase. (a) Droplets trapped inside the trapping wells before releasing. (b) The trapped droplets were about to be washed out of the trapping wells. (c) The trapping wells after rinsed by silicone oil. 178

Figure 7.12 Sketch of the trapping well design for trapping multiple droplets with a concentration gradient of reagents. The number of trapped droplets ratio in a trapping well varies from 1:3 to 3:1, which creates 5 different reagent concentrations. 179

Figure 7.13 Droplet trapping and releasing process to generate a concentration gradient captured from high-speed camera using $4\times$ objective under the setting conditions: $P_{oil1} = 480\text{mbar}$, $P_{oil2} = 480\text{mbar}$, $P_{water} = 440\text{mbar}$, $P_{dye} = 450\text{mbar}$, $P_{outlet1} = 0\text{mbar}$, $P_{outlet2} = 170\text{mbar}$. (a) ~ (h) is droplet trapping process. (i) ~ (j) is droplet releasing process. 180

List of Tables

Table 2.1 Summary of dimensionless numbers used to describe the microfluidic two-phase flows..... 7

Table 4.1 Experimental conditions..... 62

Table 4.2 Measured channel dimensions after sufficiently swelling for each specific experiment..... 64

Table 4.3 Pressure conditions applied in Exp # 1 for silicone oil and 10%glyc/water with no surfactant on a type 1 chip. 66

Table 6.1 Channel Dimensions of the loop. $L_1 \sim L_7$ are the channel lengths of each branch, w is the channel width, and h is the channel height..... 132

Table 6.2 Experimental results V.S. Calculated results under the condition of input pressure $P_{in} = 920\text{mbar}$, droplet frequency $f = 6.576\text{Hz}$, slip factor $\alpha = 1.1$, equivalent droplet length $L_{effdrop} = 450\mu\text{m}$ 133

Table 7.1 Channel dimensions of microfluidic trapping wells..... 164

Chapter 1
Introduction

1.1 Research Background

Microfluidic technology refers to the work associated with devices that control and manipulate fluids on the length scale of microns. This field has been rapidly developed and is set to have broad applications in chemistry, pharmacology, biology, healthcare and food industries [1, 2]. This technology was initially proposed to scale down sample volumes and channel dimensions to perform chemical or biological reactions with very small quantities of reagents and therefore saving processing time. One such example is to integrate all of the processing steps of a reaction or a series of reactions on a single microfluidic device. This is often referred to as Lab-on-a-Chip (LOC) or micro-Total Analysis System (μTAS) devices[3–6]. For some medical applications, microfluidic technology is developed to allow self-contained disposable devices to provide a safe and effective way to work with bio-hazardous materials. Another concept called Lab-on-a-CD was introduced in recent years for biomedical analysis targeted towards in-vitro diagnostics (IVD), which integrates complex assays in fluidic networks on centrifugal microfluidic systems[7, 8]. LOC devices have several attractive features such as low reagent consumption, minimized waste products, reduced reaction time, and relatively low cost. In addition, LOC devices have structures with length scales that are comparable to the intrinsic dimensions of cells, making them particularly useful in the study of biology and biomedicine [9]. These benefits allow researchers to perform experiments that were impossible before, such as studying the kinetics of chemical reactions, fabricating special microbeads, or screening biological properties, etc. [10], and is what makes the advancement of microfluidic technology so important.

Several standard microfabrication techniques have been used in fabricating LOC devices. LOC devices were first fabricated in glass or silicon by contact and electron beam lithography followed by isotropic or anisotropic etching and anionic bonding [11]. Although most of these methods offer great advantages such as strong chemical stability, geometric precision and durability, the high cost and time consuming fabrication process cripples advances in the field. For scientific research, minimal fabrication time and flexible design process is essential, which lead to the introduction of soft lithographic techniques such as replica molding , embossing , and mold-machining [11–14] . Since then, number of research related to LOC devices has increased exponentially.

Due to the simplicity of fabrication, microfluidic devices in labs are often fabricated by replica molding using poly(dimethylsiloxane) (PDMS), which is commercially available (kit 'Sylgard 184') from Dow Corning. It consists of a base and a curing agent mixed with a mass ratio of 10:1. First, a master is fabricated by standard photolithography using SU-8 photoresist. Then, a mold is cast by pouring the mixed PDMS onto the master followed by degassing and heat curing. After peeling off the cured PDMS mold from the master, the mold is bonded to a glass, silicon or PDMS substrate, and tubing can be directly pushed into the reservoirs. However, PDMS does not have many applications in industry due to the higher cost and slower fabrication process compared to other methods on large scale such as hot embossing and microinjection [5].

In the early days of microfluidics, researchers mainly work with single phase flow, which imparts significant physical limitations in controlling reagents, chief of which is the slow mixing effect. The slow mixing is a result of the laminar flow inside micron-scale channels, where viscous and surface forces dominate inertial and gravitational forces. This problem has attracted a large number of researchers to work on enhancing mixing in microfluidic systems [15, 16]. Another problem is the enlarged influence on flow pattern imposed by channel walls at small length scales. Depending on the particular boundary effects, the axial dispersion of the injected liquid is dependent on the width of the cross-section instead of on the smaller height of microchannels [17, 18].

To avoid these undesired influences caused by single-phase microfluidics while keeping the advantages of LOC devices, two-phase droplet-based microfluidics was introduced and has quickly grown in the last decade. In droplet-based microfluidics, each droplet is used as a movable micro-reactor that prevents precipitating of substances and eliminates cross contaminations from wetting of channel walls. The droplet volume ranges from femtoliter to nanoliter, minimizing sample consumption and reducing reaction times. This approach also allows high throughput screening applications as dispersed droplets can be formed at frequencies as high as 20 KHz with small volume variations ranging only from 1-3% [19]. Mixing happens rapidly inside the droplet due to the internal convective flow [20–24]. Compared with single phase microfluidics, droplet-based microfluidics can scale up effectively by controlling and manipulating each individual droplet including droplet formation, coalescence, splitting, trapping and sorting, etc. [25, 26]. With these merits, droplet microfluidics offers many possibilities to solve problems in applied chemistry and biology. Therefore, extensive research effort has been reported in the study of droplet-based microfluidics over the past decades, including the general techniques, governing physical principles, and applications.

Despite the demonstrated potential [27–29], there remains many challenges that prevent droplet microfluidic commercialization. First, there is a lack of physical model that captures droplet dynamics during transportation. Previous models are of experimental nature and their predictions are only valid over a small data set. Second, many droplet manipulating techniques require insertion of electric, magnetic, optics, and pneumatic components into the microfluidics device, complicating the fabrication process, reducing design freedom, and drastically increase the cost of manufacturing. Third, current imaging-based microscopy, laser-based molecular spectroscopy, electrochemical detection, capillary electrophoresis, and mass spectrometry [30], has yet to match the KHz droplet generation rate, and to realize the high throughput screening potential. Another issue of concern is related to the fabrication of devices and device materials. Polydimethylsiloxane (PDMS) is widely used in microfluidic research labs due to its flexibility, ease of implement, low cost, and natural hydrophobicity. However, it is difficult to reproduce in a scale of millions (industrial scale) by using soft lithography fabrication method. Moreover, PDMS adsorbs peptide and dye [31], which can be detrimental in some biological reactions. In recent years, several groups have used thermoplastic materials to fabricate microfluidic chips through hot-embossing method. These materials are much harder than PDMS and don't adsorb the solvents. However, special hydrophobic or hydrophilic surface treatment is needed before they can be used to produce droplets [32]. A better material and fabrication method for producing microfluidic devices still needs to be explored.

This thesis focuses on studying the fundamental principles of droplet microfluidics to better understand the mechanism of droplet formation and manipulation, which is critical for designing a microfluidic chip for high throughput screening applications. A comprehensive physical model was first developed to predict droplet formation size, frequency, and spacing in a flow focusing device operating in the squeezing regime, taking into account of various geometrical and operating conditions such as viscosity ratio between the dispersed phase and continuous phase, capillary number that indicates the competition between viscous and interfacial tension forces, and flow rate ratio of two phases. This model can better understand the mechanism of droplet generation in a flow focusing geometry and guide the design of flow focusing devices. Based on the first project, the mechanism of droplet generation in a geometry with two junctions in series was studied when two miscible liquids are used as the dispersed phase. The two miscible liquids flow through the first flow focusing junction and form a stratified flow, which is used as the dispersed phase to form droplets in the second junction. This project considered multiple miscible fluids as the dispersed phase and the results were compared with the first project. Based on the fundamental understanding , several

microfluidic designs for generating and manipulating droplets were proposed, including: i) a flow focusing device with different angles to generate monodispersed droplets, ii) a droplet on demand system using off-the-shelf solenoid valves and microcontroller, iii) a droplet pair generator with uniform droplet size and controlled spacing, iv) a droplet merging design for controlled reagent volume, and v) a droplet trapping and releasing on demand system for screening drugs. These designs were shown to have prospective applications in chemical and biomedical reactions. The final project aimed to design a complex microfluidic chip that integrates multiple functions including droplet generation, trapping, pairing, merging, mixing and releasing for biomedical reactions, such as drug screening, chemical synthesis, and cell culture, etc.

1.2 Thesis Outline

In chapter 1, the research background is introduced and some general concepts on microfluidics are summarized to illustrate the purpose and significance of this research on droplet-based microfluidics.

In chapter 2, a literature review is provided focusing on the fundamentals of two-phase flow, droplet generation and manipulation, followed by its applications. A brief summary and comparison are made on different methods of generating and manipulating droplets. This review aims to demonstrate the state of the art in droplet-based microfluidics research and point out areas that still need to be worked on.

Chapter 3 presents the methodology, fluid properties, fabrication process and experimental setup that were used in the projects.

Chapter 4 presents a 3D physical model that describes the droplet generation process in a flow focusing device operating in the squeezing regime which predicts the size, frequency of droplets and the spacing between droplets under various aspect ratio of microchannel, viscosity ratio of the dispersed phase to the continuous phase, capillary number and flow rate ratio of the two phases.

Chapter 5 describes the mechanism of droplet generation when two miscible liquids are used as the dispersed phase. The two miscible liquids flow through the first flow focusing junction and form a stratified flow, then the stratified flow is used as the dispersed phase to form droplets. This project considers multiple miscible fluids as the dispersed phase and the results are compared with the first project.

Chapter 6 reports five microfluidic designs for generating and manipulating droplets for different applications , including a flow focusing device with different angles between inlets of the dispersed

and continuous phase liquids, a droplet on demand system using off-the-shelf solenoid valves and a microcontroller, a droplet pair generator with uniform droplet size and controlled spacing, a droplet merging design for controlled reagent volume, and a droplet trapping and releasing on demand system for screening drugs.

In Chapter 7, a microfluidic chip design that integrates droplet generating, pairing, trapping, merging, mixing and releasing is demonstrated. This design is controlled entirely by liquid flow involving no electrodes, magnets or any moving parts, does not require synchronized droplet generation , yet can achieve rapid mixing between multiple droplets while controlling their reagent concentration simultaneously.

Lastly, Chapter 8 summarizes the contribution of this thesis and work that needs to be done in the future.

Chapter 2
Literature Review

Two-phase microfluidic flows are usually generated when two immiscible fluids are forced into contact in microchannels. Gas-liquid [33–38] and liquid-liquid [39–42] flows are the most important two-phase flows in LOC devices. A large number of research has been done on gas-liquid (referred to as bubble) and liquid-liquid (referred to as droplet) two-phase flows, and there is an extensive amount of review articles discussing two-phase flows [3, 10, 19, 25, 26, 43–52]. From these review papers, one can see that two-phase flow is a very broad topic. Therefore, it is impracticable to review all the aspects of two-phase flow. In this report, the review focuses on droplet-based microfluidic flows, including some fundamentals of droplet microfluidics, droplet generation, droplet manipulation and its applications.

2.1 Fundamentals of Two Phase Flow

Compared with single-phase flows, microfluidic two-phase flows have many characteristics such as increased interfacial area, shortened transfer distance and enhanced mixing which can therefore reduce mass transfer limitations [44]. The properties of two-phase flow depend on the channel geometries, fluid properties and flow conditions. All these factors can be described by some important dimensionless parameters.

2.1.1 Dimensionless Numbers

Microfluidic two-phase flows are determined by a force balance between viscous, inertial, interfacial and body forces. Several dimensionless numbers describe the relative importance of these forces including the Reynolds number (*Re*), Bond number (*Bo*), Capillary number (*Ca*) and Weber number (*We*) [44, 47].

The Reynolds number describes the relative influence of inertial forces to viscous forces, which can be expressed as $Re = \frac{\rho u L}{\mu}$ where ρ is fluid density, u is the characteristic velocity, L is the characteristic length scale and μ is the dynamic viscosity.

The influence of the gravitational force relative to the interfacial force is described by the Bond number $Bo = \frac{\Delta\rho g L^2}{\gamma}$ where $\Delta\rho$ is the fluid density difference, g is the gravitational acceleration, L is the characteristic length scale and γ is the interfacial tension of the two fluids.

The Capillary number $Ca = \frac{\mu u}{\gamma}$ compares viscous forces to the interfacial force. The relative effect of inertial forces to the interfacial force is described by the Weber number, which can be expressed as $We = \frac{\rho u^2 L}{\gamma} = Re \cdot Ca$.

At the microscale level, the flow velocity (u) and volume to surface ratio ($\frac{L^3}{L^2} \sim L$) are very small. Hence, *Re*, *Bo* and *We* are much smaller than unity. The inertial and body forces can be ignored compared to viscous and interfacial forces. As a result only two forces, viscous and interfacial forces dominate the two-phase flow. Therefore, capillary number is the most important dimensionless number for analyzing microfluidic two-phase flow. Another group of dimensionless parameters which are related to the fluid properties and operating conditions include the viscosity ratio ($\eta = \frac{\mu_d}{\mu_c}$) and flow rate ratio ($\varphi = \frac{Q_d}{Q_c}$), where the subscripts d and c represent the dispersed phase and continuous phase, respectively. The geometries of microfluidic channels also play an important role in two-phase flows, which are usually described by the height to width ratio ($\Lambda = \frac{h}{w}$). The typical dimensionless numbers used to characterize the two-phase flows are summarized in Table 2.1.

Table 2.1 Summary of dimensionless numbers used to describe the microfluidic two-phase flows

Dimensionless Number	**Reynolds Number**	**Bond Number**	**Capillary Number**	**Weber Number**	**Viscosity ratio**	**Flow rate ratio**	**Height width ratio**
Abbreviation	*Re*	*Bo*	*Ca*	*We*	η	φ	Λ
Equation	$\frac{\rho u L}{\mu}$	$\frac{\Delta\rho g L^2}{\gamma}$	$\frac{\mu u}{\gamma}$	$\frac{\rho u^2 L}{\gamma}$	$\frac{\mu_d}{\mu_c}$	$\frac{Q_d}{Q_c}$	$\frac{h}{w}$

2.1.2 Surfactants, Carrier Fluids, and Chip Material

It is important to choose appropriate carrier fluids and corresponding device material to meet the specific requirements for a particular application in droplet-based microfluidics. Surfactants are an essential part of the droplet-based microfluidics. They are used to stabilize the droplet interfaces, prevent droplets from merging, and prohibit molecular exchange between droplets (see Figure 2.1(I)). Typically, surfactants are added to either the continuous phase or the dispersed phase to lower the interfacial energy [53], i.e. to stabilize the formed droplets and prevent them from coalescing through absorption at the interface. A typical surfactant molecule consists of a hydrophilic head and a hydrophobic tail as shown in Figure 2.1 (II). The affinity of the surfactant molecules for the water and oil can be evaluated by the balance of the size and strength of its hydrophilic and hydrophobic parts, which is called the Hydrophilic-Lipophilic Balance (HLB) value [54, 55]. Surfactants with high HLB values (more hydrophilic) preferentially encapsulate oil droplets in water, and surfactants with low HLB values (more hydrophobic) easily encapsulate water droplets in oil. Therefore, choosing the appropriate surfactant is crucial in the formation of droplets. In addition, the concentration of surfactant [56, 57] and the dynamic effects of surfactant molecular transportation [58–63] are found to have significant influence on droplet formation and stabilization. Surfactant transport along the interface and in the bulk phase induce the convective-diffusive and the adsorption-desorption phenomena, which are difficult to analyze and control. Hence, a high surfactant concentration, roughly 10 times higher than the critical micelle concentration (CMC) is usually used for droplet formation when a surfactant is required [61]. At such high concentrations, surfactant transport and adsorption are much faster than droplet generation, leading to an equilibrium interfacial tension at the expanding interface of the forming droplet. Therefore, a high surfactant concentration can avoid Marangoni stress, which is caused by the depletion of surfactant near the neck of the droplet [64–67].

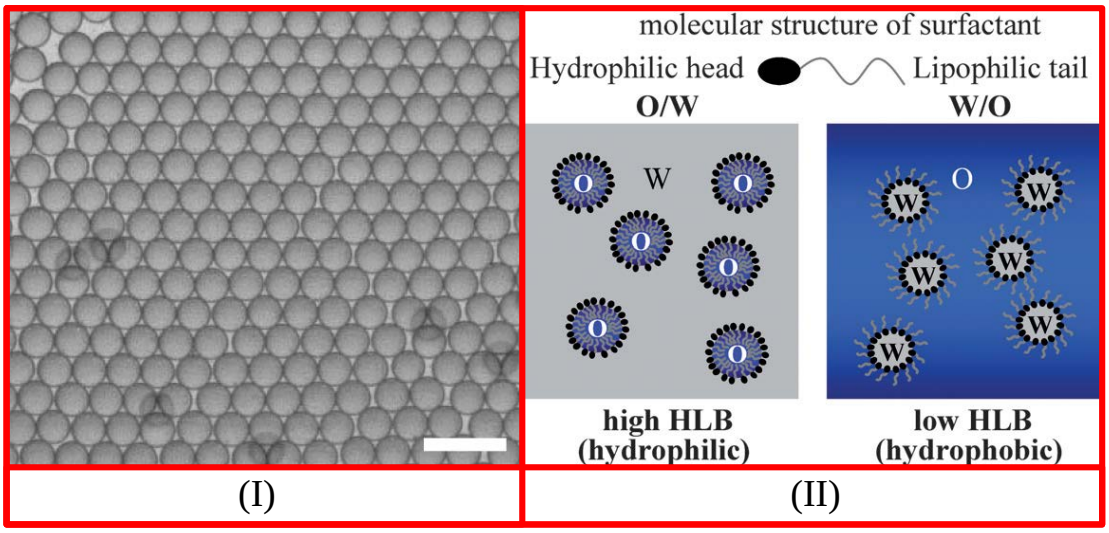

Figure 2.1 (I) An emulsion stabilized with non-ionic surfactants remains stable and monodispersed throughout incubation off chip [68] ; (II) Surfactant structure and emulsion types in macroscale emulsion preparation corresponding to HLB values. O and W represent oil and water phases, respectively [55].

A number of oils have been used as carrier fluids in different research groups including hexadecane [69], mineral oil [70], silicone oil [71], and fluorinated oil [72] in combination with standard surfactant such as Tween 20 or Span 80 to form aqueous droplets. However, most of these oils swell PDMS devices and result in change of microchannel dimensions with respect to time [73]. To overcome this effect, some research groups use alternative thermoplastic polymers such as polymethylmetacrylate (PMMA) [74–76], polycarbonate (PC) [77] and Cyclic Olefin Copolymer (COC) [78] to fabricate microchannels by a number of methods including laser ablation [74, 79, 80], milling machining [81] , hot embossing [82] and injection molding [13]. The detailed polymer microfabrication technologies are reviewed by literature [83]. Thermoplastics are a class of synthetic polymers which exhibit softening behavior above a characteristic glass transition temperature (T_g) while returning to their original chemical state upon cooling (similar to glass). Thermoplastics offer lower raw material costs and manufacturing costs compared with traditional microfluidic materials such as silicon and glass. A specialized review on these thermoplastic polymers has already summarized the physical properties and bonding techniques [84]. These types of devices and fabrication techniques are suitable for large scale manufacturing but are not frequently used for research, since the small scale production in laboratory does not justify the high equipment costs. To

reduce the influence of PDMS swelling on geometric variation, our lab estimated channel dimensions through hydrodynamic resistance measurement [85]. This technique will be discussed further in Chapter 3. In recent years, Paper-based microfluidics devices invented by the Whitesides Group of Harvard University in 2007 [86] has become an attractive alternative. Paper-based microfluidic systems, which transport liquids using pure capillary forces, are extremely cheap, easy-to-use, disposable, and equipment-free [87]. However, Paper-based microfluidic systems lack sealed microchannels, allowing droplets of nanoliter volume to evaporate quickly. This has limited Paper-based microfluidics to only a few applications so far.

The interfacial tension becomes dominant and crucial in microscale. When two immiscible fluids come into contact with a channel wall, three interfaces are created including fluid-walls and fluid-fluid. The wetting properties of the fluid-wall interface play an extremely important role in determining whether ordered or disordered patterns in two-phase flows will occur [88]. When the continuous phase completely wets the microchannel walls and the disperse phase does not wet the walls, ordered patterns can occur. In contrast, if the wetting is partial, disordered flow patterns occur. Typically, when the microchannels are hydrophobic, water-in-oil droplets are generated, vice versa [89, 90]. The hydrophobicity of a solid surface can be expressed by contact angle. When the contact angle is larger than 90^{o}, the surface is hydrophobic, while when the contact angle is less than 90^{o}, the surface is hydrophilic. PDMS is naturally hydrophobic. However, PDMS will become hydrophilic after plasma treatment which is used to bond to the substrate during the fabrication process [91]. To make water-in-oil droplets, the PDMS can be heated after plasma treatment (100℃ for 24h) [36] or chemically modified with silanizing agents to revert back to being hydrophobic [43, 91]. A review paper has summarized the materials commonly used for microfluidic chip fabrication [92].

2.2 Droplet Generation

Droplet-based microfluidics depends on the generation of droplets with controlled sizes at a large range of frequencies. The flows of the dispersed and continuous phases are driven either by syringe pumps or by pressure control. A variety of techniques have been developed to generate droplets including passive and active methods. The passive methods typically produce droplets by a geometry induced instability using different device geometries such as T-junction, co-flowing, flow focusing and step emulsification. The active methods typically use mechanical, thermal, electrical, magnetic, optical or acoustic forces to break up fluid streams and generate droplets. Most of these techniques will be reviewed and compared in the following sections.

2.2.1 T-junction

The T-junction geometry is a type of easily controllable production of monodispersed droplets and one of the most frequently used droplet generation devices, which was first presented by Todd Thorsen *et al.* [93] as shown in Figure 2.2(a). Some other geometries that are used to produce droplets, are derived from T-junction, such as “Y-junction” [94, 95] (see Figure 2.2(b)), and “V-junction” [96] (see Figure 2.2(c)).

In the T-junction, the inlet channel containing the dispersed phase perpendicularly intersects the main channel which contains the continuous phase. The two phases form an interface at the junction. The shear forces generated by the continuous phase and the pressure gradient cause the dispersed phase to elongate into the main channel until the neck of the dispersed phase decreases and pinches off eventually to form a droplet. In recent years, a number of articles were published to identify physical parameters and laws that govern the droplet breakup mechanism based on experimental results [36, 97, 98] , numerical simulation[99–102], and theoretical analysis [103–107]. Several physical parameters have been identified which affect the droplet generation such as flow rates and viscosities [108–110], channel wall wettability [111], surfactants [55, 61], interfacial tension [112] and channel dimensions [94].

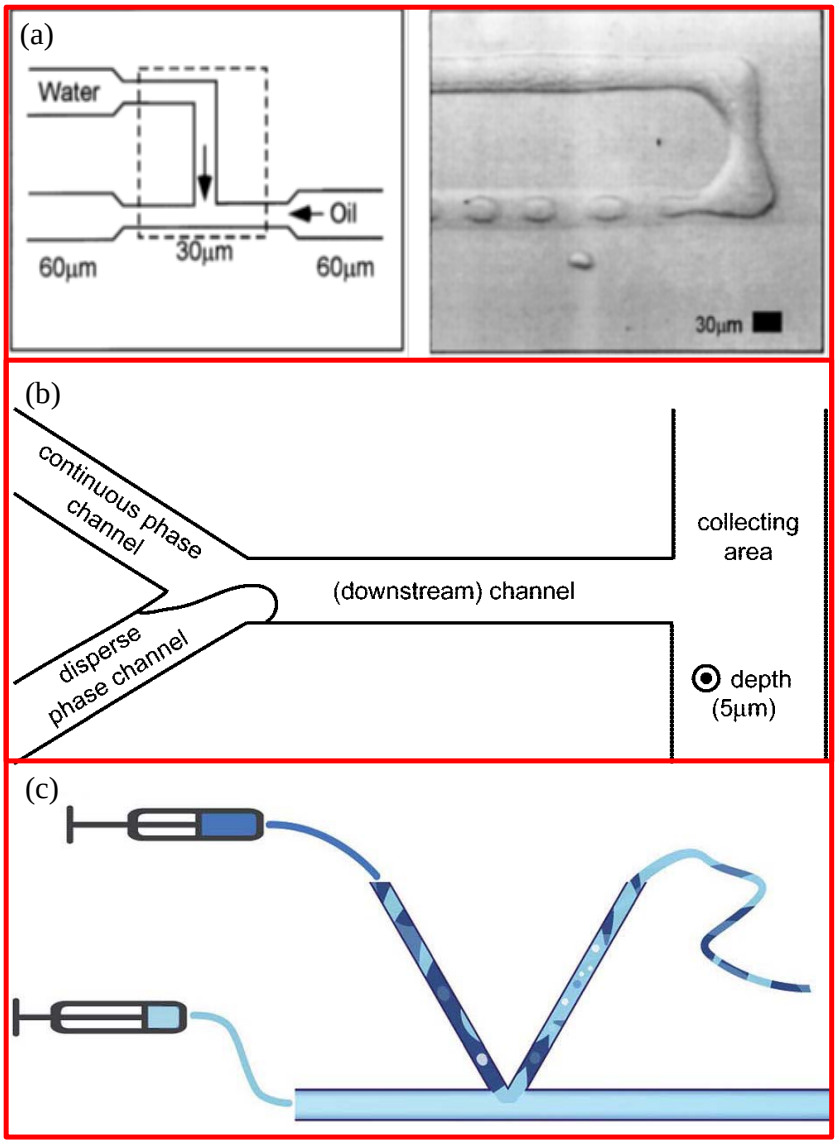

Figure 2.2 (a)Microfabricated T-junction geometry to generate water-in-oil droplet first presented by Todd Thorsen *et al.* [93]. Dashed rectangle indicates area in photomicrograph; (b) Outline of the Y-junction presented by Steegmans *et al.* [94]; (c) schematic of the V-junction structure presented by Ding *et al.* [96].

Generically, droplet breakup can be characterized by the competition between three forces including the shear stress, the increasing upstream pressure due to droplet blocking the main channel, and interfacial tension. The shear stress and upstream pressure act to elongate the droplet, and interfacial tension acts to resist deformation. Based on the degree of dominance of different forces,

the flow can be divided into three regimes, i.e. squeezing regime, dripping regime and jetting regime [36, 85,113]. Droplet generation in the squeezing regime is mainly caused by pressure built up upstream when the dispersed phase plugs into the main channel. In the squeezing regime, the droplet is strongly confined by the main channel with a very small capillary number of the continuous phase (Ca_c). On increasing Ca_c, the flow pattern enters into the dripping regime, and the transition between the squeezing and the dripping regime is characterized by the capillary number Ca_c. In the dripping regime, droplet generation is dependent on the competition between viscous force and interfacial tension. At high flow rates of the continuous and dispersed phases, the flow operates in the jetting regime characterized by the formation of long threads of the dispersed phase before its breakup. For generating monodispersed droplets, the jetting regime should be avoided due to its instability.

In the squeezing and transition regime, lots of articles have been published to predict the droplet size. Garstecki *et al.* [36, 114] found that the droplet size scaling is well captured by the simple relation $l / w = 1 + \alpha\varphi$, where l is the droplet length, w is the width of the main channel, α is a constant and φ is the flow rate ratio between the dispersed phase and continuous phase. Van Steijn *et al*. [104] further improved the model of predicting droplet volume in a T-junction by considering the 3D shape of droplets and found that the volume of droplet can be expressed as $\frac{V}{w^2 h} = \frac{V_{\text{fill}}}{w^2 h} + \alpha\varphi$ and presented the expression of α. This 3D model illustrates that final droplet volume is the sum of volume of droplet during the filling stage and the volume of dispersed phase pumped into the droplet during the necking stage. Tom Glawdel *et al.* [85, 103] further improved the model by considering more influencing parameters, such as channel geometries, flow rate ratio, viscosity contrast and capillary number.

In the dripping and jetting regime, less work has been done to study the mechanism of droplet formation due to its complexity. Xu *et al.* [110] developed a model for the dripping regime based on previous models and found that droplet size is almost independent on the flow rate of the dispersed phase.

A number of numerical simulations for the droplet size scaling were also studied and compared with experimental results [46, 100, 102, 114–117]. These numerical simulations focus on the droplet breakup process working in the squeezing regime and transition from squeezing to dripping regime, considering the influence of viscosity contrast, geometry, flow ratio and capillary number. The results

partially agree well with experimental situations. A review of numerical modeling methods of two phase flows in microfluidics can be found in literature [101].

Another research aspect is to integrate a number of T-junctions and generate droplets in parallel in order to increase droplet production rates. However, the parallel T-junction generators will affect each other during operation due to the variation of hydrodynamic resistance caused by the droplets downstream. Barbier *et al.* [118] studied the coupling of droplet generation between two parallel T-junctions, and observed complex dynamic behavior in the parallel system. While such complexity induces difficulties for producing uniform droplets, the problem can be overcome by using appropriate geometries to decouple the effects between parallel T-junction droplet generators.

2.2.2 Co-flowing

A second geometry used to generate droplets in microfluidic devices is called 'co-flowing'. The co-flowing device consists of two concentric capillaries with the continuous phase fluid flowing in the outer capillary and the dispersed phase fluid in the inner capillary. The two flow streams flow together and finally the dispersed phase decays into droplets by viscous stress [119]. The first concept of droplet production in co-flowing streams was demonstrated by Umbanhowar *et al.* [119] as shown in Figure 2.3.

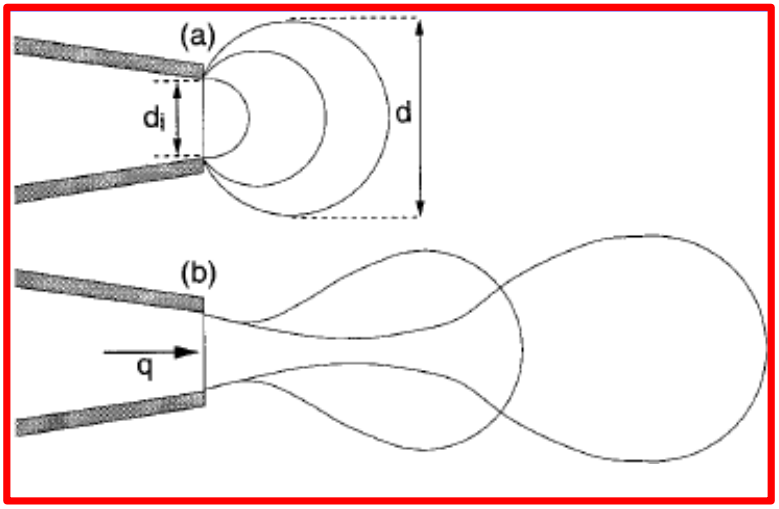

Figure 2.3 Co-flowing droplet generation device for (a) drop growth and (b) drop separation, which was first proposed by Umbanhowar *et al.* [119]

There are two distinct droplet generating regimes in the co-flowing geometry: dripping where droplets breakup near the capillary orifice and jetting where droplets pinch off after an elongated thread downstream. The dripping to jetting transition in a co-flowing geometry was studied experimentally by Utada *et al.* [39]. Experimental results indicate the critical capillary number of the continuous phase $Ca \approx 0.1$ in the dripping to jetting transition regime [39]. The size of bubbles in a co-flowing device in the dripping regime was predicted by Hoeve *et al.* [120] using the Navier Stokes equation. It is reported that when flow rate ratio $\frac{Q_{in}}{Q_{out}} \to 0$, the diameter of the bubbles is proportional to the square root of the flow rate ratio, independent of the viscosity ratio. However, for finite values of the flow rate ratio $\frac{Q_{in}}{Q_{out}} < 1$, and very small values of viscosity ratio $\frac{\mu_{in}}{\mu_{out}} << 1$, the bubble radius scales as $r_b \propto \left(\frac{Q_{in}}{Q_{out}} \right)^{\beta}$ with β varying from two limiting values $\beta = 0.5$ for $\frac{Q_{in}}{Q_{out}} \to 0$, and $\beta = 5/12$ for $\frac{\mu_{in}}{\mu_{out}} \to 0$ [122, 123]. Cramer *et al.*[122] studied the dynamics of liquid-liquid droplet formation in a co-flowing device by considering the impact of the velocity of the continuous phase, flow rate of the dispersed phase, superimposed pressure oscillations of the dispersed phase, and the viscosity of the dispersed phase. A Capillary-number-Ohnesorge-number phase diagram for the viscosity-driven dampening of droplet formation in co-flowing liquid-liquid systems was proposed to generalize periodic dripping dynamics. Experiments show that the viscosity of the dispersed phase liquid and capillary number of the continuous phase play an important role in abating the flow-induced sequencing of droplet detachment. Xu *et al.* [123] experimentally measured the dispersed phase differential pressures in a co-flowing device during drop formation using a Capillary Laplace Gauge (CLG). They studied the relationship between pressure fluctuation and *Ca* number.

Compared to T-junction and flow focusing devices, relatively little research has been done on co-flowing geometry due to the difficult fabrication process, which involves aligning capillaries in a concentric manner in microchannels.

2.2.3 Flow Focusing

The flow focusing device was an improvement over the co-flowing device, in which the continuous and dispersed phases flow coaxially at the junction and are additionally focused through an orifice. In such a flow focusing geometry, the two immiscible liquids pass through the small orifice and can

generate smaller droplets compared to T-junction geometry. Although the flow focusing device has more complex geometry and more fluidic inlets than the T-junction, it allows users to vary the effective geometry by adjusting flow rates of the dispersed and continuous phases, and offers a larger flexibility in controlling droplet size. In addition, the continuous phase flows on both sides of the dispersed phase, leading to more symmetric shearing, hence improvement in stability and control during droplet formation [43]. These features are the reason why flow focusing is one of the most used geometries in micro-devices for droplet generation.

The flow focusing geometry in a planar microfluidic device was first demonstrated by Anna *et al.* [124] as shown in Figure 2.4.

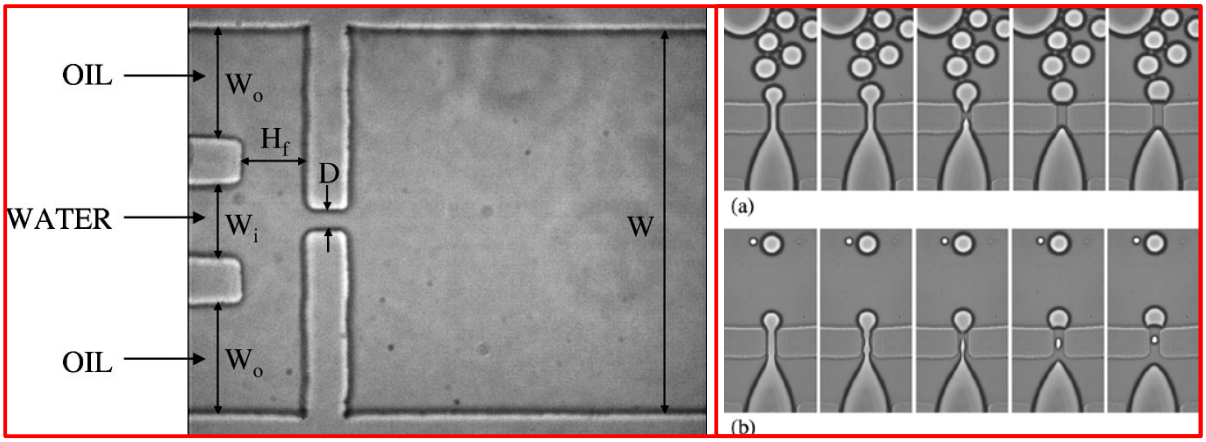

Figure 2.4 Left: first flow-focusing geometry implemented in a microfluidic device. Right: Experimental images of droplet breakup sequences (a) uniform-sized droplets are formed without visible satellites; (b) with small satellite droplets [124].

Later a flow focusing device with round orifices was fabricated and used for three dimensional flowing focusing [125] and multi emulsions like water-in-oil-in-water (W/O/W) or oil-in-water-in-oil (O/W/O) were produced using flow focusing devices [126], [127].

The flow focusing also operates in three primary regimes depending on the flow rate ratio similar to T-junction [128]. Figure 2.5 shows the three primary regimes in a flow focusing device.

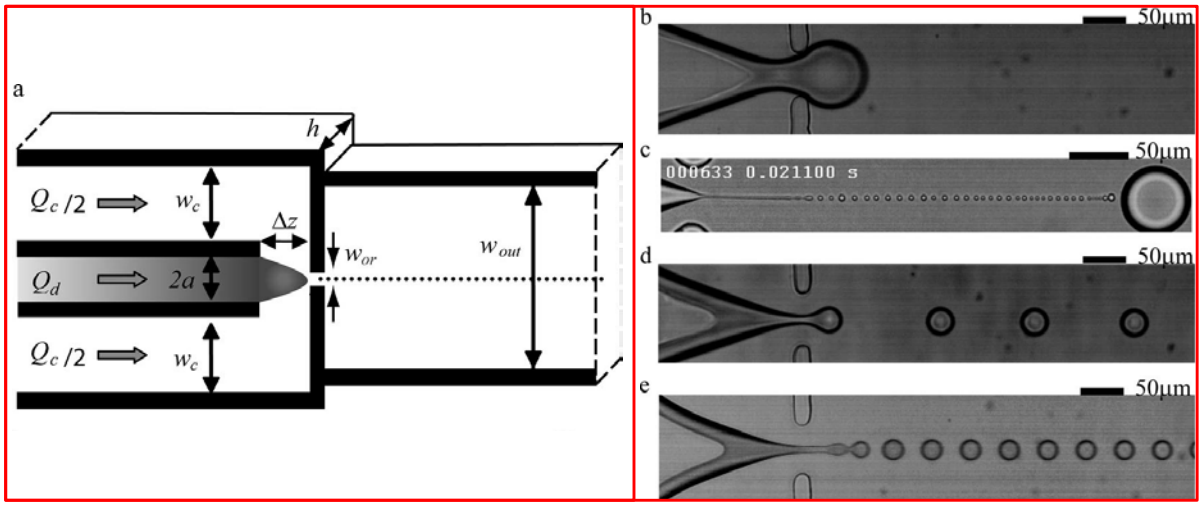

Figure 2.5 (a) Schematic of a planar flow focusing geometry. (b) - (e) are representative of each of the different droplet breakup regimes, including (b) squeezing, (c) thread formation, (d) dripping and (e) jetting [128].

Cubaud *et al.* divided the flow patterns into droplet regime and non-droplet regime, a flow map was then drawn based on two capillary numbers of the continuous and dispersed phases as shown in Figure 2.6 [129]. Empirical equations were presented to describe the size of droplets in each regime based on experimental results.

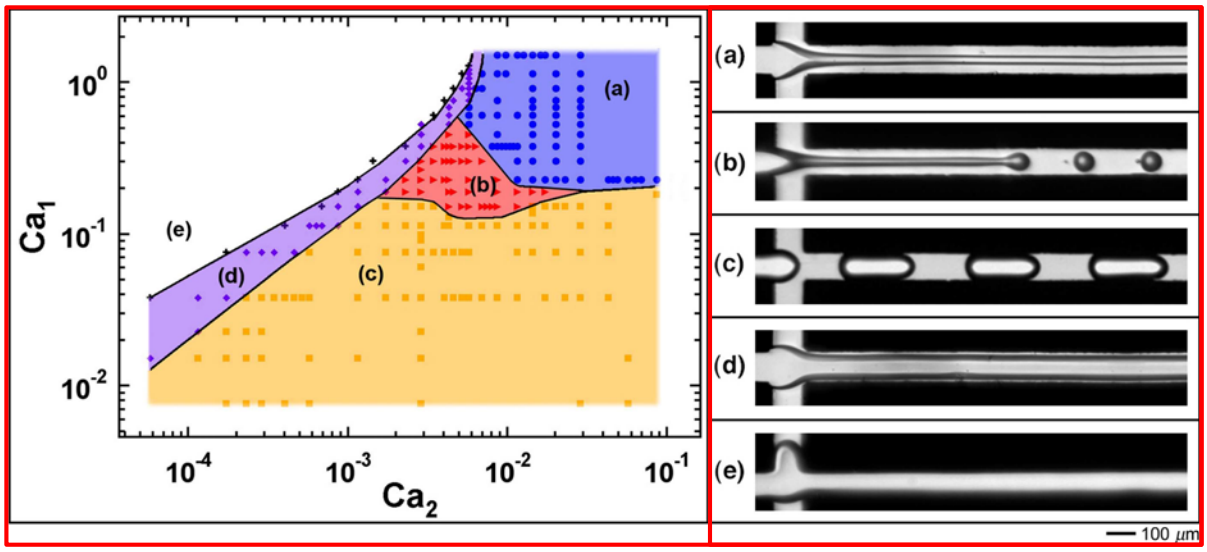

Figure 2.6 Typical capillary number based flow map in a flow focusing device with flow patterns (a) threading; (b) jetting; (c) dripping; (d) tubing; (e) viscous displacement [129]

In a flow focusing geometry, the mechanism of generating droplets was often thought to be different from that of T-junction. However, Abate *et al.*[130] experimentally measured the dynamic pressures of the continuous and dispersed phases during droplet generation in a flow focusing device using a Laplace pressure sensor and a fluctuation of pressure was observed even at a large capillary number. The mechanism of droplet generation in a flow focusing device is quite similar to that in a T-junction [131]. The influence of numerous parameters on droplet generation in flow focusing devices was studied, including the effect of viscosity contrast [132], channel wettability [133], surfactant concentration [134], capillary number [135], the formation of satellite droplets [138, 139] and the comparison between pressure and volume controlled flow [138]. Lee *et al.* [128] derived scaling laws to describe flow focusing droplet production for squeezing regime, thread formation and dripping regime in a typical geometry based on the experimental results. They concluded that droplet breakup depends solely on the upstream geometry and associated flow field, and not on the geometry of the channel downstream of the flow focusing orifice. By contrast, the elongation and breakup of the fine thread during the thread formation mode of breakup depends solely on the geometry and flow field in the downstream channel. Numerical simulations have also been studied to understand more details of the droplet breakup mechanism in the flow focusing geometry [141–145]. A review article on numerical simulation of droplet dynamics was presented by Cristini *et al.* [46].

In addition, to increase the flexibility of flow focusing devices such as to generate various droplet sizes at given flow rates, improve the monodispersity of the droplet or increase the frequency of droplet generation, approaches similar to the T-junctions were proposed. Parallel integrated flow focusing devices were used to generate droplets with different dimensions simultaneously [35, 146, 147]. The feedback of produced droplets downstream in a flow focusing device was studied by Stone *et al.* [146], and also a feedback control for the fluid flow rates was proposed depending on droplet size [147].Although a large amount of work has been done to study flow focusing droplet generation, most of them only present scaling laws or correlations based on experimental data. These scaling laws ignore 3D curvature of the droplets, which highly influences the accuracy of droplet volume as in the case of the T-junction geometry. Additionally, droplet generation is highly dependent on the experimental conditions, which makes it difficult to apply the existing empirical models to external setting. A complete model of the breakup process considering the influence of the channel geometry, viscosity contrast, capillary number and flow rate ratio is still lacking.

2.2.4 Step Emulsification

Step emulsification is a modified version of the co-flowing geometry. It uses a sudden expansion in the microchannel to trigger droplet formation, which was first characterized by Priest *et al.* [148] and is shown in Figure 2.7. The two phases are brought into a high aspect ratio channel, which suppresses interfacial tension and induces instabilities. The stream of the dispersed phase abruptly breaks up into droplets at the step where the stabilizing walls suddenly end. The step emulsification geometry also has various droplet formation regimes which are similar to the co-flowing case [151, 152]. In the "T junction" regime, Droplet breakup occurs before reaching the step at low flow rate ratio. At intermediate flow rate ratio, dripping occurs precisely at the step, which is called the "step-emulsification" regime. At large values of the flow rate ratio, the dispersed phase forms a stratified flow beyond the step, slowly thinning, eventually breaking up downstream. We call this regime as jetting regime (see Figure 2.7 (b)). Breakup occurring at the step can produce the best monodispersed droplets. Therefore, most research on physical mechanisms focus on the "step-emulsification" regime. The scaling of droplet size with channel geometries was experimentally studied by Malloggi *et al.* [151]. They concluded that the capillary focusing of the dispersed phase yields a tongue-shaped tip at the step and controls the droplet size.

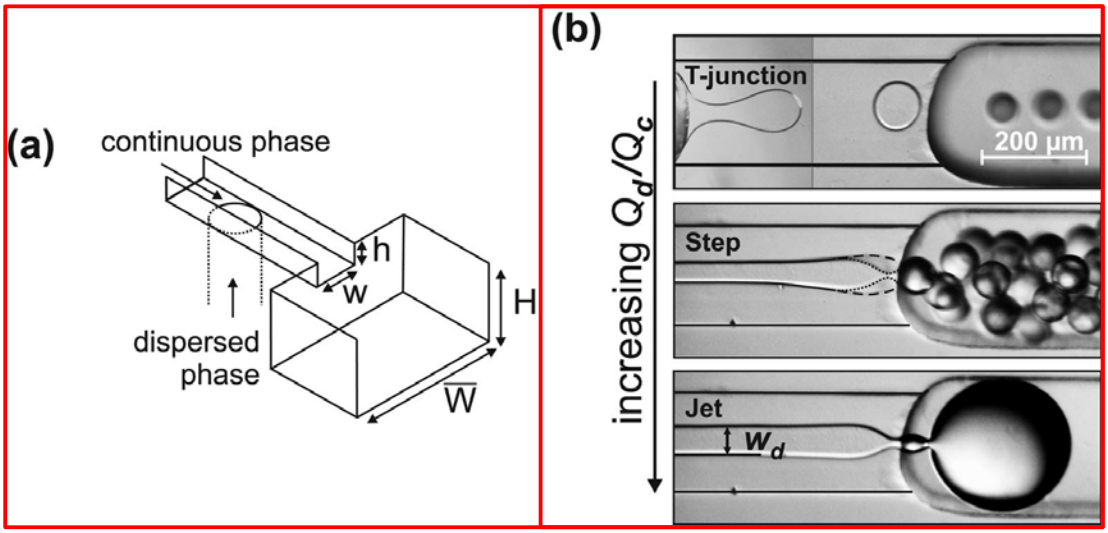

Figure 2.7 (a) Schematic of step emulsification device. (b) Photos of droplet detachment via T-junction, step and jet breakup mechanisms. Step breakup occurs precisely at the step and jet breakup occurs downstream [148].

Dangla *et al*.[152] provided a geometric model for droplet breakup in the "step-emulsification" regime based on a quasi-static balance between the curvature of the thread inside the inlet channel and the curvature of the "bulb" downstream of the step. They found that the bulb curvature always decreases below a critical value, below which equilibrium shapes of the interface cannot exist if the reservoir has a larger height than the inlet channel, which generates a backflow of the continuous phase upstream of the step, leading to the drop breakup. The droplet size does not depend on the value of the interfacial tension. However, this curvature balance model does not directly predict the actual size of the formed droplets.

Li *et al*.[153] recently presented a comprehensive model that combines experimental and theoretical study to predict the droplet size in the "step-emulsification" regime, which is based on quasi-2D Hele-Shaw hydrodynamics. The diameter of droplets can be described as $\frac{d}{h} = 3\left[1 + \frac{(1+k)}{w/h}\right]^{-1}$, where d is the diameter of droplets, h is the channel height before the step, w is the channel width before the step, and $k = \frac{\mu_c Q_c}{\mu_d Q_d}$. The diameter of the smallest droplet that can be formed in the "step-emulsification" regime varies between $\approx 2h$ and $3h$.

Step emulsification offers the best monodispersed droplets at extremely high dispersed phase volume ratios (up to 96%), and allows droplet generation frequency to be varied within more than two orders of magnitude without affecting the droplet size. The droplet size is no longer controlled by the microchannel cross-section dimensions, but rather by the smallest spatial dimensions of the inlet microchannel. Hence, this geometry allows high-throughput generation of monodispersed microdroplets with submicron diameters , as oppose to multistep splitting required in a T-junction [154] and flow focusing device [155]. Additionally, this type of geometry can be easily integrated for parallel dispensing several liquid streams using the same geometric step, and thus offers an extremely robust synchronization mechanism to generate droplet pairs [156]. The step emulsification also has some disadvantages compared to other geometries. First, the fabrication is more complicated due to the high aspect ratio channel (fabrication is 3D). Second, the flow parameter has to be carefully chosen and leads to a limit of droplet production frequency.

2.2.5 Active Techniques and Methods

Active droplet generators usually have moving parts which physically break up the fluid stream using mechanical, thermal, electrical, magnetic, or optical forces. These moving parts are mostly combined with passive droplet generators such as T-junctions and flow focusing geometries. The active methods are usually used to generate droplets on demand; that is to generate droplets and bubbles of arbitrary volumes and at arbitrary times of emission.

Micro-valves are widely used to control the fluid stream. Abate *et al.* [157] developed a valve based flow focusing device for droplet formation, which uses single-layer membrane valves to control the drop size and frequency without adjusting flow rates in real time. Chen *et al.* [158] presented inflatable chambers using pneumatic air combined with a flow focusing geometry to vary the orifice dimension and thus control the droplet production. Choi *et al.* [159] designed pneumatic valve actuators integrated into a T-junction to generate droplets. Droplets produced by T-junction were broken into smaller droplets by a pneumatically actuated valve. Several other groups also induced the pneumatic valves to form droplets based on similar ideas that break up the flow streams by periodically opening and closing the microvalves [162–164]. Garstecki *et al.* [163]developed a droplet on demand system utilizing a computer controlled off-the-shelf microvalves. Guo *et al.* [164] generated droplet on-demand by integration of electronic solenoid microvalves with programed control. Moreover, microvalves driven by thermal capillary [165] or electromagnet [166] were also used to generate droplets.

Thermally controlled droplet formation was presented by Tan *et al.* [167] and Stan *et al.* [168], respectively. The two groups adjusted the droplet size by manipulating the temperature dependence of the fluid viscosity and surface tension.

Electric fields have also been widely used to generate droplets. Electro-spraying was applied to droplet devices in order to generate very small droplets (below 1 μm) [171–174]. Another example is the use of piezoelectric actuators which are integrated into a microfluidic devices to produce droplets [175, 176]. Other unconventional methods which use electric fields to form droplets include using electrorheological fluids as the dispersed phase [177, 178] and electrowetting [179, 180].

Magnetic and optical forces can be used to generate droplets as well. Several articles have investigated the generation of ferrofluid droplets which integrates an electromagnet or permanent magnet into a T-junction or flow focusing geometry to change the viscosity of the ferrofluid and hence influence the droplet generation [181–184]. Park *et al.*[183] reported a pulse laser-driven

droplet generation mechanism which can produce droplets on demand at rates up to 10,000 droplets per second.

Most of these active techniques and methods are rarely used for microfluidic applications because of the complex structures of microdevices compared to passive methods.

2.2.6 Comparison of Droplet Generators

T-junction and flow focusing geometries are most commonly used in microfluidic devices because of their simple geometry and easily controllable production. Co-flowing has the disadvantage of a more complicated fabrication and operation process because of the increased complexity of fabricating the concentrically aligned capillaries within the microchannels. Step emulsification can offer the best homogeneity of droplets and the highest droplet generation frequency at a single step, but the fabrication is more difficult due to the high height/width ratio channel. Active techniques are rarely used for typical microfluidic applications because adding external forces to the microdevices makes the structures more complicated. Therefore, they are mostly used in droplet on demand applications. As for the T-junction and flow focusing, both of them have their advantages and disadvantages. T-junctions have very simple structure and fewer inlets so they are easy to fabricate and operate. Flow focusing has a more complex geometry and more inlets are needed, but the geometry is symmetric which improves stability and control over droplet formation. Compared with T-junctions, flow focusing can offer a wider range of droplet sizes by changing the orifice diameter with better monodispersity and superior frequency up to thousands of Hertz; although, unexpected satellite droplets are often generated in flow focusing devices which is not the case in T-junction geometry. The main disadvantage of both passive methods is that the frequency and size of formed droplets are coupled by the flow rates and thus the control over these parameters is not independent.

2.3 Droplet Manipulation

In section 2.2, droplet formation is widely discussed and shows the very important role which the method of droplet formation has in droplet-based microfluidics, but it’s certainly only the first step in practical applications. It is also crucial that the generated monodispersed droplets can be reliably manipulated and controlled through sorting, detecting, sensing, merging, splitting, mixing, trapping and storing techniques. Similar to droplet formation, manipulation of droplets can be done by both passive and active methods. Therefore, section 2.3 summarizes the commonly used techniques to manipulate droplets in microfluidic devices.

2.3.1 Droplet Sorting

Sorting is essential in droplet-based applications which can be divided into passive and active methods, since droplets with different sizes or contents are often transported along the microchannels in practical applications. Passive sorting is mostly based on the size of droplets [186–190]. Tan *et al.*[184] demonstrated a filter system to filter out satellite droplets from the generation of parent droplets through the shear stress gradient controlled by the widths of the bifurcating channels[189] shown in Figure 2.8 (I) . Mazutis *et al.* [186] presented a sorting system based on the particular flow profile in a microchannel according to droplet sizes as shown in Figure 2.8 (II). Droplets with diameters larger than the channel width will flow slower than the average flow velocity of the continuous phase, while droplets with significantly smaller diameters than the channel dimensions will flow faster than the average velocity because they mainly focus in the center of the flow profile where the maximum flow velocity occurs. Hatch *et al.*[187] presented a passive hydrodynamic droplet sorting device using viscoelastic flow focusing (see Figure 2.8 (III)). Sorting is achieved by tuning the viscous and viscoelastic properties of droplets relative to the continuous phase to achieve a positive or negative lateral migration toward high or low shear gradients in the microchannel. Droplets with a viscosity ratio between 0.5~10 migrate toward a high shear gradient near the channel walls, while droplets with viscosity ratio smaller than 0.5 or larger than 10 migrate toward a low shear gradient at the channel centerline. The sorting efficiency is dependent on droplet size, intrinsic fluid elasticity, viscosity, droplet deformability, and fluid shear rates. The authors achieved more than100 fold enrichment with droplet sorting frequencies larger than 200Hz.

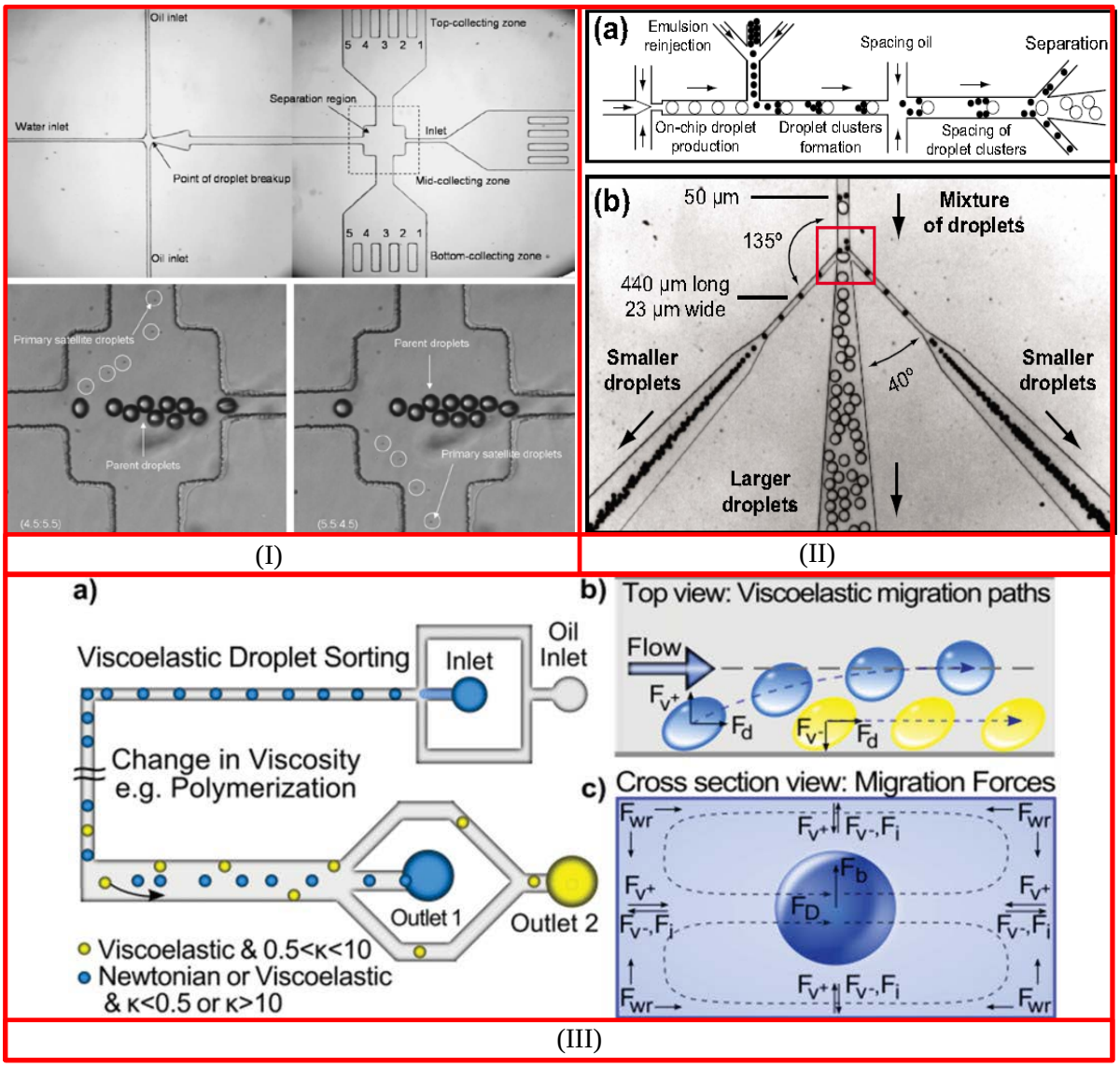

Figure 2.8 (I): Channel design for controlling the dynamic separation of satellite droplets. It consists of a droplet generation region and a separation region. The separation region separates the satellite droplets according to their position across the width of the channel. (Bottom) Parent droplets are collected into the mid-collecting zone while the satellite droplets can be switched into either the top or bottom collecting zone [184]; (II): (a) Schematic of the sorting system. (b) Passive droplet separation module [186]; (III): Illustration of viscoelastic droplet sorting based on bi-modal equilibrium positions [187].

Active sorting is achieved through a locally applied electric field in the channel to sort droplets by variable electric properties. The dielectrophoresis (DEP) effect was first used for high speed droplet sorting by Ahn *et al.* [190]. The electrodes were designed to maximize the electric field gradient for deflecting the droplets. An optically induced dielectrophoresis (ODEP) was used to sort droplets by several research groups [191–194]. Droplets can be positioned and sorted individually using this method as the movement of each droplet can be programmed by an adjustable laser beam. The disadvantage of ODEP technology is that it requires a special fabrication technique and an external laser setup. Recently Sciambi *et al.* [195] reported a microfluidic design that can sort droplets with frequency up to 30KHz and more than 99% accuracy by applying electric field. Compared to previous work, the authors replaced the hard divider separating the outlets with a gapped divider, allowing a much higher sorting frequency.

Fluorescence-activated droplet sorting is another important tool, which was developed based on Fluorescence-Activated-Celling-Sorting (FACS) technique. FACS is a commercially available technique which was invented by Fulwyler *et al.* [196] in 1969. The cells are rendered differentially fluorescent and pass sequentially through a laser beam. The fluorescent light from the cells can be transferred to electrical signals. Then, the signals are used to trigger electrodes for sorting cells. This technique is capable of evaluating cells at extremely high rates up to 50KHz [197]. Fluorescence-activated droplet sorting method uses similar strategy to sort droplets by adding fluorescent dye into droplets. Recently, several groups have successfully used FACS methods to sort small microfluidic droplets ($10\sim20\mu m$) with frequencies at 10-15 KHz [198, 199].

Several other active methods used to control droplets use different types of forces such as mechanical, thermal, magnetic and acoustic forces. Mechanical micro-valves are often employed to change or stop flow streams by opening and closing valves [197, 200, 201]. This method has no special demands on the emulsion properties or droplet size, but the disadvantage is that the response time for the valve opening or closing is relatively long and thus has a low sorting frequency compared to other methods. The thermocapillary effect can be used to manipulate droplets by influencing the interfacial tension which is a function of temperature [202]. Baroud *et al.* [165] introduced a thermocapillary valve for droplet sorting by locally heating one channel with a laser and directing droplets into the selected channel. Magnetic particles can also be added into either the droplets or the continuous phase and directed by using magnetic fields. Using this technique the droplets can be forced into the selected channel as the movement of the magnetic particles forces the droplets to alter

their path. The fluids with magnetic particles are often named ferrofluids which can be used in both the dispersed phase [203] and the continuous phase [204]. Similar to magnetic fields, electrorheological fluids can be also used in the dispersed [181] or continuous phase [176] for droplet manipulation. The viscosity of electrorheological fluids can be increased when applying an electric field. In addition, ultrasonic force fields [205] or Surface acoustic waves (SAW) [206–209] are also reported to direct cells or droplets in different channels.

2.3.2 Droplet Detecting and Sensing

It is necessary to track the position of each individual droplet and analyze the content inside them for controlled manipulation of reactions. A number of techniques have been developed to detect and sense droplets such as electrical, optical or thermal techniques.

Several articles have shown the detection of droplets using electrical signals. Droplets can be detected by their impedance signal using thin electrodes embedded within the microchannels [210–212]. Alternatively, droplets can be detected by capacitance measurements combined with electrorheological fluids [213]. Elbuken *et al.* [214] presented one scalable and inexpensive system of detecting droplet size and speed by using commercially available capacitive sensors, and further improved with a following work to detect droplet content by Isgor *et al.*[215] (see Figure 2.9 (I)). Recently, Boybay *et al.* [216] proposed a microwave system integrated with microfluidic devices to detect nanoliter-sized droplets as shown in Figure 2.9 (II). This microwave system can distinguish between contents inside droplets with different electrical properties. The operating frequency of the resonator will shift when droplets pass through it, which can be used for counting the number of droplets and analyzing the content inside droplets. Optical methods are mostly used to monitor and control droplets based on microscopes and high speed cameras. Fluorescence microscopy techniques are often added which allows us to distinguish between different materials. Fluorescent dyes are mixed with fluid phases and change the emission wavelength based on the chemical surroundings. Then, the fluorescence signal can be analyzed and used to detect the content inside droplets [217–220]. Droplets can also be detected by using thermal responses. Yi *et al.* [221] reported a method to detect droplets and determine the protein content of droplets in a microfluidic system using 3ω method, which can easily detect thermal response changes in a microfluidic device.

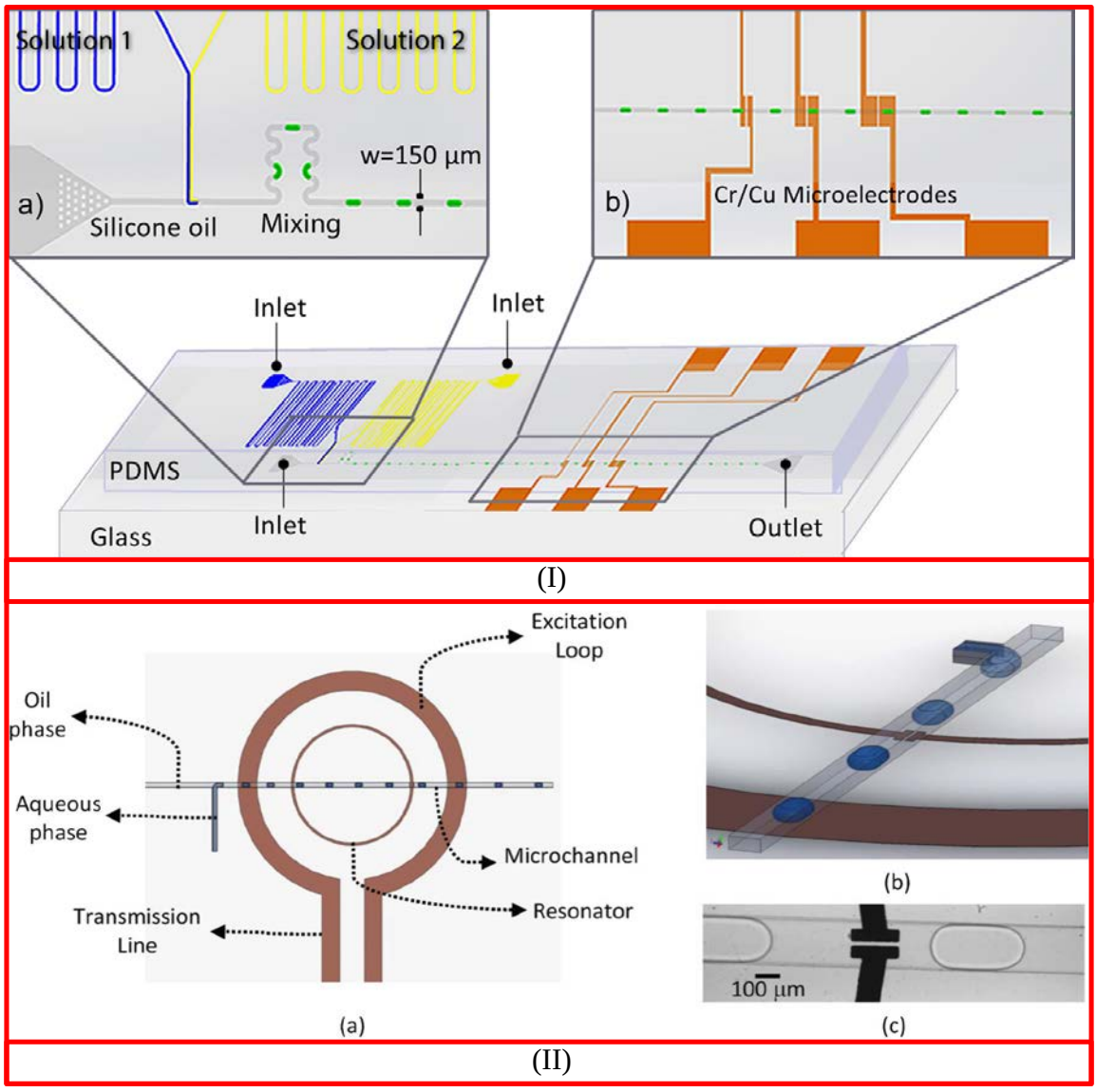

Figure 2.9 (I): Schematic of the microfluidic device. The insets show the (a) droplet generation region and mixing region, (b) detection region [215]; (II): Schematic of microwave components for detecting droplets [216].

2.3.3 Droplet Merging and Splitting

When performing chemical or biological reactions in droplet-based platforms, reagents are normally injected together in a co-flowing stream just prior to droplet formation [222]. However, this configuration is not applicable to a fast or aggressive reaction, since the reaction starts at the interface before the droplet generation. Therefore, reagents should be kept separately before droplet generation.

In order to add new reagents to pre-formed droplets or remove some sample from droplets at some defined times, it is necessary to merge two individual droplets which are generated with a precisely defined volume or split one droplet into two daughter droplets with precisely controlled volumes. Droplets can be either merged (split) by passive methods (channel geometry) or by active methods (thermal, electrical effects, or surface acoustic waves).

Droplet coalescence can be realized by a suitably shaped channel geometry, which is mainly used for a surfactant free droplet device. The most important task is to reduce the distance between droplets and bring them in contact with each other which can be done by implementing several different channel geometries. Bremond *et al.*[223] proposed a diverging then converging chamber, where droplets are observed to merge while they are being pulled apart as shown in Figure 2.10 (I). An approximate model which quantitatively predicts the position of merging droplets is given by Lai *et al.* [224] and the flow behavior of a droplet train in such a chamber was studied experimentally by accounting for different viscosities and flow rates by Jose *et al.* [225]. A different strategy was developed by Niu *et al.* [226] to bring droplets into contact and induce their merging as shown in Figure 2.10 (II). The channel geometry combines the widening section mentioned previously with a sequence of pillars which could trap the incoming droplet by squeezing its front end until the droplet behind merges. Furthermore, coalescence can be induced by colliding two droplets in a T-junction [227, 228]. It is important to note that no surfactant was added in these experiments which may explain the ability of droplets to merge under compression.

Mazutis *et al.*[229] provided a controlled one-to-one fusion of droplet pair technique by pairing one surfactant-stabilized droplet and the other not fully stabilized by surfactant. The fused droplets contain enough surfactant to inhibit further fusion with other droplets. The authors claimed more than 96% fusion efficiency when the surfactant-stabilized droplets contain 5-fold surfactant concentration excess at KHz frequencies. A further study by this group showed that the coalescence of one droplet with surfactant-stabilized droplet and the other not fully stabilized by surfactant is dependent on the contact time between droplets prior to coalescence and the interfacial surfactant coverage of droplets [230]. This technique cannot be applied to when all droplets are stabilized with surfactant. Deng *et al.* [231] presented a surgery-like strategy for merging surfactant stabilized droplets. When a pair of preformed droplets flows across a micro-lancet, droplet surfaces are scratched by the micro-lancet, leading to temporarily scattering of surfactants at the scratch. Thus, the droplet pair can merge through the scratched wounds.

Active methods are able to merge droplets regardless of surfactant-stabilized droplets or not. Two main active methods using thermo-capillary or electro-coalescence have been developed to merge droplets. Similar to applications in droplet sorting, the thermo-capillary effect can be employed to create a convective motion within each droplet by changing the surface tension. Coalescence occurs at a critical heating temperature [232]. The first droplet is stopped at a laser spot by the thermo-capillary effect until a second droplet arrives and merges with the first droplet [233]. The most widely applied method is to supply an electric field to the droplets [234–238]. The droplets were observed to merge under an electric field with a broad range of gradient intensities from 1 to 100kV / m. Priest *et al.* [234] explained the dependence of the coalescence voltage on droplet size, surface tension and separation distance, but detailed models of the interaction between the electric field and the fluid interfaces are still lacking due to the strong coupling between them. Other active methods that have been developed to merge droplets include surface acoustic waves [239], Chemically induced coalescence [240], and pneumatic actuators [241].

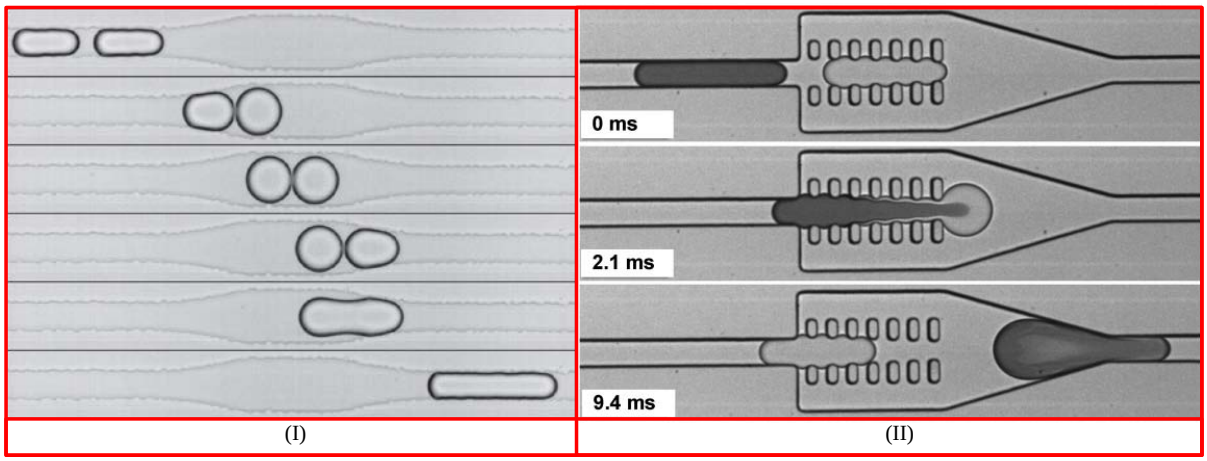

Figure 2.10 Geometries for passive coalescence of droplets. (I) Decompression merging by Bremond *et al.* [223]. (II) Pillar induced droplet merging by Niu *et al.* [226].

For some biological or chemical reactions, it is desirable to split droplets into several daughter droplets for incubation, screening, or increasing the droplet generation frequency. The majority of splitting droplet methods are passive using microfluidic geometries like T-junctions [97, 154, 242–244] or Y-junctions [155] as shown in Figure 2.11. Leshansky *et al.* [242] proposed a 2D model of the droplet breakup in a symmetric T-junction. They concluded that the mechanism working in a two-dimensional setting where the Rayleigh-Plateau instability of a cylindrical liquid thread is the cause of breakup suggested by Link *et al.* [154] is not operative, and they derived a dependence of the

critical droplet extension on the capillary number *Ca* by combining a simple geometric construction for the interface shape with lubrication analysis in a narrow gap. Their resulting analysis got an equation that was in agreement with 2D numerical simulations. Hoang *et al.* [245]numerically studied the dynamics of droplet breakup in a T-junction. Their simulations show that the breakup process comprises two phases. The droplet goes through a quasi-steady deformation, driven by the externally applied flow in the first phase. In the second phase, the droplet pinches into two daughter droplets rapidly driven by a surface tension and is independent of the externally applied flow. The size of the two daughter droplets can be controlled by making the two branch channels asymmetric [154, 244, 246].

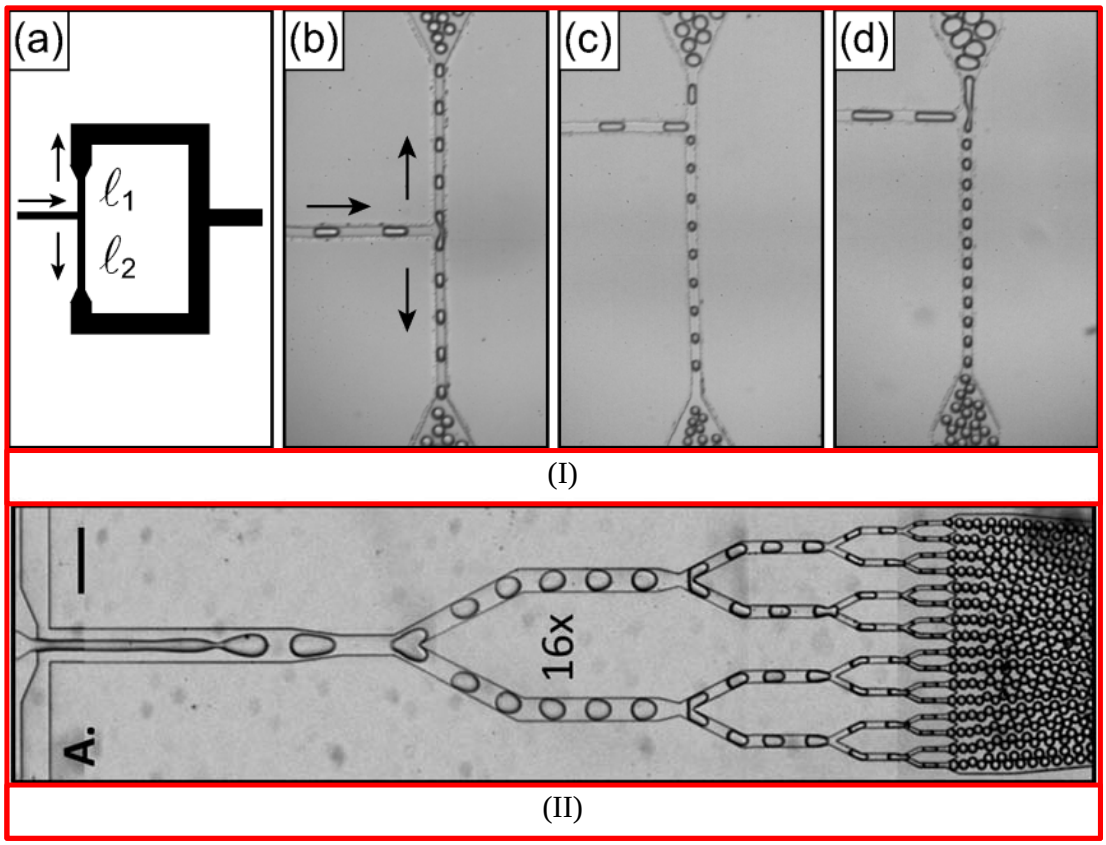

Figure 2.11 Droplet breakup in a T-junction (I) provided by Link *et al.* [154] and in a Y-junction (II) provided by Abate *et al.* [155].

2.3.4 Droplet Pairing and Synchronization

Droplet merging is favorable to add reagents to pre-formed droplets as discussed in section 2.3.3. The key requirement for the successful droplet merging is the perfect pairing of the droplets.

Uncontrolled droplet pairing results in incorrect droplet coalescence. Droplet pairing can be achieved either by alternating droplet formation, or synchronization of two separate droplet streams.

Alternating droplet formation has been realized by active control of droplet formation using microvalves [160] and electric fields [176]. Passive methods of alternating droplet formation mainly utilize the hydrodynamic coupling effects at multiple droplet generators [69, 156, 238, 247–251]. Zheng *et al.*[247] demonstrated the alternating droplet formation at two opposing T-junctions. Generating droplet ratios of two reagents are dependent on the capillary number and water fraction. Hung *et al.*[248] improved this design by adding two triangular wings between the inlets and the T-junctions in order to reduce the flow instability and prevent reagents from back flowing (see Figure 2.12 (I)). Chokkalingam *et al.* [156] also presented a self-synchronizing pairwise production of droplets with two step-emulsification devices sharing the continuous phase (see Figure 2.12 (II)). Hashimoto *et al.* [69] reported two or four flow-focusing generators that shared inlets for delivering the continuous phase and a shared outlet channel to generate pairs of droplets (see Figure 2.12 (III)). In addition, Frenz *et al.* [249] studied a microfluidic dual nozzle for the production of droplet pairs (see Figure 2.12 (IV)). Droplets are paired by the hydrodynamic coupling of two nozzles, and the size ratio between paired droplets is directly controlled by the flow rates of the dispersed phase. All of these hydrodynamic coupling droplet generators have the problems with irregular fluid flow rates and pressure fluctuations, which could disrupt the droplet formation. Later, Hong *et al.* [250] modified the nozzles by adding a pressure oscillator and an oil regulator to overcome the problems with respect to irregularities in channel dimensions and fluid flow rates, and allow high-throughput droplet pairing. The pressure oscillator was designed to restore timing between separately generated droplets *via* a fluidic link, and the oil regulator was used to reduce the pressure difference at the furcate junction (see Figure 2.12 (V)). However, this design still only works under some rigorous conditions, such as identical droplet generation frequencies at each nozzle, monodispersed droplet size and droplet spacing as a function of flow rate in both nozzles, and a constant time difference between pre-associated droplets from each nozzle.

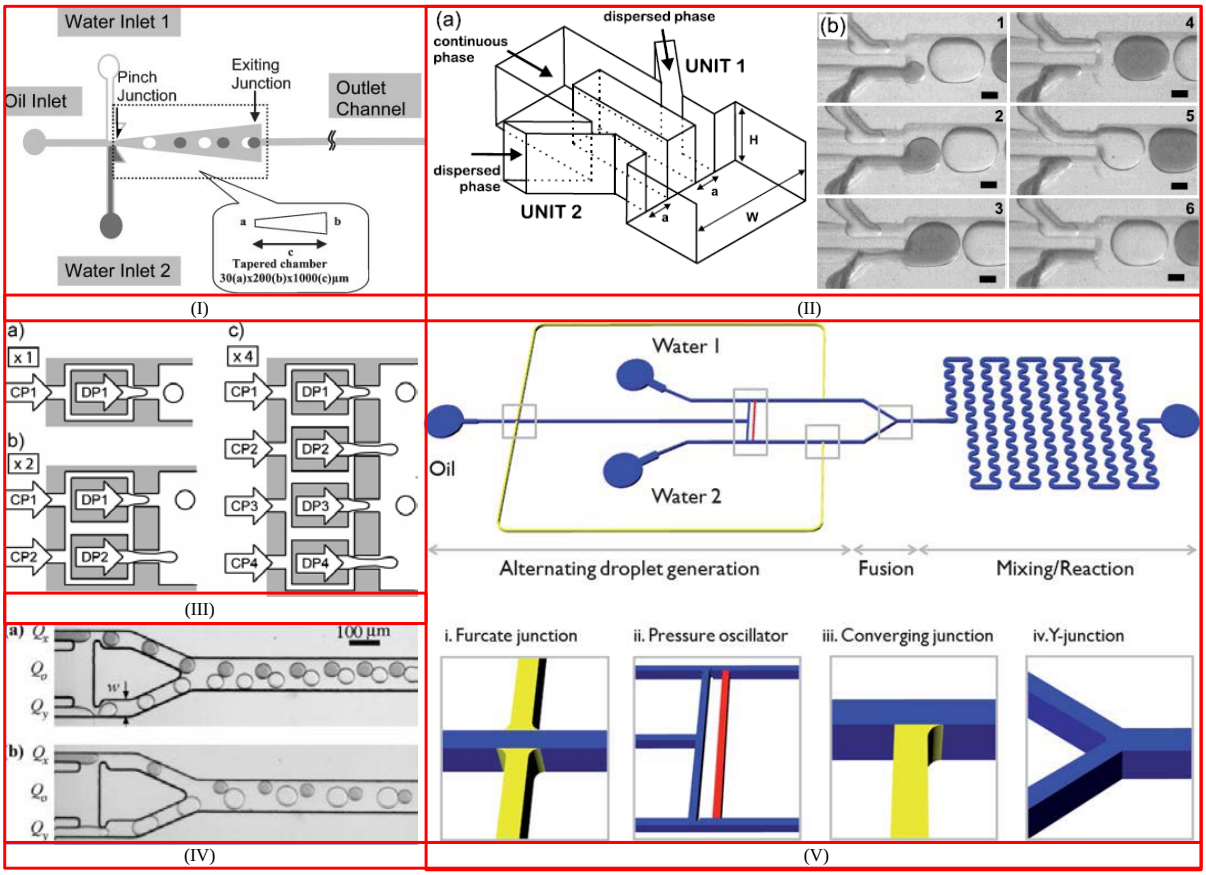

Figure 2.12 (I): Schematic diagram of the microchannel pattern demonstrated by Hung *et al.* [248] ; (II): (a) Schematic of the double-step-emulsification device with production units 1 and 2. (b) Time series of optical images displaying the droplet formation mechanism presented by Chokkalingam *et al.* [156]; (III): Schematic illustration of the systems of flow-focusing generators: a) a single flow-focusing generator; b, c) coupled flow-focusing generators reported by Hashimoto *et al.* [69]; (IV): Pairing module. Two aqueous phases are injected by the outer channels and synchronously emulsified by the central oil channel studied by Frenz *et al*. [249]; (V): Schematic diagrams of droplet-based microfluidic devices showed by Hong *et al.* [250]. The pressure oscillator is red and the oil regulator is yellow.

The second strategy for forming droplet pairs is to synchronize pre-formed droplets from two separated droplet generators. Prakash and Gershenfeld [252] presented a ladder structure for air bubbles synchronization, in which a top and a bottom channel were connected with a ladder network as shown in Figure 2.13 (I). Two streams of bubbles generated from two independent generators entered the top and the bottom channel, respectively. The pressure difference between the top and

bottom channels drives the carrier oil flowing through the ladder network until the pressure in each channel is balanced, leading to synchronization of two streams of bubbles. This design requires the bubble size must be larger than the microchannel width (must be slugs) to prevent the continuous phase flowing across the bubbles. Ahn *et al.* [253] used the same ladder network to synchronize two trains of water-in-oil droplets, and experimentally studied the synchronization efficiency under the influence of droplet length and droplet generation frequency. The synchronization efficiency can reach up to 95% when droplet generation frequency difference in two streams is minimized, but can drop dramatically when the generation frequency difference is high. Song *et al.* [254] numerically analyzed the traffic of droplets in the ladder structure and built a theoretical model by considering the network geometry, flow rates, and droplet resistance. Recently, Maddala *et al.* [255] investigated the dynamics of droplets travelling in a asymmetric ladder network. They found that asymmetric ladder networks enhanced temporal control of droplet spacing compared to symmetric ladders.

Voldman research group presented another microfluidic device to pair different cell types in a high throughput manner using flow-induced cell trapping as shown in Figure 2.13 (II) [256], and later improved the design by using flow-induced deformation of cells [257]. Since the cells were randomly trapped, many cells bypassed the pillars without getting trapped leading to a pairing efficiency around 70%. Huebner *et al.* [258] provided a similar trapping design to pair two droplets in one trap, which can only reach approximately 50% contained heterogeneous droplet pairs due to the random distribution of pre-formed droplets.

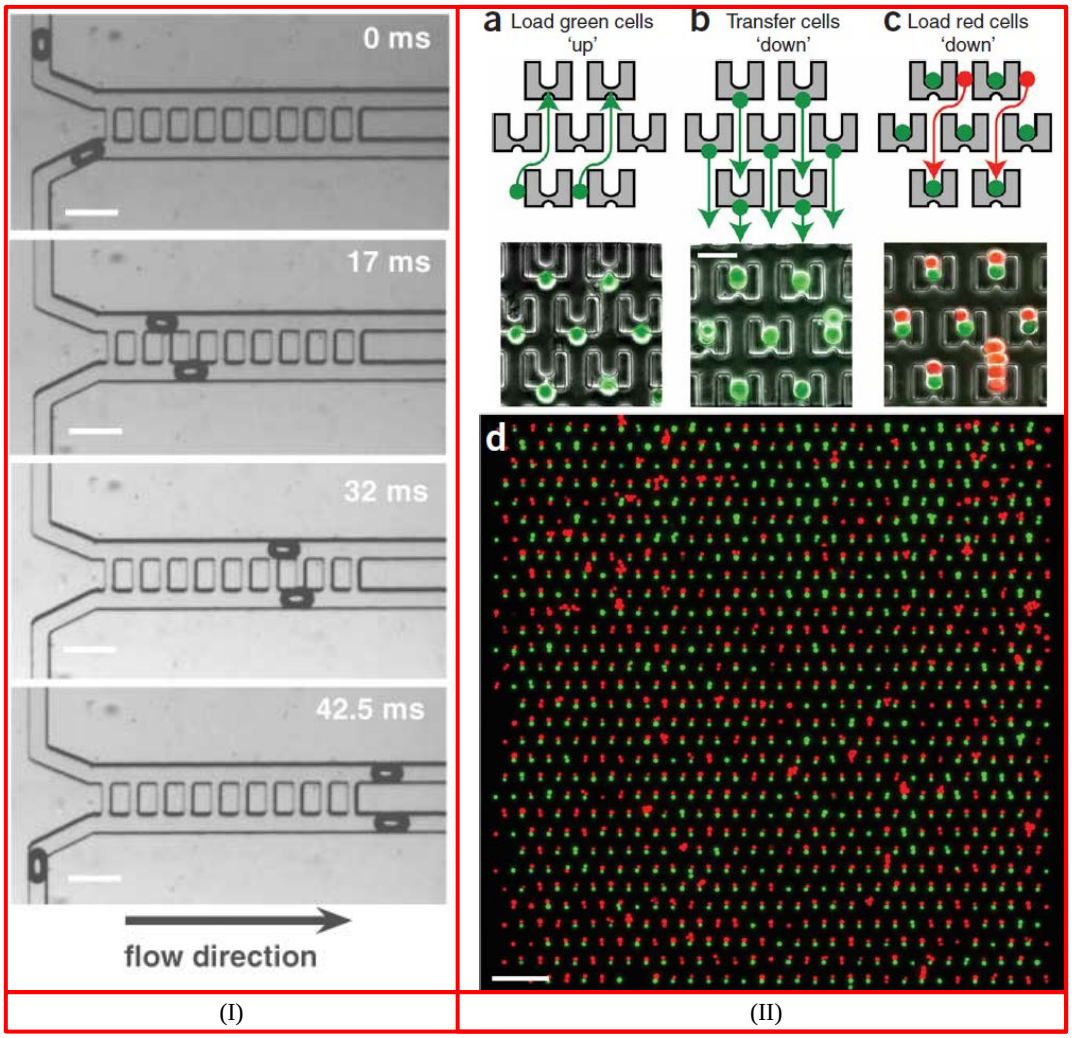

Figure 2.13 (I): A fluidic ladder network for bubble synchronization reported by Prakash and Gershenfeld[252]; (II) Microfluidic device for cell capture and pairing presented by Skelley *et al.* [256].

2.3.5 Droplet Mixing

As mentioned before, mixing is very challenging in a single phase microfluidic flow due to low *Re*, and mixing is mainly reached through diffusion. One of the advantages of using droplet-based microfluidics is that droplets enhance mixing compared to single phase flow which was described by Tice *et al.* [259], where the topology of the counter-rotating recirculation inside a droplet is shown in Figure 2.14. The visualization of internal flow in a moving droplet has been studied using micro-Particle Image Velocimetry (μPIV) [260–262]. Several articles found some scaling laws which

describe the influence of viscosity [22] and the chaotic advection [263] on mixing. Verguet *et al.* [264] analyzed the mechanisms of shear stress transfer at the liquid-liquid interfaces and associated enhanced mixing. They show that decreasing the thickness of lubrication films between droplet and channel walls leads to greater advection velocities inside droplets, which can enhance mixing. In addition, mixing can be enhanced by passing the droplets through a serpentine channel [265, 266] as shown in Figure 2.14 (III). Verguet *et al.* [267] analyzed the mechanics of liquid-liquid interfaces and mixing enhancement in a serpentine channel with bumps on the microchannel walls proposed by Liau *et al.* [266]. The authors show that proportional thinning of the continuous phase lubrication layer at the bumps leads to larger advection velocities within the droplets, which enhances mixing. The analysis also indicated that adding surfactants will reduce mixing.

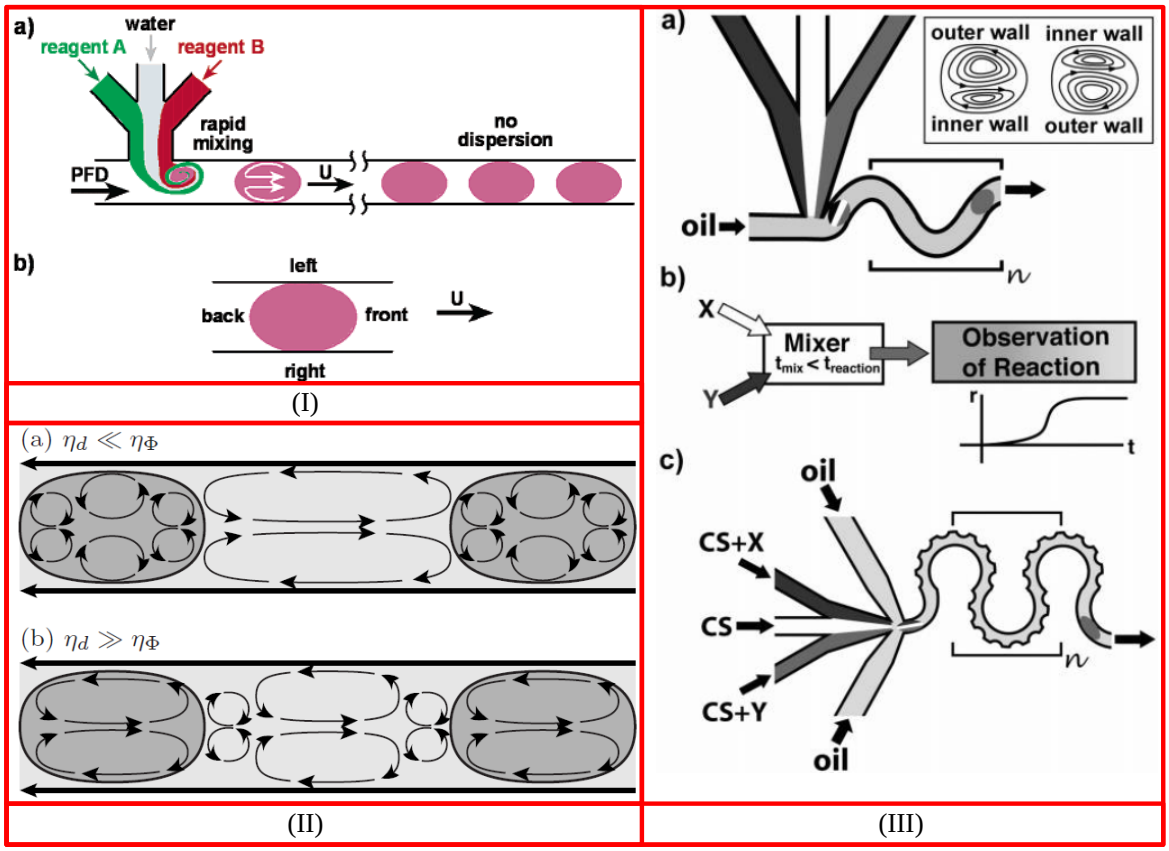

Figure 2.14 (I): Schematic illustration of droplets mixing rapidly by recirculation [259]; (II): The topology of the counter-rotating eddy pairs in front, behind and within the droplets moving in a channel [268]; (III): Serpentine type mixer with bumps on the microchannel walls proposed by Liau *et al.* [266].

Alternatively, a similar recirculation inside a static droplet can be achieved by the thermo-capillary effect induced by a laser spot [269].

2.3.6 Droplet Trapping, Storing and Releasing

Many biological studies involve incubation of cells or expression of proteins, which require a long residence time of droplets to a range from hours to days [270]. A straight forward method for increasing the residence time is to increase the channel length. However, delay-channels can only extend the residence time over several minutes [271], because long channels lead to a proportional increase in back-pressure and disruption in droplet generation. Several other practical methods to elongate the resistance time include trapping droplets inside microchannels by adding some narrow constriction geometries or storing droplets inside a large chamber through adding surfactants to keep them from merging. In addition, releasing droplets is another critical step to control the residence time.

Tan *et al*.[272] first proposed a trap-and release integrated microfluidic system containing a repeated sequence of loops as shown in Figure 2.15 (I) to trap and release selected microbeads. Each loop consists of two branches with one branch containing a hydrodynamic trap and the other containing a bypass channel. When the trap is empty, flow resistance of the trap is lower than that of the bypass channel, allowing one bead go into the trap. After the bead gets trapped, the flow resistance of the trap is higher than that of the bypass channel and the following beads will go through the bypass channel. Figure 2.15 (I-B) shows the releasing mechanism using microbubbles. IR laser is focused onto the aluminum pattern, causing localized heating and bubble formation. Then, the formed bubble can drive the trapped particle into the main flow. This method requires additional integration of aluminum pattern into the microfluidic chip, which is not convenient for high-throughput manipulation. Several other groups used the similar design to trap droplets for studying the behavior of *Caenorhabditis elegans* [273], and the growth kinetics of microalgae [274], in where the droplets were stored up to 33 days.

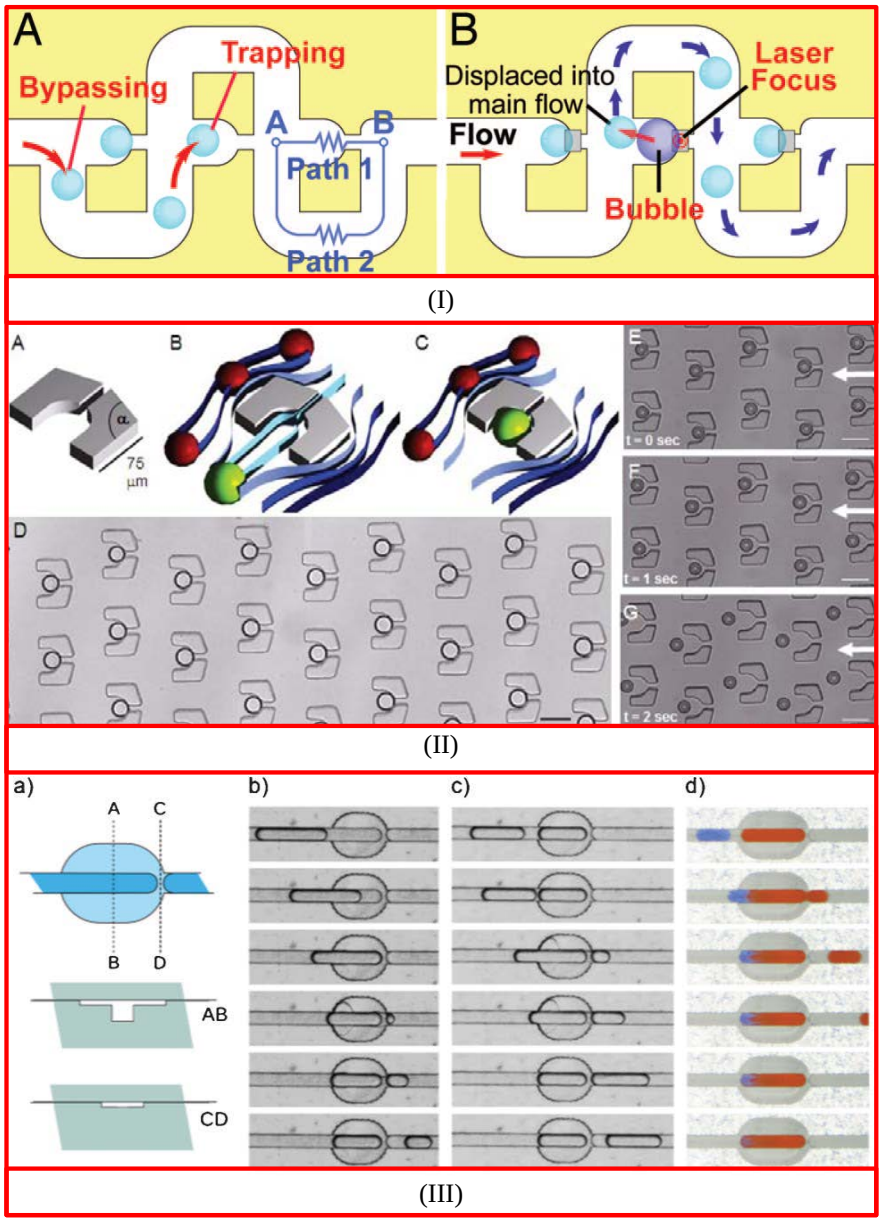

Figure 2.15 (I): Trap-and-release mechanism and experimental setup proposed by Tan *et al.* [272]; (II): Droplet trapping arrays presented by Huebner *et al.* [275]; (III): Architecture of the metering trap demonstrated by Korczyk *et al.* [276].

Bithi *et al.*[277] experimentally studied the behavior of a train of droplets flowing through this type of trapping loops. They defined four flow patterns corresponding to the resistance ratio of the trapping channel to the bypass channel, and the flow rate ratio of the dispersed phase to the continuous phase, including: 1. Bypassing; 2. Uniform trapping; 3. Breakup induced nonuniform

trapping; 4. No trapping-squeeze through (see Figure 2.16). In order to reach uniform trapping of droplets, the droplet size, droplet spacing, and the magnitude of Laplace pressure need to be tuned optimally. Nevertheless, a quantitatively analysis is still lack to guide this type of design.

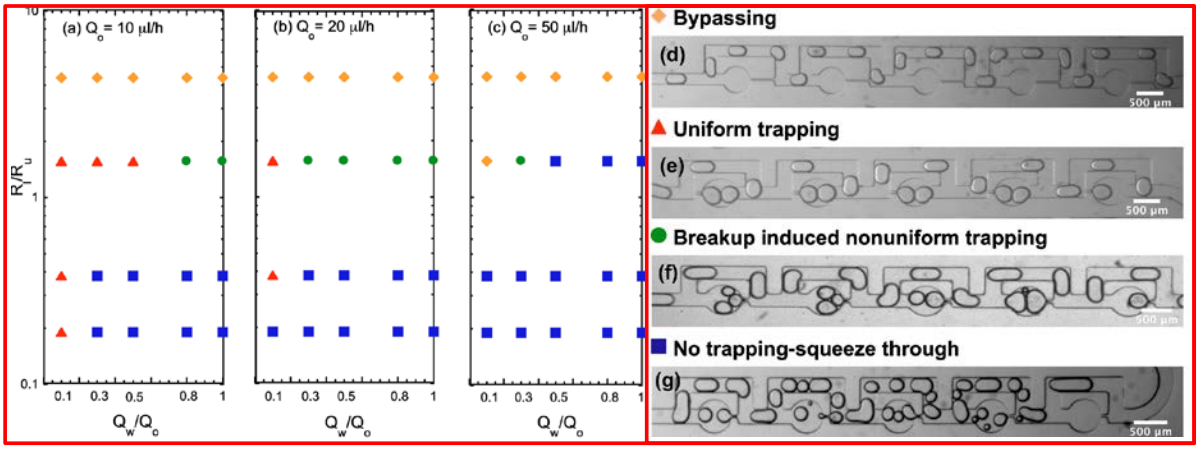

Figure 2.16 State diagram showing the four different behaviors observed in experiments at three different oil flow rates: (a) $Q_o = 10\mu l/h$, (b) $Q_o = 20\mu l/h$, and (c) $Q_o = 50\mu l/h$. Images (d)-(g) are representative snapshots of these behaviors[277].

Huebner *et al.*[275] described another droplet trapping geometry for enzymatic and cell-based assays as shown in Figure 2.15 (II). When a trap is empty, oil is able to flow through the pillars. As long as a droplet is captured in on pillar, it b locks the exit leading to the termination of fluid flow within the trap and keeping a second droplet from entering the trap. This design just randomly captures droplets flowing through the channel, and most droplets pass through the chamber without being trapped. However, this design is helpful to release trapped droplets by just applying a reverse flow of the continuous phase. This design is oriented from the approach reported by Di Carlo *et al.* [278] for trapping single cells in a microfluidic array. Bai *et al.* [279] modified this design to trap a pair of droplets for studying mass transport across a droplet-droplet interface. Kim *et al.*[188] varied the gap width between different columns of array to a certain range for size-selective trapping and sorting micro-particles.

Several groups trapped droplets inside a microfluidic channel by adding gaps instead of pillars [276, 280, 281] (see Figure 2.15 (III)). This type of geometry requires 3D channel fabrication.

Some active methods were also used to trap and release droplets on demand. Simon *et al.* [282] trapped and resealed droplets by utilizing a Laplace pressure, in where droplets can be trapped when

pressure gradient is less than the Laplace pressure, and can be released when the pressure gradient is increased to overcome the Laplace pressure. A membrane valve was integrated under the bypass channel, which can be pressurized to change the pressure gradient. Recently, Jin *et al*. [283] presented a programmable microfluidic static droplet array, allowing for droplet generation, transportation, fusion, storage, and retrieval in one chip by adding membrane valves into the chip. Wang *et al*. [284, 285] proposed an on-demand droplet trapping and releasing microfluidic system by adding a DC electric field next to the trapping well.

Besides trapping droplets, Holtze *et al*. [68] synthesized some biocompatible surfactants to stabilize droplets so that droplets can be collected in a large chamber inside the chip. The droplets still remained in a good shape without merging after an incubation time of 17 hours. Droplets can be also stored off microfluidic chips. Storing droplets on chip is limited by the chamber size and is difficult to scale up. Trivedi *et al*. [286] stored droplets by wrapping a flexible capillary tube around a spool for high throughput screening as shown in Figure 2.17. The authors estimated that commercially available PEEK capillary tubing with a 150 μm inner diameter can store up to 3300 droplets per meter.

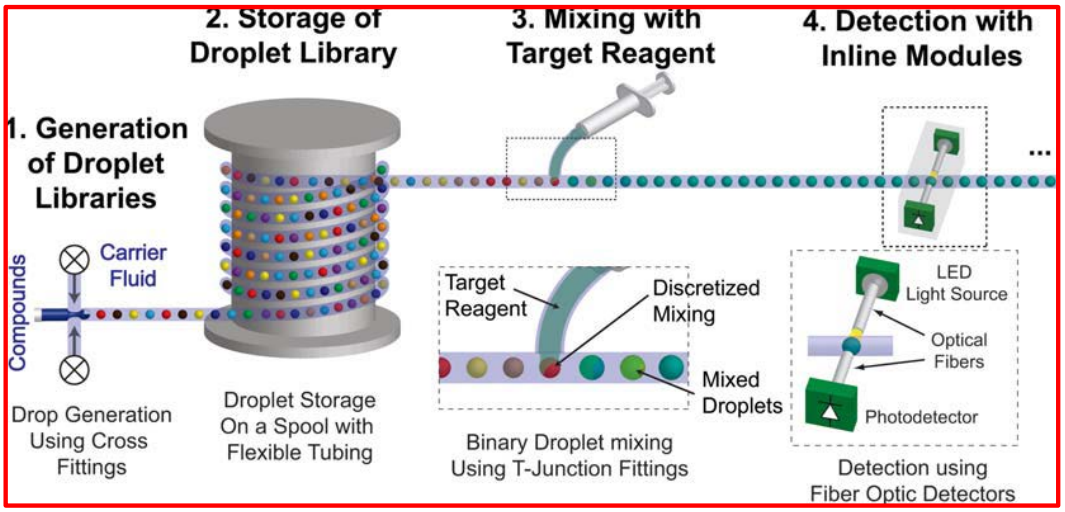

Figure 2.17 A modular approach to droplet-based screening system using off-the-shelf components demonstrated by Trivedi *et al.* [286]

2.4 Dynamics of Droplet Transport

In order to manipulate the droplet trains, the dynamic interactions of droplets confined by microchannels need to be well understood [287]. The following discussion focuses on the transport of droplets with length larger than channel width which are often called slugs.

2.4.1 Droplet Velocity

Slugs induce hydrodynamic interactions in local and global flow fields since they are confined by the channel geometries. Consider a large droplet transporting in a microchannel with a velocity U_d, a thin lubrication film of the continuous phase is formed between the droplet and the channel walls as shown in Figure 2.18.

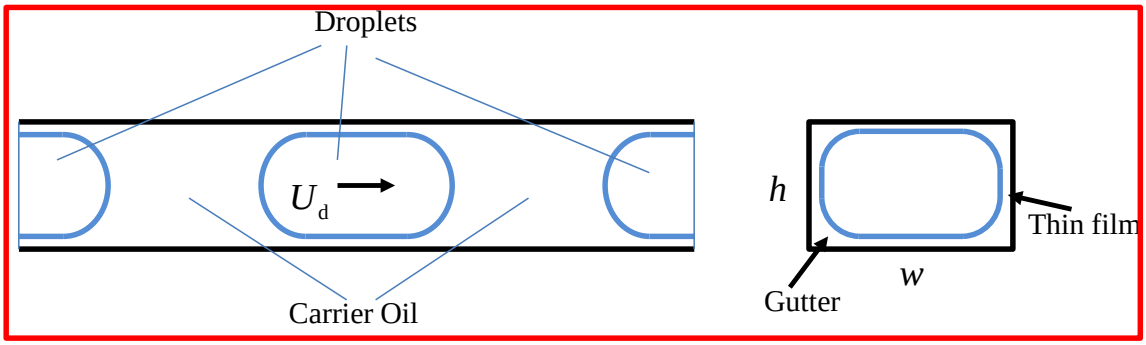

Figure 2.18 Left: droplet train transporting in a carrier fluid; Right: cross-section view of a large moving droplet in a rectangular capillary with thin lubrication films and corner gutters.

When the droplets move from left to right, they pull the carrier fluid from right to left due to viscous force which induces a thin lubrication film between the droplet and the walls. On the other hand, the pressure inside the droplet is larger than that in the continuous phase due to the Laplace pressure jump at the interface. The Laplace pressure jump pushes against the microchannel walls and dislodges the continuous phase liquid from the film into the bulk. The competition between the viscous drag and interfacial force determines the thickness of lubrication films *e* which can be described by the capillary number of the continuous phase. The elongated bubbles/droplets separated by a carrier fluid in a microchannel is typically the so-called Taylor flow [288]. Numerous studies on Taylor flow have been carried out both experimentally [289–294] and theoretically [99, 295–303]. Fairbrother and Stubbs [289] first experimentally studied the relationship between the velocity of an air bubble U_b and the mean velocity of a liquid U_m in a circular capillary. They found a simple

empirical relationship $m = \frac{U_b - U_m}{U_b} = Ca^{\frac{1}{2}}$ for $7.5\times10^{-5} < Ca < 0.014$ and bubble length larger than three times of the capillary radius. Taylor [290] extended the experiments to a much larger capillary number to $Ca = 1.9$ by using very viscous fluids. He found that the experimental results agreed well with Fairbrother and Stubbs's approximation $m = Ca^{1/2}$ when $0 < Ca < 0.09$, while m was less than $Ca^{1/2}$ when Ca increased beyond 0.09, and was found to be approaching an asymptotic value 0.56. The sketch of possible streamlines is shown in Figure 2.19 provided by Taylor.

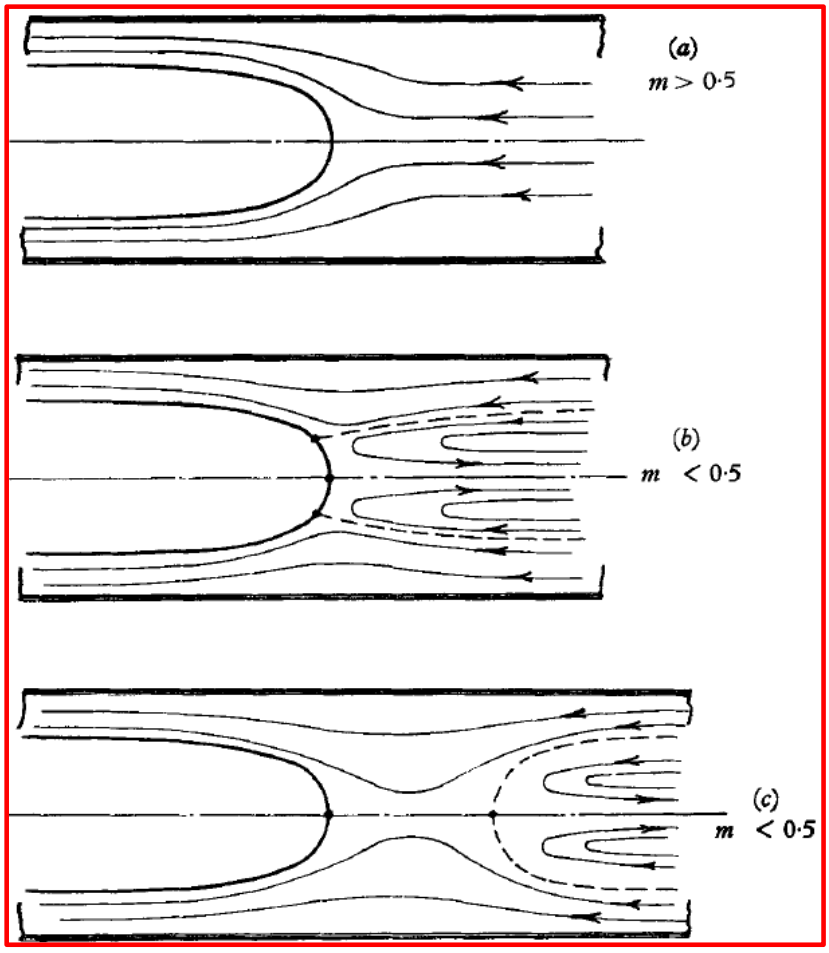

Figure 2.19 Rough sketch of possible streamlines in a Taylor flow provided by Taylor [290]. (a) The flow is reduced to steady motion with only one stagnation point, when $m > 0.5$. (b) There is one stagnation point on the vertex and a stagnation ring on the meniscus, when $m < 0.5$. (c) There are two stagnation points on the axis, when $m < 0.5$.

In 1961, Bretherton [295] theoretically developed an equation $m = 1.29(3Ca)^{2/3}$ for estimating the bubble velocity in a circular capillary for $Ca < 5 \times 10^{-3}$. Later, similar scaling results have extended for any polygonal cross-section geometry [297–299], and have been derived for moving viscous droplets [304], and bubbles travelling in alternating curved microchannels [305, 306]. Recently, the expression of the bubble velocity in a circular capillary has been extended to $Ca = 2.0$ [302]. Wong *et al.* [298, 299] concluded that the droplet velocity is lower than the carrier fluid's by an amount $m \propto -Ca^{-1/3}$.

As for viscous droplets, it becomes much more complicated due to the coupling between flows inside and outside the droplets. The velocity difference for viscous droplets has a much wider range than the case of inviscid droplets. Fuerstman *et al.* [307] reported a slip factor $\alpha = \frac{U_{\mathrm{d}} wh}{Q_{\mathrm{m}}}$ [308] of 0.83 for bubbles, where w and h are the width and height of the microchannel, respectively, Q_{m} is the mean flow rate. Labrot *et al.* [268] reported a slip factor as large as 1.6 for viscous droplets. Garstecki *et al.* [309] experimentally studied the speed of viscous droplets in microfluidic channels as a function of the capillary number, volume of droplets and viscosity contrast. The results showed a complex dependency on all three parameters. For small viscosity ratio $\eta = 0.3$, the slip factor strongly depends on the size of droplets varying from 0.95 to 1.35 when the length of droplets L / w varies between 1.5 and 3, and nearly becomes constant $\alpha \approx 1$ for length of droplets L / w larger than 3. For moderate viscosity ratio $\eta = 3.3$, the slip factor is always smaller than 1 varying from 0.6 to 0.95. For high viscosity ratio $\eta = 33.3$, the trend between the slip factor and the size of droplets was linear. Although experimental results showed some trend of viscous droplet velocity difference from the carrier fluid, no theoretical model has been built to investigate this complex behavior. More work is urgently needed to study the viscous droplet interactions during transport in a confined channel.

2.4.2 Pressure Drop

Another key area of study is the hydrodynamic resistance of droplet-based microfluidics during transportation which is expressed by the relationship between the pressure drop and flow rate, similar to the electrical resistivity in Ohm's law. Several groups have attempted to develop compact pressure versus flow rate models for droplet microfluidic flow but the physics is rather complex [268, 307, 308, 310, 311]. As sketched in Figure 2.18, the channel contains droplets and plugs of continuous phase,

separated by transition regions around the interfaces. The total pressure drop ΔP_{Total} across the channel is the sum of the viscous resistance from the continuous phase plugs ΔP_{nb} and from the droplets ΔP_{body} plus the Laplace pressure jump due to the interface curvatures ΔP_{caps} as shown in Figure 2.20 [307].

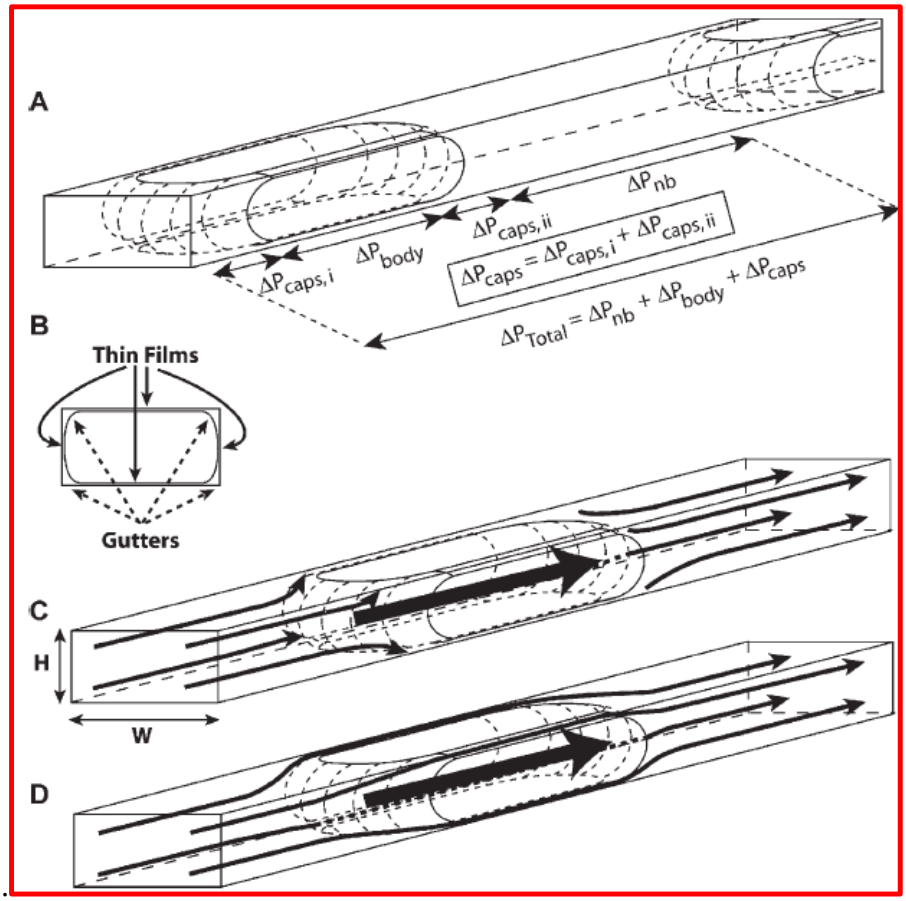

Figure 2.20 (A) Sketch of the pressure drop along a microchannel containing a bubble train. (B) Crosse-section view of the bubble down the long axis of the channel. (C) A schematic diagram when the liquid does not flow past the bubble through the gutters. (D) A schematic diagram when liquid flows past the bubble through the gutters [307].

For pressure drop caused by each plug, the pressure can be expressed as Equation (2.1) which is similar to Ohm's law.

$$\Delta P_c = a\frac{\mu_c}{wh^3}L_c Q_c = a\frac{\mu_c}{h^2}L_c U_c \qquad \textbf{(2.1)}$$

where a is a dimensionless constant, μ_c is the viscosity of continuous phase, L_c is the length of plug, Q_c is the flow rate of the continuous phase, and U_c is the mean velocity of the continuous phase [307].

The Laplace pressure jump due to the interface curvature has only been investigated in the case of an inviscid bubble at small capillary number [295, 298, 299]. The pressure drop caused by the bubbles can be estimated as [307]:

$$\Delta P_{caps} = N_d c \frac{\gamma}{h} Ca^{2/3} \quad \textbf{(2.2)}$$

where N_d is the number of bubbles, c is a dimensionless parameter which depends on geometric parameters (w, h, L_{bubble}). The inviscid theory remains valid for low viscosity ratios ($\eta << 1$, where η is the viscosity ratio of bubble to the continuous phase). However, for comparable viscosity of droplets to continuous phase, the viscous dissipation inside the droplets is no longer negligible and it's common to calculate the pressure drop ΔP_d using $\Delta P = Q \cdot R$ [311]. Therefore, the overall pressure drop due to a train of viscous droplets is:

$$\Delta P_{d+caps} = b \frac{\mu_d}{h^2} L_d U_d + N_d c \frac{\gamma}{h} Ca^{2/3} \quad \textbf{(2.3)}$$

where b is a dimensionless parameter, μ_d, L_d and U_d are the viscosity, length and average velocity of viscous droplets, respectively. The total pressure drop then becomes:

$$\Delta P = \Delta P_c + \Delta P_{(d+caps)} = a \frac{\mu_c}{h^2} L_c U_c + b \frac{\mu_d}{h^2} L_d U_d + N_d c \frac{\gamma}{h} Ca^{2/3} \quad \textbf{(2.4)}$$

A sketch of the pressure drop along a microchannel is shown in Figure 2.21. From Equation (2.4) one can see that the pressure drop model is too complex for general use because the parameters *a*, *b*, and *c* depend on the geometries of the channel and droplets. For this reason, some other simpler models have been presented based on empirical equations [268, 312, 313]. Although these scaling laws can capture the trend of pressure drop in the droplet microfluidics, a comprehensive model is still required to study the pressure and flow rate relationship which will definitely help to understand the fundamentals of droplet transport.

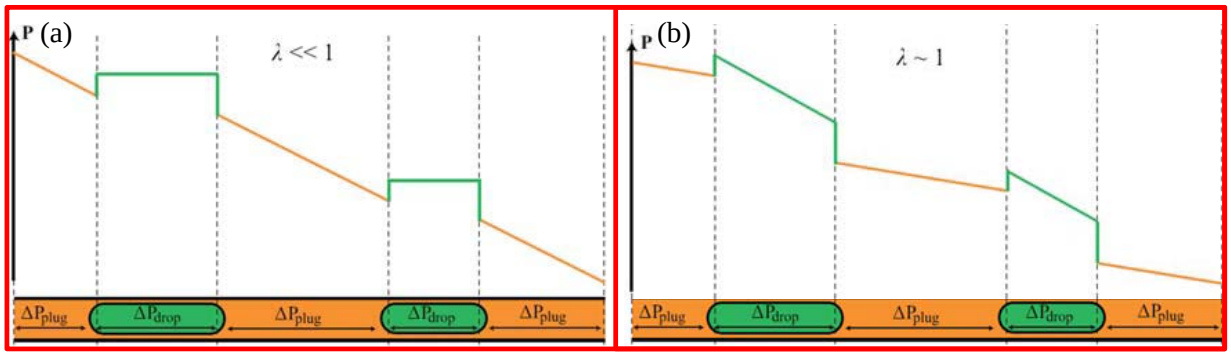

Figure 2.21 A qualitative plot of the pressure along a microchannel containing a droplet train in the case of (a) inviscid droplets ($\eta << 1$) and (b) viscous droplets ($\eta \sim 1$) [287]

2.5 Applications of Droplet Microfluidics

Droplet-based microfluidics have broad range of potential applications which have been summarized by several review papers [25, 27, 44, 314–317]. In this section, some applications of droplet microfluidics are introduced including applications in chemistry, biology and medicine.

2.5.1 Chemical Applications

Compared to single phase microfluidics, droplets are particularly suitable for chemical synthesis, allowing for precise control over multiple reagent phases, relative rapid mixing and high throughput operations. Each droplet can be used as individually addressable microreactor, which can dramatically reduce the sample cost. In addition, large ratios of surface area to volume ensure thermal homogeneity inside droplets and rapid heat transfer between the device and the reagents. Researchers have synthesized many types of materials using droplets including copolymers [318], microbeads [319–321], molecular probes [322], nanostructures/particles [323–328], and microgels [329–331] etc. Importantly, Kim *et al.*[320] reported synthesis of magneto-chromatic microspheres using droplets as shown in Figure 2.22 (I). The droplet microfluidics combined with magnetic self-assembly and photo-polymerization process allows controlling the size and color of microbeads. Marquis *et al.*[331] recently demonstrated the use of droplets to produce Janus hydrogel microbeads made of pectin-pectin (homo Janus) and pectin-alginate (hetero Janus) (see Figure 2.22 (II)). In addition, droplet-based microfluidic devices are able to control multi-step reactions in parallel. Jebrail *et al.* [332] developed a droplet system which was used to carry out the synchronized synthesis of five peptide

macrocycles from three different components. This method is fast, amenable to automation, compatible with a wide range of solvents and is particularly well suited for parallel processing.

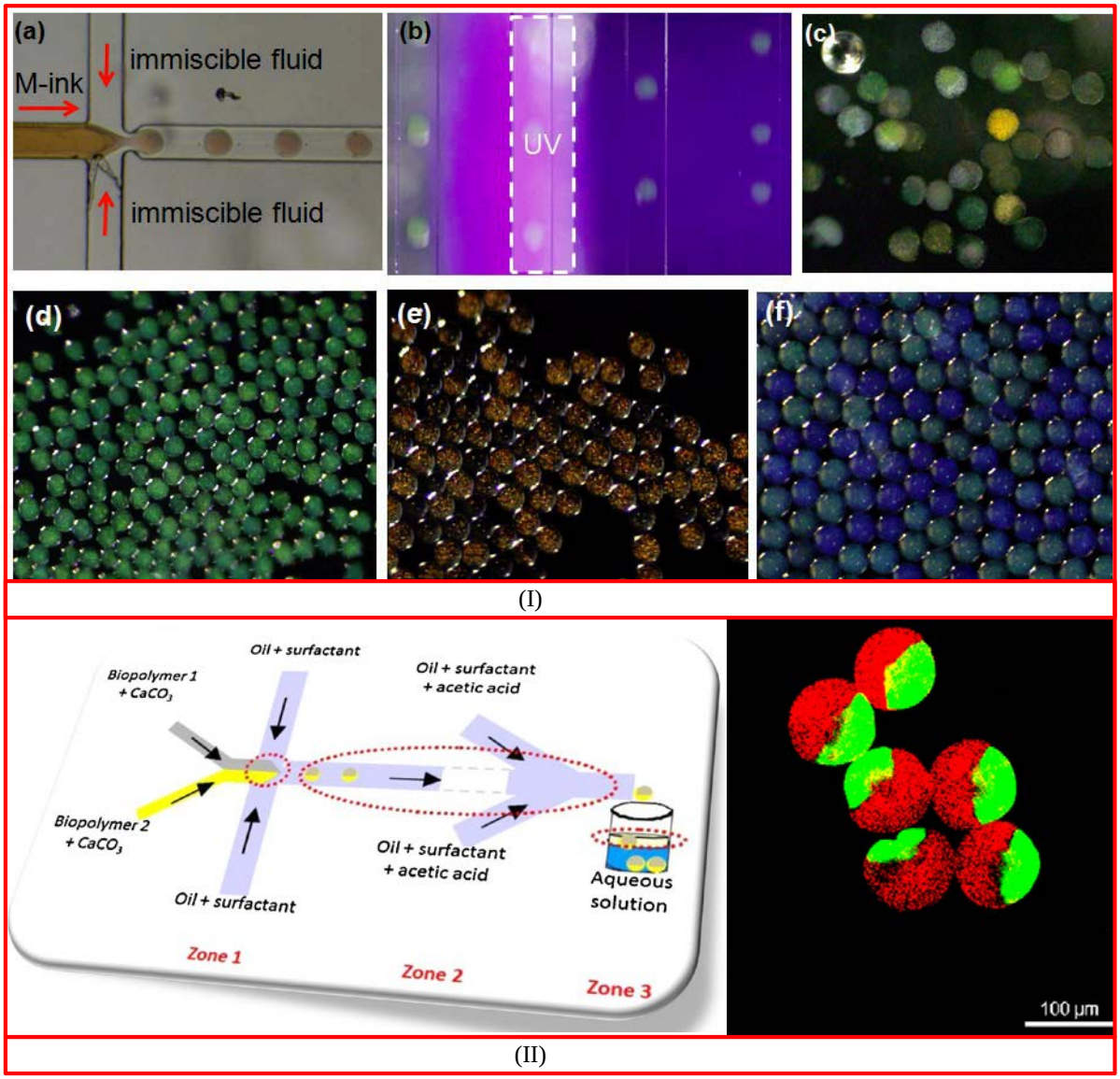

Figure 2.22 (I): Droplet microfluidic system used to synthesize magnetochromatic microspheres reported by Kim *et al.*[320]. (II): Schematic of the microfluidic device for Janus droplet generation and produced Janus microparticles demonstrated by Marquis *et al.*[331].

2.5.2 Biological Applications

One of the most promising applications of droplet-based microfluidics is in the field of biology, where droplets can be used to handle samples of DNA, proteins or living cells. Droplets are ideal containers for biological materials, because the droplets are separated by a thin film (continuous phase) which reduces the opportunity for biomolecules to contact the channel walls and be adsorbed to device surfaces. Also, droplet-based microfluidics can prevent sample loss or contamination from outside influences [333].

Chang *et al.* [334] reported a microfluidic chip for polymerase chain reaction (PCR) applications utilizing droplets. Several crucial procedures including sample transportation, mixing and DNA amplification were performed on the integrated chip using electro-wetting-on-dielectric (EWOD) effect with an operation voltage of $12 V_{\mathrm{RMS}}$ at a frequency of 3 KHz. This system consumed less sample and reagent and could reduce the detection time compared to large-scale counterparts for DNA amplification. In other works, Tewhey *et al.* [335] reported an enriched approach based on micro-droplet PCR, which enabled 1.5 million amplifications in parallel as shown in Figure 2.23. They sequenced six samples enriched by microdroplet and generated high quality data with high specificity and sensitivity, which demonstrates that the microdroplet technique is well suited for processing DNA amplification in large scale. In addition, droplets are also used for immunoassay applications [336].

Droplet-based microfluidics has also been widely used in cell-based assays. Several groups have encapsulated different types of cells into microdroplets including bacteria [337, 338], yeast [339–341] and mammalian cells [342, 343]. Brouzes *et al.* [343] presented a droplet-based microfluidic technique which offered high throughput screening of single human monocytic U937 cells . They demonstrated the high viability of encapsulated human monocytic U937 cells over a period of 4 days. In addition, an optically-coded droplet library was developed enabling the identification of the droplets composition during the assay read-out.

One key issue with encapsulating single cells into droplets is how to increase the ratio of single cell encapsulated into one droplet. Random encapsulation of single cells follows a Poisson distribution[342] given by $f(\lambda;n)=\frac{\lambda^n e^{-\lambda}}{n!}$, where n is the number of cells in the droplet, and λ is the average number of cells per droplet. A recent review paper [49] summarized the methods for beating the Poisson distribution. Sorting droplets after encapsulation is a straight forward method for

increasing the ratio of single cell in one droplet, which has been reported by many groups [344–347]. However, this strategy wastes most of the droplets with empty or multiple cells, and is not applicable especially when samples are very expensive. Some other methods utilized channel geometries, hydrogels or Dean flows etc. to beat the Poisson distribution. For example, Edd *et al.* [348] lined up cells as they travelled in a high aspect ratio microchannel, where cell diameter occupied most fraction of the channel's narrow dimension, and thus the cells can self-organize into a line. Cells entered the droplet generator with the same frequency of droplet formation so that almost every droplet can contain exactly one cell. Abate *et al.* [349] beat the Poisson encapsulation statistics by first loading cells into gel particles, and then lined up the gel particles for encapsulation. These get particles are deformable with an average size of 30 μm , and thus avoid clogging the microchannel. Kemna *et al.* [350] arranged cells into one line by utilizing Dean flow in a curved microchannel, and reached 77% single cell droplet encapsulation rate with a high speed 2700cells/s.

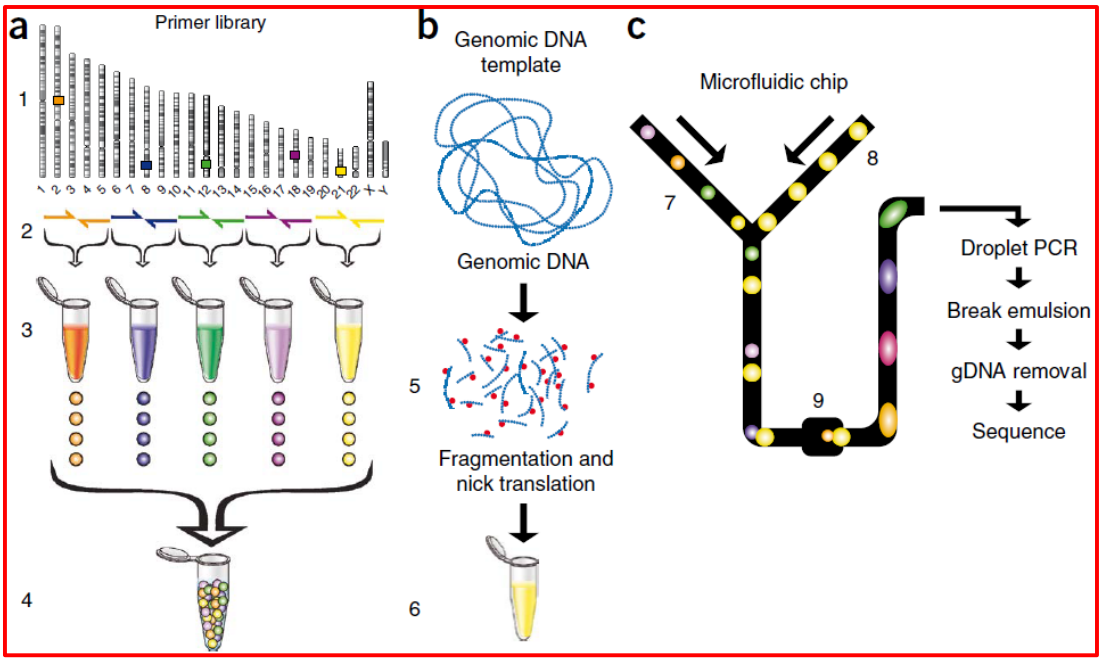

Figure 2.23 Microdroplet PCR workflow provided by Tewhey *et al.* [335].

2.5.3 Medical Applications

Droplets are also well suited for medical applications because of the precise control over reagent volumes as summarized by Kaler *et al.*[51]. Sirnivasan *et al.* [351] developed a droplet-based lab-on-a-chip for clinical diagnostics of human physiological fluids and performed a colorimetric enzymatic

glucose assay on serum, urine and saliva to show the feasibility of performing bioassays in droplets. Mousa *et al.* [352] developed a digital (droplet) microfluidic method to extract estrogen in 1 µL samples of breast tissue homogenate, as well as in whole blood and serum. This method used a sample size which was 1000-4000 times smaller than traditional methods for the extraction and quantification of estrogen and was 20-30 times faster. Jebrail *et al.* [353] presented a droplet system for quantification of amino acids in dried blood spots (DBSs). Analytes are extracted, mixed with internal standards, derivatized and reconstituted for analysis by (off-line and in-line) tandem mass spectrometry. This method is fast, robust, precise and compatible with automation. Miller *et al.*[354] developed a microfluidic system that utilizes droplets to generate high-quality dose-response data for drug screening. They successfully built up each dose-response curve for tested compounds containing approximately 10,000 data points, that is 1,000 times more than in conventional systems.

Many biomedical reactions for disease diagnosis, and drug screening etc. should be performed *via* a series of experiments with different compound concentrations. Therefore, concentration gradient generators are critical to monitor reaction kinetics for biomedical systems [355]. The first strategy for generating concentration gradients in droplet microfluidics is to control the flow rates of two samples that are injected together as a co-flowing stream before the droplet generation [356–358], which relies on the stability of flow controlled by microvalves or syringe pumps (see Figure 2.24 (I)). The second method is based on sample diffusion in a stratified flow. The principle for generating concentration gradient is that the sample with a higher concentration merges into the sample with a lower concentration through diffusion. Diffusion is a very predictable phenomenon, allowing the generation of gradients through different micro-structures such as radial distributor s[359, 360], and Y-junctions [361, 362] as shown in Figure 2.24 (III). For these platforms, the range of concentration gradient is quite limited because the microchannel network design becomes increasingly complex with the number of distinct concentrations required. In addition, these platforms cannot be applied in aggressive reactions, since the reaction can happen at the interface through diffusion. Therefore, the third strategy for gradients is to merge and mix between multiple pre-formed droplets [363–365] (see Figure 2.24 (II)). Moreover, Sun *et al.* [366] introduced another concentration gradient generator, which produces arrays of droplets with a concentration gradient by sequentially mixing of trapped droplets with a long moving diluting slug.

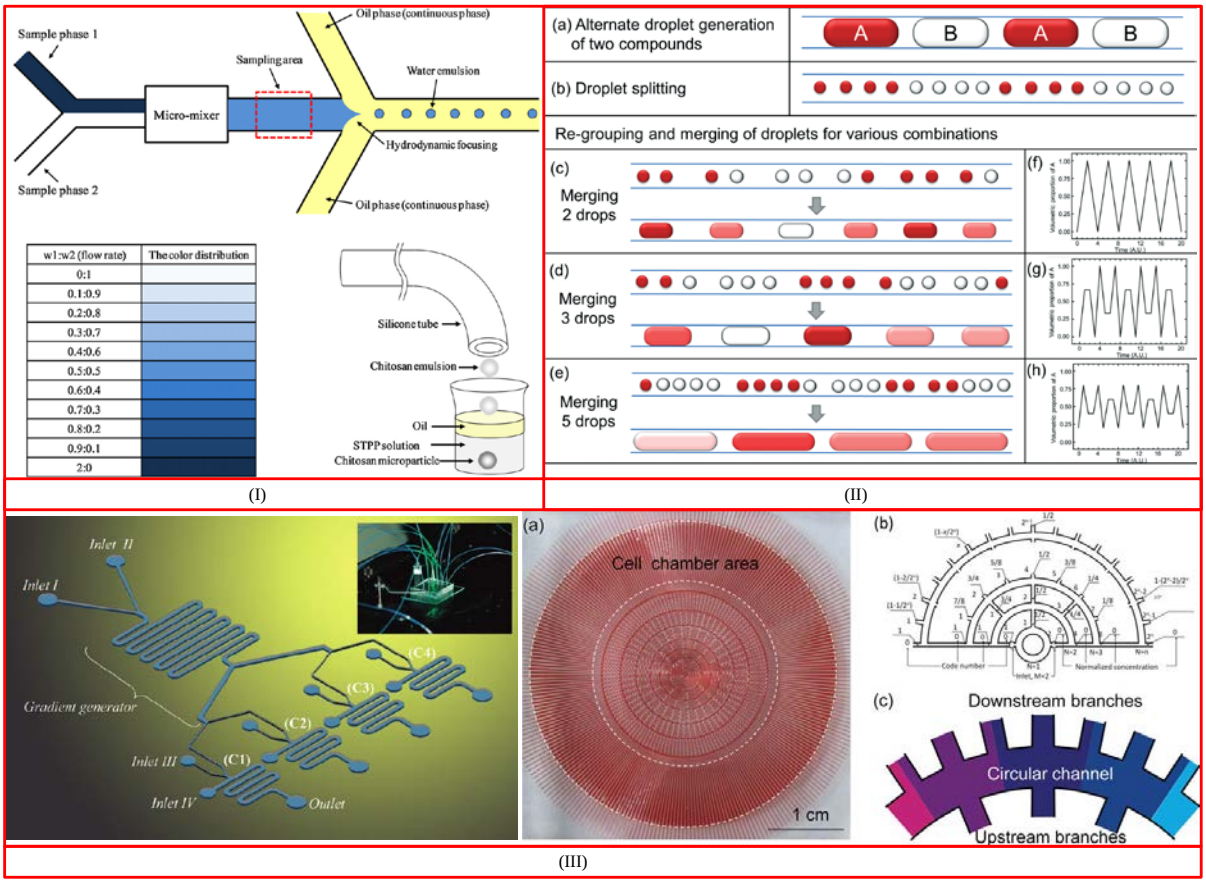

Figure 2.24 Concentration gradient platforms. (I): Concentration gradient generator by controlling the flow rates of two samples reported by Yeh *et al.* [358]; (II) Concentration gradient generator by merging and mixing pre-formed droplets presented by Um *et al.*[365]. (III): Concentration gradient structures through diffusion between two samples, such as Y-junction by Bui *et al.* [361] and Radial distributor by Yang *et al.* [359];

2.6 Summary

In this chapter, various methods for generating and manipulating droplets such as sorting, detecting, merging, splitting, pairing, mixing, trapping, storing and releasing were reviewed. In addition, the dynamics of droplet transport in microchannels was briefly discussed, which has a high influence on the degree of precision with which a droplet can be controlled during transportation. Finally, some applications for droplet-based microfluidics were listed, focusing especially on chemical, biological and medical applications.

Chapter 3
Experimental Setup and Fabrication Techniques

This chapter describes the experimental devices and methods used to complete the research projects. Details of experimental setup and procedures, chip fabrication, fluid properties, methodology of microchannel dimension measurement are provided.

3.1 Experimental Setup

The experimental setup is shown in Figure 3.1. The whole system consists of fluid reservoirs, a pressure control system for driving fluids into microfluidic chips, three in-line flow sensors for measuring flow rates, a microscope and a high speed camera to capture the dynamic flow of droplets. A Labview program was written to manipulate the experimental setup.

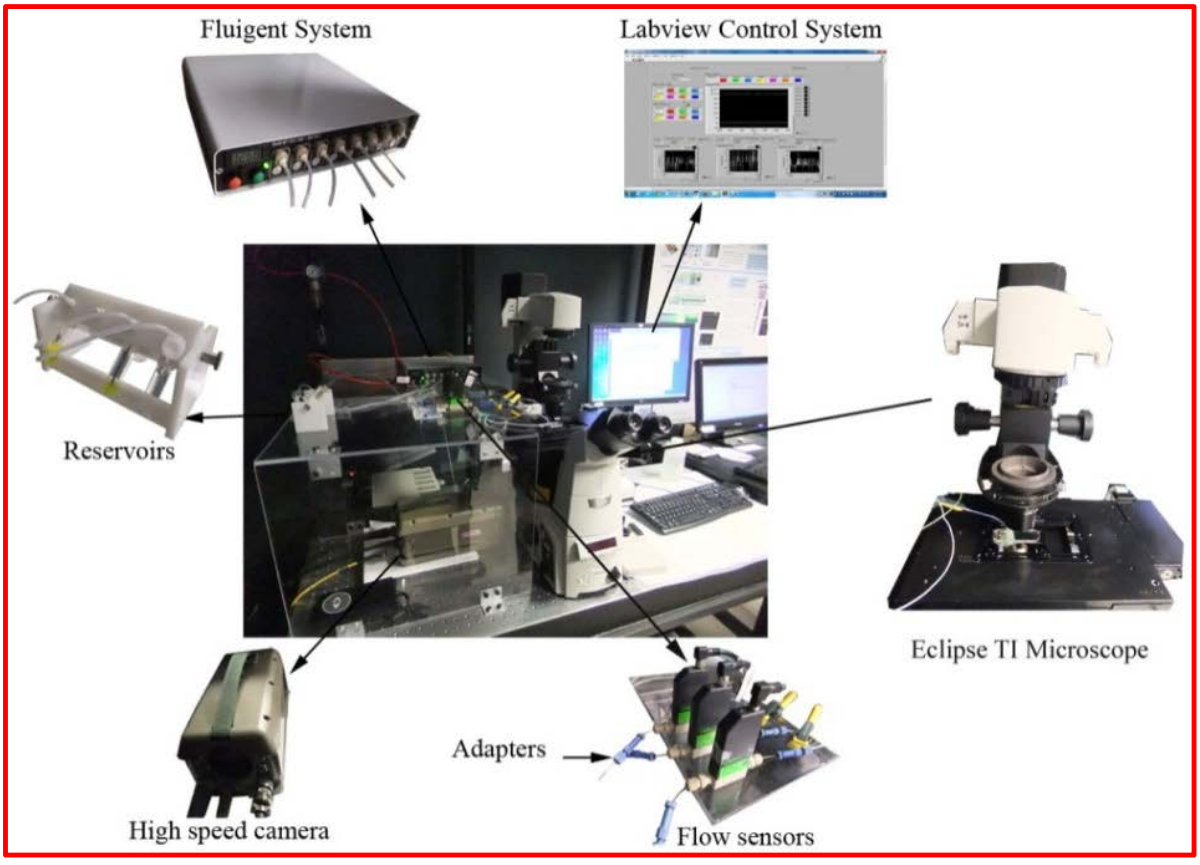

Figure 3.1 Photos of experimental setup. The central photo shows the whole connection of components

3.1.1 Pressure-Driven System

Both syringe pumps and pressure control systems have been widely used to pump fluids in a droplet microfluidic system. Syringe pumps produce a constant flow rate output, while a pressure control system provides a constant pressure source. Using syringe pumps for droplet microfluidic studies causes lots of problems as documented in one of my previous lab members' studies [367] and other studies as well [368]. Briefly, syringe pumps lead to short term oscillations in the output caused by the stepper motor and long term oscillations in the output caused by imperfections in the drive screw. Korczyk *et al*. [368] demonstrated the oscillation in the generated droplet volume when using syringe pumps and the uniformity of the generated volume when using a pressure control system. Therefore, in this study, a high-precision microfluidic pressure control system (MSFC 8C, Fluigent) was used to pump fluids. This system can control up to 8 output channels at the same time with a maximum pressure of 1bar and accuracy of 0.5mbar. Each reservoir is connected to the MSFC 8C via an air pressure tube, while another tube is inserted into the bottom of the reservoir as output. The fluctuation of flow rate with a pressure control system is caused by the dynamic pressure resistance of micro-channels caused by droplets forming and leaving the system. In order to maintain a constant flow rate of both the dispersed and continuous phases during droplet generation, long feed lines with a small diameter (254um) were used before connecting to the chip in order to increase the hydrodynamic resistance of the microfluidic system. By doing this, the fluctuation of the system resistance can be minimized. Therefore, the experiments were performed with constant flow rates, which were also verified by flow sensors and by tracking the velocity of moving droplets.

3.1.2 Flow Sensors

An in-line flow sensor (SLG 1430, Sensirion) is inserted between each reservoir, both the dispersed and continuous phases, and the chip. This flow sensor is able to measure water flow rates up to 40μL/min with frequency of 100Hz. The inside diameter of the glass capillary within the sensor is 480μm. The sensor detects the flow rate based on thermal anemometry principles and is thus sensitive to the physical properties of fluids. Therefore, the sensor has to be recalibrated before use. The sensor runs in a 'raw' mode where direct temperature measurements are outputted as 'tick' counts. The typical operational curve for the flow sensor has a sigmoid shape. The desirable measurement should be in the linear portion of the curve. For water, the measurement range is from -40~40 μl/min which is already calibrated by the company. For silicone oil and glycerol/water mixtures, the linear portion is much smaller under 6μl/min. The flow sensor is non-linear when the flow rate is above 7μl/min. So

we only use flow rates under 6µl/min during experiments. The flow sensor calibration process is described as follows:

- Fill appropriate fluid (oil or glycerol/water mixture) into 1ml syringe (Hamilton Inc.)
- Connect syringe to the flow sensor via micro-tubing
- Put syringe on a high precision syringe pump (33 Twin, Harvard Apparatus) and pump fluid at various flow rates from 0 to 6µl/min
- Record data and plot calibration curves. At each flow rate, data are averaged over 10mins (about 500 data points)

The calibration curves for silicone oil and 3 types of glycerol/water mixtures are presented in Figure 3.2. During experiments, the slope and intercept are inputted into the Labview control program to measure the flow rates of the dispersed and continuous phases. The curves for all three flow sensors were utilized, one for silicone oil, the second one for 10%glyc/water, the third one for 60%glyc/water and 80%glyc/water.

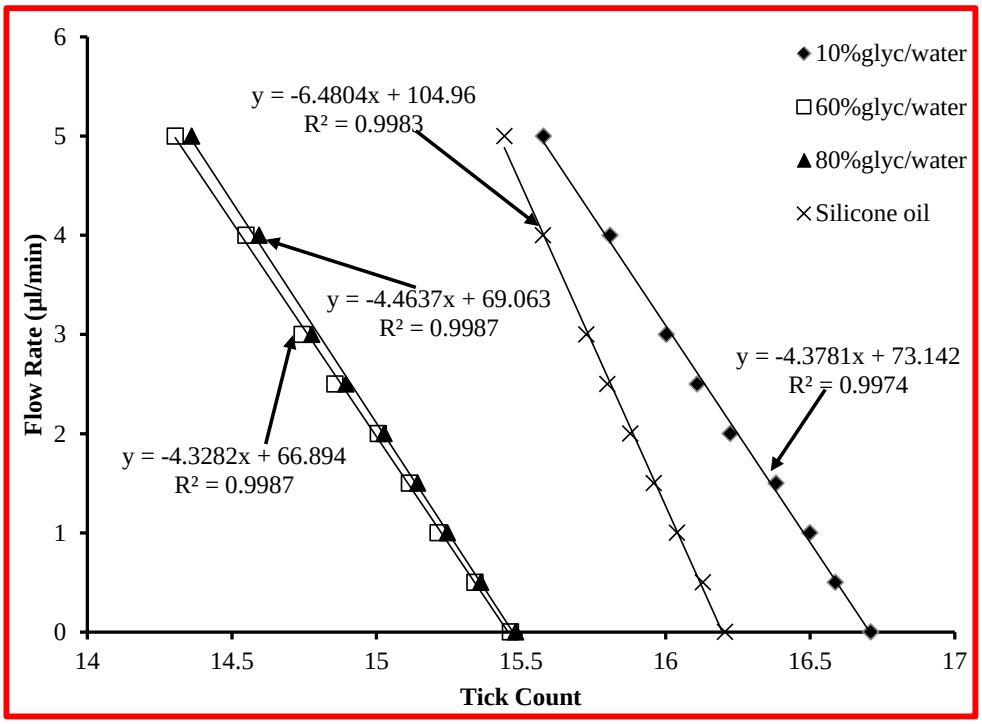

Figure 3.2 Calibration curve of flow rate vs 'tick' count for the SLG 1430 flow sensor. Linear regression profiles are: -6.4804x +104.96 (silicone oil), -4.3781x + 73.142 (10%glyc/water), -4.3282x + 66.894 (60%glyc/water), -4.4637x + 69.063 (80%glyc/water) with $R^2 > 0.997$ for all profiles.

The flow sensors measure the flow rate through the wall of a thin walled glass capillary using the heat propagation through the glass wall and the heat exchange with the medium. Formation of deposits on the glass wall may block the heat transfer, leading to inaccurate measurement. Typical signs of depositions on the glass capillary are measurement deviations over the whole flow range and/or offsets of the measurement. This should be avoided by cleaning the sensors after usage and before storing the sensor for longer periods. Do not let the sensors dry with media in the capillary tube without flushing clean, and also avoid letting the filled sensor sit for extended periods depending on the liquid. Before storing the sensors, drain of fluid, flush with acetone followed by flushing with isopropanol, blow out and dry the capillary. Close the flow sensors with sensor plugs for storage. The advantage of using clean isopropanol after flushing with acetone is that isopropanol evaporates without residue in contrast to acetone.

3.1.3 Microscope and High-speed Camera

Droplet formation and transport are visualized using an inverted epifluorescence microscope system (Eclipse Ti, Nikon). The system mainly consists of a 3D programmable stage (x, y, z), objective nose piece, fluorescence turret and shutters. The properties of the objectives are (NA, working distance):10x (0.3, 16mm), 20x (0.5, 2.1mm), 40x (0.75, 0.72mm). Filter cubes are provided for Rhodamine B (500-550nm ex, 565nm) and Fluorescein (495nm ex, 505nm) dyes. Illumination is supplied by a 100 W halogen lamp for bright field applications, and a 100W mercury halide lamp (Intensilight C-HGFIE, Nikon) for fluorescence applications. Images are recorded by a Retiga 2000R Fast 1394 monochrome CCD camera attached to the right port of the microscope. The digital image quality is 12 bit with a maximum speed of 10 fps at full resolution (1600x1200). The capture speed can increase up to 110 fps with binning (8x8 binning). A custom software coming with the microscope controls the entire system for taking images at specified times and positions.

A high speed CMOS camera (Phantom v210, Vision Research) is connected to the microscope on the left port using a C-mount adapter (1X DXM, Nikon). The camera can take images at 2190 fps, with a 12 bit digital image quality at full resolution (1280x800). By lowering the resolution, or cropping the field of view, the capture speed can easily exceed 10k fps. The camera continuously records images to the buffer and then downloads them to the camera via fire wire once the trigger is activated.

3.2 Soft Lithography Fabrication Method for Microfluidic Chips

The chips are fabricated using PDMS via soft-lithography techniques. At the beginning, a photo mask with an image of the microchannel layout is designed via AutoCad and printed commercially on Mylar films with 20k dpi resolution (CAD/Art services). The following step is to fabricate a master for molding PDMS microchannels. Steps for fabricating a master on a 4-in silicon wafer are summarized below:

- Before the fabrication, photoresist SU-8 is poured from the large bottle to a dispensing pipe and left for at least 12hours to remove bubbles.
- Dehydration. Pick up a silicon wafer and bake it on a 190℃ hot plate for at least 20min which helps to prevent photoresist from peeling off the substrate.
- SU-8 2005 is deposited onto the silicon wafer with thickness of 5μm as the substrate by spin coating (200 CB, Brewer Science). The thickness of the film depends on the type of SU-8 and the spin coating speed. Su-8 is deposited using a precision pneumatic dispensing system (Ultra 1400, Engineered Fluid Dispensing).
- A soft bake is performed at 65°C and 95°C on a set of level hot plates to evaporate the solvent in the photoresist and harden the film. The baking time depends on the film thickness. The silicon wafer is first baked on 65°C, and then on 95°C hot plates in order to reduce thermal stress.
- The silicon wafer is placed in a UV exposure system (Newport) and illuminated with UV light (~365nm).
- A hard bake at 65°C and 95°C was performed and left in room temperature to cool down.
- Choose a specific type of SU-8 according to the required channel height and deposit SU-8 onto the substrate following the same step as depositing SU-8 2005. The speed and time of spin coating are set based on the calibration curve.
- Afterwards, soft bake is performed at 65°C and 95°C.
- The wafer is covered with the photo mask that contains the microchannel design and illuminated with UV light. During the illumination, a pump is turned on to create vacuum of 10 mmHg in order to minimize the gap between the mask and the wafer. The exposed regions undergo photopolymerization and begin to cross-link.
- Hard bake is repeated at 65°C and 95°C.

- The silicon wafer coated with SU-8 is put in a dark place for at least 12 hours to release the thermal stress in the SU-8. After that, the master is immersed in a large bath of SU-8 developer to dissolve the unexposed SU-8 regions.
- The wafer is then washed with clean SU-8 developer, isopropanol, deionized water and finally is blown dry with air.
- A small amount of glue (Loctite 3311) is coated around the edge of the wafer and hardened with UV light which helps to prevent photoresist from peeling off the substrate.

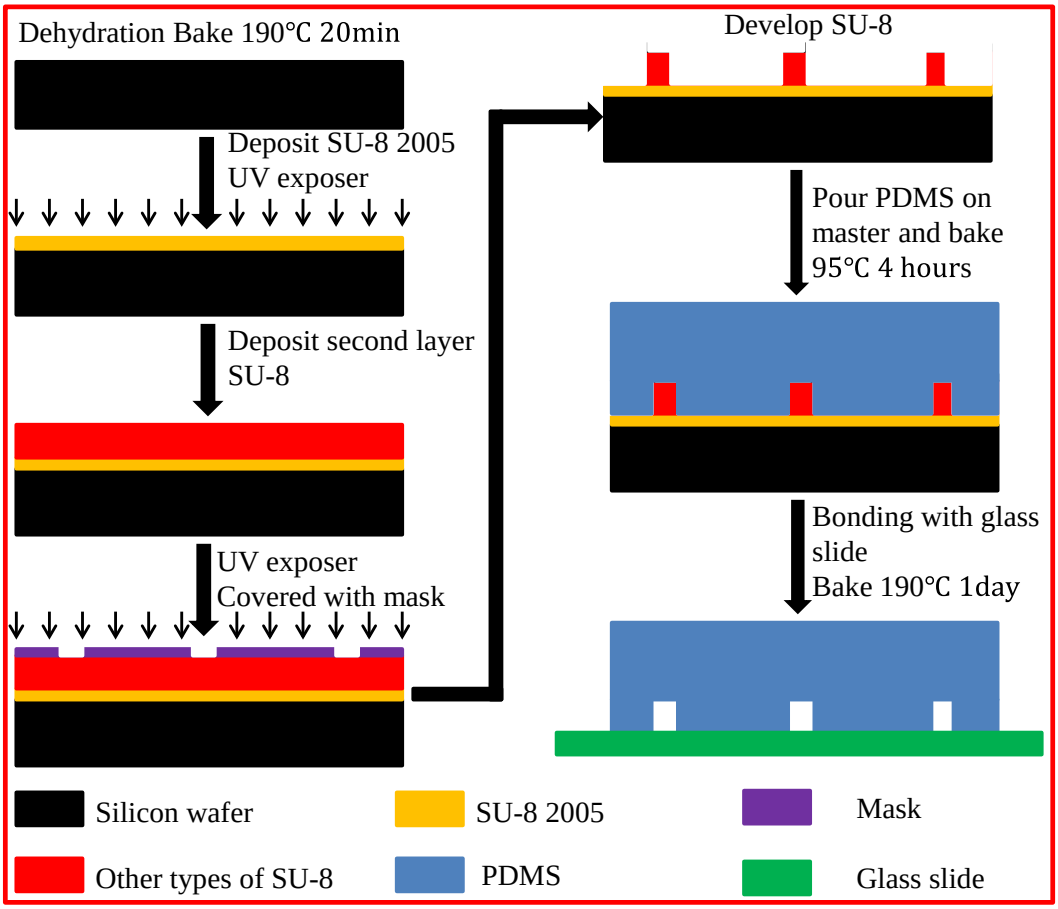

Figure 3.3 Schematic of soft lithography fabrication procedure

After the master is fabricated, PDMS (Sylgard 184, Dow corning) is mixed with a ratio of 10:1 (base: curing agent) and put into a vacuum oven to remove bubbles. Then, the PDMS is poured on top of the master placed in an aluminum dish and cured at 95°C for at least 3 hours. When PDMS molds are cooled down, they are bonded to a glass slide coated with PDMS using oxygen plasma in order to

create a homogeneous microchannel. PDMS coated glass slides are fabricated by spin coating at 3000rpm for 60s and baked at 95°C for 5min. The two substrates are exposed to oxygen plasma (PDC-001, Harrick Plasma) with power of 29.6W at 500mTorr for 10s. However, the plasma treatment changes the wetting property of PDMS from hydrophobic to hydrophilic. Since we generate water in oil droplets, PDMS chips are heated at 190°C for at least one day to revert them back to hydrophobic. After the chip is examined and measured under a microscope, the process of fabricating a PDMS chip is finished. A schematic of fabrication procedure is shown in Figure 3.3.

3.3 Fluid Properties Used in Experiments

Silicone oil with various viscosities 5cSt, 10cSt, 20cSt, and 50cSt (DC200, Sigma Aldrich) are used as the continuous phase. Different viscosities are chosen in order to match the hydrodynamic resistance of microchannels instead of changing the microchannel dimensions and expand a large range of the capillary number. A series of glycerol/water mixtures (10%, 60% and 80% in wt %) are used as the dispersed phase to ensure a wide range of viscosity ratios between the two phases while maintaining a relatively constant interfacial tension. Viscosity is measured using a programmable rheometer (LVDV-III Ultra CPE, Brookfield Instruments) with a cone-plate spindle (CPE-40). Interfacial tension between the fluid pairs is measured using a Wilhemy plate tensiometer (Data Physics, DCAT 11). In addition, methylene blue dye is used to create a phase contrast between two streams of droplets.

3.4 Microchannel Dimension Measurement

Silicone oil is slightly soluble in PDMS which causes the dimensions (w, h) of microchannels to shrink. Therefore, it is very difficult to measure the actual channel height using standard procedures such as profilometers. Instead, measurements of the channel dimensions must be made in situ for each chip. Since accurate channel dimensions at the junction are critical to analyze the droplet generation process, flow sensors and the pressure controller are used to estimate the equivalent hydrodynamic resistance ($R_h = P / Q$) of the dispersed channel and main channel which are connected by the junction.

For a rectangular cross section microchannel operating under laminar flow, the hydrodynamic resistance can be calculated by Equation (3.1) [369],

$$R_h = \frac{12\mu L}{wh^3}\left[1-\frac{h}{w}\left(\frac{192}{\pi^5}\sum_{n=1,3,5}^{\infty}\frac{1}{n^5}\tanh\left(\frac{n\pi w}{2h}\right)\right)\right]^{-1} \quad \textbf{(3.1)}$$

This equation can be simplified as Equation (3.2) when $h < w$,

$$R_h \approx \frac{12\mu L}{wh^3(1-0.63h/w)} = \frac{P}{Q} \quad \textbf{(3.2)}$$

where *w*, *h* and *L* are the width, height and length of the channel, respectively. μ is the viscosity of the fluid flowing in the channel, *P* applied pressure and *Q* measured flow rate.

The tubing (*D*=1mm) and flow sensor capillary (*D*=480μm) have much larger diameter than the microchannel, thus the hydrodynamic resistance caused by the connectors can be neglected. Since the hydrodynamic resistance is inversely proportional to h^3, the estimation is very sensitive to the measured parameters (*P*, *Q*) and hence it is an effective way of measuring the channel height. Before performing experiments, silicone oil was pumped into a microfluidic chip and sufficiently swelled the PDMS channel for at least 40min. After that, three different pressures in a large range (for example, 400mbar, 700mbar, and 1000mbar) were applied at the inlet of the microchannel, and three flow rates were obtained accordingly. A Matlab program was written to calculate the channel height based on Equation (3.2). Three values of the channel height were calculated under three pressure conditions with fluctuation less than 1%. Figure 3.4 shows a schematic of the flow focusing junction and the equivalent hydrodynamic circuit.

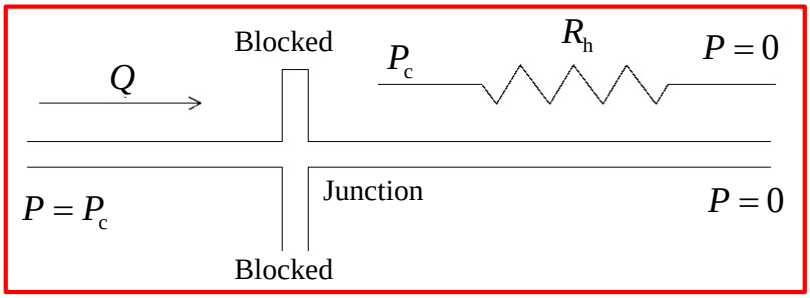

Figure 3.4 Sketch of flow focusing equivalent hydrodynamic resistance measurements for calculating the junction height. The continuous phase is blocked and silicone is pumped from the inlet of disperse phase to the outlet of main channel. Pressure is controlled by the Fluigent system, and flow rate is measure by the flow sensor.

Before starting each droplet experiment, channel dimension measurements are performed after the channel is sufficiently swollen. The junction is captured by the camera and the width can be measured by software ImageJ. A calibrated scale is used to convert the number of pixels into distance on the image. The length of channel can be calculated from the photo mask design. After that three different levels of pressures are applied to the channel and flow rates are recorded. Substituting these parameters into Equation (3.2), the height of channel is calculated.

Chapter 4
Model of Droplet Generation in Flow Focusing Devices Operating in the Squeezing Regime

Flow focusing generators have been widely used to generate droplets for many applications which call for accurate physical models that describe the droplet formation process in such configurations for design and operation purposes. Most existing models are empirical correlations obtained based on extensive experimental results and thus very sensitive to their own data sets. A comprehensive model that involves less parameter fitting by incorporating more theoretical arguments and thus has an improved applicability is urgently needed to guide the design and operation of flow focusing generators. This chapter presents a 3D physical model describing the droplet formation process in microfluidic flow focusing generators that operate in the squeezing regime where droplet size is usually larger than the channel width. This model incorporates an accurate geometric description of the 3D droplet shape during the formation process, an estimation of the time period for the formation cycle based on the conservation of mass and a semi-analytical model predicting the pressure drop over the 3D corner gutter between the droplet curvature and channel walls, which allow an accurate determination of the droplet size, spacing and formation frequency. The model considers the influences of channel geometry (height to width ratio), viscosity contrast, flow rate ratio and capillary number with a wide variety. This model is validated by comparing predictions from the model with experimental results obtained through high speed imaging.

4.1 Introduction and Project Objectives

Droplet-based microfluidics has drawn ever-increasing attention in many different fields requiring high-throughput combinatorial analysis and material synthesis. One of the key requirements is the production of monodispersed droplets for quantitative analysis as reviewed in Chapter 2. There are two commonly used droplet generator designs, namely, T-junction and flow focusing configurations. There have been many experimental and modelling studies reported to understand the droplet formation process in both generator designs. Some excellent physical models which are very useful for design optimization and operational control purposes have been reported to describe the droplet formation process in T-junctions [36, 85, 104, 114]. However there are few reported for the flow focusing configuration although a few excellent empirical correlations are available in literature [128, 129].

The operating regimes of droplet formation in the flow focusing geometry are normally divided into four categories: threading, jetting, squeezing and dripping [128, 129]. Droplet generation process in flow focusing geometries is different from that observed in T-junctions [130]. Therefore, the models developed for the T-junctions cannot be directly applied to flow focusing generators which calls for new models to describe the droplet formation process in these generators. Flow focusing generators often involve the use of orifices as an additional tool to control droplet size. In general, small droplets (compared to the channel width) can be formed easily with an orifice in the downstream of the junction, while slugs are formed without an orifice [10, 124, 129]. In many biological analyses, larger droplets are desired for mixing multiple reagents [314]. Therefore, this study focuses on developing a physical model describing the droplet formation process in flow focusing generators without orifices.

Most existing models for predicting droplet size in flow focusing geometries are empirical correlations obtained from extensive experimental results or numerical simulations [128, 129, 132–134, 136–142, 370–372]. For example, Cubaud *et al.* [129] presented several empirical laws to qualitatively describe the physical mechanisms in different operating regimes. They found that the droplet formation strongly depends on the capillary number of each phase, Ca_{d} and Ca_{c} (the subscript *d* and *c* designate the dispersed phase and continuous phase, respectively), and the droplet size is characterized by a dimensionless parameter, αCa_{c} in the dripping regime. Lee *et al.* [128] performed theoretical and experimental studies on droplet formation in planar flow focusing geometries. They defined a new capillary number which contains all of the geometric dimensions of the flow focusing generator except the width of the downstream channel in order to standardize experimental designs. They concluded that droplet formation can be divided into two processes: upstream process (squeezing, dripping regimes) and downstream process (jetting, tip-streaming) of the orifice. In the upstream process, the droplet size is a power function of the newly defined capillary number ($d / D_{\mathrm{h}} \propto Ca^{-1/3}$ where *d* is the droplet length and D_{h} hydraulic diameter). However, these scaling laws did not consider the 3D curvature of the droplet shape which greatly influences the accuracy of the predicted droplet volume as proved in the T-junction cases [85, 103] . Therefore, a comprehensive model that can capture the droplet volume, frequency and spacing during the droplet formation process must be developed with minimal curve fitting processes. In this study, we minimize curve fitting by incorporating an accurate description of the 3D droplet shape, a force balance model to predict the pressure drop across the droplet during the formation process, and systematic studies of

the effects of the controlling parameters on droplet formation so that it can be adopted by future studies.

Most droplet generators work in the squeezing and transition regimes where highly monodispersed droplets are produced. This study focuses on developing a model to study the mechanism of droplet generation in the squeezing regime in flow focusing devices without orifices. In this regime, the dispersed phase penetrates into the downstream channel, blocking the perpendicular flows of the continuous phase. The pressure in the continuous phase arising due to the blockage squeezes the dispersed phase and eventually pinches off a droplet [373]. The length of droplet is usually larger than the channel width. In this regime, droplet generation depends on the channel geometry (height to width ratio), capillary number ($Ca = \mu u / \gamma$), flow rate ratio ($\varphi = Q_d / Q_c$) and viscosity contrast ($\eta = \mu_d / \mu_c$) of the two phases. To make the developed model widely applicable, experiments were systematically designed and carefully executed with variation in these four impact parameters as listed in Table 4.1. We tracked several parameters during droplet formation, from which a physical model was developed to describe the generator output including droplet volume, frequency and spacing.

Table 4.1 Experimental conditions.

Exp #	Disp. Ph.	Cont. Ph.	h (µm)	w (µm)	Visco. ratio η (mPa.s)	γ (mN/m)
1	Glyc/Water 10% wt	silicone oil	40	100	1.37/9.96	37.1
2	Glyc/Water 60% wt	silicone oil	40	100	9.93/9.96	34.8
3	Glyc/Water 80% wt	silicone oil	40	100	44.1/9.96	33.8
4	Glyc/Water 10% wt	silicone oil	53	100	1.37/9.96	37.1
5	Glyc/Water 60% wt	silicone oil	53	100	9.93/9.96	34.8
6	Glyc/Water 80% wt	silicone oil	53	100	44.1/9.96	33.8
7	Glyc/Water 10% wt	silicone oil	60	100	1.37/9.96	37.1
8	Glyc/Water 60% wt	silicone oil	60	100	9.93/9.96	34.8
9	Glyc/Water 80% wt	silicone oil	60	100	44.1/9.96	33.8

4.2 Experiments

4.2.1 Materials

The microchannels were fabricated using polydimethylsiloxane (PDMS) via standard soft-lithography techniques. Detailed fabrication procedures can be found in Section 3.2. For all the experiments, the continuous phase was low-viscosity silicone oil (DC200, Sigma Aldrich, 10 cSt). A series of glycerol/water mixtures (10%, 60% and 80% in wt %) were used as the dispersed phase to ensure a wide range of viscosity ratios (0.14 ~ 4.4) between the two phases while maintaining a relatively constant interfacial tension (34~37 mN/m). Viscosity was measured at room temperature (22 °C) using a programmable rheometer (LVDV-III Ultra CPE, Brookfield Instruments) with a cone-plate spindle (CPE-40). Interfacial tension between the fluid pairs was measured using a Wilhemy plate tensiometer (Data Physics, DCAT 11). No surfactant was added to either of the phases to avoid the influence of mass transfer effects on the interfacial tension. Therefore, the following model is only valid for droplet generation with a uniform interfacial tension.

Dispersed phase to continuous phase flow rate ratio φ was varied from 0.15 to 1 to ensure that the flow is in the squeezing regime. The resulting capillary number of the continuous phase Ca ranged from 0.001 to 0.006 (Ca represents the capillary number of the continuous phase in the following sections unless clarified). The cross-sectional shape of the microchannels was rectangular and the channel depth for each chip was assumed to be uniform. Since silicone oil swells PDMS, the actual dimensions of the microchannels were smaller than the nominal dimensions and therefore were experimentally measured after PDMS channels were sufficiently swollen by using the method provided in Section 3.4. The global microfluidic channel network was designed in compliance with the suggestions outlined by Glawdel *et al.* [367] to minimize fluctuations in the output of the generator operating with pressure driven flow control. Detailed actual channel dimensions are provided in Table 4.2.

Table 4.2 Measured channel dimensions after sufficiently swelling for each specific experiment.

Exp #	Channel Type	Nominal *w* (µm)	Nominal *h* (µm)	Disp. Ph.	Cont. Ph.	Actual *w*(µm)	Actual *h* (µm)	Length (µm)
1	Type1	100	40	10% Glyc	Silicone oil	89 ± 1	35.0	38500
2	Type1	100	40	10% Glyc	Silicone oil	89 ± 1	35.5	38500
3	Type1	100	40	60% Glyc	Silicone oil	89 ± 1	35.5	38500
4	Type1	100	40	60% Glyc	Silicone oil	88 ± 1	35.2	38500
5	Type1	100	40	80% Glyc	Silicone oil	89 ± 1	35.8	38500
6	Type1	100	40	80% Glyc	Silicone oil	89 ± 1	36.8	38500
7	Type2	100	53	10% Glyc	Silicone oil	83 ± 1	46.8	38500
8	Type2	100	53	10% Glyc	Silicone oil	83 ± 1	49.4	38500
9	Type2	100	53	60% Glyc	Silicone oil	83 ± 1	49.1	38500
10	Type2	100	53	60% Glyc	Silicone oil	83 ± 1	49.2	38500
11	Type2	100	53	80% Glyc	Silicone oil	84 ± 1	48.4	38500
12	Type2	100	53	80% Glyc	Silicone oil	83 ± 1	47.7	38500
13	Type3	100	60	10% Glyc	Silicone oil	79 ± 1	54.1	38500
14	Type3	100	60	10% Glyc	Silicone oil	80 ± 1	53.5	38500
15	Type3	100	60	60% Glyc	Silicone oil	80 ± 1	53.6	38500
16	Type3	100	60	60% Glyc	Silicone oil	80 ± 1	53.3	38500
17	Type3	100	60	80% Glyc	Silicone oil	80 ± 1	52.7	38500
18	Type3	100	60	80% Glyc	Silicone oil	80 ± 1	53.7	38500

4.2.2 Chip Design

The channel layout is illustrated in Figure 4.1 which was proposed based on the design criteria reported by Glawdel *et al*. [367]. That study showed that the global network design influences the

performance of droplet generator and reported a set of design criteria to minimize the fluctuation of droplet production. In particular, the widths of the dispersed and continuous phase branches were set to be the same ($w = w_c = w_d = 100\mu m$) at the junction to reduce the fluctuation in the flow rates. The width of the continuous phase channel (400 μm) was set to be much larger than that of the dispersed phase channel (100 μm) at the inlet to satisfy the rule that the hydrodynamic resistance of the dispersed phase channel should be much higher than that of the continuous phase and should be close to the main channel branch. The length of the main channel was set to be 2.5cm. If it is too short, the number of droplets in it will be too small which will lead to large fluctuations when one droplet enters or exits the main channel. If it is too long, the hydrodynamic resistance will be too large and the pressure control system cannot provide enough pressure to drive the flow. The length of the dispersed phase channel was set to be 1.3cm due to the spacing limit. Different diameters of tubing were used to match the hydrodynamic resistance balance of the different fluids. For low viscosity fluids (10% glyc/water wt), small tubing was connected to the inlet. For high viscosity fluids (80% glyc/water wt), a relative large size of tubing was used.

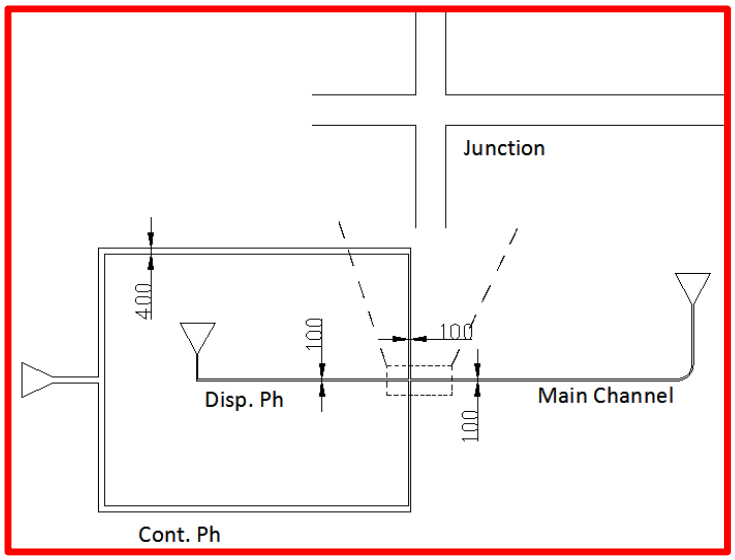

Figure 4.1 Sketch of global network design, the widths of the dispersed phase and continuous phase are the same at the flow focusing junction.

4.2.3 Experimental Procedure

During experiments, each chip was mounted on the microscope stage. Constant pressure flow was used to manipulate the fluid flow using the Fluigent pressure system, and a high speed CMOS camera

(Phantom v210, Vision Research) was used to capture the droplet formation process with a frame rate of 8000 fps. Details of the experimental setup can be found in Chapter 3. Considering the small capillary number in the squeezing regime and the flow sensor restriction as described before, the maximum flow rate was restricted to 5µl/min and minimum was 0.5µl/min in order to get accurate readings. The maximum/minimum applied pressure can be estimated by the hydrodynamic resistance of the channels and the required flow rates, but the maximum value was set to be 1050mBar limited by the Fluigent system. The minimum flow rate applied to the continuous phase should be larger than that of the dispersed phase in order to form monodispersed droplets. For each experiment, the estimated pressure conditions for the continuous phase, P_c, were divided into 3-4 levels depending on the estimated pressure range which attempted to span the capillary number as large as possible (for study the influence of *Ca* on droplet formation). At each P_c level, a series of P_d were applied to create different flow rate ratios. After each P_d level, the flow rate of the dispersed phase was carefully checked using Labview to ensure it was in the applicable range. Usually 4-8 levels of P_d were applied at each P_c level. An example of a set of experimental conditions for Exp #1 is listed in Table 4.3.

Table 4.3 Pressure conditions applied in Exp # 1 for silicone oil and 10%glyc/water with no surfactant on a type 1 chip.

Step #	**1**	**2**	**3**	**4**	**5**	**6**	**7**	**8**	**9**	**10**
P_c **(mbar)**	1000	1000	1000	1000	1000	1000	1000	800	800	800
P_d **(mbar)**	910	900	880	860	840	820	800	750	730	710
Step #	**11**	**12**	**13**	**14**	**15**	**16**	**17**	**18**	**19**	**20**
P_c **(mbar)**	800	800	800	800	800	600	600	600	600	600
P_d **(mbar)**	700	680	660	640	610	540	520	500	480	460

A brief overview of the experimental procedure is listed below:

- Before starting the experiment, several chips with a specific height were fabricated and prepared.
- Clean reservoirs, tubing and flow sensors for the first time use or switching to a new type of oil.
- Flow sensors are calibrated for each fluid following the procedure. Then they are mounted on a piece of polycarbonate and labeled for specific fluid.

- Connect the chip with the pressure system and pump silicone oil through the chip for at least 40 minutes so that the chip is sufficiently swelled. The chip is then checked carefully for any debris which might block the channels.
- If the chip is in good condition, the channel width and height are then measured (after swelling).
- Apply pressures to the two phases and waited for several minutes until stable droplets are generated.
- Record the pressures and flow rates for both phases shown in the Labview program.
- Analyze the videos and extract experimental data

Each experiment was repeated at least twice.

4.2.4 Experimental Data

Droplet volume, spacing and formation frequency as metrics were used to describe the output of the droplet generator. Droplet formation is considered a quasi-steady state process where the flow rates are constant. Hence, the volume of each droplet is calculated as,

$$V_{\mathrm{d}} = \frac{Q_{\mathrm{d}}}{f} \tag{4.1}$$

where f is the frequency of droplet generation which can be calculated by counting the number of droplets and frames captured during one droplet generation cycle.

$$f = N_{\mathrm{drop}} \frac{F}{N_{\mathrm{frame}}} \tag{4.2}$$

where N_{drop} is the number of the captured droplets, N_{frame} the total number of frames, and F the frame rate. The spacing, s, is calculated by,

$$s^* = \frac{1+\varphi}{f^*} \tag{4.3}$$

where the dimensionless forms for volume, frequency and spacing are defined as,

$$V_{\mathrm{d}}^* = \frac{V_{\mathrm{d}}}{w^2 h},\ f^* = f \cdot \frac{w^2 h}{Q_{\mathrm{c}}},\ s^* = \frac{s}{w}$$

By substituting the measured w, h, Q_d, Q_c, N_{drop} and N_{frame} into Equations (4.1) ~ (4.3), one can obtain the dimensionless droplet volume, frequency and spacing for each experiment.

In order to verify that the droplet generation is a quasi-steady state process where the flow rates of both the dispersed and continuous phases are constants, the droplet speed over a droplet formation cycle was tracked. Figure 4.2 shows one example of droplet speed over a droplet formation cycle. Results show that the droplet speed is almost constant within variation less than 2%, which indicates that the droplet formation process is under quasi-steady state.

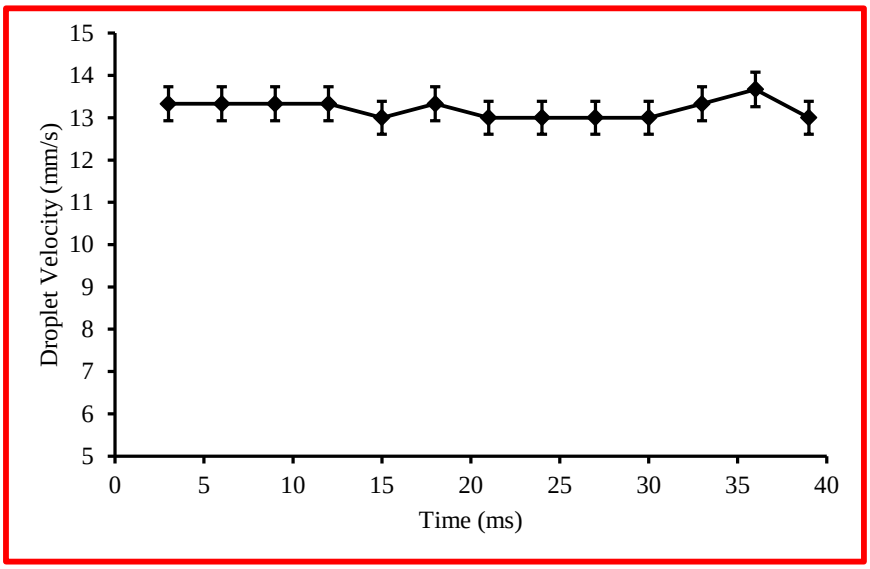

Figure 4.2 Droplet speed over a formation cycle for the case where the dispersed phase is glyc/water 60% wt, height/width ratio $h^* = 0.58$, $Q_d = 1.69$μl/min , and $Q_c = 3.59$μl/min .

Figure 4.3 illustrates the parameters used to describe the droplet formation process. The cycle consists of three stages. First, a filling stage (I), where the dispersed phase is injected into the main channel. The interface continues to grow while the continuous phase bypasses the droplet filling the space between the previously formed droplet and the new droplet. Eventually the growing interface blocks the flow from the side channels causing the upstream pressure to increase until it reaches a critical value where the continuous phase begins to squeeze the interface and the necking stage begins [130] (II). During the necking stage, the dispersed phase is still being injected into the droplet at a constant flow rate while the neck collapses. Once the neck reaches a critical size, the collapse accelerates triggering the pinch-off stage (III) which culminates with the droplet detaching. The newly formed droplet is pushed downstream and the cycle restarts. The pinch-off time is small and

negligible as compared to the first two stages, which was also experimentally verified by van Hoeve *et al.*[374]. Hence, the formation period, T, consists of the filling period, $\Delta t_{\text{filling}}$ and the necking period, $\Delta t_{\text{necking}}$ expressed as,

$$T = \Delta t_{\text{filling}} + \Delta t_{\text{necking}} \tag{4.4}$$

The detailed definitions for the filling and necking period are provided in section 4.3.

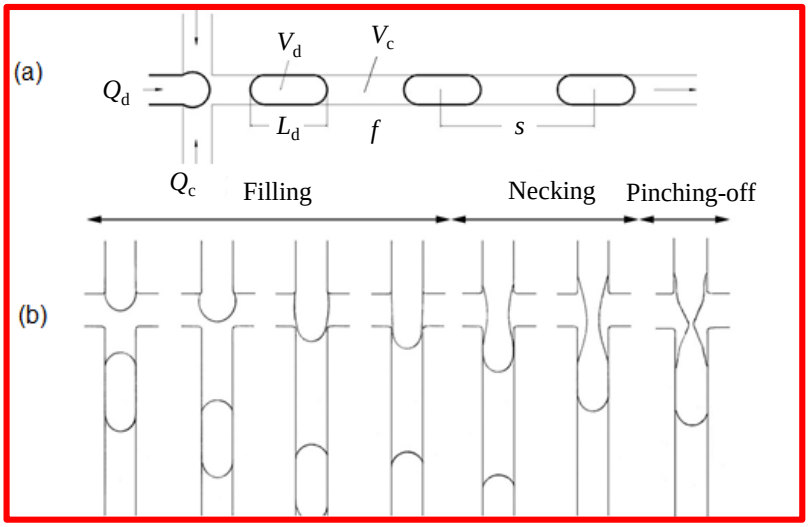

Figure 4.3 (a) Video captured from Exp #4 listed in Table 4.1. The flow rates of the continuous and dispersed phases are $Q_c = 3.74\mu\text{l/min}$ and $Q_d = 2.87\mu\text{l/min}$, respectively. V_d is the droplet volume, V_c the oil volume between two adjacent droplets, L_d the droplet length, f the frequency of droplet generation and s the spacing between two adjacent droplets. (b) Droplet generation cycle in the flow focusing generator with three stages: (i) filling stage (ii) necking stage, and (iii) pinch-off stage. The figures are not captured with the same Δt.

4.3 Theoretical Model

The approach to modelling the droplet generation cycle is to decompose the model into two sections (filling stage and necking stage) and estimate the time of each section, separately, as summarized in Equation (4.4). This estimation is based on the conservation of mass for the dispersed and continuous phases. As part of this modelling, equations were derived to describe the evolution of the droplet shape from one stage to the next which involves force balances on the interface.

4.3.1 Assumption of 3D Shape of Droplets

Van Steijn *et al*. [104] found that droplet shape is 3D curved, and using droplet length to represent droplet size is not accurate. The 3D droplet shape was also examined using a μPIV system by Kinoshita *et al.* [261]. The assumption of 3D droplet shape is based on their study. Figure 4.4 shows the 3D droplet shape and the transitions between each stage. The formed droplet is confined by the channel walls and the edges of the droplet are curved due to interfacial tension. In this study, the method developed by van Steijn *et al*. [104] was adopted to calculate the curved volume. By assuming that the radius of the droplet curvature is half of the channel depth ($h/2$), which is an accurate assumption for well controlled wetting conditions, this method calculates the volume by multiplying the 2D top-view area of the curved object with the height and then subtracting the volume of the continuous phase in-between the surfaces: top and bottom walls, interface perpendicular to the top/bottom walls around the perimeter of the curved object and curved surface along the perimeter,

$$V = hA - \frac{h^2}{2}(1-\frac{\pi}{4})l \qquad \textbf{(4.5)}$$

where V is the volume of the curved object, h the height, A the 2D top-view area, and l the 2D top-view perimeter of the curved object.

It is clear that the assumption of "radius of the droplet curvature is half of the channel depth" is not accurate under some conditions, especially when the contact angle is less than 135°. The assumed configuration of the droplet cross-section is shown in Figure 4.5(a) as compared to the actual configuration in Figure 4.5(b). To estimate the error, let us consider an extreme condition that the droplet fully touches the wall. Under this condition, the cross-section area of droplet is $A_{\max} = wh$. Under the assumption of "radius of the droplet curvature is half of the channel depth", the cross-section area of droplet is $A = \pi\left(\frac{h}{2}\right)^2 + h(w-h) = wh - \left(1-\frac{\pi}{4}\right)h^2$. If configuration Figure 4.5 (b) occurs, the droplet size should be between $A \times L_{\text{drop}}$ and $A_{\max} \times L_{\text{drop}}$. Therefore, the maximum error can be estimated as:

$$1 - \frac{A}{A_{\max}} = 1 - \frac{wh - \left(1-\frac{\pi}{4}\right)h^2}{wh} = \left(1-\frac{\pi}{4}\right)h^*$$

where h^* is the height to width ratio. For $h^* = 0.5$, the maximum error would be around 10.7%. However, the error cannot be that high under well controlled wetting conditions, since there always exist gutters surrounding the droplet. The actual error is expected to be less and is estimated to be around 2-5%.

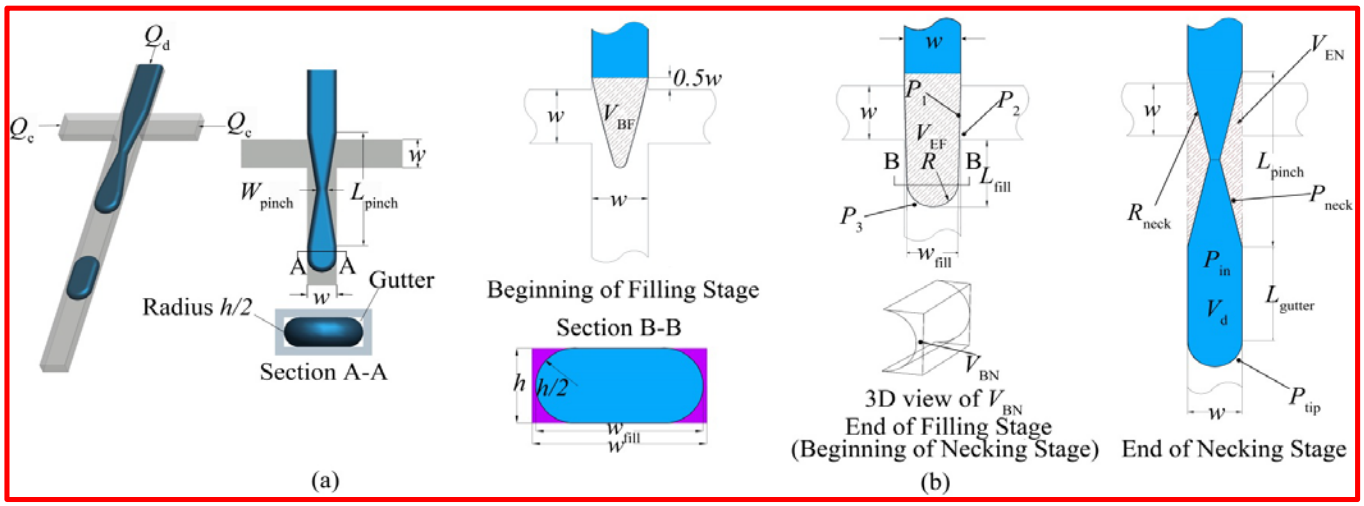

Figure 4.4 (a) The estimated 3D shape of droplet. The out of plane curvature is approximated as $h/2$. (b) The 2D shapes of droplet at the transitions between each stage, where V_{BF} and V_{EF} represent the droplet volume at the beginning and end of the filling stage, respectively, V_{BN} and V_{EN} the volume of the continuous phase in the V-shape at the beginning and end of the necking stage, and V_{gutter} the volume of the continuous phase bypassing the gutter during the necking stage.

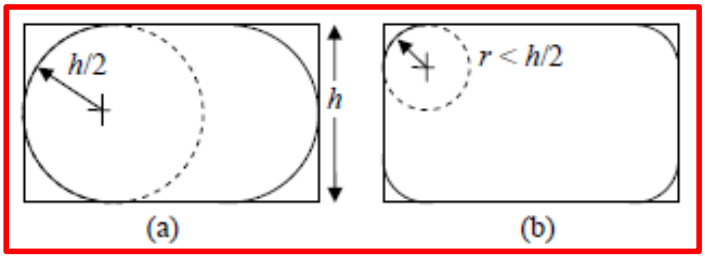

Figure 4.5 (a) Assumed configuration of the droplet cross-section; (b) Actual configuration of the droplet cross-section

In order to determine the droplet generation cycle, we must define the filling and necking period properly. In this study, $\Delta t_{filling}$ is defined from the beginning of droplet formation to the end of the filling stage, and $\Delta t_{necking}$ from the end of the filling stage to the end of the necking stage. We identify

the end of the filling stage when the edge of the interface along the dispersed channel turns into a straight line, as shown in Figure 4.4(b). During the necking period, the width of the neck decreases linearly until it reaches the pinch-off stage. To estimate the time of the filling stage and necking stage, four parameters, $W_{\text{fill}}, L_{\text{fill}}, W_{\text{pinch}}, L_{\text{pinch}}$ are introduced as marked in Figure 4.4. L_{fill} is the droplet length that penetrates into the main channel at the end of the filling stage, W_{fill} the width of the tip, L_{pinch} the distance between the two points of the V-shape at the end of the necking stage, and W_{pinch} the width of the neck at the end of the necking stage. Accurate determination of these four parameters is a key to the accuracy of the model, which will be elaborated below. Dimensionless parameters are defined as follows, which will be used in the following sections.

$$L_{\text{fill}}^* = \frac{L_{\text{fill}}}{w},\ W_{\text{fill}}^* = \frac{W_{\text{fill}}}{w},\ L_{\text{pinch}}^* = \frac{L_{\text{pinch}}}{w},\ W_{\text{pinch}}^* = \frac{W_{\text{pinch}}}{w},\ h^* = \frac{h}{w},\ T^* = T\frac{Q_{\text{c}}}{w^2 h},\ \varphi = \frac{Q_{\text{d}}}{Q_{\text{c}}}$$

$$V_{\text{BF}}^* = \frac{V_{\text{BF}}}{w^2 h},\ V_{\text{EF}}^* = \frac{V_{\text{EF}}}{w^2 h},\ V_{\text{BN}}^* = \frac{V_{\text{BN}}}{w^2 h},\ V_{\text{EN}}^* = \frac{V_{\text{EN}}}{w^2 h},\ V_{\text{gutter}}^* = \frac{V_{\text{gutter}}}{w^2 h}$$

4.3.2 Filling Stage

As shown in Figure 4.4 (b), the filling time, $\Delta t_{\text{filling}}$ can be expressed as the time it takes for the interface to change shape from the beginning (V_{BF}) to the end (V_{EF}) of the filling stage:

$$\Delta t_{\text{filling}} = \frac{V_{\text{EF}} - V_{\text{BF}}}{Q_{\text{d}}} \tag{4.6}$$

Then, V_{BF}^* and V_{EF}^* can be estimated based on Equation (4.5) and the description in Figure 4.4(b). First, calculate V_{BF}^*: as shown in Figure 4.6, the first step is to calculate the volume of V_{BF}^* without considering the curvature of the interface:

$$V_{\text{BF\_1}} = A_1 \times h \tag{4.7}$$

where A_1 is estimated as a triangle. The experimental results show that the V-shape at the end of the necking stage is almost symmetric which allows the length of V_{BF}^* and V_{EF}^* to be estimated as $L_{\text{pinch}}^*/2$ and $L_{\text{fill}}^* + 1.5$, respectively.

Hence, A_1 can be expressed as,

$$A_1 = \frac{1}{2} \times w \times \frac{L_{\text{pinch}}}{2} = \frac{wL_{\text{pinch}}}{4} \tag{4.8}$$

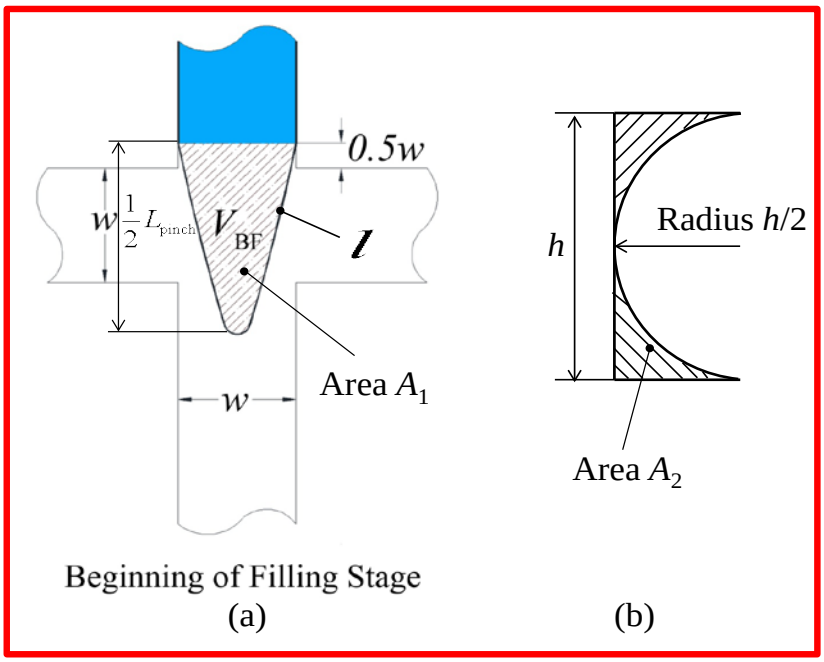

Figure 4.6 (a) 2D top-view area A_1 of V_{BF}^* at the beginning of filling stage. (b) Cross-section area of the curved interface A_2

The second step is to calculate the volume of the continuous phase in-between the curved interface. The cross-section area of the curved interface A_2 can be expressed as,

$$A_2 = \frac{h}{2} \times h - \frac{1}{2}\pi\left(\frac{h}{2}\right)^2 = \left(1 - \frac{\pi}{4}\right)\frac{h^2}{2} \tag{4.9}$$

The perimeter of the curved interface V_{BF}^* can be calculated as,

$$l_{\text{BF}} = 2 \times \sqrt{\left(\frac{w}{2}\right)^2 + \left(\frac{L_{\text{pinch}}}{2}\right)^2} = \sqrt{w^2 + L_{\text{pinch}}^2} \tag{4.10}$$

Therefore, the volume of the continuous phase in-between the curved interface V_{BF}^* is,

$$V_{\text{BF\_2}} = A_2 \times l_{\text{BF}} = \left(1 - \frac{\pi}{4}\right)\frac{h^2}{2}\sqrt{w^2 + L_{\text{pinch}}^2} \tag{4.11}$$

Hence, the volume of the forming droplet at the beginning of filling stage can be expressed as,

$$V_{\mathrm{BF}} = V_{\mathrm{BF\_1}} - V_{\mathrm{BF\_2}} = \frac{L_{\mathrm{pinch}}}{4} wh - \left(1 - \frac{\pi}{4}\right)\frac{h^2}{2}\sqrt{w^2 + L_{\mathrm{pinch}}^2} \tag{4.12}$$

The dimensionless form is,

$$V_{\mathrm{BF}}^* = \frac{V_{\mathrm{BF}}}{w^2 h} = \frac{L_{\mathrm{pinch}}^*}{4} - \frac{h^*}{2}\left(1 - \frac{\pi}{4}\right)\sqrt{1 + \left(L_{\mathrm{pinch}}^*\right)^2} \tag{4.13}$$

Second, V_{EF}^* can be obtained by using the same method. As shown in Figure 4.7 (a), the 2D top-view area of forming droplet at the end of the filling stage A_{EF} can be calculated as,

$$A_{\mathrm{EF}} = \frac{1}{2}\pi\left(\frac{w_{\mathrm{fill}}}{2}\right)^2 + \frac{1}{2}\left(L_{\mathrm{fill}} - \frac{w_{\mathrm{fill}}}{2} + 1.5w\right)\left(w + w_{\mathrm{fill}}\right) \tag{4.14}$$

The perimeter of the curved interface can be calculated as,

$$l_{\mathrm{EF}} = \frac{\pi w_{\mathrm{fill}}}{2} + 2\sqrt{\left(\frac{w - w_{\mathrm{fill}}}{2}\right)^2 + (L_{\mathrm{fill}} - \frac{w_{\mathrm{fill}}}{2} + 1.5w)^2} \tag{4.15}$$

Therefore,

$$\begin{aligned} V_{\mathrm{EF}} &= \frac{1}{2}\pi\left(\frac{w_{\mathrm{fill}}}{2}\right)^2 h + \frac{1}{2}\left(L_{\mathrm{fill}} - \frac{w_{\mathrm{fill}}}{2} + 1.5w\right)\left(w + w_{\mathrm{fill}}\right)h \\ &- \frac{h^2}{2}(1 - \frac{\pi}{4})(\frac{\pi w_{\mathrm{fill}}}{2} + 2\sqrt{\left(\frac{w - w_{\mathrm{fill}}}{2}\right)^2 + (L_{\mathrm{fill}} - \frac{w_{\mathrm{fill}}}{2} + 1.5w)^2}) \end{aligned} \tag{4.16}$$

Dimensionless form,

$$\begin{aligned} V_{\mathrm{EF}}^* &= \frac{V_{\mathrm{EF}}}{w^2 h} = \frac{1}{2}\left[\pi\left(\frac{W_{\mathrm{fill}}^*}{2}\right)^2 + \left(L_{\mathrm{fill}}^* - \frac{W_{\mathrm{fill}}^*}{2} + 1.5\right)(1 + W_{\mathrm{fill}}^*)\right] \\ &- \frac{h^*}{2}\left(1 - \frac{\pi}{4}\right)\left(\frac{\pi}{2}W_{\mathrm{fill}}^* + 2\sqrt{\left(\frac{1 - W_{\mathrm{fill}}^*}{2}\right)^2 + \left(L_{\mathrm{fill}}^* - \frac{W_{\mathrm{fill}}^*}{2} + 1.5\right)^2}\right) \end{aligned} \tag{4.17}$$

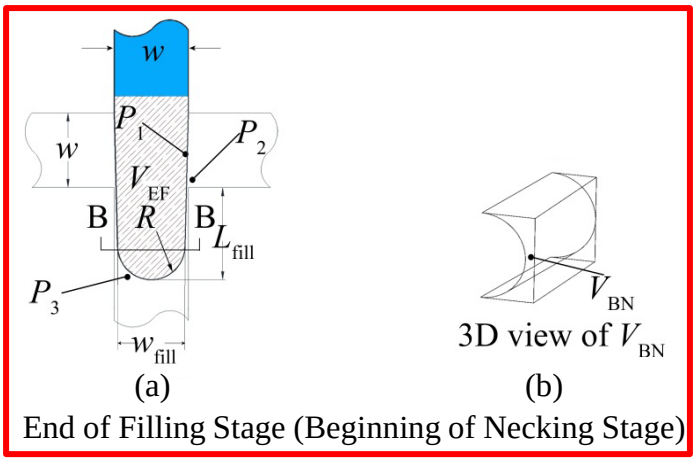

Figure 4.7 (a) 2D top-view area of V_{EF}^{*} and (b) 3D view of V_{BN}^{*} at the end of filling stage (also called "at the beginning of necking stage")

4.3.3 Necking Stage

During the necking stage, the majority of the continuous phase flows into the V-shape squeezing the droplet while the rest bypasses the droplet through the corner gutter. Therefore, one can obtain the necking time by,

$$V_{EN} - V_{BN} + V_{gutter} = Q_c \Delta t_{necking} \tag{4.18}$$

where $V_{EN} - V_{BN}$ represents the volume of the continuous phase that actually squeezes the droplet neck and V_{gutter} represents the continuous phase bypassing the droplet through the gutter. During the necking stage, the droplet length is larger than the channel width with most of its interface almost touching the channel walls as shown in Figure 4.8.

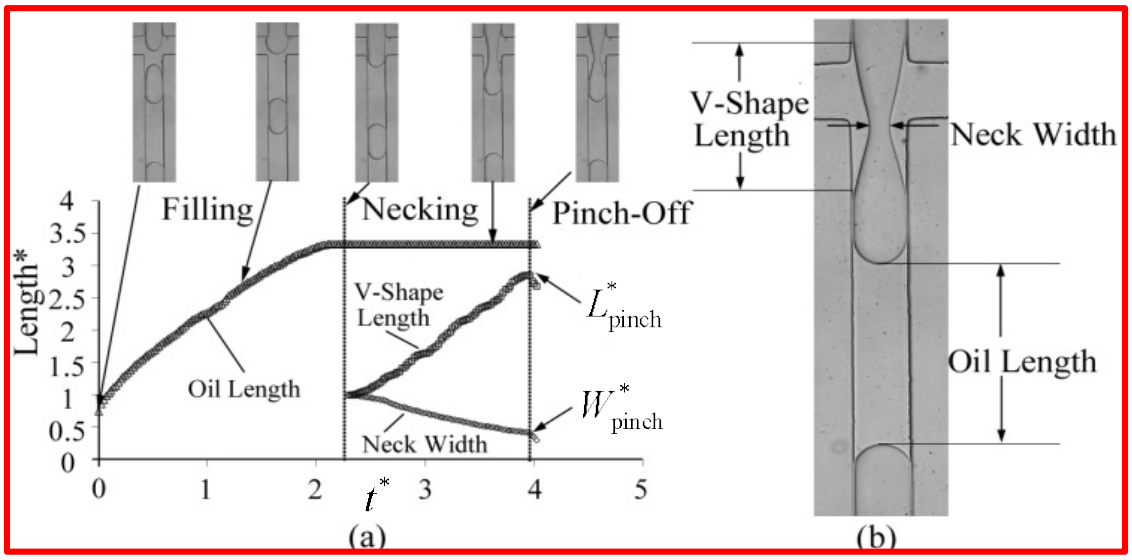

Figure 4.8 (a) Variations of the V-shape length, neck width and oil length during a droplet formation cycle for the case where the dispersed phase is glyc/water 60% wt, height/width ratio $h^* = 0.58$, $Q_d = 1.69\mu l/min$, and $Q_c = 3.59\mu l/min$. (b) Image of the V-shape length, neck width and oil length.

The slip factor, which describes the difference between the droplet velocity and the average velocity of the continuous phase, is estimated to be unity [309] for such conditions. This is also true in this study. The oil spacing between the previously formed and the newly formed droplet during the necking stage was measured and found that it remains constant as shown in Figure 4.8(a). The constant oil length in the necking stage also implies that the continuous phase does not collapse the neck instead only fills the growing gutter matching the growing droplet. Therefore, V_{gutter} can be estimated as the thin film volume plus the volume of the curved space,

$$V_{gutter} = 2L_{gutter}\left[\frac{1-W_{fill}}{4}h + \frac{h^2}{2}\left(1-\frac{\pi}{4}\right)\right] \quad \textbf{(4.19)}$$

where $(1-W_{fill})/4$ is the average width of the gutter and L_{gutter} represents the length of the gutter at the end of the necking stage as shown in Figure 4.9. Dimensionless form is,

$$V^*_{gutter} = \frac{V_{gutter}}{w^2 h} = 2\left[\frac{1-W^*_{fill}}{4} + \frac{h^*}{2}\left(1-\frac{\pi}{4}\right)\right]L^*_{gutter} \quad \textbf{(4.20)}$$

The volume of droplet V_d can also be estimated via the geometric shape at the end of necking stage.

The 2D top view area of the forming droplet at the end of necking stage can be estimated as a summation of a triangle, a rectangle and a semi-circle (see Figure 4.9), and expressed as,

$$\frac{1}{2}\cdot w\cdot\frac{1}{2}L_{\text{pinch}}+L_{\text{gutter}}\cdot w+\frac{1}{2}\pi\left(\frac{w}{2}\right)^2$$

The perimeter of the droplet at the end of necking stage can be estimated as,

$$2\sqrt{\left(\frac{w}{2}\right)^2+\left(\frac{L_{\text{pinch}}}{2}\right)^2}+2L_{\text{gutter}}+\frac{\pi}{2}w$$

Therefore, the volume of droplet V_d can be estimated as,

$$V_d=\left[\frac{1}{2}\cdot w\cdot\frac{1}{2}L_{\text{pinch}}+L_{\text{gutter}}\cdot w+\frac{1}{2}\pi\left(\frac{w}{2}\right)^2\right]h-\frac{h^2}{2}(1-\frac{\pi}{4})\left[2\sqrt{\left(\frac{w}{2}\right)^2+\left(\frac{L_{\text{pinch}}}{2}\right)^2}+2L_{\text{gutter}}+\frac{\pi}{2}w\right]$$

Dimensionless form,

$$V_d^*=\left(\frac{L_{\text{pinch}}^*}{4}+L_{\text{gutter}}^*+\frac{\pi}{8}\right)-\frac{h^*}{2}\left(1-\frac{\pi}{4}\right)\left(\sqrt{1+\left(L_{\text{pinch}}^*\right)^2}+2L_{\text{gutter}}^*+\frac{\pi}{2}\right) \quad \textbf{(4.21)}$$

By combining Equations (4.20) and (4.21), one can obtain an expression of V_{gutter}^*:

$$V_{\text{gutter}}^*=\frac{\frac{1}{2}\left(1-W_{\text{fill}}^*\right)+\left(1-\frac{\pi}{4}\right)h^*}{1-\left(1-\frac{\pi}{4}\right)h^*}\left[V_d^*-\frac{1}{4}\left(L_{\text{pinch}}^*+\frac{\pi}{2}\right)+\frac{h^*}{2}\left(1-\frac{\pi}{4}\right)\left(\sqrt{1+(L_{\text{pinch}}^*)^2}+\frac{\pi}{2}\right)\right] \quad \textbf{(4.22)}$$

Calculate V_{BN}^*:

The 2D top-view area of the continuous phase at the junction at the beginning of the necking stage A_{BN} (see Figure 4.7(b)) can be estimated as,

$$A_{\text{BN}}=2\times\frac{1}{2}w\frac{w-w_{\text{fill}}}{2}$$

The perimeter of the continuous phase at the junction at the beginning of the necking stage, l_{BN} can be estimated as,

$$l_{BN} = 2 \times \sqrt{\left(\frac{w - w_{fill}}{2}\right)^2 + w^2}$$

Therefore,

$$V_{BN} = 2[h \times \frac{1}{2} w \frac{w - w_{fill}}{2} + \frac{h^2}{2}(1 - \frac{\pi}{4}) \sqrt{\left(\frac{w - w_{fill}}{2}\right)^2 + w^2}] \quad \textbf{(4.23)}$$

Dimensionless form,

$$V_{BN}^* = \frac{1 - W_{fill}^*}{2} + h^* \left(1 - \frac{\pi}{4}\right) \sqrt{\left(\frac{1 - W_{fill}^*}{2}\right)^2 + 1} \quad \textbf{(4.24)}$$

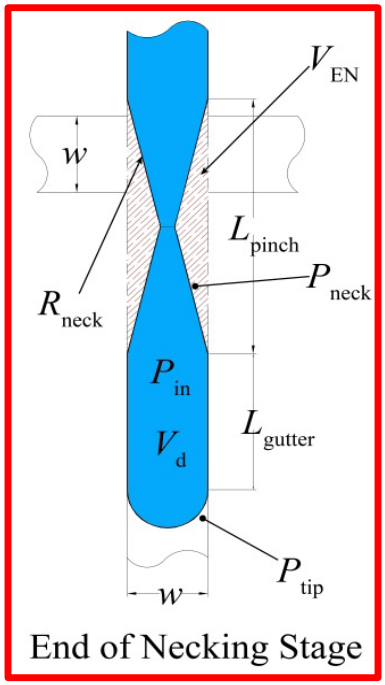

Figure 4.9 2D top-view area of the forming droplet at the end of necking stage.

Calculate V_{EN}^* :

As shown in Figure 4.9, the 2D top-view area of the continuous phase at the junction at the end of the necking stage, A_{EN} can be estimated as,

$$A_{EN} = 2 \times \frac{L_{pinch}}{2} \left(\frac{w - w_{pinch}}{2}\right)$$

The perimeter of the continuous phase at the junction at the end of the necking stage, l_{EN} can be estimated as,

$$l_{\mathrm{EN}} = 4 \times \sqrt{\left(\frac{w - w_{\mathrm{pinch}}}{2}\right)^2 + (\frac{L_{\mathrm{pinch}}}{2})^2}$$

Therefore,

$$V_{\mathrm{EN}} = 2 \times \frac{L_{\mathrm{pinch}}}{2}\left(\frac{w - w_{\mathrm{pinch}}}{2}\right)h + 2 \times h^2(1 - \frac{\pi}{4})\sqrt{\left(\frac{w - w_{\mathrm{pinch}}}{2}\right)^2 + (\frac{L_{\mathrm{pinch}}}{2})^2} \qquad \textbf{(4.25)}$$

Dimensionless form,

$$V_{\mathrm{EN}}^* = L_{\mathrm{pinch}}^* \frac{1 - W_{\mathrm{pinch}}^*}{2} + h^*\left(1 - \frac{\pi}{4}\right)\sqrt{\left(1 - W_{\mathrm{pinch}}^*\right)^2 + \left(L_{\mathrm{pinch}}^*\right)^2} \qquad \textbf{(4.26)}$$

Note that the second part volume on the right hand side of the Equations (4.20), (4.24) and (4.26) are added to the total volume when calculating V_{gutter}^*, V_{BN}^* and V_{EN}^*, because these parameters are related to the continuous phase, which fills the curved gutters.

Combining Equations (4.4), (4.6) and (4.18), the non-dimensional period of droplet generation cycle can be expressed as,

$$T^* = \frac{V_{\mathrm{EF}}^* - V_{\mathrm{BF}}^*}{\varphi} + V_{\mathrm{EN}}^* - V_{\mathrm{BN}}^* + V_{\mathrm{gutter}}^* \qquad \textbf{(4.27)}$$

The volume of droplet,

$$V_{\mathrm{d}}^* = \left(V_{\mathrm{EF}}^* - V_{\mathrm{BF}}^*\right) + \left(V_{\mathrm{EN}}^* - V_{\mathrm{BN}}^* + V_{\mathrm{gutter}}^*\right)\varphi \qquad \textbf{(4.28)}$$

where $\varphi = \frac{Q_{\mathrm{d}}}{Q_{\mathrm{c}}}$ is the flow rate ratio of the dispersed phase to the continuous phase.

Define $\alpha = V_{\mathrm{EF}}^* - V_{\mathrm{BF}}^*$, $\beta = V_{\mathrm{EN}}^* - V_{\mathrm{BN}}^* + V_{\mathrm{gutter}}^*$, then

$$V_{\mathrm{d}}^* = \alpha + \beta\varphi \qquad \textbf{(4.29)}$$

One can thus interpret the physical meaning of α as the volume of the dispersed phase flowing into the droplet during the filling stage, and β as the volume of the continuous phase flowing into the junction (both into the V-shape and droplet gutter) during the necking stage.

The four key parameters describing the droplet generation in a flow focusing generator are L^*_{fill}, W^*_{fill} L^*_{pinch} and W^*_{pinch}. These parameters vary with the geometry (height/width ratio), fluid properties, flow rate ratio and capillary number as discussed in the following sections.

4.3.4 Calculation of Parameter W^*_{fill}

The penetration of the dispersed phase into the main channel is always confined by the channel walls as shown in Figure 4.8. Wong *et al.* [298, 299] mentioned that the thin film thickness is proportional to the capillary number raised to the two-thirds power when $Ca < 0.01$, which means the thin film has a thickness on the order of 1% to 5% of the half channel width. Therefore, it is assumed that the gap between the droplet and channel wall is very thin (i.e. 0.02*w*) leaving W^*_{fill} to be 0.96 based on the rough measurements. Therefore, this model limits itself to the squeezing regime with a capillary number below 0.01.

4.3.5 Calculation of Parameter L^*_{fill}

At the end of the filling stage, the neck shape at the junction becomes a straight line. The majority of the continuous phase fluid starts squeezing the neck and stops bypassing the gutter which is verified by the measured constant oil length between the newly formed droplet and the preceding droplet during formation cycles. The length, L_{fill}, is defined as the droplet length from its tip to the entrance of the junction as illustrated in Figure 4.4(b), which is related to the pressure drop across the emerging droplet, $\Delta P = P_2 - P_3$.

In this work, a semi-analytical model was developed to describe the relationship between the pressure drop and the droplet length L_{fill}. Numerical simulations were performed to analyze the pressure drop through the gutter, which consists of three walls and the fourth being the interface between the dispersed phase and continuous phase. This model is built upon the study presented by Tchikanda *et al.* [375] for the pressure-driven flow in open rectangular channels with three walls and the forth being an arbitrary curved interface (see Figure 4.10(a)) , and its further improvement for droplet applications presented by Glawdel *et al.*[103].

Compared to the study by Tchikanda *et al.* [375], the gutter between the droplet and walls in this work is more complex due to the following two aspects: i) the cross-section of the gutter in our work is not uniform due to the tip shape of the droplet end while Tchikanda *et al.* [375] calculated the pressure drop for a uniform cross-section; and ii) They used a zero-shear boundary condition at the free surface, which is not valid in our study because both the continuous and dispersed phase are viscous liquids. Our model considers these two factors. Tchikanda *et al.* [375] defined a dimensionless average velocity in the gutter occupied by the fluid, $\overline{u}_{\mathrm{g}}^{*}$, and obtained the values by blending known asymptotic solutions for the limits of channel aspect ratios and interface curvature.

$$\overline{u}_{\mathrm{g}}^{*} = \frac{Q}{A}\frac{\mu}{h^2(\Delta P / L)} \tag{4.30}$$

where h is the channel height, A the area of the conduit, μ the fluid viscosity, Q flow rate, and $\Delta P / L$ the pressure gradient. Rearranging Equation (4.30), the pressure drop can be obtained as,

$$\Delta P = \frac{\mu Q}{\overline{u}_{\mathrm{g}}^{*} A h^2} \cdot L \tag{4.31}$$

For the gutter flow in this study, Equation (4.31) will still be employed because of its simplicity and accuracy but with modifications to consider the non-uniform cross-section of the gutter and viscous fluid interface. The modified equation takes the form of,

$$\Delta P = \frac{\mu Q}{\overline{u}_{\mathrm{g}}^{*} A h^2} \cdot L_{\mathrm{eqv}} \cdot g(\eta) \tag{4.32}$$

where L_{eqv} is the equivalent droplet length of the uniform cross-section for the minimum gap that produces the same pressure drop over the actual droplet gutter and $g(\eta)$ accounts for the non-zero shear boundary condition for the viscous droplet interface.

Tchikanda *et al*. [375] provided an expression for the non-dimensional velocity $\overline{u}_{\mathrm{g}}^{*}$ by blending known asymptotic solutions for the limits of channel aspect ratios λ_{gap} which is defined as,

$$\lambda_{\mathrm{gap}} = \frac{h}{w_{\mathrm{gap}}}$$

Figure 4.10(b) shows the relation between the non-dimensional mean velocity $\overline{u}_{\mathrm{g}}^{*}$ and the gap aspect ratio λ_{gap} provided by Tchikanda *et al*. [375]. When the gap aspect ratio is very large, it's limited to a corner flow where the non-dimensional mean velocity is approaching to a constant $\overline{u}_{g}^{*}$=0.0027 . When the gap aspect ratio is small, it's limited to a parallel plate flow and $\overline{u}_{\mathrm{g}}^{*}$ approaching to a limit 1/12. In this study, the gap between the droplet and the channel walls is assumed to be very small (i.e. 2% of the channel width) and thus used $\overline{u}_{g}^{*}=0.0027$.

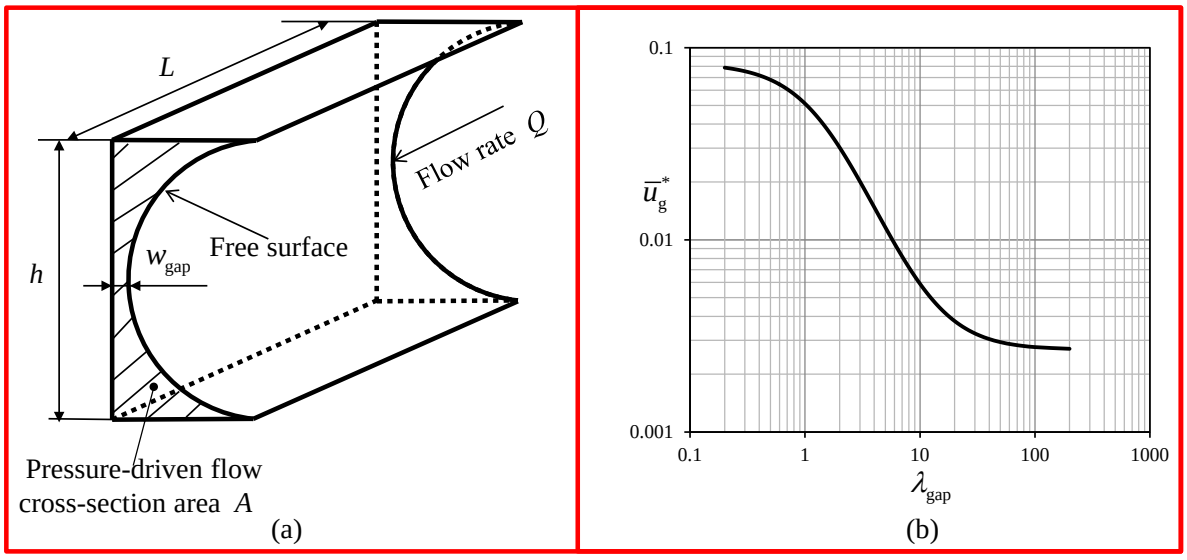

Figure 4.10 (a) Sketch of the open rectangular channel (the gutter)with three walls and the forth being an arbitrary curved interface studied by Tchikanda *et al*. [375]; (b) Non-dimensional mean velocity $\overline{u}_{\mathrm{g}}^{*}$ as a function of the gap aspect ratio $\lambda_{\mathrm{gap}}=\dfrac{h}{w_{\mathrm{gap}}}$ provided by Tchikanda *et al*. [375].

4.3.5.1 Effective Pressure Droplet Penetrating Length

In this subsection, a model was developed to describe the effective pressure drop penetrating length, L_{eqv} . To do so, the pressure drop over the gutter region of the non-uniform cross section must be obtained. Due to the complexity of the 3D gutter flow, the flow field is obtained using the creeping flow module of COMSOL multiphysics 4.2. The simulation domain is shown in Figure 4.11, which is only a quarter of the droplet due to the symmetric geometry.

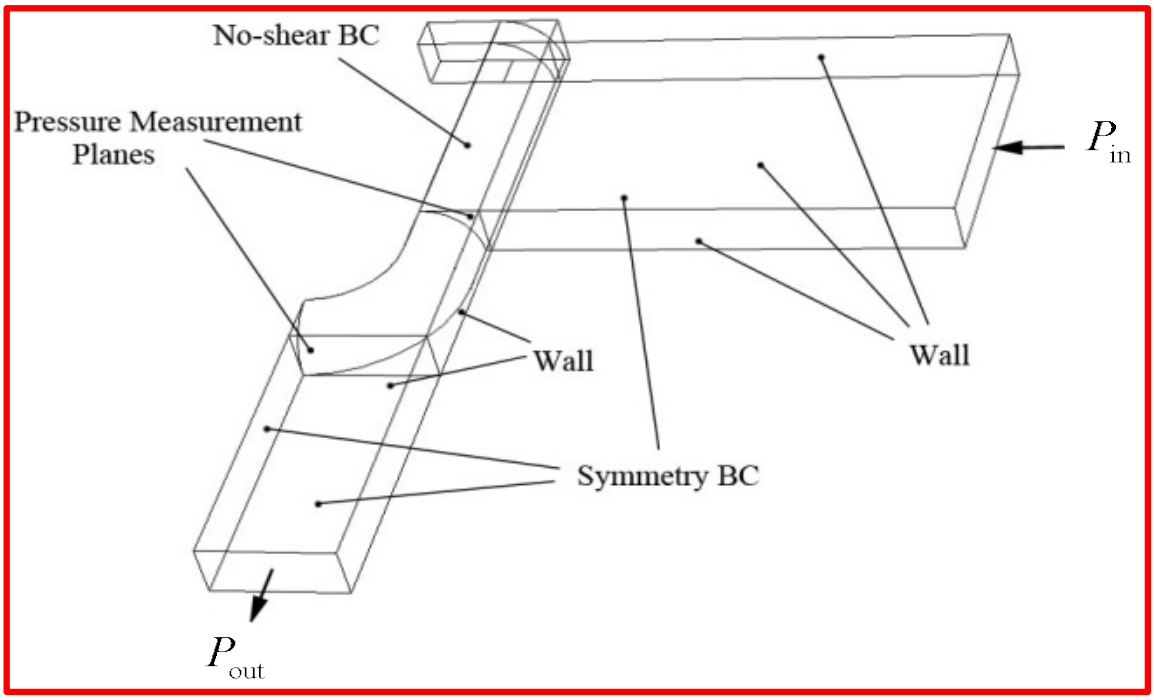

Figure 4.11 Simulation domain of the 3D numerical model with, $L^*_{fill} = 0.7$ height/width ratio $h^* = 0.41$ and a fluid viscosity of 9.96 mPa.s (continuous phase).

In this simulation, all of the boundary conditions were kept the same as used in literature [375] in order to compare the pressure drop with symmetric gutter (results provided by Tchikanda *et al.*) and that with 3D tip gutter (droplet). Therefore, no-slip conditions were applied to the channel walls, and no-shear condition was applied to the interface of the droplet. Symmetric boundary conditions were applied to the planes of symmetry. In the simulation, three different channel heights, $h^* = 0.41, 0.58, 0.66$ and the same droplet tip shape with eight different penetrating lengths, where $L^*_{fill} = 0.5 \rightarrow 5$, were considered.

The simulation results allow the pressure drop and flow rate through the 3D gutter to be calculated. Under the same flow rate condition, the pressure drop over the equivalent length of the uniform cross-section gutter is then obtained using the asymptotic model provided by Tchikanda *et al.* [375]. Mathematically, this relationship can be expressed by the ratio of the pressure drop from the 3D numerical simulations (ΔP_{3D}) to the pressure drop from the asymptotic model (ΔP_{asy}),

$$L^*_{fill} = \frac{\Delta P_{asy}}{\Delta P_{3D}} L^*_{eqv} \qquad \textbf{(4.33)}$$

Figure 4.12 plots the ratio $\Delta P_{asy} / \Delta P_{3D}$ as a function of L^*_{fill} for different heights of channel. When L^*_{fill} approaches infinite, the 3D curvature of the droplet tip has little influence on the hydrodynamic resistance. In this case, the 3D gutter is approaching the situation of the uniform cross-section as indicated by the fact that $\Delta P_{asy} / \Delta P_{3D} \to 1$. When L^*_{fill} is small, $\Delta P_{asy} / \Delta P_{3D}$ is close to a power function of L^*_{fill}. The relationship can be described by a blend of limiting solutions consisting of a power function and a constant 1,

$$\frac{\Delta P_{asy}}{\Delta P_{3D}} = \left(1 + 0.2 L^{*\,-1.4}_{fill}\right)^2 \qquad \textbf{(4.34)}$$

By substituting Equation (4.34) into Equation (4.33), the relationship between the equivalent droplet length and the actual droplet length is obtained which accounts for the 3D geometry in the gutter,

$$L^*_{eqv} = \frac{L^*_{fill}}{\left(1 + 0.2 L^{*\,-1.4}_{fill}\right)^2} \qquad \textbf{(4.35)}$$

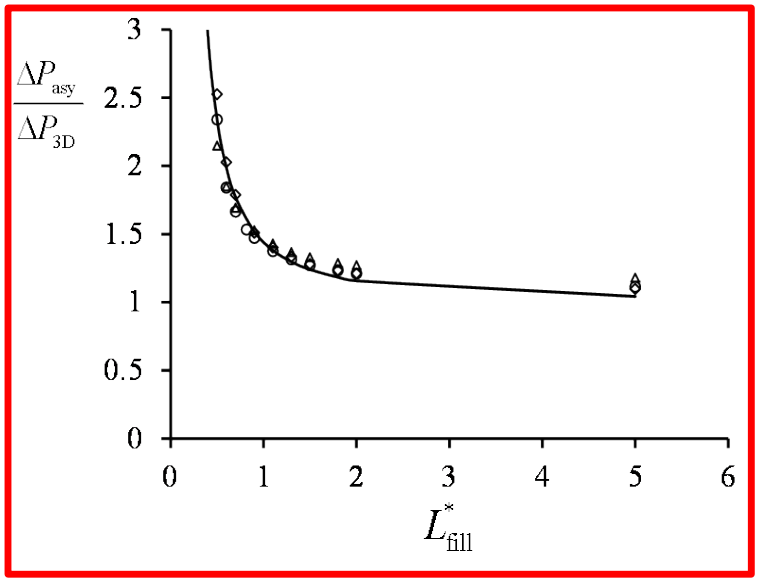

Figure 4.12 Equivalent pressure drop length coefficient in the gutter region as a function of the penetrating drop length at the end of the filling stage with different height/width ratios, $h^* = 0.41$ (◇), $h^* = 0.58$ (○), and $h^* = 0.66$ (△). The fitting curve is an asymptote, $\left(1+0.2L^{*\,-1.4}_{fill}\right)^2$

4.3.5.2 Effect of Viscosity Ratio

In this subsection, the effect of the viscosity contrast on the pressure drop was studied. Increasing the viscosity ratio is expected to increase the hydrodynamic resistance of the gutter and hence increase the pressure drop for a given flow rate. To estimate this effect, 2D numerical simulations were performed, which emulated the cross-section view of the gutter in 2D similar to that studied by Glawdel *et al*. [103]. A pressure gradient was applied in the continuous phase while the flow in the dispersed phase is caused by the drag force at the interface due to the bypassing continuous flow. No-slip boundary conditions are applied to all the channel walls and continuity at the interface. Simulations were performed for viscosity ratios from 0 to 15. The detailed simulation process can be found elsewhere [103].

Figure 4.13shows the influence of the viscosity ratio on the pressure drop as compared to the no-shear condition based on the numerical simulation results. The fit function is induced based on two conditions: (i) when $\eta = 0$, the relative pressure drop is equal to 1, and (ii) when $\eta \to \infty$, the equation should approach an asymptote. Herein, the simulation was performed with a large viscosity ratio $\eta = 1{,}000{,}000$ and found the asymptote to be 2.7, which leads to the following curve fit,

$$g(\eta) = 2.7 - \frac{1.7}{0.082\eta + 1} \tag{4.36}$$

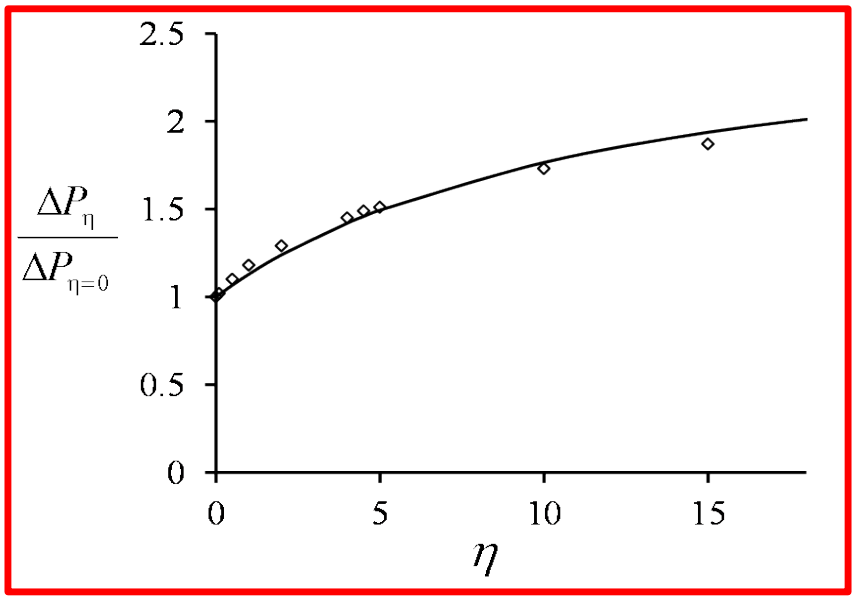

Figure 4.13 Relative pressure drop versus viscosity ratio.

At the end of the filling stage the coefficient of mobility of droplet can be estimated as unity [309], which means the droplet velocity is the same as the average velocity of the continous phase. Hence, Q_{gap} can be estimated by $Q_{\text{gap}}/A_{\text{gap}} = Q_{\text{c}}/(wh)$, which allows Equation (4.32) to be rewritten as,

$$\Delta P = \frac{\mu_{\text{c}} Q_{\text{c}}}{\overline{u}_g^* A_{\text{c}} h^2} \cdot L_{\text{eqv}} \cdot g(\eta) \tag{4.37}$$

where $A_{\text{c}} = wh$. On the other hand, the pressure drop through the gutter can also be expressed by the Laplace pressure drop. According to the Young-Laplace equation,

$$P_1 - P_2 = \gamma\left(\frac{1}{\infty} + \frac{2}{h}\right) = \gamma\frac{2}{h} \tag{4.38}$$

$$P_1 - P_3 = \gamma\left(\frac{2}{W_{\text{fill}}} + \frac{2}{h}\right) \tag{4.39}$$

where P_1, P_2 and P_3 are marked in Figure 4.4(b). Combining Equations (4.38) and (4.39), the pressure drop across the emerging droplet is obtained,

$$\Delta P = P_2 - P_3 = \gamma\frac{2}{W_{\text{fill}}} \tag{4.40}$$

Combining Equations (4.37) and (4.40), and non-dimensionalizing the integrated equation leads to,

$$L_{\text{eqv}}^* = \frac{2\overline{u}_g^*}{W_{\text{fill}}^* g(\eta)} \cdot \frac{h^{*2}}{Ca} \tag{4.41}$$

Substituting Equation (4.35) into Equation (4.41) leads to the equation of calculating L_{fill}^*,

$$\frac{L_{\text{fill}}^*}{\left(1 + 0.2{L_{\text{fill}}^*}^{-1.4}\right)^2} = \frac{2\overline{u}_g^*}{W_{\text{fill}}^* g(\eta)} \cdot \frac{h^{*2}}{Ca} \tag{4.42}$$

where L_{fill}^* is the only variable that can be calculated by iterating until the two sides of Equation (4.42) are equal.

Figure 4.14 shows the calculated L_{fill}^* compared with the experimental results for three different channel height-to-width ratios and three different viscosity ratios. From the figure, we can see that Equation (4.42) captures the experimental tendency of L_{fill}^*, as most results are within $\pm 10\%$. The

errors may come from several sources. First, the accuracy of the measured channel height highly influences the calculated results because the calculated L^*_{fill} is proportional to the cube of the measured channel height as shown in Equation (4.42), $L^*_{\text{fill}} \propto \frac{h^{*2}}{Ca} \propto h^{*3}$. 3% error in channel height measurement will lead to around a 9% error in L^*_{fill}. Second, the gap between the droplet and wall is estimated to be 0.02. However, the actual gap dimension is unknown which has a little influence on the estimation of $\bar{u}^*_{\text{g}}$. Considering all the above error sources, this model is very accurate in describing L^*_{fill}.

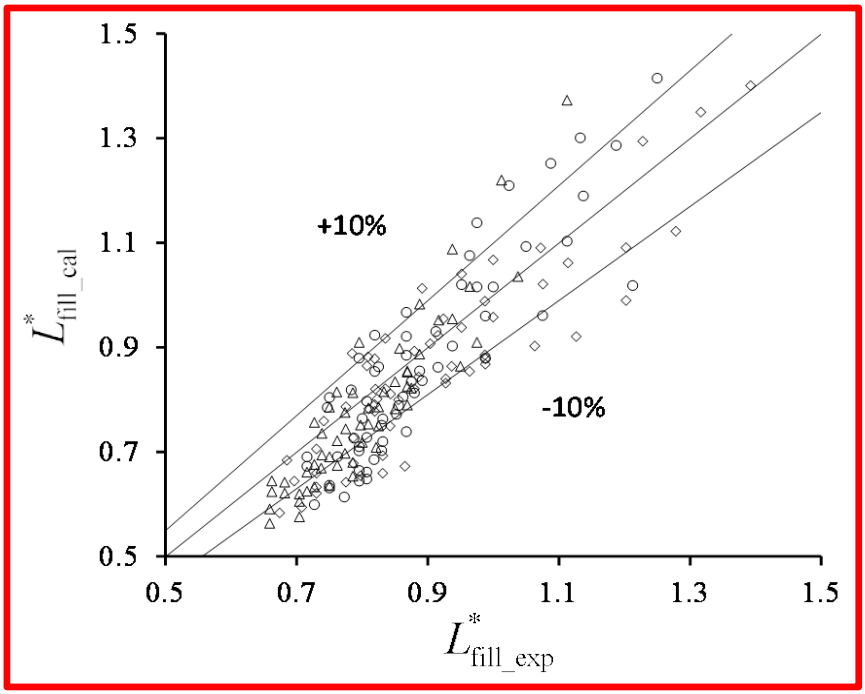

Figure 4.14 Plots of non-dimensional L^*_{fill}. Experimental results VS. Calculated results in conditions of $h^* = 0.41$, $h^* = 0.58$ and $h^* = 0.66$, with the dispersed phase, glyc/water 10% by wt. (◇), glyc/water 60% by wt. (○) and glyc/water 80% by wt. (△), respectively.

4.3.6 Calculation of Parameter W^*_{pinch}

The neck begins to pinch-off when the Laplace pressure at the neck is equal to the Laplace pressure at the tip of the droplet (no pressure drop in the gutter). This means most of the continuous phase flows into the V-shaped neck. According to Young-Laplace equation, at the end of necking stage shown in Figure 4.4(b),

$$P_{neck} - P_{tip} = \gamma\left(\frac{2}{w} + \frac{2}{h}\right) - \gamma\left(-\frac{1}{R_{neck}} + \frac{2}{W_{pinch}}\right) = 0 \qquad \textbf{(4.43)}$$

Since the radius of curvature, $R_{neck} >> W_{pinch}/2$ one can assume $1/R_{neck} \approx 0$ in comparison to $2/W_{pinch}$, which simplifies Equation (4.43) and allows the non-dimensional form of W^*_{pinch} to be obtained as,

$$W^*_{pinch} = \frac{h^*}{1+h^*} \qquad \textbf{(4.44)}$$

The model predicted W^*_{pinch} agrees well with the experimentally measured W^*_{pinch} as shown in Figure 4.15. The discrepancy may be caused by the error in determining the exact pinch off frame.

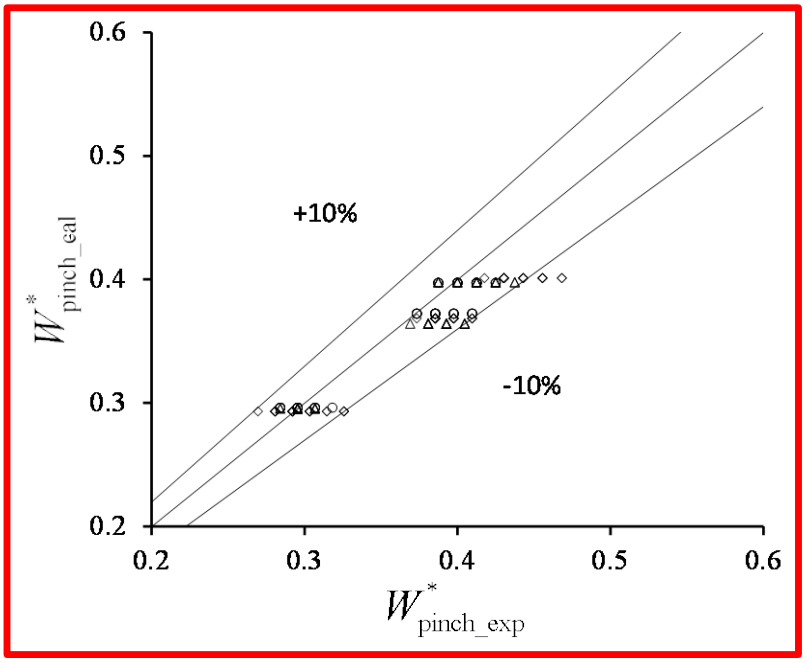

Figure 4.15 Plot of non-dimensional W^*_{pinch}. Experimental results VS. Calculated results in conditions of $h^* = 0.41$, $h^* = 0.58$ and $h^* = 0.66$, with dispersed phase, glyc/water 10% by wt. (◇), glyc/water 60% by wt. (○) and glyc/water 80% by wt. (△), respectively.

4.3.7 Calculation of Parameter L^*_{pinch}

During the necking stage, most of the continuous phase flows into the V-shape and squeezes the droplet with a small amount bypassing the gutter. The neck starts to decrease from *w* (width of

channel) to W_{pinch}; meanwhile the length of the V-shape starts to increase from *w* to L_{pinch}. The variations in both the neck width and V-shape length are tracked along with time during the necking stage. Figure 4.8 shows one typical example. Results show that the V-shape decreases linearly with time in the horizontal direction (neck width) and also increases linearly in the vertical direction (length of V-shape) which agrees well with that reported by Garstecki *et al.* [373]. The continuous phase fills the V-shape causing the deformation of the shape in both the length and width directions which can be described by,

$$\frac{\Delta L^*_{\text{pinch}}}{\Delta W^*_{\text{pinch}}} = \frac{v^*_{\text{l}}}{v^*_{\text{w}}} \tag{4.45}$$

where $\Delta L^*_{\text{pinch}} = L^*_{\text{pinch}} - 1$ and $\Delta W^*_{\text{pinch}} = 1 - W^*_{\text{pinch}}$ are the deformations of the V-shape in the droplet length and width direction during the necking stage, respectively, v^*_{l} is the slope of L^*_{pinch} variation and v^*_{w} the slope of W^*_{pinch} variation, both of which are constants. By tracking the experimental results of v^*_{l} and v^*_{w}, its ratio, $v^*_{\text{l}} / v^*_{\text{w}}$ can be expressed as,

$$\frac{v^*_{\text{l}}}{v^*_{\text{w}}} = C \frac{Q_{\text{c}}}{Q_{\text{c}} - \bar{Q}_{\text{gutter}}} g(\eta) \tag{4.46}$$

where $Q_{\text{c}} / (Q_{\text{c}} - \bar{Q}_{\text{gutter}})$ only considers the continuous phase flowing into the V-shape leading to the deformation of W^*_{pinch}, and $\bar{Q}_{\text{gutter}}$ is the average flow rate through the gutter during the necking stage. The coefficient, $g(\eta)$ considers the viscosity contrast. The higher the droplet viscosity, the more difficult it is to squeeze the neck. This is quite similar to the situation of squeezing a solid beam which leads to deformations in both directions and the deformation ratio depends on the properties of the material. The constant, *C*, also depends on the properties of the dispersed phase. Therefore, L^*_{pinch} can be calculated by,

$$L^*_{\text{pinch}} = 1 + \Delta L^*_{\text{pinch}} = 1 + Cg(\eta) \frac{1 - W^*_{\text{pinch}}}{1 - V^*_{\text{gutter}}} \tag{4.47}$$

Substituting Equation (4.44) into Equation (4.47), one can obtain,

$$L^*_{\text{pinch}} = 1 + Cg(\eta) \frac{1}{1 - V^*_{\text{gutter}}} \frac{1}{1 + h^*} \tag{4.48}$$

When $C = 2$, it agrees well with the experimental results as shown in Figure 4.16. It is noted that C is a fitting parameter here.

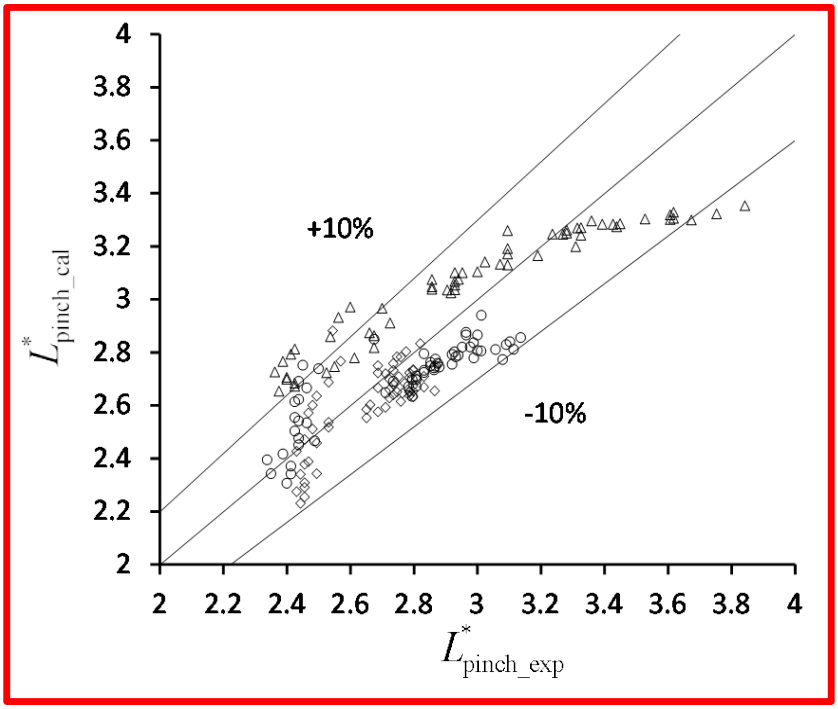

Figure 4.16 Parity plot of the experimentally measured and model predicted non-dimensional L^*_{pinch} for the conditions with different channel heights ($h^* = 0.41$, $h^* = 0.58$ and $h^* = 0.66$) and different dispersed phase (glyc/water 10% by wt. (◇), glyc/water 60% by wt. (○) and glyc/water 80% by wt. (△)), respectively.

There are several reasons for the errors. First, it is difficult to determine which frame is the exact frame when the droplet pinches off. Second, the errors may come from the channel height measurement. However, this model is still acceptable, because the results show that most of the calculating data fall within error $\pm 10\%$ compared to the experimental results.

4.4 Model Validation

Once the four parameters, W_{fill}, L_{fill}, W_{pinch}, L_{pinch} are determined, the droplet volume can be calculated by substituting these four parameters into Equation (4.28). After V_d^* is calculated, the period, T^* frequency, f^* and spacing, s^* can be determined accordingly. A flow chart of the steps of calculating droplet volume, V_d^* frequency, f^* and spacing, s^* is shown in Figure 4.17.

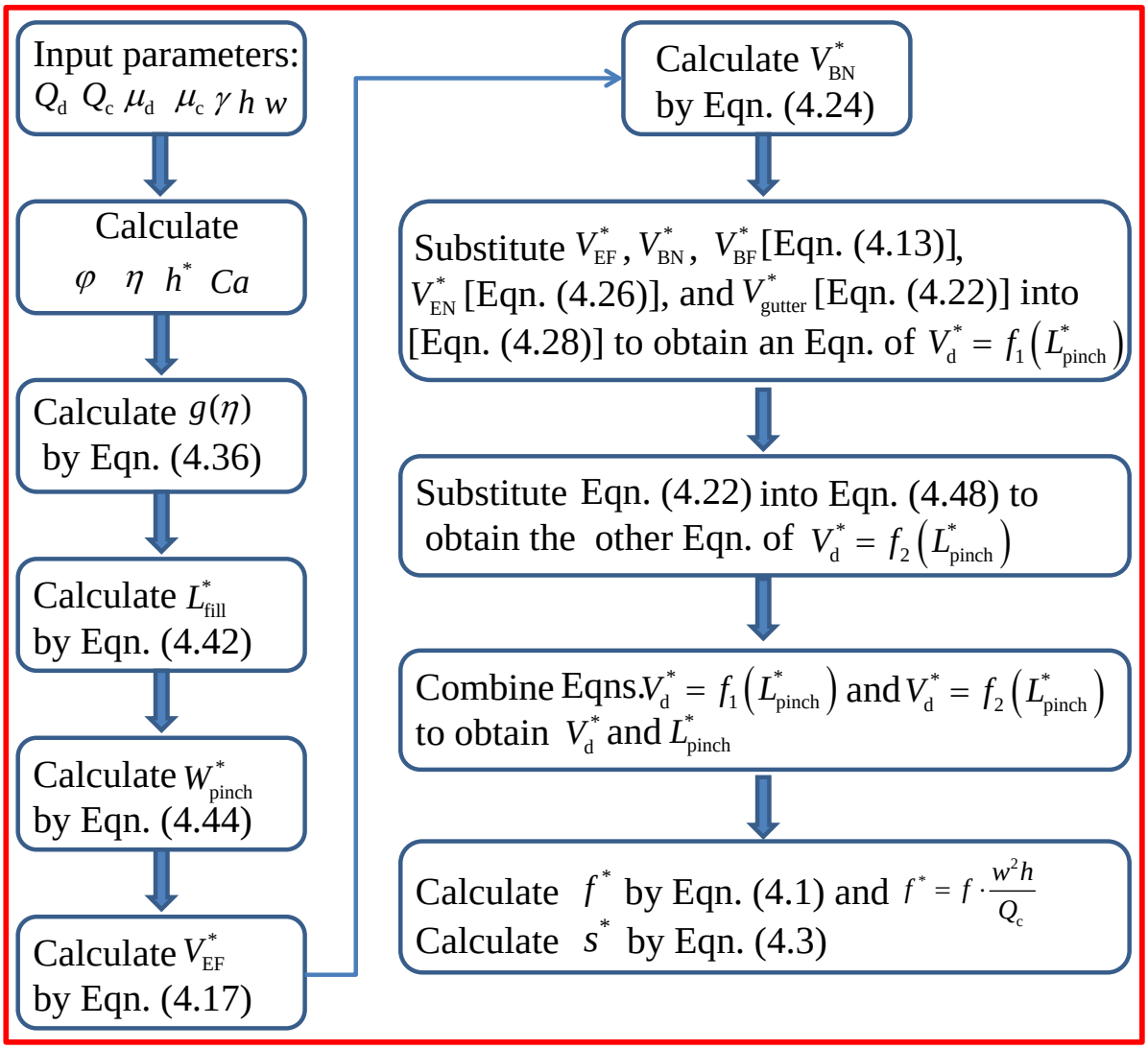

Figure 4.17 Flow chart of the steps of calculating droplet volume, V_d^* frequency, f^* and spacing, s^*.

Figure 4.18 shows the parity plot for the droplet volume, frequency and spacing. The frequency and spacing were measured experimentally and calculated by Equation (4.1) and Equation (4.3), respectively. The figure shows that the model agrees well with the experimental results, with most of the data falling within $\pm 10\%$, by considering variations of Ca from 0.001 to 0.006, channel height from 0.41 to 0.66, viscosity ratio from 0.1 to 4.4 and flow rate ratio from 0.15 to 1.

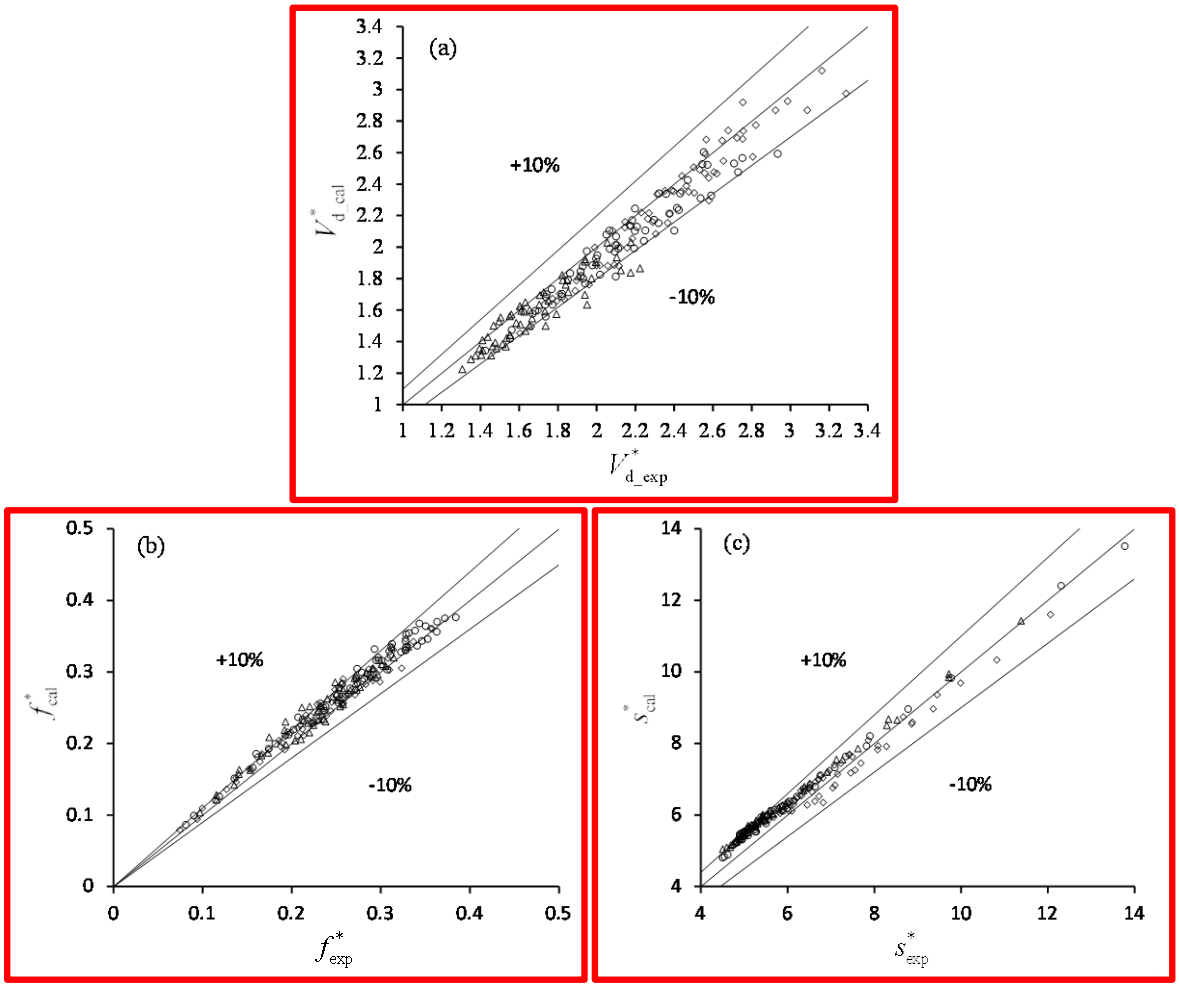

Figure 4.18 Parity plot for the non-dimensional (a) droplet volume, (b) formation frequency and (c) droplet spacing for all the experimental data including different channel heights ($h^* = 0.41$, $h^* = 0.58$ and $h^* = 0.66$), and different dispersed phase (glyc/water 10% by wt. (◇), glyc/water 60% by wt. (○) and glyc/water 80% by wt. (△), respectively.

4.5 Model Error Analysis

First, it should be noted that ideal experimental studies should investigate the effect of one particular influencing parameter on the flow phenomena by varying this parameter while maintaining the rest. However, in our experiments, it is challenging, if not impossible, to isolate one parameter from the others. For example, the channel height-to-width ratio is one critical parameter affecting droplet formation processes. The current fabrication technique does not guarantee that this ratio is achieved after each fabrication. In addition, practical issues such as the fact that most oils swell PDMS which is used in this study resulting variations in channel dimensions. Therefore, the channel

dimensions must be carefully evaluated using other means which were done in this study for each experiment after fabrication and saturation of oil swelling. The change of channel dimensions will result in changes in other operating conditions such as flow rate ratios due to the coupled flow conditions of the pressure driven system in order to ensure the capillary number falls in the range of the squeezing regime. As a result, each experimental datum has a specific set of parameters including capillary number and flow rate ratio which were recorded through the flow sensor, droplet frequency and droplet volume obtained using video analysis. Therefore, parity plots were used to compare the experimental results and model predicted results in this work. For the readers' interest, detailed experimental data are provided in Appendix A.

Second, as discussed in subsection 4.3.1, the assumption of 3D droplet shape is an accurate assumption for well controlled wetting conditions (Typically, contact angles for the oil and PDMS must be low <60˚, and for the water and PDMS high >120˚), which induces error within 2-5%.

In addition, the calculation of parameters L^*_{fill}, W^*_{fill}, W^*_{pinch}, and L^*_{pinch} has an error within $\pm 10\%$. However, the total influence of these parameters on the calculation of droplet volume is unknown. Therefore, uncertainties of V^*_{d} due to these parameters are discussed below:

- Uncertainty from W^*_{fill}

Wong *et al.* [298, 299] mentioned that the thin film thickness is proportional to the capillary number raised to the two-thirds power when $Ca < 0.01$, which means the thin film has a thickness on the order of 1% to 5% of the half channel width. Therefore, we assume that the gap between the droplet and channel wall is very thin (i.e. 0.02w) leaving to be 0.96 based on the rough measurements. The variation of thin film thickness is in an extremely small range within ± 0.03 (can be treated as a constant). Therefore, the variation of the volume of droplets caused by the variation of W^*_{fill} can be ignored compared to other three parameters L^*_{fill}, L^*_{pinch} and W^*_{pinch}.

- Uncertainty From L^*_{fill} ($\pm 10\%$), L^*_{pinch} ($\pm 10\%$), and W^*_{pinch} ($\pm 10\%$)

Since the variation of W^*_{fill} is very small within ± 0.03, W^*_{fill} can be treated as a constant. Using a first order Taylor expansion, uncertainty of V^*_{d} caused by L^*_{fill}, L^*_{pinch} and W^*_{pinch} can be expressed as,

$$\frac{\Delta V_{\mathrm{d}}^*}{V_{\mathrm{d}}^*}=\frac{1}{V_{\mathrm{d}}^*}\frac{\partial V_{\mathrm{d}}^*}{\partial L_{\mathrm{fill}}^*}\Delta L_{\mathrm{fill}}^*+\frac{1}{V_{\mathrm{d}}^*}\frac{\partial V_{\mathrm{d}}^*}{\partial L_{\mathrm{pinch}}^*}\Delta L_{\mathrm{pinch}}^*+\frac{1}{V_{\mathrm{d}}^*}\frac{\partial V_{\mathrm{d}}^*}{\partial W_{\mathrm{pinch}}^*}\Delta W_{\mathrm{pinch}}^* \tag{4.49}$$

Substitute $W_{\mathrm{fill}}^*=0.96$ into Equations (4.13), (4.17), (4.22), (4.24), and (4.26), one can obtain,

$$V_{\mathrm{BF}}^*=\frac{L_{\mathrm{pinch}}^*}{4}-\frac{h^*}{2}\left(1-\frac{\pi}{4}\right)\sqrt{1+\left(L_{\mathrm{pinch}}^*\right)^2}=0.25L_{\mathrm{pinch}}^*-0.11h^*\sqrt{1+\left(L_{\mathrm{pinch}}^*\right)^2} \tag{4.50}$$

$$V_{\mathrm{EF}}^*=\frac{1}{2}\left[\pi\left(\frac{W_{\mathrm{fill}}^*}{2}\right)^2+\left(L_{\mathrm{fill}}^*-\frac{W_{\mathrm{fill}}^*}{2}+1.5\right)(1+W_{\mathrm{fill}}^*)\right]-\frac{h^*}{2}\left(1-\frac{\pi}{4}\right)\left(\frac{\pi}{2}W_{\mathrm{fill}}^*+2\sqrt{\left(\frac{1-W_{\mathrm{fill}}^*}{2}\right)^2+\left(L_{\mathrm{fill}}^*-\frac{W_{\mathrm{fill}}^*}{2}+1.5\right)^2}\right) \tag{4.51}$$

$$=1.36+0.98L_{\mathrm{fill}}^*-0.11h^*\left(3.55+2L_{\mathrm{fill}}^*\right)$$

$$V_{\mathrm{gutter}}^*=\frac{\frac{1}{2}\left(1-W_{\mathrm{fill}}^*\right)+\left(1-\frac{\pi}{4}\right)h^*}{1-\left(1-\frac{\pi}{4}\right)h^*}\left[V_{\mathrm{d}}^*-\frac{1}{4}\left(L_{\mathrm{pinch}}^*+\frac{\pi}{2}\right)+\frac{h^*}{2}\left(1-\frac{\pi}{4}\right)\left(\sqrt{1+(L_{\mathrm{pinch}}^*)^2}+\frac{\pi}{2}\right)\right] \tag{4.52}$$

$$=\frac{0.02+0.21h^*}{1-0.21h^*}\left[V_{\mathrm{d}}^*-0.25L_{\mathrm{pinch}}^*-0.39+0.11h^*\left(\sqrt{1+(L_{\mathrm{pinch}}^*)^2}+1.57\right)\right]$$

$$\begin{aligned}V_{\mathrm{BN}}^*&=\frac{1-W_{\mathrm{fill}}^*}{2}+h^*\left(1-\frac{\pi}{4}\right)\sqrt{\left(\frac{1-W_{\mathrm{fill}}^*}{2}\right)^2+1}\\&=0.02+0.11h^*\end{aligned} \tag{4.53}$$

$$\begin{aligned}V_{\mathrm{EN}}^*&=L_{\mathrm{pinch}}^*\frac{1-W_{\mathrm{pinch}}^*}{2}+h^*\left(1-\frac{\pi}{4}\right)\sqrt{\left(1-W_{\mathrm{pinch}}^*\right)^2+\left(L_{\mathrm{pinch}}^*\right)^2}\\&=0.5L_{\mathrm{pinch}}^*\left(1-W_{\mathrm{pinch}}^*\right)+0.21h^*\sqrt{\left(1-W_{\mathrm{pinch}}^*\right)^2+\left(L_{\mathrm{pinch}}^*\right)^2}\end{aligned} \tag{4.54}$$

Substitute Equations (4.50) ~ (4.54) into Equation (4.28), we can obtain,

$$\begin{aligned}&\left(1+(1-\frac{1.02}{1-0.21h^*})\varphi\right)V_{\mathrm{d}}^*=1.36+0.98L_{\mathrm{fill}}^*-0.25L_{\mathrm{pinch}}^*-0.11h^*\left(3.55+2L_{\mathrm{fill}}^*-\sqrt{1+\left(L_{\mathrm{pinch}}^*\right)^2}\right)\\&+\varphi\left\{0.5L_{\mathrm{pinch}}^*\left(1-W_{\mathrm{pinch}}^*\right)+0.21h^*\sqrt{\left(1-W_{\mathrm{pinch}}^*\right)^2+\left(L_{\mathrm{pinch}}^*\right)^2}-(0.02+0.11h^*)\right\}\\&+\varphi(1-\frac{1.02}{1-0.21h^*})\left\{0.25L_{\mathrm{pinch}}^*+0.39-0.11h^*\left(\sqrt{1+(L_{\mathrm{pinch}}^*)^2}+1.57\right)\right\}\end{aligned} \tag{4.55}$$

For a typical channel height $h^*=0.5$, substitute $h^*=0.5$ into Equation (4.55), we can get,

$$V_{\mathrm{d}}^{*}=\frac{1}{\left(1-0.14\varphi\right)}\left[1.16+0.87L_{\mathrm{fill}}^{*}-0.25L_{\mathrm{pinch}}^{*}+0.055\sqrt{1+\left(L_{\mathrm{pinch}}^{*}\right)^{2}}\right]$$
$$+\frac{\varphi}{\left(1-0.14\varphi\right)}\left[0.465L_{\mathrm{pinch}}^{*}-0.5L_{\mathrm{pinch}}^{*}W_{\mathrm{pinch}}^{*}+0.11\sqrt{\left(1-W_{\mathrm{pinch}}^{*}\right)^{2}+\left(L_{\mathrm{pinch}}^{*}\right)^{2}}+0.0077\sqrt{1+(L_{\mathrm{pinch}}^{*})^{2}}-0.17\right] \quad \textbf{(4.56)}$$

Therefore,

$$\frac{\partial V_{\mathrm{d}}^{*}}{\partial L_{\mathrm{fill}}^{*}}=\frac{0.87}{\left(1-0.14\varphi\right)} \quad \textbf{(4.57)}$$

Because the flow rate ratio $0<\varphi<1$, one can know $0.86<1-0.14\varphi<1$. Therefore,

$$\frac{1}{V_{\mathrm{d}}^{*}}\frac{\partial V_{\mathrm{d}}^{*}}{\partial L_{\mathrm{fill}}^{*}}\Delta L_{\mathrm{fill}}^{*}=\frac{0.87}{\left(1-0.14\varphi\right)}\frac{\Delta L_{\mathrm{fill}}^{*}}{V_{\mathrm{d}}^{*}}<1.01\frac{\Delta L_{\mathrm{fill}}^{*}}{V_{\mathrm{d}}^{*}} \quad \textbf{(4.58)}$$

With $\left|\Delta L_{\mathrm{fill}}^{*}\right|\le 10\%L_{\mathrm{fill}}^{*}$, and L_{fill}^{*} much smaller than V_{d}^{*} from experimental results ($\frac{L_{\mathrm{fill}}^{*}}{V_{\mathrm{d}}^{*}}<0.5$), we can estimate that,

$$\left|\frac{1}{V_{\mathrm{d}}^{*}}\frac{\partial V_{\mathrm{d}}^{*}}{\partial L_{\mathrm{fill}}^{*}}\Delta L_{\mathrm{fill}}^{*}\right|<5\% \quad \textbf{(4.59)}$$

$$\frac{\partial V_{\mathrm{d}}^{*}}{\partial L_{\mathrm{pinch}}^{*}}=\frac{-0.25}{\left(1-0.14\varphi\right)}+\frac{0.055}{\left(1-0.14\varphi\right)}\frac{L_{\mathrm{pinch}}^{*}}{\sqrt{1+\left(L_{\mathrm{pinch}}^{*}\right)^{2}}}$$
$$+\frac{0.465\varphi}{\left(1-0.14\varphi\right)}-\frac{0.5\varphi W_{\mathrm{pinch}}^{*}}{\left(1-0.14\varphi\right)}+\frac{0.11\varphi}{\left(1-0.14\varphi\right)}\frac{L_{\mathrm{pinch}}^{*}}{\sqrt{\left(1-W_{\mathrm{pinch}}^{*}\right)^{2}+\left(L_{\mathrm{pinch}}^{*}\right)^{2}}}+\frac{0.0077\varphi}{\left(1-0.14\varphi\right)}\frac{L_{\mathrm{pinch}}^{*}}{\sqrt{1+(L_{\mathrm{pinch}}^{*})^{2}}} \quad \textbf{(4.60)}$$

Experimental results show that $2<L_{\mathrm{pinch}}^{*}<4$, $0.2<W_{\mathrm{pinch}}^{*}<0.5$ hence, we can obtain,

$$1<\frac{1}{\left(1-0.14\varphi\right)}<1.16,\ 0<\frac{\varphi}{1-0.14\varphi}<1.16,\ 0.9<\frac{L_{\mathrm{pinch}}^{*}}{\sqrt{1+\left(L_{\mathrm{pinch}}^{*}\right)^{2}}}<1,\ \frac{L_{\mathrm{pinch}}^{*}}{\sqrt{\left(1-W_{\mathrm{pinch}}^{*}\right)^{2}+\left(L_{\mathrm{pinch}}^{*}\right)^{2}}}\approx 1$$

Therefore,

$$\left|\frac{\partial V_{\mathrm{d}}^{*}}{\partial L_{\mathrm{pinch}}^{*}}\right| < \frac{-0.25}{(1-0.14\varphi)} + \frac{0.055}{(1-0.14\varphi)} + \frac{0.465\varphi}{(1-0.14\varphi)} - \frac{0.5\varphi W_{\mathrm{pinch}}^{*}}{(1-0.14\varphi)} + \frac{0.11\varphi}{(1-0.14\varphi)} + \frac{0.0077\varphi}{(1-0.14\varphi)}$$
$$= \frac{(0.58-0.5W_{\mathrm{pinch}}^{*})\varphi - 0.195}{(1-0.14\varphi)} < 0.33 \quad \textbf{(4.61)}$$

Then, $\left|\frac{1}{V_{\mathrm{d}}^{*}}\frac{\partial V_{\mathrm{d}}^{*}}{\partial L_{\mathrm{pinch}}^{*}}\Delta L_{\mathrm{pinch}}^{*}\right| < 0.33\left|\frac{\Delta L_{\mathrm{pinch}}^{*}}{V_{\mathrm{d}}^{*}}\right|$ considering $\left|\Delta L_{\mathrm{pinch}}^{*}\right| \le 10\% L_{\mathrm{pinch}}^{*}$, and L_{pinch}^{*} is close to V_{d}^{*} from experimental results, we can estimate that,

$$\left|\frac{1}{V_{\mathrm{d}}^{*}}\frac{\partial V_{\mathrm{d}}^{*}}{\partial L_{\mathrm{pinch}}^{*}}\Delta L_{\mathrm{pinch}}^{*}\right| < 0.33\left|\frac{\Delta L_{\mathrm{pinch}}^{*}}{V_{\mathrm{d}}^{*}}\right| < 3.3\% \quad \textbf{(4.62)}$$

With the same method, one can obtain,

$$\frac{\partial V_{\mathrm{d}}^{*}}{\partial W_{\mathrm{pinch}}^{*}} = -\frac{0.5L_{\mathrm{pinch}}^{*}\varphi}{(1-0.14\varphi)} - \frac{0.11\varphi}{(1-0.14\varphi)}\frac{1-W_{\mathrm{pinch}}^{*}}{\sqrt{\left(1-W_{\mathrm{pinch}}^{*}\right)^{2}+\left(L_{\mathrm{pinch}}^{*}\right)^{2}}} \quad \textbf{(4.63)}$$

$$\frac{\partial V_{\mathrm{d}}^{*}}{\partial W_{\mathrm{pinch}}^{*}} \approx -\frac{0.5L_{\mathrm{pinch}}^{*}\varphi}{(1-0.14\varphi)} - \frac{0.11\varphi}{(1-0.14\varphi)}\frac{1-W_{\mathrm{pinch}}^{*}}{L_{\mathrm{pinch}}^{*}}$$

$$\left|\frac{\partial V_{\mathrm{d}}^{*}}{\partial W_{\mathrm{pinch}}^{*}}\right| \approx \frac{0.5L_{\mathrm{pinch}}^{*}\varphi}{(1-0.14\varphi)} + \frac{0.11\varphi}{(1-0.14\varphi)}\frac{1-W_{\mathrm{pinch}}^{*}}{L_{\mathrm{pinch}}^{*}} < 2.76$$

Therefore, considering $\left|\Delta W_{\mathrm{pinch}}^{*}\right| \le 10\% W_{\mathrm{pinch}}^{*}$, and $\left|\frac{W_{\mathrm{pinch}}^{*}}{V_{\mathrm{d}}^{*}}\right| < 0.2$ from experimental results, we can obtain,

$$\left|\frac{1}{V_{\mathrm{d}}^{*}}\frac{\partial V_{\mathrm{d}}^{*}}{\partial W_{\mathrm{pinch}}^{*}}\Delta W_{\mathrm{pinch}}^{*}\right| < 2.76\left|\frac{\Delta W_{\mathrm{pinch}}^{*}}{V_{\mathrm{d}}^{*}}\right| < 5.52\% \quad \textbf{(4.64)}$$

Therefore, the total error of V_{d}^{*} due to the uncertainties of L_{fill}^{*} ($\pm 10\%$), L_{pinch}^{*} ($\pm 10\%$) and W_{pinch}^{*} ($\pm 10\%$) should be,

$$\frac{\Delta V_{\mathrm{d}}^{*}}{V_{\mathrm{d}}^{*}} < \pm(5\% + 3.3\% + 5.52\%) = \pm 13.82\% \quad \textbf{(4.65)}$$

This error estimation considers all the extreme conditions. The actual error is expected to be much smaller than 13.82%. In conclusion, L^*_{fill} L^*_{pinch} and W^*_{pinch} with errors within $\pm 10\%$ are accurate to predict droplet volumes.

4.6 Conclusions

This work presents a model describing the droplet formation process in flow focusing devices operating in the squeezing regime. Firstly, the shape deformation of droplet during a formation cycle is accurately modelled based on the conservation of mass for the dispersed and continuous phases by considering the 3D curved surface of the droplet. Four parameters W_{fill}, L_{fill}, W_{pinch}, L_{pinch} are used to describe the droplet shape and thus its volume. Secondly, models are built to predict these parameters based on the pressure driven flow. The model for predicting L^*_{fill} incorporates the 3D curvature of the droplet and viscosity contrast of the two phases into the analytical approximation of the pressure drop across an emerging droplet. Finally, predictions from the model are in good agreement with experimental data for various conditions including different geometries, flow rate ratio, capillary number and viscosity contrast. Most of the experimental data fall within $\pm 10\%$ of the predicted values. The results also validate the assumption for constant Q_{d} and Q_{c} in the experiments. The model developed here applies to the droplet formation in the squeezing regime where the droplet length is usually larger than channel width (slugs). For droplet length small than the channel width, it is not applicable.

4.7 List of symbols

2D	Two dimensional
3D	Three dimensional
PDMS	Polydimethylsiloxane
A	Area
Ca	Capillary number
D_{h}	Hydraulic diameter
F	Frame rate
f	Droplet generation frequency
h	Channel height
L_{eqv}	Equivalent droplet length of the uniform cross-section
L_{fill}	Droplet length that penetrates into the main channel at the end of the filling stage
L^{*}_{gutter}	Length of the gutter at the end of the necking stage
L_{pinch}	Distance between the two points of the V-shape at the end of the necking stage
$\Delta L^{*}_{\mathrm{pinch}}$	Variation of the V-shape in the droplet length direction during the necking stage
N_{drop}	Number of the captured droplets in one video
N_{frame}	Total number of frames in one video
P_1	Pressure of the forming droplet at the end of the filling stage
P_2	Pressure of the continuous phase at the cross at the end of the filling stage
P_3	Pressure of the continuous phase surrounding the tip of forming droplet at the end of the filling stage
ΔP_{3D}	Pressure drop from the 3D numerical simulations
ΔP_{asy}	Pressure drop from the asymptotic model
P_{neck}	Pressure of the continuous phase at the cross at the end of necking stage
P_{tip}	Pressure of the continuous phase surrounding the tip of forming droplet at the end of the necking stage
Q	Flow rate
$\bar{Q}_{\mathrm{gutter}}$	Average flow rate through the gutter during the necking stage

R_{neck} Radius of the V-shape neck at the end of the necking stage

s Spacing between two droplets

T Droplet generation period

$\Delta t_{filling}$ Filling period

$\Delta t_{necking}$ Necking period

μ Fluid velocity

$\overline{u}_g$ Average fluid velocity in the gutter

V_{BF} Volume of droplet at the beginning of the filling stage

V_{BN} Volume of the continuous phase in the V-shape at the beginning of the necking stage

V_d Droplet volume

V_{EF} Volume of droplet at the end of the filling stage

V_{EN} Volume of the continuous phase in the V-shape at the end of the necking stage

V_{gutter} Volume of the continuous phase bypassing the gutter during the necking stage

v_l^* The slope $\Delta L_{pinch}^* / \Delta t$

v_w^* The slope $\Delta W_{pinch}^* / \Delta t$

W_{fill} Width of the tip at the end of the filling stage

W_{pinch} Width of the neck at the end of the necking stage

ΔW_{pinch}^* Variation of the V-shape in the droplet width direction during the necking stage

w Channel width

Greek symbols

α Defined as $V_{EF}^* - V_{BF}^*$

β Defined as $V_{EN}^* - V_{BN}^* + V_{gutter}^*$

φ Dispersed phase to continuous phase flow rate ratio

γ Interfacial tension

η Dispersed phase to continuous phase viscosity ratio

μ	Fluid viscosity

Subscripts

c	Continuous phase
d	Dispersed phase

Superscripts

*	Dimensionless form of variables

Chapter 5

Experimental Study on droplet generation in a flow focusing device using stratified flow with viscosity contrast and its impact on single encapsulation

In Chapter 4, droplet generation in a flow focusing device was studied both experimentally and theoretically, in where only one fluid was used as the dispersed phase. However, in many chemical or biomedical applications, two or more compounds are added into droplets, and sometimes cells or particles are required to be encapsulated into droplets. When performing chemical or biological reactions in droplet-based platforms, reagents are normally injected together in a co-flowing stream just prior to droplet formation. The co-flowing stream forms a stratified flow under low Reynolds number. The stratified flow with viscosity contrast has a significant impact on droplet formation process and single cell or particle encapsulation. This study employs a simple flow focusing device with two junctions in series and glycerol solutions with different concentrations which result in viscosity contrasts to form stratified flow in the first junction and thus droplets in the second junction. The droplet formation process was experimentally studied in the flow focusing generator by varying the flow rate ratio between fluids and the viscosity contrast while maintaining the operation is within the squeezing regime. To obtain a comprehensive understanding of the droplet formation dynamics involving stratified flow, five different scenarios were considered including two cases with pure 10%glycerol and pure 80%glycerol as the dispersed phase respectively and three other cases where these two fluids are either side by side or one is accompanied by the other. Droplet size and formation period for these cases were compared and analyzed considering the same geometric and flow conditions. It is found that stratified flow structure strongly influence droplet formation dynamics such as droplet size and formation frequency and the scenario with 80%glycerol surrounded by 10%glycerol in the first junction generates the largest droplet size. Each structure finds its own applications. For the purpose of single encapsulation, the scenario with 80%glycerol surrounded by 10%glycerol in the first junction provides the optimized means because high viscosity of 80%glycerol allows particles to be focused into a thin stream and spaced before entering droplets. The efficiency for single encapsulation was demonstrated up to 80% for 10 μm polystyrene beads. However, the scenario with two fluids side by side in the first junction generates droplets with high monodispersity

for a larger range of flow ratios, which is useful for high throughput reactions involving different reagents.

5.1 Introduction

As discussed in section 2.5, Droplet-based microfluidics has been increasingly developed due to its capability to perform high-throughput combinatorial testing for biological, chemical, and material applications [3, 25, 27, 50], such as polymerase chain reactions (PCR) [335, 376], cell culture [377], drug screening [354], microbeads [329] or nanoparticles synthesis [324, 326, 327]. One of the key functions demanded in exploiting droplet microfluidics for high throughput analysis is encapsulation of single cells or particles within individual droplets, which enables the efficient use of the droplets as micro-vessels at the highest droplet generation rate, while preventing interactions between cells or particles. In general, encapsulation of single cells or particles in droplets can be achieved during droplet formation cycles where an aqueous solution suspended with cells or particles is the dispersed phase, and an immiscible oil that is compatible with the aqueous phase and chip material for desirable assays is the continuous phase. To ensure uniform and high-throughput biochemical reactions in droplets, numerous studies have been reported to address two key problems: increasing the rate of single encapsulation (i.e. the number of droplets that are encapsulated with single cell/particle over the total number of droplets generated) and generating monodispersed droplets.

When cells are randomly distributed in the suspension, the number of cells encapsulated in droplets follows the Poisson distribution [342]. Therefore, the cell concentration is often highly diluted to ensure single-cell encapsulation, which however results in a large number of empty droplets and thus increases the waste of reagents, and the need for additional droplet sorting procedures [346, 378]. To increase the rate of single encapsulation, a number of approaches have been reported. Edd *et al.* [348] used hydrodynamic self-organization within a high aspect-ratio microchannel to distribute evenly spaced cells, and then synchronize cell encapsulation with the frequency of droplet generation, resulting in a rate of single encapsulation as high as 80%. Another work followed the similar cell self-organization mechanism by using Dean flow in a curved microchannel and achieved an efficiency of single encapsulation up to 77% [350]. Although these methods are excellent in achieving high efficiency for single encapsulation, the use of high flow rates generally required for self-ordering encapsulation makes the system sensitive to inherent and induced uncertainties because the system operates in dripping to jetting transitions.

Alternatively, the strategy of modifying the dispersed phase or the cells/particles using gel-based solutions has been used for encapsulation. For example, a close-packed ordering method was reported by Abate *et al*. [349], which encapsulated compliant gel particles into individual droplets using a configuration with two flow-focusing junctions in series and achieved an efficiency of encapsulation as high as 98%. This method could be employed for encapsulation of cells or particles into droplets; however cells or particles must be encapsulated into gels first. Polymer hydrogels have also been utilized to encapsulate cells in a similar configuration [330] where the mixture of hydrogel solutions and cell suspension is the dispersed phase while paraffin oil is the continuous phase. This configuration allows the chemical composite and concentration of the dispersed phase to be well controlled in the first junction and eventually in the droplet generated in the second junction. In addition, the dispersed phase is accompanied by the continuous phase on both sides resulting in more symmetric shearing which improves stability and control over droplet formation. Therefore this configuration is one of the ideal choices for encapsulation strategies. Adding hydrogel solutions or other water-cosolvent mixtures into the cell suspension could potentially cause spatial variation in its viscosity and the interfacial tension between the dispersed and continuous phase, which would greatly affect the droplet generation dynamics and thus affect the monodispersity of the droplets [379]. Many existing studies on droplet generation in flow focusing geometries considered uniform viscosity between different flow streams that form the dispersed phase[36, 85, 103, 104, 128, 129] with few considering the influence of viscosity contrast between different flow streams on droplet formation and control as encountered in the practical applications for cell encapsulation.

It would be very important to develop fundamental understanding and ultimately design tools for the two-series flow focusing configurations involving viscosity contrast during droplet formation processes which prompts the study presented here. It is expected that the output of this study would also provide operational guidance to improve their robustness for practical applications. In this study, a configuration with two flow-focusing junctions in series is considered, where water-cosolvent mixtures, which have been widely used for pharmaceutical and cosmetic applications, are the dispersed phase and a low-viscosity silicone oil is the continuous phase. Among the commonly used cosolvents [380] such as ethanol, propylene glycol, glycofural and polyethylene glycols, and glycerol, glycerol is chosen in this study because the viscosity of glycerol and water mixtures could be varied significantly by changing the concentration of glycerol while their interfacial tension remains roughly the same. In this work, droplet formation was experimentally investigated by varying the concentration of glycerol and water (by weight) which results in as large as 32 in viscosity contrast

between flow streams that form the dispersed phase while maintaining a similar interfacial tension between the dispersed and continuous phase. The measured values are provided later. Droplet size, frequency and monodispersity were measured to study the droplet generation dynamics by varying the flow rate ratio, the capillary number and inlets of the dispersed phases.

5.2 Materials and Methods

For all experiments, a low-viscosity silicone oil (DC200, Sigma Aldrich, 10 cSt) was used as the continuous phase. Two glycerol/water mixtures (10% and 80% in wt %) were used to form the dispersed phases with different scenarios as illustrated in Figure 5.1. Viscosity was measured at room temperature (22℃) using a programmable rheometer (LVDV-III Ultra CPE, Brookfield Instruments) with a cone-plate spindle (CPE-40). Interfacial tension was measured using a Wilhemy plate tensiometer (Data Physics, DCAT 11). No surfactant was added to either of the phases to avoid the influence of mass transfer effects on the interfacial tension. The measured viscosity and interfacial tension for the 10% glycerol/water mixture (10%Glyc) were 1.37mPa.s and 37.1mN/m, respectively and for the 80% glycerol/water mixture (80%Glyc) were 44.1mPa.s and 34.8mN/m, respectively. The microchannels were fabricated using polydimethylsiloxane (PDMS) via standard soft-lithography techniques.

The flow system consists of a high precision microfluidic pressure control system (MSFC 8C, Fluigent) and three in-line flow sensors (SLG 1430, Sensirion). Droplet formation was visualized using an inverted epifluorescence microscope (Eclipse Ti, Nikon) with a 20x objective and a high speed camera (Phantom v210, Vision Research). The frame rate for each video was set to be 5000fps. The detailed experimental setup can be found in Chapter 3. For each scenario with a particular viscosity contrast, different input pressures were applied to span a large range of capillary number and flow rate ratios. The flow rates of each experimental scenario are provided in Appendix B.

The channel network as shown in Figure 5.1(a) is designed to ensure that its performance is insensitive to uncertainties such as flow rate fluctuations and tubing compliances and the required pressure is within the limit of the pressure system which is 1bar. In brief, the distance between the two junctions cannot be too long so that the diffusion between the dispersed phases can be neglected. On the other hand, the distance should be long enough to make sure that the stratified flow is fully developed before fluids penetrate into the second junction. In the design, the distance was set to be 300 μm after preliminary testing. The cross-sectional shape of the microchannel is rectangular and the

channel depth for each chip is assumed to be uniform. Since silicone oil swells PDMS, the actual dimensions of the microchannels are smaller than the nominal dimensions and therefore were experimentally measured after the PDMS channels were sufficiently swollen. The actual channel width and height were measured as 88 µm and 36.3 µm, respectively. The method for measuring channel height can be found in section 3.4.

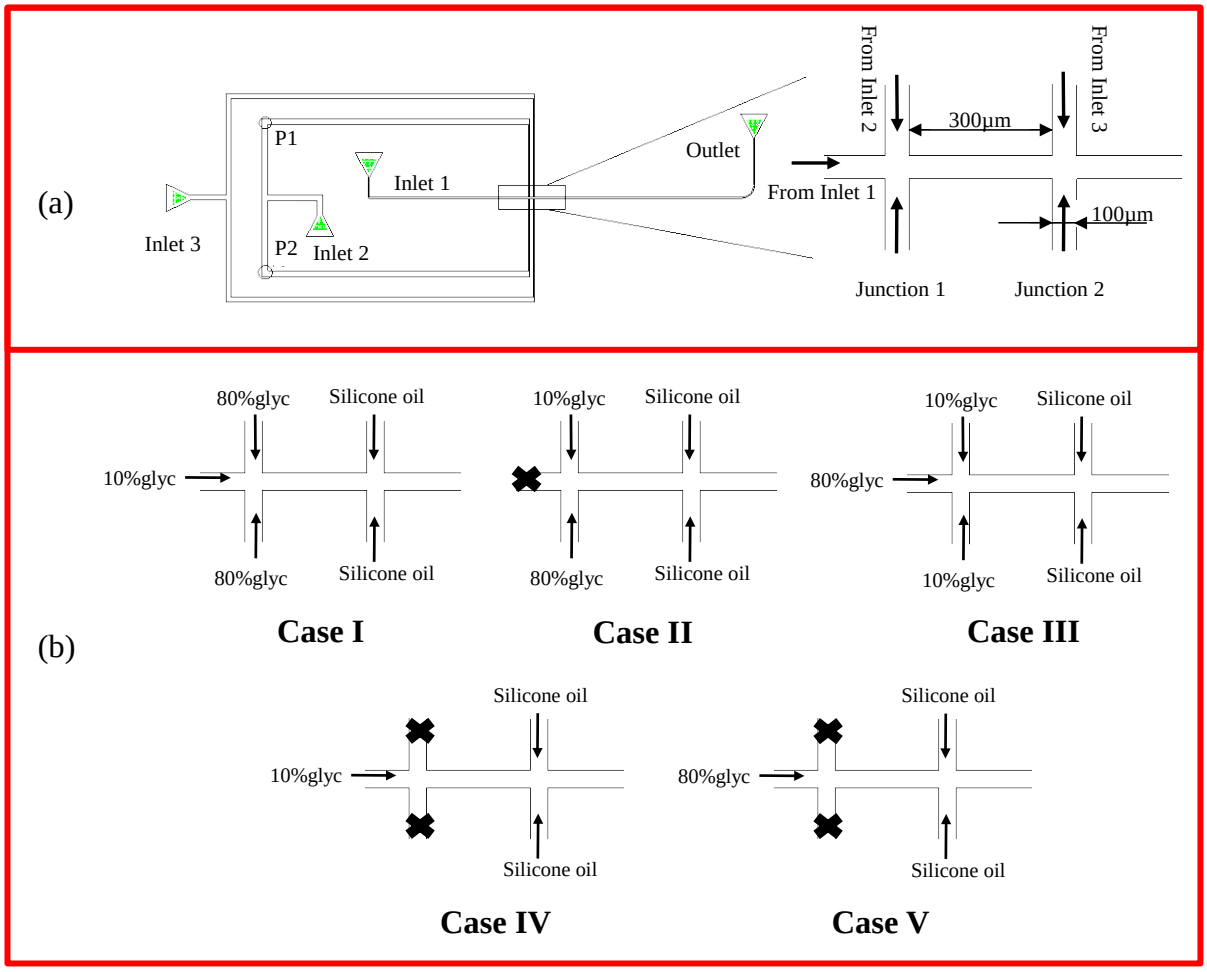

Figure 5.1 (a) Sketch of the microchannel design. The channel width is set to be 100µm, the height 40µm and the distance between the two junctions 300µm. Inlets 1 and 2 are for the dispersed phase and inlet 3 is for the continuous phase. (b) Sketch of flow combinations at the flow focusing junctions.

The flow scenarios are illustrated in Figure 5.1(b). During the droplet formation process, the glycerol mixtures were injected into the first flow-focusing from inlet 1 and 2 which formed a stratified flow at the first junction. The stratified flow stream was then squeezed into droplets by the continuous phase in the second junction. There are three combinations of the stratified flow structure corresponding to the two miscible liquids flowing into the first junction. In Case I, the low viscosity liquid (10%glyc) is pumped into the first junction from inlet 1, and the high viscosity liquid (80%glyc) is pumped into the first junction from inlet 2, which forms a sandwiched structure with the 10% glyc in the middle and 80% glyc accompanying its two sides. In Case II, both inlet 1 and 2 are blocked and two new inlets are made at P1 and P2 through which 10%glyc and 80%glyc are pumped respectively forming a stratified flow side by side. In Case III, 80%glyc is pumped from inlet 1 and 10%glyc from inlet 2 forming a sandwiched structure, opposite to Case I with 80% glyc surrounded by 10% glyc. Each structure finds its own applications. For example, the sandwiched structure allows cells or particles to be focused and spaced so that encapsulation is controllable while the stratified flow structure is useful for reactions involving different reagents.

In order to fully understand the influence of stratified flow on encapsulation, experimental results obtained for the above three cases are compared with that obtained from the cases without stratified flow structures - pure 10%glyc or 80%glyc as the dispersed phase as shown in Case IV and Case V, respectively. In these two cases, inlet 2 is blocked and the dispersed phase is pumped into the second junction through inlet 1 with a flow rate equal to the total flow rate of the dispersed phase for Case I – III (a combination of 10%glyc and 80%glyc).

5.3 Experimental Results and Discussions

5.3.1 Droplet generation with either pure 10%glyc or pure 80%glyc as the dispersed phase

To compare the droplet generation process between two scenarios - using a stratified flow with a viscosity contrast as the dispersed phase and using pure 10%glyc or 80%glyc solution as the dispersed phase, experimental conditions such as channel layout and geometry and flow rates were kept the same. Figure 5.2(a) and Figure 5.2 (b) show an example of droplet formation cycle which consists of three stages for both Case IV and Case V, respectively. First, a filling stage (I), where the dispersed phase returns to a semilunar shape due to the interfacial tension after the dispersed phase pinches off and starts filling the main channel. The interface continues to grow while the continuous

phase bypasses the droplet filling the space between the previously formed droplet and the new one. Eventually, the growing interface blocks the flow from the side channels, causing the upstream pressure in the continuous phase to increase until it reaches a critical value where the continuous phase begins to squeeze the interface and the necking stage begins (II). During the necking stage, the dispersed phase is still being injected into the droplet at a constant flow rate while the neck collapses. Once the neck reaches a critical size, the collapse accelerates, triggering the pinch-off stage (III), which culminates with the droplet detaching. The newly formed droplet is pushed downstream and the cycle restarts. The pinch-off time is small and combined with the necking stage.

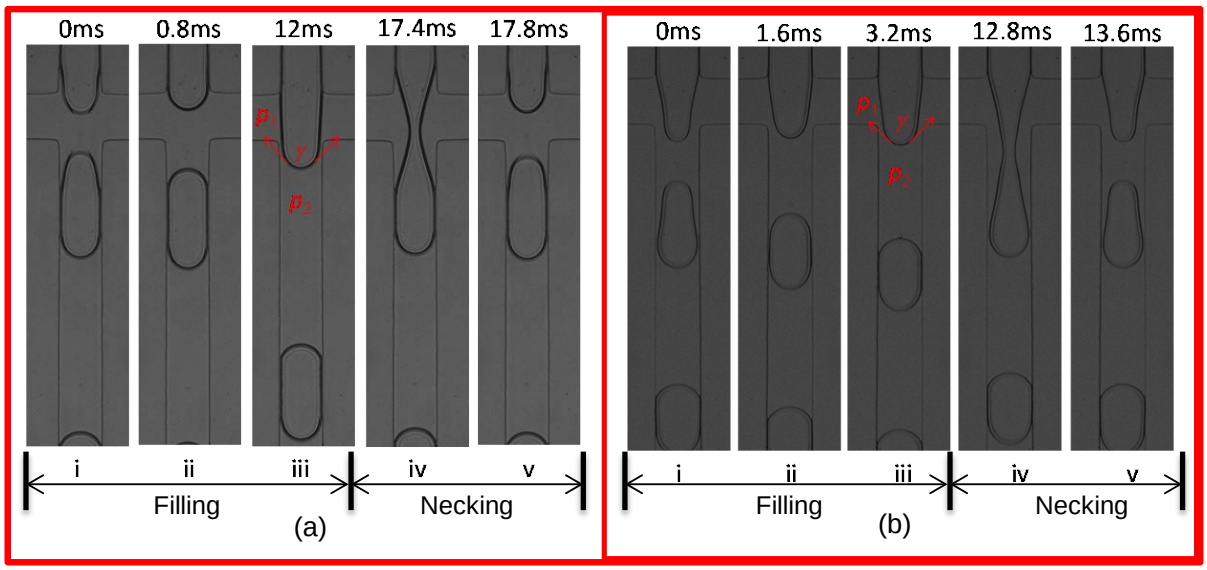

Figure 5.2 Droplet generation process. (i) Droplet pinches off; (ii) Dispersed phase returns back to semilunar shape due to the interfacial tension and starts filling the main channel; (iii) End of filling stage and the silicone oil starts squeezing the dispersed phase; (iv) The necking width reaches to a critical value and droplet starts pinching off; (v) Droplet pinches off and a new droplet is forming. (a) Pure 10%glyc as the dispersed phase with the flow rate of silicone oil and 10%glyc as $Q_{\text{oil}} = 4\mu\text{l/min}$ and $Q_{10\%\text{glyc}} = 1.62\mu\text{l/min}$, respectively; and (b) pure 80%glyc as the dispersed phase with flow rate of silicone oil and 80%glyc as $Q_{\text{oil}} = 4\mu\text{l/min}$ and $Q_{80\%\text{glyc}} = 1.62\mu\text{l/min}$, respectively.

With the same flow rates of both liquids and the same channel dimensions, Figure 5.2 shows that the filling time of 10%glyc ($\Delta t_{\text{filling\_10\%}} = 12\text{ms}$) is much longer than that of 80%glyc ($\Delta t_{\text{filling\_80\%}} = 3.2\text{ms}$), which can be understood from the force balance. There are three forces acting on the droplet: shear

force, interfacial tension force and pressure gradient. Since the droplet generation is confined in the squeezing regime (Ca<0.006 for all experimental conditions), the shear force can be ignored. Figure 5.2 shows the direction of interfacial tension force, which suspends the droplet from penetrating into the main channel. The interfacial tensions are similar for 10%glyc and 80%glyc which results in similar interfacial tension forces for both cases. However, the similar interfacial tension force cannot pull back 80%glyc as much as it does for 10%glyc due to the high viscosity of 80%glyc, as shown in stage (ii) in Figure 5.2(b). As a result, 80%glyc quickly fills in the intersection causing the pressure in the continuous phase to build up and quickly reach the critical value due to the higher resistance associated with 80%glyc, which triggers the necking stage.

The necking time for 10%glyc ($\Delta t_{\text{Necking\_10\%}}$=5.8ms) is shorter than that for 80%glyc ($\Delta t_{\text{Necking\_80\%}}$=10.4ms) because 80%glyc has a larger resistance to compression due to its high viscosity. The pinch-off position of 80%glyc is lower than that of 10%glyc (see stage iv in Figure 5.2(b)). Although the necking time of 80%glyc is longer than that of 10%glyc, its filling time is shorter. Therefore, the total droplet generation process for 80%gylc is shorter than that for 10%glyc resulting in a smaller droplet size which is scaled with the time of droplet formation. A comprehensive model for predicting the size of droplet generated in a flow focusing geometry with one single liquid as the dispersed phase has been previously reported for the squeezing regime, expressed as,

$$\frac{V_{\text{d}}}{w^2 h} = \alpha + \beta\varphi \qquad \textbf{(5.1)}$$

where V_{d} is the droplet volume, w the channel width, h the channel height, $\alpha = \frac{Q_{\text{d}} \times \Delta t_{\text{filling}}}{w^2 h}$, $\beta = \frac{Q_{\text{c}} \times \Delta t_{\text{necking}}}{w^2 h}$, and φ the flow rate ratio, $Q_{\text{d}} / Q_{\text{c}}$. Therefore, experimental results show that under the same flow conditions, less viscous fluid has a larger α and a smaller β compared to more viscous fluid.

5.3.2 Droplet generation with stratified flow as the dispersed phase

Droplet generation dynamics can be greatly influenced by the nonuniform viscosity of the dispersed phase. To study the influence of viscosity contrast on droplet generation, we considered a mixture of 10%glyc and 80%glyc as the dispersed phase where the flow rate ratio of 10%glyc to the

total flow rate of the dispersed phase, $\lambda = \frac{Q_{10\%glyc}}{Q_{10\%glyc} + Q_{80\%glyc}}$ was varied. For all the experiments the flow rate of the continuous phase and the total flow rate of the dispersed phase were fixed at $4\mu l/min$ and $1.62\mu l/min$, respectively, so that the flow rate ratio between the dispersed phase and the continuous phase, φ, was fixed at $\varphi = 0.4$, which renders the flow in the squeezing regime. λ was varied from $0 \sim 1$ where '$\lambda = 0$' represents pure 80%glyc as the dispersed phase, while '$\lambda = 1$' represents pure 10%glyc as the dispersed phase. The rest of experimental conditions are listed in Appendix B, as Exp #1 - #7. Figure 5.3 shows the non-dimensional droplet volumes with the variation of λ for three cases.

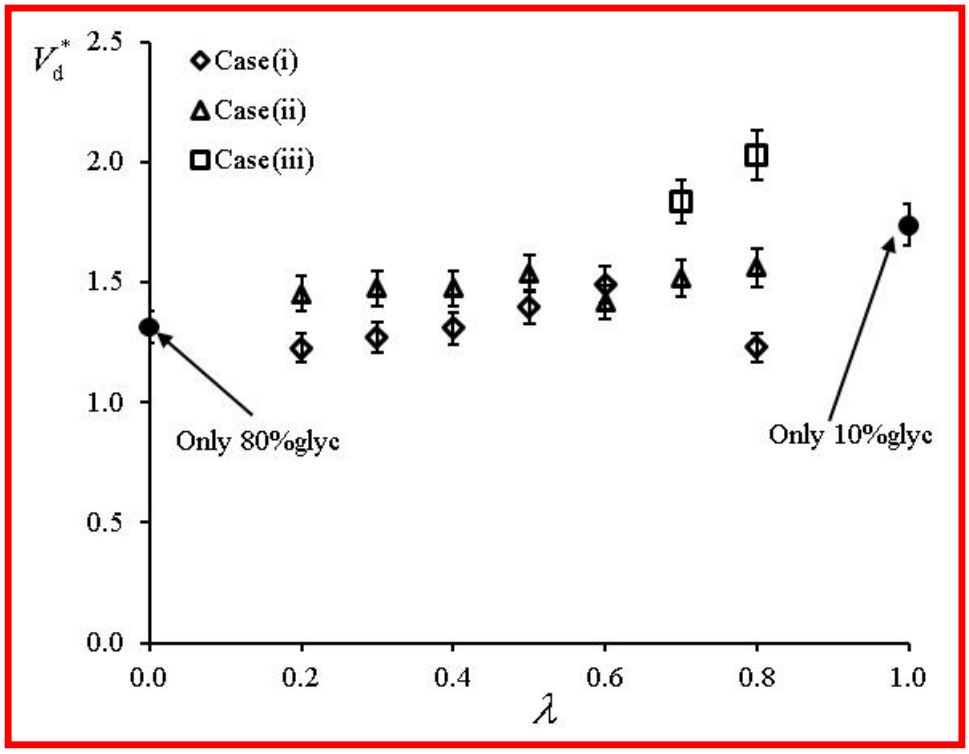

Figure 5.3 Non-dimensional droplet volume under different flow ratios of 10%glyc/ (10%glyc+80%glyc), with a fixed flow rate of $Q_{oil} = 4\mu l/min$ for the continuous phase and $Q_{10\%glyc+80\%glyc} = 1.62\mu l/min$ for the dispersed phases. Non-dimensional droplet volume is defined as $V_d^* = \frac{V_d}{w^2 h}$, where w is the channel width, h channel height.

Case I: In this case, low viscosity 10%glyc is surrounded by high viscosity 80%glyc. Droplet volume increases with the flow rate of 10%glyc when $\lambda < 0.6$, however; decreases dramatically when λ reaches 0.8. At $\lambda = 0.7$, droplets are generated with one bigger and one smaller droplet alternately. As discussed in subsection 5.3.1, the filling time depends on the resistance that the dispersed phase experiences when penetrating into the main channel, which is a combined effect of interfacial tension force for pulling back and pressure gradient for pinching during the formation cycle. Lower viscosity fluids have a longer filling stage and a shorter necking stage while higher viscosity fluids have a shorter filling stage and a longer necking stage. For stratified flow, the increase in pressure gradient in the continuous phase mainly depends on the fluid that contacts the continuous phase which is the outer layer of the fluid, so does the filling time.

In Case I, when λ is small, 80%glyc fully occupies the oil-water interface during the filling stage as shown in Figure 5.4(a), and thus the filling time is close to that when $\lambda = 0$ (the case of 80%glyc only) though the necking time is shorter because the inner fluid of 10%glyc reduces the resistance to compression during the necking process. Therefore, the resulting droplet size is smaller than that when $\lambda = 0$. When λ increases, the proportion of 10%glyc in droplet will increase and will be partially present at the oil-water interface resulting in an increase in the filling time. Meanwhile, the necking time will decrease due to the increase of 10%glyc in the neck region. Overall, the total time of the droplet generation process and droplet size will increase with λ.

When λ increases to 0.7, 10%glyc partially occupies the oil-water interface during the filling stage and necking stage, which creates two necks as shown in Figure 5.4(b). Therefore $\lambda = 0.7$ will generate droplets with one bigger and one smaller alternately. It is a transition regime between small λ and large λ. When λ is large enough ($\lambda = 0.8$ in the experiment), 80%glyc is still on the oil-water interface during the filling stage, which leads to a short filling time, but 10%glyc fully occupies the neck during the necking stage, which leads to a very short necking time, as shown in Figure 5.4(c). Therefore, the droplet size will dramatically decrease, much smaller than when $\lambda = 0$ (the only 80%glyc case)

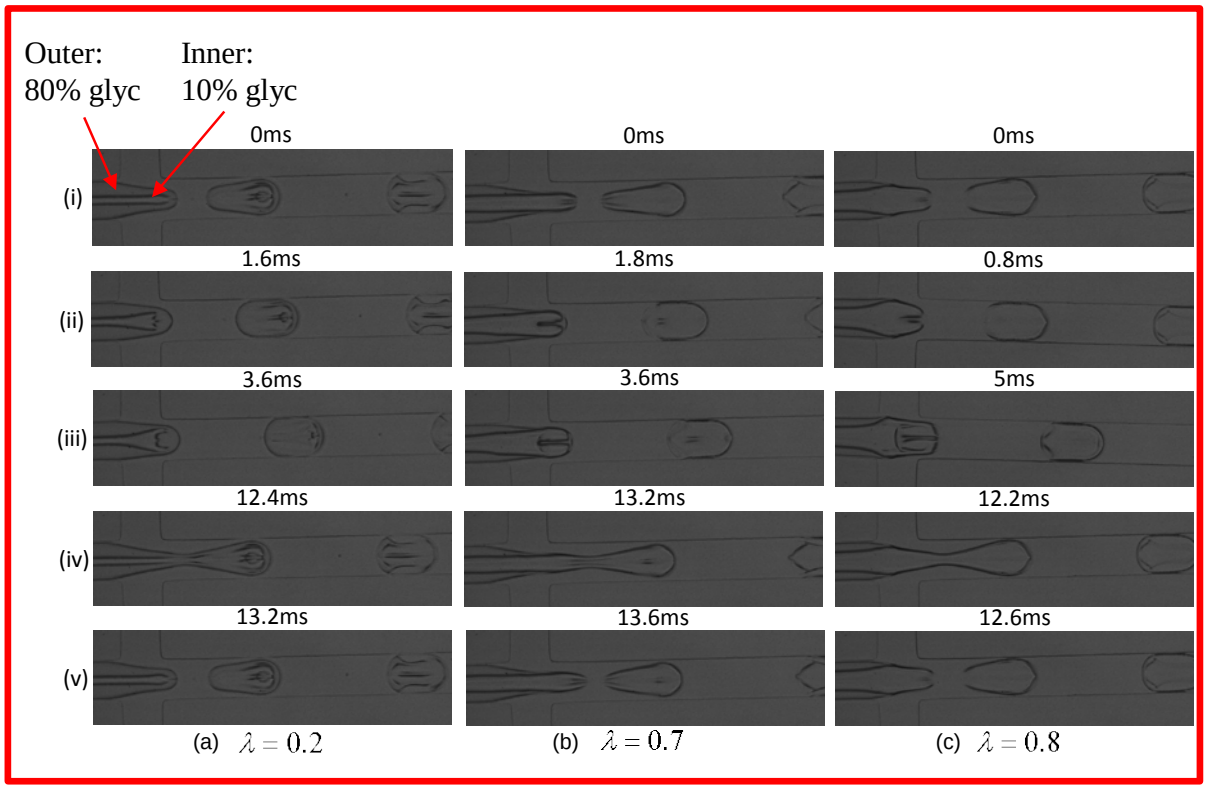

Figure 5.4 Droplet generation process (i) Droplet pinches off; (ii) Dispersed phase returns back to semilunar shape due to the interfacial tension and starts filling the main channel; (iii) End of filling stage, and the silicone oil starts squeezing the dispersed phase; (iv) The necking width reaches a critical value and droplet starts pinching off; (v) Droplet pinches off, and a new droplet is forming. (a) $\lambda = 0.2$, $Q_{oil} = 4\mu l/min$, $Q_{10\%glyc} = 0.32\mu l/min$, $Q_{80\%glyc} = 1.3\mu l/min$; (b) $\lambda = 0.7$, $Q_{oil} = 4\mu l/min$, $Q_{10\%glyc} = 1.13\mu l/min$, $Q_{80\%glyc} = 0.49\mu l/min$; (c) $\lambda = 0.8$, $Q_{oil} = 4\mu l/min$, $Q_{10\%glyc} = 1.30\mu l/min$, $Q_{80\%glyc} = 0.32\mu l/min$

Case II: in this case, 10%glyc and 80%glyc penetrate into the mail channel side by side with 10%glyc coming from the top and 80% from the bottom. Each fluid occupies one side of the oil-water interface, both in the filling and necking stages, as shown in Figure 5.5(a) ~ (c). Therefore, both the filling and necking times will be between those for the cases with $\lambda = 0$ and $\lambda = 1$, and thus the droplet size will be between those two cases as well. The droplet size will increase with λ because the droplet generation process will get close to the case with pure 10%glyc when 10%glyc proportion increases. Case II generates uniform droplets in the full range of λ.

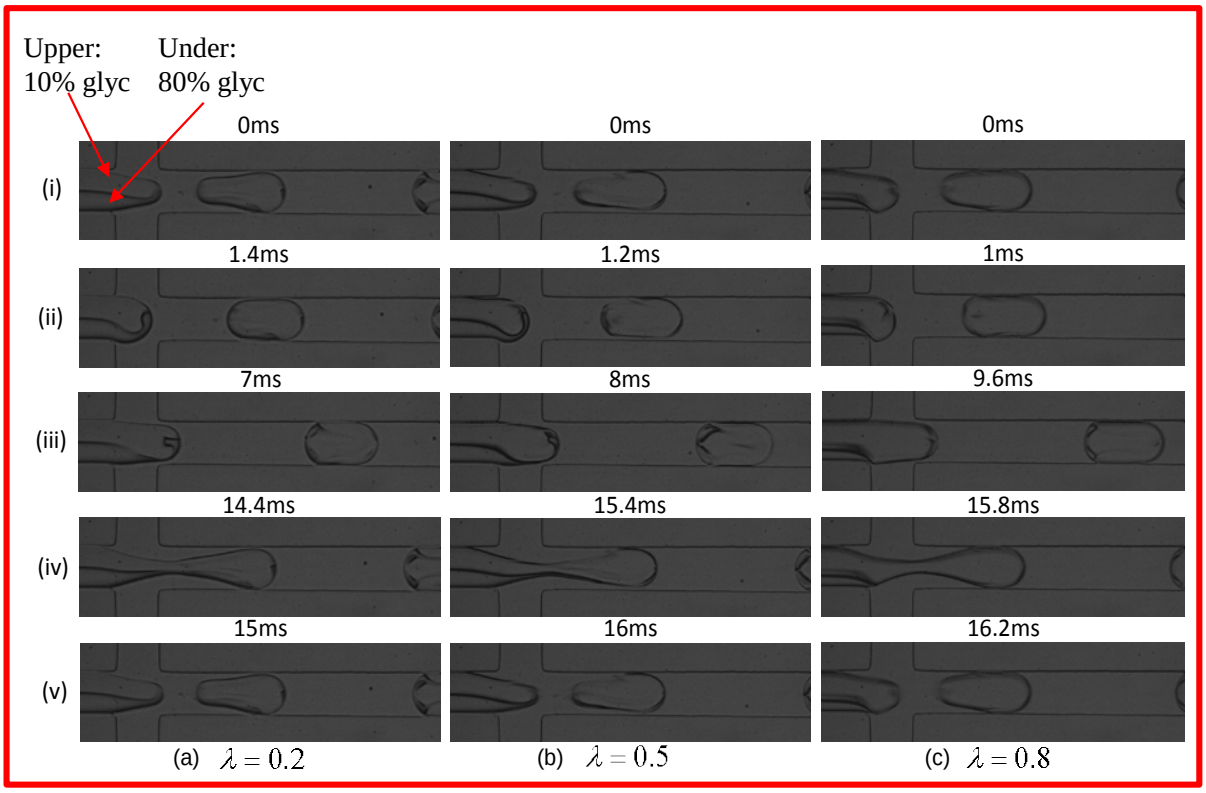

Figure 5.5 Droplet generation process (i) Droplet pinches off; (ii) Dispersed phase returns back to semilunar shape due to the interfacial tension and starts filling the main channel; (iii) End of filling stage, and the silicone oil starts squeezing the dispersed phase; (iv) The necking width reaches a critical value, and the droplet starts pinching off; (v) Droplet pinches off, and a new droplet forms. (a) $\lambda = 0.2$, $Q_{oil} = 4\mu l/min$, $Q_{10\%glyc} = 0.32\mu l/min$, $Q_{80\%glyc} = 1.3\mu l/min$; (b) $\lambda = 0.5$, $Q_{oil} = 4\mu l/min$, $Q_{10\%glyc} = 0.81\mu l/min$, $Q_{80\%glyc} = 0.81\mu l/min$; (c) $\lambda = 0.8$, $Q_{oil} = 4\mu l/min$, $Q_{10\%glyc} = 1.30\mu l/min$, $Q_{80\%glyc} = 0.32\mu l/min$

Case III: in this case, 80%glyc is the inner fluid that is surrounded by 10%glyc. When $\lambda \leq 0.6$, 80%glyc will occupy most of the channel cross-section due to its low velocity. The 80%glyc plays a role like a 'soft wall'. This case will create two necks during the necking stage. Therefore, it generates two different sizes of droplets alternately, as shown in Figure 5.6(a). When $\lambda \geq 0.7$, it starts generating uniform droplets as shown in Figure 5.6(b). The 10%glyc fully occupies the oil-water interface during the necking stage. Hence, the filling time is almost the same as for $\lambda = 1$ (the only 10%case). During the necking stage, the neck consists of both 10%glyc and 80%glyc, which

increases the resistance to compression compared to $\lambda = 1$ the case. Therefore, the necking time is longer than when $\lambda = 1$, leading to droplet size larger than 'pure 10%glyc case'.

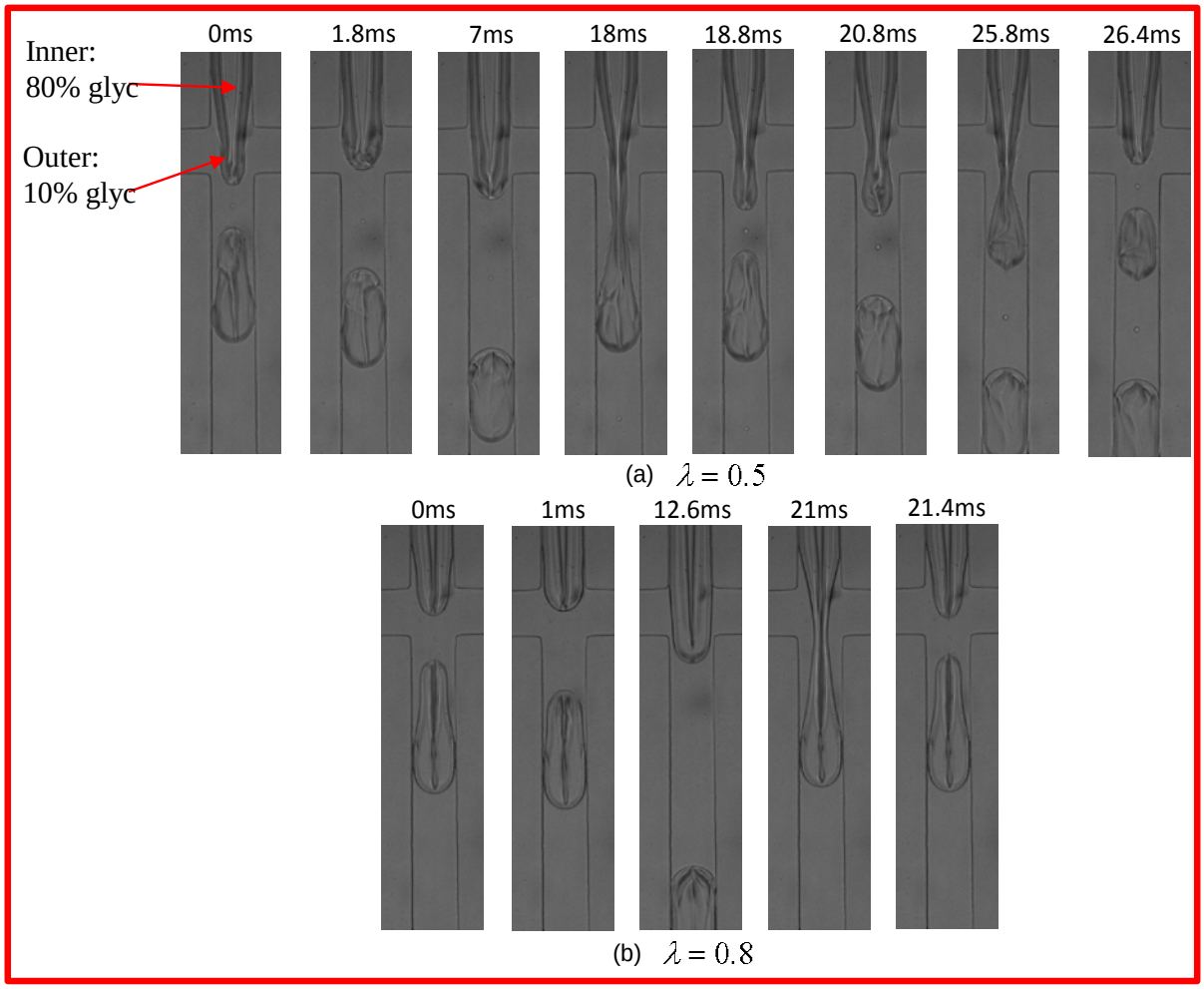

Figure 5.6 Droplet generation process with (a) $\lambda = 0.5$, $Q_{oil} = 4\mu l/min$, $Q_{10\%glyc} = 0.81\mu l/min$, $Q_{80\%glyc} = 0.81\mu l/min$ and (b) $\lambda = 0.8$, $Q_{oil} = 4\mu l/min$, $Q_{10\%glyc} = 1.30\mu l/min$, $Q_{80\%glyc} = 0.32\mu l/min$.

To verify the conclusion, more experiments (#8 - #37 in Appendix B) were performed for the five cases under the same flow rates of the dispersed and continuous phases, and microchannel dimensions with a reasonable range of flow rates and capillary numbers operating in the squeezing regime. The non-dimensional droplet volumes are plotted in Figure 5.7. From this figure, we can see that droplet sizes are the largest in case III, even larger than that in the 'pure 10%glyc case'. Case II generates droplets with sizes between those of the 'pure 10%glyc' and 'pure 80%glyc' cases. Droplet sizes in

case I depend on the flow percentage of 10%glyc and will fall into different regimes. Figure 5.3 and Figure 5.7 provide two maps for estimating droplet size under the three cases.

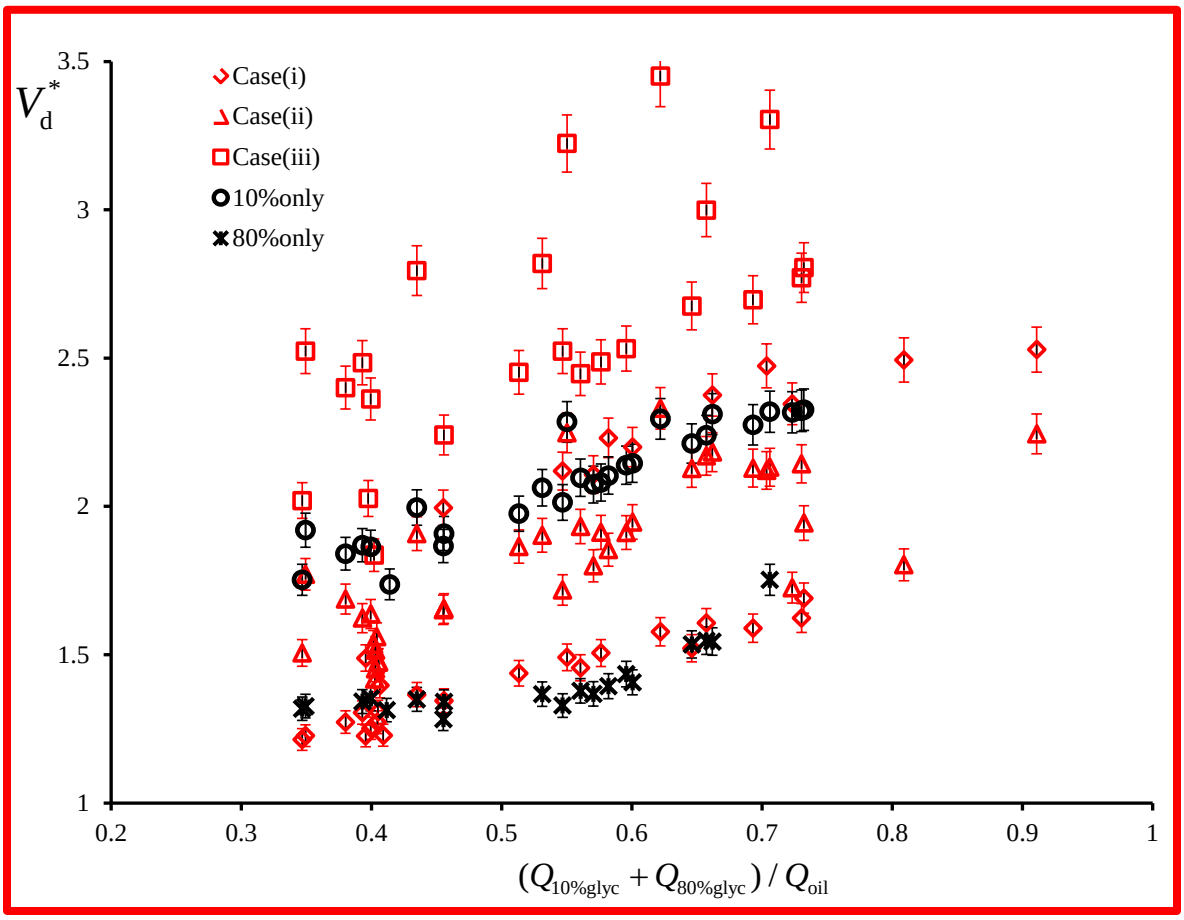

Figure 5.7 Non-dimensional droplet volumes under different flow ratios and capillary numbers. Experiment #1~37 were performed for each case (i, ii, iii, 10%glyc only and 80%glyc only), within flow rate errors in $\pm 3\%$.

5.3.3 Stratified flow with a viscosity contrast and its impact on single encapsulation

The stratified flow was studied with viscosity contrast under three cases: Case I - low viscosity fluid surrounded by high viscosity fluid; Case II -high viscosity fluid parallel to low viscosity fluid; and Case III -high viscosity fluid surrounded by low viscosity fluid, as shown in Figure 5.8.

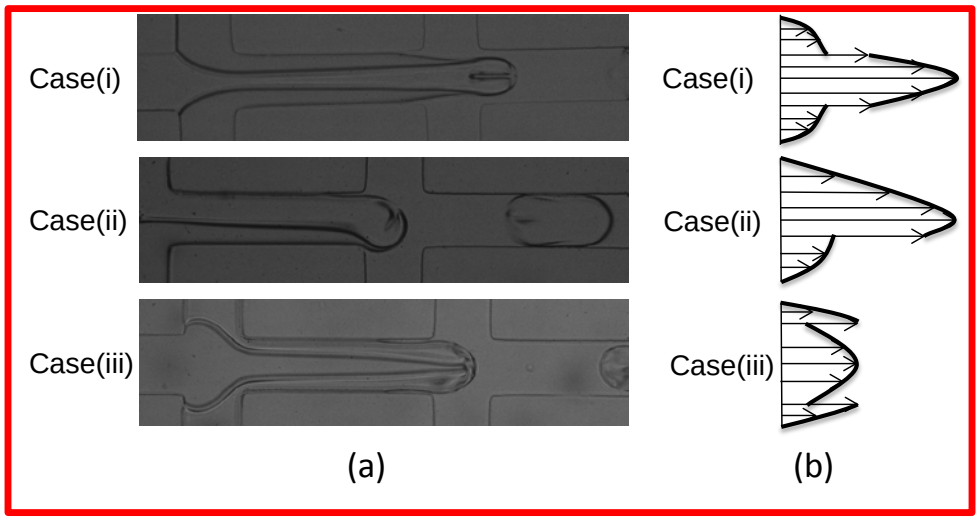

Figure 5.8 (a) Viscosity-stratified flow shapes when the dispersed phases start filling the main channel with flow rates $Q_{oil} = 4\mu l/min$, $Q_{10\%glyc} = 1.13\mu l/min$, $Q_{80\%glyc} = 0.49\mu l/min$ .Case I: 10%glyc is surrounded by 80%glyc, Case II: 10%glyc is parallel to 80%glyc, and Case III: 80%glyc is surrounded by 10%glyc. (b) Sketch of the velocity profile of viscous stratified flows in rectangular channel at the first junction for three cases.

The stratified flow with a viscosity contrast in a rectangular channel can be considered as the Poiseuille's flow due to its low Reynolds number. Hence, the velocity profile can be considered as a parabola. When the two different fluids go into the first junction, there exists a velocity contrast at the interface, as illustrated in Figure 5.8(b). Therefore, a shear force is present at the interface when the two fluids meet, which tends to increase the velocity of 80%glyc and reduce the velocity of 10%glyc until there is no velocity contrast at the interface. The stream width of each flow can be expressed as:

$$\varepsilon \propto \frac{Q}{\bar{v}} \tag{5.2}$$

where ε is the stream width, Q the flow rate, and $\bar{v}$ the area-average velocity. When the viscous stratified flow moves downstream, $\bar{v}_{80\%glyc}$ will increase and $\bar{v}_{10\%glyc}$ will decrease due to the shear force on the interface. Hence, $\varepsilon_{10\%glyc}$ will increase and $\varepsilon_{80\%glyc}$ will decrease. These findings were verified by experimental results, as shown in Figure 5.8(a), where one can see that 80%glyc speeds up and becomes thinner as it moves along the channel. When the stratified flow penetrates into the silicone

oil, 80%glyc keeps speeding up and occupies the front tip, then is forced back due to the interfacial tension.

As mentioned before, one of the strong motivations driving this study is to develop a tool for design optimization and operational guidance for single encapsulation using flow focusing geometries. Figure 5.8(a) indicates that Case III is the best choice for encapsulating single cells/particles within droplets because the inner stream (i.e. high viscosity 80%glyc) is being gradually focused downstream. If cells/particles are suspended in this fluid, they can be arranged in line and separated to ensure each droplet contains a single cell/particle. Each method has pros and cons. Despite the success of the existing methods for single encapsulation, it is clear that this method offers a few advantages. For example, it avoids the blockage problem that is often seen in the designs with high aspect-ratio channels as the high viscosity fluid acts as 'soft wall' and the width of that 'soft wall' can be controlled relatively easily by varying the aqueous flow rates. In addition, high aspect ratio channels are challenging to achieve with PDMS material due to its softness. In cases I and II, the middle stream where cells/particles are supposed to be suspended cannot be focused and thus are difficult to be aligned and synchronized with droplet generation.

To demonstrate single encapsulation in droplets by using case III, polystyrene microbeads (Polysciences, Inc.) with a diameter of $10\,\mu m$ were added to the 80%glyc solution. The particle suspension had a very high concentration of 1×10^{7} particles/ml after being mixed with 80%glyc. The particle ordering and subsequent encapsulation are shown in Figure 5.9. Single particle encapsulation was greatly improved with a stratified flow of Case III where beads are focused and spaced (Figure 5.9 (b)) and then encapsulated in droplets. On average, the single encapsulation is achieved with an efficiency of around whereas for the case without stratified flow, encapsulation of single or more particles was observed. Reduction of multiple encapsulation is possible by reducing the concentration of bead, which however will result in large number of empty droplets by following the Poisson distribution as discussed earlier.

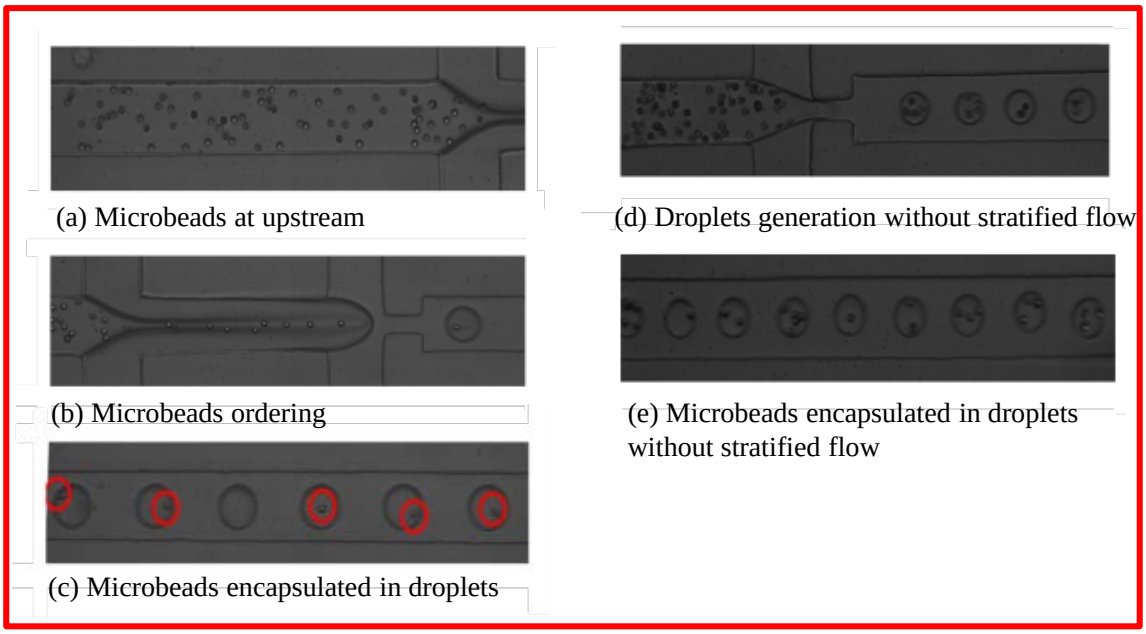

Figure 5.9 Images captured from experimental videos showing single particle encapsulation with a stratified flow of case (iii) (a ~ c) and without a stratified flow (d ~ e)

5.4 Conclusion

This work experimentally studied the droplet generation process in a flow focusing device using stratified flow with a viscosity contrast as the dispersed phase, which will provide operational guidance to improve the robustness of droplet generation in such configurations and achieve high efficiency in single encapsulation without the need for intensive liquid preparation or special channel geometry. The droplet size and forming period between different combinations of viscosity-stratified flow were compared and analyzed based on the physical model that developed in Chapter 4. Experimental results show that case III which has high viscous 80%glyc surrounded by 10%glyc in the first junction generates the largest droplet size, even larger than in only 10%glyc case. Droplet sizes in case II are between the cases with pure 10%glyc (Case IV) and pure 80%glyc (Case V). Droplet sizes in case I which has 10%glyc surrounded by 80%glyc in the first junction depend on the flow percentage of 10%glyc and will fall into different regimes.

Based on this study, it is found that each configuration has its own applications. For example, case III allows cells or particles to be focused and spaced so that single encapsulation is controllable while Case II generates stable and monodispersed droplets in a larger range of flow ratios between each reagent, which is useful for high throughput reactions requiring uniform droplet size.

5.5 List of Symbols

Ca	Capillary number
f	Droplet generation frequency
F	Frame rate
h	Channel height
N_{drop}	Number of the captured droplets
N_{frame}	The total number of frames
PDMS	Polydimethylsiloxane
Q	Flow rate
Q_{c}	Flow rate of the continuous phase
Q_{d}	Flow rate of the dispersed phase
$Q_{\text{10\%glyc}}$	Flow rate of 10% glycerol/water mixture
$Q_{\text{10\%glyc+80\%glyc}}$	Total flow rate of 10% glycerol/water mixture and 80% glycerol/water mixture
$Q_{\text{80\%glyc}}$	Flow rate of 80% glycerol/water mixture
Q_{oil}	Flow rate of silicone oil
$\Delta t_{\text{filling\_10\%}}$	Filling time of 10% glycerol/water mixture
$\Delta t_{\text{filling\_80\%}}$	Filling time of 80% glycerol/water mixture
$\Delta t_{\text{Necking\_10\%}}$	Necking time of 10% glycerol/water mixture
$\Delta t_{\text{Necking\_80\%}}$	Necking time of 80% glycerol/water mixture
$\overline{v}$	Area-average velocity
$\overline{v}_{\text{10\%glyc}}$	Area-average velocity of 10% glycerol/water mixture
$\overline{v}_{\text{80\%glyc}}$	Area-average velocity of 80% glycerol/water mixture
V_{d}	Droplet Volume
w	Channel width

Greek symbols

α	Defined as $\frac{Q_{\mathrm{d}} \times \Delta t_{\mathrm{filling}}}{w^2 h}$
β	Defined as $\frac{Q_{\mathrm{c}} \times \Delta t_{\mathrm{necking}}}{w^2 h}$
φ	The flow rate ratio of the dispersed phase to the continuous phase $Q_{\mathrm{d}} / Q_{\mathrm{c}}$
λ	Defined as the flow rate ratio $\frac{Q_{\mathrm{10\%glyc}}}{Q_{\mathrm{10\%glyc}} + Q_{\mathrm{80\%glyc}}}$
ε	Stream width

Subscripts

10%glyc	10% glycerol/water mixture
80%glyc	80% glycerol/water mixture
c	Continuous phase
d	Dispersed phase

Superscripts

*	Dimensionless form of variables

Chapter 6
Several Microfluidic Designs for Droplet Generation and Manipulation

This chapter presents several microfluidic designs for droplet generation and manipulation. These projects were finished by collaborating with other colleagues.

6.1 Droplet Generation in Flow Focusing Devices with Various Junction Angles

In Chapter 4, Droplet generation in a flow focusing device has been extensively discussed. The flow focusing device discussed in Chapter 4 has an angle of 90° at the junction, while flow focusing devices with other angles at the junction has not been discussed yet. This project aims to compare the operation of flow focusing devices with three different angles 45°, 90° and 135° as shown in Figure 6.1(a) ~ (c). The study started from Esther Amstad, a postdoctor from Harvard University, who used flow focusing devices with different angles to generate monodispered microparticels. She found that devices where the continuous phase is injected in the opposite direction to the flow direction of the dispersed phase (angle at the junction is larger than 90°) operate more robustly than conventional flow focusing generators (angle at the junction is 90°) as shown in Figure 6.1(d) ~ (f). The junction geometry also influences the drop size: Drops produced in devices with perpendicularly intersecting inlets are consistently smaller than those produced in other devices under identical conditions.

Esther Amstad produced microfluidic flow focusing devices from poly(dimethyl siloxane) (PDMS) using soft lithography. All channels are 40 μm wide and 40 μm tall, keeping the volume of the intersection constant at 64000 μm^3. The channel walls are modified with a perfluorinated oil (HFE7500) containing 1% of a perfluorinated trichlorosilane to make the channel walls non-wetting for aqueous solutions. She ran all the experiments by using HFE7500 as the continuous phase and added 1 vol% of a perfluorinated surfactant to stabilize the emulsion drops, and aqueous solution containing 2 vol% poly (ethylene glycol) (PEG, $M_w = 6\text{kDa}$) as the dispersed phase. The continuous phase has a viscosity of 1 mPa.s, and the dispersed phase has a viscosity of 2 mPa.s.

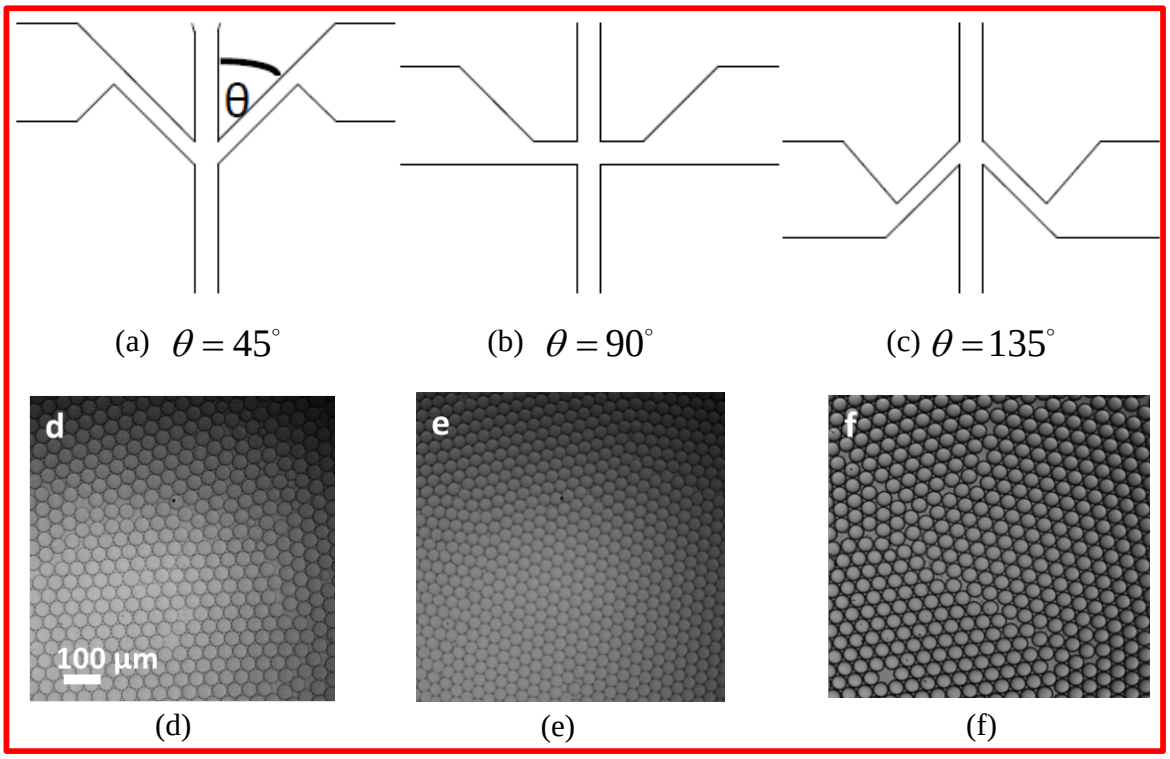

Figure 6.1 (a) ~(c) microfluidic flow focusing device geometries with different angles at the junction. The angle between the inlet of the dispersed phase and the continuous phase θ is (a) 45°, (b) 90° and (c) 135°. (d) ~ (f) Optical micrographs of drops produced in microfluidic devices with $\theta =$ (d) 45°, (e) 90° and (f) 135°. The viscosity of the dispersed phase is 8 mPas, that of the continuous phase is 1 mPas. The flow rate of the dispersed phase is 100 µl/h, that of the continuous phase 1 ml/h. The Experiments were done by Esther Amstad.

The mean droplet size was quantified by averaging at least 500 drops. The size of drops is consistently smaller if they are produced in devices with $\theta = 90^\circ$, as shown in Figure 6.2(a) ~ (b). I helped to analyze the data after got the experimental data from Esther. The difference in the size of drops produced in devices with $\theta = 90^\circ$ and those produced in the other devices becomes smaller if we increase the viscosity of the outer phase ten-fold by adding 30wt% of Krytox PGL107; nevertheless, even if the viscosity of the continuous phase is five times higher than that of the dispersed phase, drops produced in devices with $\theta = 90^\circ$ are still smaller, as shown by the empty symbols in Figure 6.2(a). Similarly, drops produced in devices with $\theta = 90^\circ$ are smaller if we keep the flow rate of the dispersed phase constant at 100 µl/h but increase the flow rate of the continuous phase, as shown in

Figure 6.2(b). However, if we plot the drop size as a function of the flow rate component of the continuous phase directed perpendicular to the main channel while it flows through the inlet, $q_{o,x}$ the sizes of drops produced in all three devices are very similar, as shown in Figure 6.2(c). This indicates that only $q_{o,x}$ and not the total flow rate of the continuous phase influences the drop size. The coefficient of variation, defined as the variance in the drop size divided by its mean, is independent on the device geometry, as indicated by the error bars in Figure 6.2. From Figure 6.2(c), one can see that droplet size decreases with the increase of $q_{o,x}$. With the same flow rate of the continuous phase, $q_{o,x}$ is the largest when $\theta = 90^\circ$, leading to smallest droplet size compared to $\theta = 45^\circ$ or 135°.

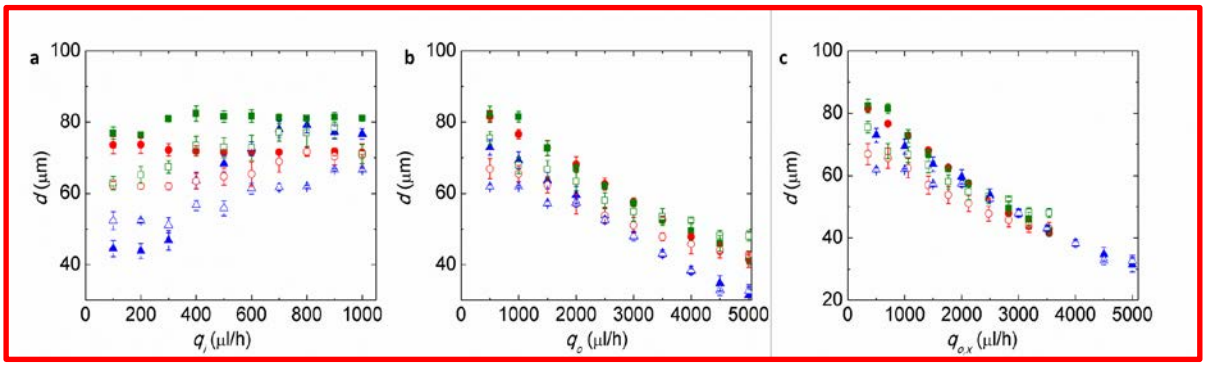

Figure 6.2 The size of drops produced in microfluidic flow focusing devices with $\theta = 45^\circ$ (●), 90° (▲), and 135° (■). The viscosity of the dispersed phase is 1 mPas, that of the continuous phase is 1 mPas (filled symbols) and 10 mPas (open symbols). (a) The flow rate of the continuous phase is 1 ml/h, that of the dispersed phase is varied between 100 μl/h and 1000 μl/h. (b-c) The drop size as a function of the (b) flow rate of the continuous phase and (c) the velocity component of the continuous phase in the inlet that is directed perpendicular to the main channel. The flow rate of the dispersed phase is 500 μl/h.

In conclusion, the size of drops produced in flow focusing devices depends on the velocity component of the continuous phase directed perpendicular to the main channel while the fluid is in the inlet. Thus, the angle at which the inlet intersects the main channel, influences the drop size. Devices with $\theta = 90^\circ$ produce the smallest droplets because they have the largest velocity component perpendicular to the main channel. Moreover, this angle strongly impacts the robustness of the device operation: Devices with $\theta = 135^\circ$ operate more robustly.

6.2 A Droplet Generation on Demand System for Controlled Droplet Size

T-junction and flow-focusing geometries are the two most commonly used configurations to generate droplets. Both of them have very simple structures and can be easily integrated in a microfluidic system. However, the droplet size and frequency are very difficult to control because they are influenced by many factors, such as channel geometry, fluid properties and flow rates. Moreover, these parameters have non-linear influence on droplet size and frequency as analyzed in Chapter 4. The equations for calculating the droplet size are complex, which makes the adjusting of droplet size difficult in a short time. For example, if one needs to generate a stream of droplets with controlled droplet size gradient. It is hard to control droplet size on demand by using passive methods. Performing thousands of different reactions on a single chip will certainly require computer controlled droplet generation. Some droplet on demand systems were introduced in section 2.2.5. Here, a droplet on demand system was presented by using solenoid valves and a microcontroller.

The photograph of the droplet on demand system is shown in Figure 6.3(a). The purpose of the microcontrollers is to send appropriate signals to open or close the solenoid valves. The microcontrollers were first bought by a previous master student Boyang Yu to control pumps in a microflow cytometry system. I reused the microcontrollers for the droplet on demand system by modifying the design and rewriting the Real time operating system (RTOS) code. The microcontrollers (Renesas dev kit M32C/87) have more than 100 digital I/O pins which can manage over 100 valves in parallel, built-in clock and timers, serial connection to PC and interrupt handlers which can provide real-time processes. The microcontroller can be pre-programmed to manipulate the solenoid valves. The users can simply send high level commands to the controller via the serial port with a friendly interface. Therefore, one can use this microcontroller for high throughput droplet generation. RTOS code for generating digital output signals is attached in Appendix C. The code is modified and developed based on Boyang Yu's work [381].

The two solenoid valves are connected to the inlets of the continuous phase and the dispersed phase, respectively. The sketch of valve connection to a T-junction droplet generator is shown in Figure 6.3(b). The solenoid valves (ASCO AL1106) have fast response with a response time as low as 12ms. The orifice size inside the valves is 0.025 inch, and the power supply is only 6V. Therefore, they are suitable for controlling microfluidic flows. The maximum frequency of droplet generation can reach up to 40Hz. The flow can be controlled by opening or closing the solenoid valves. When solenoid valve 1 is closed, and solenoid valve 2 is open, the dispersed phase is injected into the main

channel and a droplet is formed. When solenoid valve 1 is open, and solenoid valve 2 is closed, the continuous fluid is injected into the main channel to stop droplet generation. The amount of the dispersed fluid that is injected into the main channel is purely determined by the valve opening time and flow rate of the dispersed phase, leading to a linear control over the droplet size.

Solenoid valves cannot be directly handled by the controller unit because they require 24V power, while the microcontroller only supplies 5V power. Therefore, optical switches are used to isolate the solenoid valves from the low power controllers due to its fast response and durability.

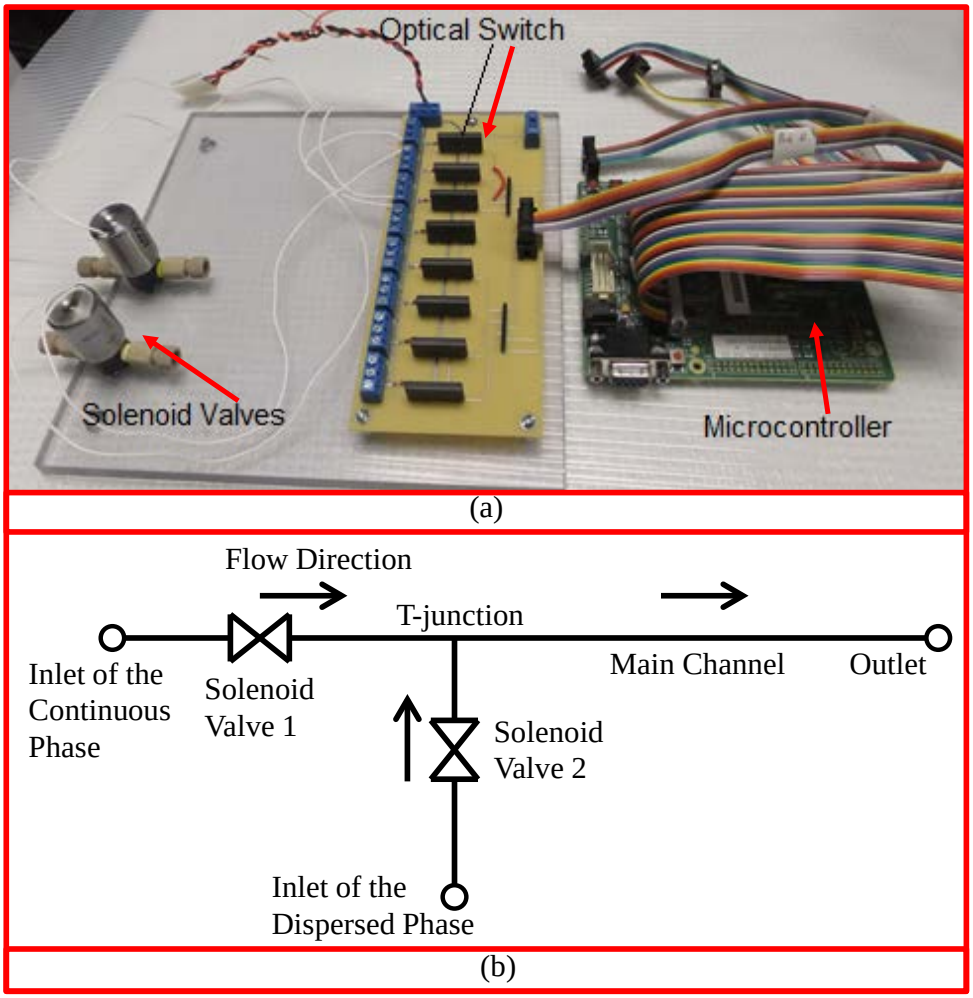

Figure 6.3 (a) Photograph of a droplet on demand system, consisting of a microcontroller, optical switches and two solenoid valves. (b) Sketch of valve connection to a T-junction droplet generator. The two solenoid valves are connected with the inlets of the continuous phase and the dispersed phase, respectively.

Figure 6.4 shows one example of droplet generation on demand. A signal sent from one of the digital outputs of the microcontroller with one short high level output voltage (Voh), and three long Voh, repetitively, is used to control valve 2. The other signal is used to control valve 1. When one signal is at Voh, the other one is at low level output voltage (Vol). The droplet size can be expressed as,

$$V_d = Q_d \cdot \Delta t \tag{6.1}$$

where V_d is droplet volume, Q_d is flow rate of the dispersed phase, and Δt is the valve opening time. With a constant flow rate Q_d, droplet volume is proportional to the valve opening time. From Figure 6.4, one can see that droplet sizes are proportional to the time of the signal at Voh, which indicates that this droplet on demand system works very well.

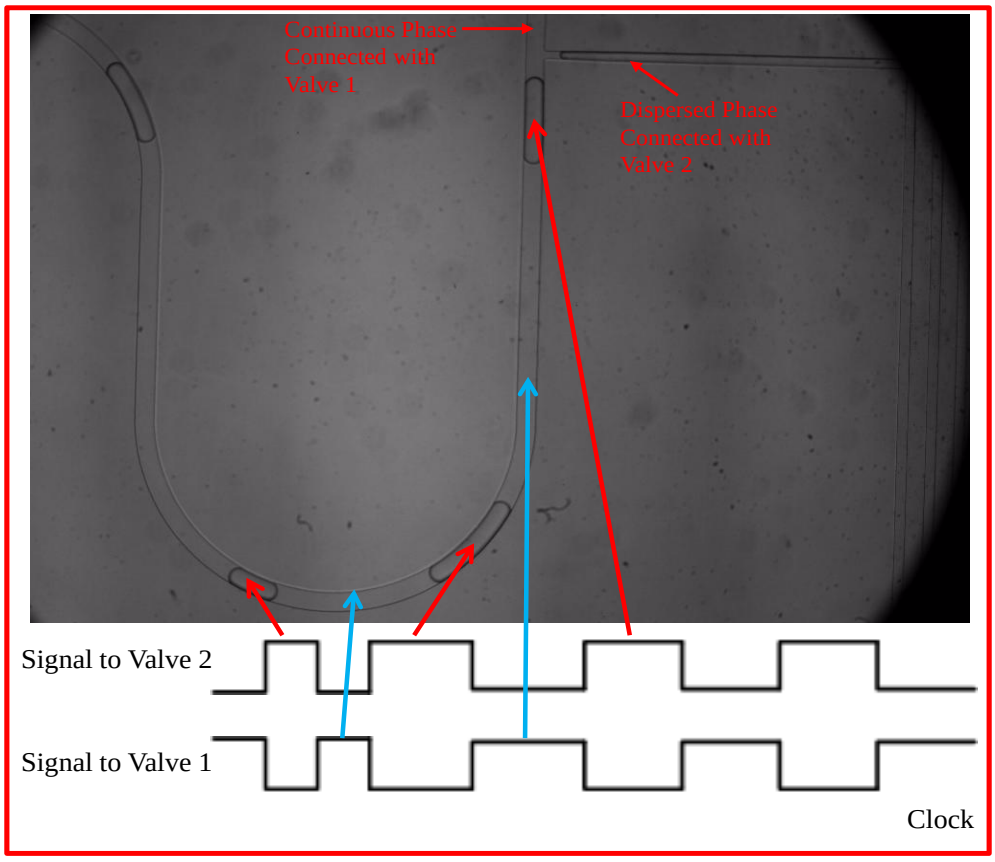

Figure 6.4 Droplet generation on demand captured from video using $4\times$ objective. Signals are sent from the digital outputs of microcontroller. Droplet length is determined by the opening time of valve 2.

6.3 A Microfluidic Design for Droplet Pairs Generation

6.3.1 Introduction

Since microfluidic chips are only a few centimeters in width, it is inevitable to add some curved microchannels during microfluidic circuit design. When droplets travelled through a curved microchannel, several of our lab members observed that the spacing between a droplet pair changed, which attracts our attention. The spacing between two droplets has a crucial influence on droplet passive sorting, and is usually considered as a constant during droplet travelling in a steady flow [382, 383]. The assumption of constant spacing between two droplets may not be true when droplets travel through curved microchannels. Therefore, it is urgent to study the motion of droplets travelling in curved microchannels for better manipulation of droplets. The motion of droplets in a straight channel has been widely studied as discussed in section 2.4. When a long bubble travels in a straight channel, the continuous phase liquid leaks through the thin films [295, 298, 299]. The bubble speed is different from the average speed of the continuous phase liquid, and the difference in speeds is controlled by the capillary number. However, the thin film thickness in a straight rectangular channel is reported to be uniform [298, 299], which indicates that the spacing between droplets doesn't change in a straight channel. The motion of a single large bubble in curved microchannels was numerically studied by Muradoglu *et al*. [305], who reported that the thin film between a bubble and the channel walls is thinner on the inside of a bend than on the outside of a bend. However, as far as I know, little work has been done on a train of droplets travelling in a curved channel, where the interaction between a droplet pair can change the spacing between droplets.

In order to study the interaction between droplets, a microfluidic design for generating a droplet pair is required. One of the key requirements for a droplet generator in this project is to ensure that droplet pairs have uniform size in order to eliminate the influence of droplet size variation on spacing change. As reviewed in subsection 2.3.4, many droplet pair generators have been proposed, such as breaking one droplet into two daughter droplets [223], alternating droplet formation at two opposing T-junctions [247] , a microfluidic dual nozzle [249], and a ladder structure for droplet synchronization [252] , etc. However, these droplet pair generators are very sensitive to pressure fluctuation in the microfluidic channels. A little fluctuation may lead to non-uniform droplet size in a pair. Hence, a novel design was developed to generate droplet pairs with well controlled spacing and uniform size. The uniqueness of this design is that it is capable of controlling the spacing between

two droplets with only one droplet generator, which eliminates the coupled effect of parallel droplet generators and hence, guarantees the uniformity of droplets.

6.3.2 Droplet Pair Generator Design

The droplet pair generator consists of one droplet generator, two diluting streams, and a droplet sorting structure as sketched in Figure 6.5. In the upstream, monodispersed droplets are generated by whatever the geometry, either flow focusing or T-junction. Then, the microfluidic channel is divided into two branches with a bypass connected between them. The bypass controls the droplets alternatively to flow into the up and down branch under proper conditions [384]. The slightly asymmetrical loop allows one droplet to catch up the other and thus to make droplet pairs. Two diluters are used to control the spacing between droplets.

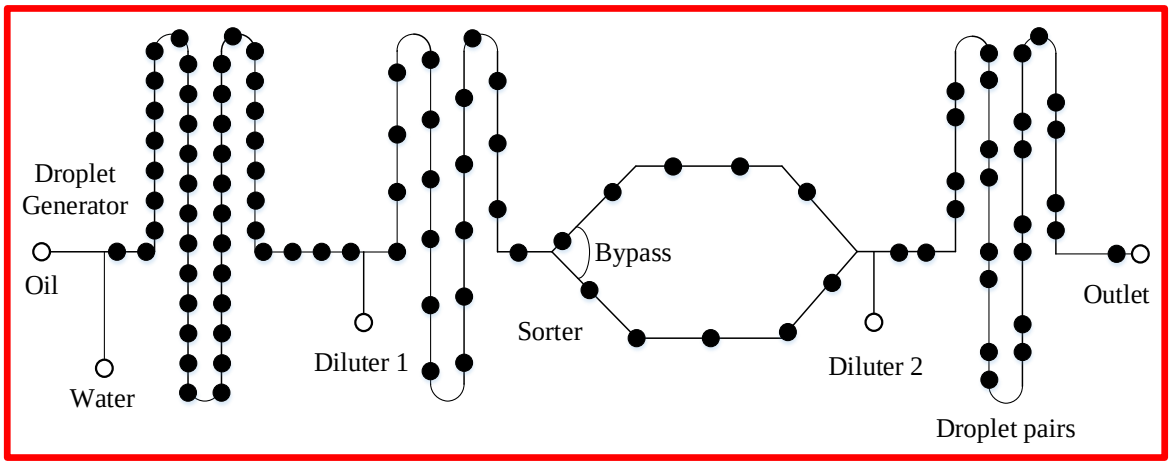

Figure 6.5 Sketch of droplet pair generator consisting of one droplet generator, two diluting streams, and a droplet sorting structure. The droplet generator is used to generate monodispersed droplets. The continuous phase liquid is pumped through two diluting streams to control the droplet spacing. The sorting structure is used to guide droplets into two branches alternatively.

The sorting device consists of two branches (branch 1 and 2) with a bypass connected between them as shown in Figure 6.6. The direction of the droplets flowing into either branch depends on the sign of $Q_{b1} - Q_{b2}$, where Q_{b1} is the flow rate of branch 1, and Q_{b2} is the flow rate of branch 2. If Q_{b1} is larger than Q_{b2}, the droplet will go into branch 1. If Q_{b1} is smaller than Q_{b2}, the droplet will go into branch 2. The bypass channel is set to very small hydrodynamic resistance and doesn't allow the droplet to flow through it. Hence, we can assume the pressure drop ($P_{b1} - P_{b2}$) between branch 1 and

branch 2 can be ignored. Therefore, the pressure drop in branch 1 $\Delta P_{b1} = P_Y - P_{b1}$ is the same as that in branch 2, $\Delta P_{b2} = P_Y - P_{b2}$ where P_Y is the pressure at the Y-junction, P_{b1} is the pressure at the end of branch 1, and P_{b2} is the pressure at the end of branch 2. According to Equations (6.2) and (6.3), the direction of droplet is determined by the hydrodynamic resistances of branch 1 and branch 2. When $R_{b1} < R_{b2}, Q_{b1} > Q_{b2}$ droplets go into branch 1. When $R_{b1} > R_{b2}, Q_{b1} < Q_{b2}$, droplets go into branch 2.

$$Q_{b1} = \frac{\Delta P_{b1}}{R_{b1}} \tag{6.2}$$

$$Q_{b2} = \frac{\Delta P_{b2}}{R_{b2}} \tag{6.3}$$

where R_{b1} and R_{b2} are the hydrodynamic resistances of branches 1 and 2, respectively. $\Delta P_{b1} = \Delta P_{b2}$.

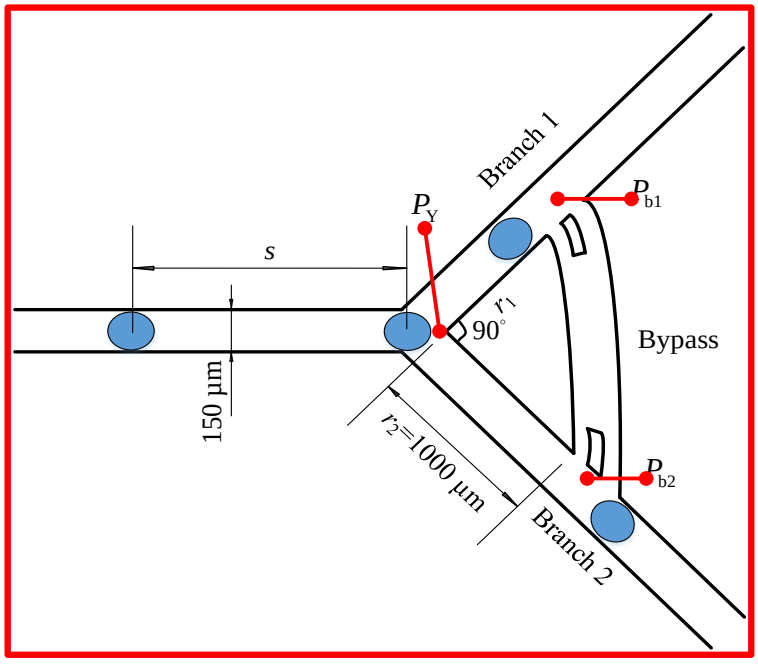

Figure 6.6 Sketch of bypass design for sorting droplets into two branches. The Y-junction angle is set to 90°. P_Y is the pressure at the Y-junction, P_{b1} is the pressure at the end of branch 1, P_{b2} is the pressure at the end of branch 2, s is the spacing between two droplets, r_1 is the length of branch 1, and r_2 is the length of branch 2. The pillars inside the bypass channel are used to prevent droplets from going into the bypass channel.

The length of branch 1 is set to be slightly smaller than the length of branch 2 ($R_{b1} < R_{b2}$). Therefore, the first droplet will go into branch 1, and this droplet will increase the hydrodynamic resistance of branch 1, leading to $R_{b1} > R_{b2}$. Hence, the next droplet will go into branch 2. By setting appropriate droplet spacing, s this design is able to let the droplets go into the two branches alternatively. In order to guarantee there is only one droplet in either of the two branches, the initial spacing between droplets s must satisfy the condition, i.e. $r_1 < s < 2r_1$, where r_1 is the length of branch 1. If the initial spacing is too large ($s > 2r_1$), the first droplet has already left branch 1 before the second droplet arrives at the Y-junction. Therefore, the droplets will always go into branch 1. The bypass channel acts like a filter. If the initial spacing is too small ($s < r_1$), when the third droplet arrives at the Y-junction, the first droplet hasn't left branch 1, yet. In this case, $R_{b1} < R_{b2}$ is not guaranteed when the third droplet arrives. Therefore, the droplets can't go into the branches alternatively.

To control the spacing between the droplet pairs, a model based on electric circuit analogy [385] is built to predict droplet spacing under different droplet frequency. The loop of the microfluidic network can be equivalent to a circuit which is shown in figure 4. The equivalent hydrodynamic resistance of the loop R_{eqv} can be expressed as,

$$R_{eqv} = \frac{R_2 R_3 \left(\frac{1}{R_2} + \frac{1}{R_4} + \frac{1}{R_5} \right) \left(\frac{1}{R_3} + \frac{1}{R_4} + \frac{1}{R_6} \right) - \frac{R_2 R_3}{R_4^2}}{\frac{R_3}{R_5} \left(\frac{1}{R_3} + \frac{1}{R_4} + \frac{1}{R_6} \right) + \frac{R_2}{R_6} \left(\frac{1}{R_2} + \frac{1}{R_4} + \frac{1}{R_5} \right) + \frac{R_2}{R_4 R_5} + \frac{R_3}{R_4 R_6}} \quad \textbf{(6.4)}$$

The hydrodynamic resistance in each branch R_i ($i = 1 \sim 7$) consists of two parts, i.e. the resistance of the continuous phase liquid and resistance of droplets inside each channel, which can be expressed as,

$$R_i = R_c + N \cdot R_{drop} \quad \textbf{(6.5)}$$

where R_c is the resistance of the continuous phase liquid, R_{drop} is the resistance of droplet, N is the number of droplets in each branch.

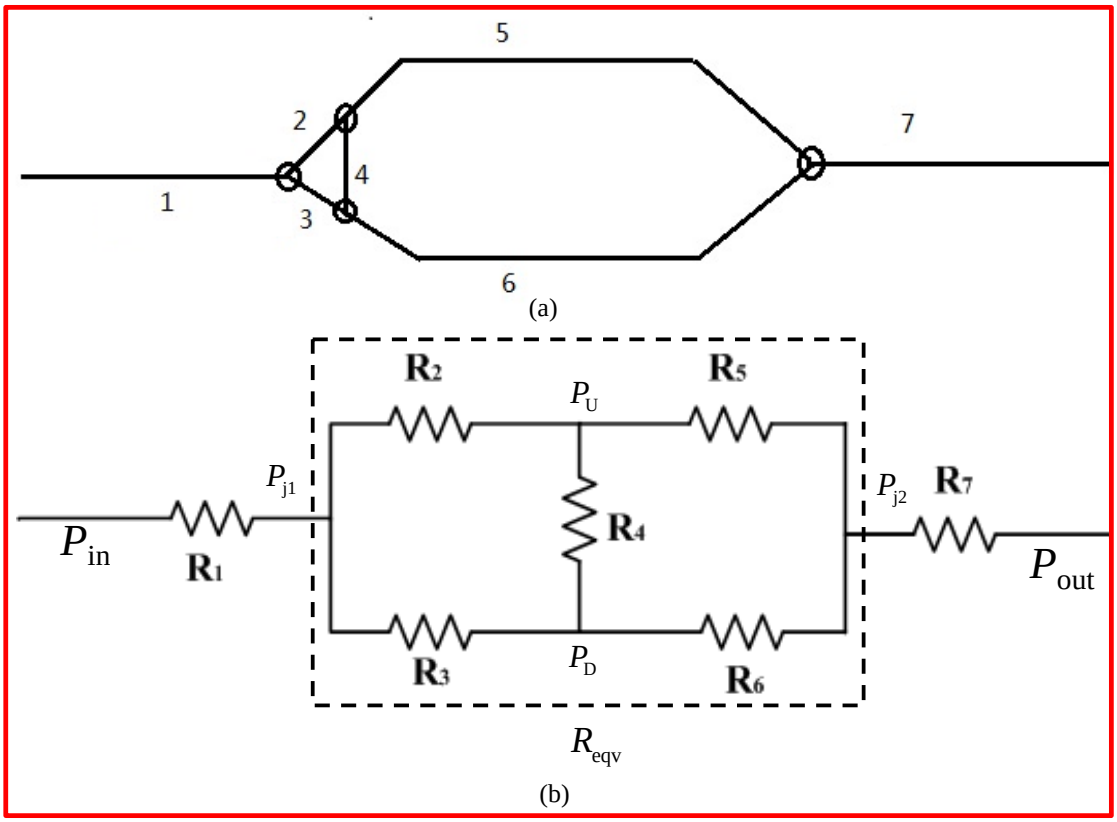

Figure 6.7 (a) Sketch of the bypass loop, 1 ~ 7 are the channel number; (b) Equivalent circuit network of the bypass loop. P_{in} is the pressure at the inlet of droplets, P_{out} is the pressure at the outlet of droplets, P_U is the pressure at the end of up branch, P_D is the pressure at the end of down branch, P_{j1} is the pressure at beginning of the loop, P_{j2} and is the pressure at the end of the loop. $R_1 \sim R_7$ are the hydrodynamic resistances of each channel, respectively.

The resistance of the continuous phase liquid can be estimated by the formula [369],

$$R_c = \frac{12\mu L}{wh^3\left(1-\frac{h}{w}\left(\frac{192}{\pi^5}\sum_{n=1,3,5}^{\infty}\frac{1}{n^5}\tanh\left(\frac{n\pi w}{2h}\right)\right)\right)} \quad \textbf{(6.6)}$$

where w, h, L are the width, height and length of the channel, respectively, and μ is the viscosity of the continuous phase liquid.

The resistance of a single droplet is estimated typically ~2-3 times larger than the equivalent resistance of oil that it replaced [383]. Here, the equivalent droplet length is defined as $L_{effdrop} = 3L_d$μm

, where L_d is the actual droplet length. The hydrodynamic resistance of a single droplet can be estimated by substituting $L_{effdrop}$ into Equation (6.6).

The pressures P_U and P_D can be expressed as,

$$P_U = \frac{\frac{R_4}{R_2}\left(1+\frac{R_4}{R_3}+\frac{R_4}{R_6}+\frac{R_2}{R_3}\right)P_{j1}+\frac{R_4}{R_5}\left(1+\frac{R_4}{R_3}+\frac{R_4}{R_6}+\frac{R_5}{R_6}\right)P_{j2}}{\left(1+\frac{R_4}{R_2}+\frac{R_4}{R_5}\right)\left(1+\frac{R_4}{R_3}+\frac{R_4}{R_6}\right)-1} \quad \textbf{(6.7)}$$

$$P_D = \frac{\frac{R_4}{R_3}\left(1+\frac{R_4}{R_2}+\frac{R_4}{R_5}+\frac{R_3}{R_2}\right)P_{j1}+\frac{R_4}{R_6}\left(1+\frac{R_4}{R_2}+\frac{R_4}{R_5}+\frac{R_6}{R_5}\right)P_{j2}}{\left(1+\frac{R_4}{R_2}+\frac{R_4}{R_5}\right)\left(1+\frac{R_4}{R_3}+\frac{R_4}{R_6}\right)-1} \quad \textbf{(6.8)}$$

Hence, the pressure drop in the bypass channel can be calculated as,

$$P_U - P_D = \frac{\left(\frac{R_4^2}{R_2R_6}-\frac{R_4^2}{R_3R_5}\right)\left(P_{j1}-P_{j2}\right)}{\left(1+\frac{R_4}{R_2}+\frac{R_4}{R_5}\right)\left(1+\frac{R_4}{R_3}+\frac{R_4}{R_6}\right)-1} \quad \textbf{(6.9)}$$

where $P_{j1} - P_{j2}$ is the pressure drop between the microfluidic loops.

The droplet distribution in the microfluidic network can be calculated following the steps:

1. Calculate the pressure drop P_i and flow rate Q_i for each branch ($i = 1 \sim 7$);
2. Calculate velocity of droplet using the formula $v_i = \alpha \frac{Q_i}{wh}$, where α is the slip factor[309]. In the experiments, the slip factor is measured as 1.1.
3. Calculate the minimum time Δt when the change of R_i in any channel happens, i.e. a new droplet comes into one channel, one droplet leaves any of the channels.
4. Update R_i for each channel and repeat step 1
5. After repeat enough times (stable), for example, 5000 droplets, calculate the spacing between the droplets

Matlab is used to run the simulation. The detailed Matlab code is attached in Appendix D.

The results show that the model agrees well with experimental measurements with most of the data in the error $\pm 10\%$.

6.3.3 Experimental Results

In order to verify the working principle of droplet pair generator, PDMS chips were fabricated using soft-lithography technique. T-junction geometry was used to generate droplets upstream following with a long channel (5 mm) in order to reduce the fluctuation of hydrodynamic resistance when a droplet comes in or goes out of the channel. Diluter 1controls the initial spacing between droplets to make sure droplets go into the two branches of the loop alternatively. The two branches after the bypass channel are set to be a little bit asymmetric (L_6 is around $360\mu m$ smaller than L_5) in order to generate droplet pairs after merging. The difference between branches 5 and 6 is less than 2% of the length of branch 5. Therefore, this asymmetry doesn't have obvious influence on the imbalance of hydrodynamic resistance in each channel of the loop. The parameters of the loop are listed in Table 6.1.

Table 6.1 Channel Dimensions of the loop. $L_1 \sim L_7$ are the channel lengths of each branch, w is the channel width, and h is the channel height.

Parameters	L_1 (μm)	L_2 (μm)	L_3 (μm)	L_4 (μm)	L_5 (μm)	L_6 (μm)	L_7 (μm)	w (μm)	h (μm)
Value after Swelling	53160	1150	1300	1806	15888	15520	45944	140	51

10% glycerol/water mixture was used as the dispersed phase and low-viscosity silicone oil (DC200, Sigma Aldrich, 10cSt) was used as the continuous phase without any surfactant. A series of pressures are applied for the T-junction inlets and diluter 1 in order to control the droplet spacing and frequency. Droplet size was kept a little bit larger than the width of channel, and set as a constant during different experimental settings. The spacing of droplet pairs downstream was measured with respect to different droplet frequency and initial spacing as shown in Figure 6.8. s_1 and s_2 are the spacing between two nearby droplets, respectively. From Figure 6.8, we can see a droplet is trapped inside the bypass channel, which is caused by the unsteady flow at the beginning of applied pressures. After the flow is stable, the droplets start going into the two branches alternatively. The droplet inside

the bypass channel doesn't have any influence on the flow pattern, because the flow rate in the bypass channel is almost zero after the flow is in steady state. Experimental results show that $2s = s_1 + s_2$, which indicates that the flow is stable. Parameters were experimentally measured under different experimental settings, and compared with the calculated values by Matlab, including the initial spacing between droplets s, droplet spacing in channel 5 (s_{c5}) and in channel 6(s_{c6}), droplet velocities before entering the loop (U_{d1}) and after leaving the loop (U_{d7}), spacing between two nearby droplets after the loop, s_1 and s_2. One example of the results is listed in Table 6.2, which shows that the model can predict the spacing between droplet pairs with errors within $\pm 10\%$. Therefore, the model can be used to guide the design for generating droplet pairs with controlled spacing. Other detailed results can be found in Appendix E. It is noted that the slip factor and equivalent droplet length are estimated as constants. In factor, the two factors are influenced by the flow rates of both phases and capillary number, which are still difficult to be precisely described. The estimation is reasonable, but can still cause some errors. A fine adjustment of the droplet pair spacing can be done by adding a diluting stream (diluter 2) as shown in Figure 6.5.

Table 6.2 Experimental results V.S. Calculated results under the condition of input pressure $P_{in} = 920\text{mbar}$, droplet frequency $f = 6.576\text{Hz}$, slip factor $\alpha = 1.1$, equivalent droplet length $L_{effdrop} = 450\mu\text{m}$

Parameters	s (μm)	s_{c5} (μm)	s_{c6} (μm)	s_1 (μm)	s_2 (μm)	U_{d1} (mm/s)	U_{d7} (mm/s)
Experimental	2065	2105	2005	960	2965	13.48	13.38
Calculated	1938	1962	1917	957	2922	12.72	12.72
Error	6.15%	6.79%	4.39%	0.31%	1.45	5.64%	4.93%

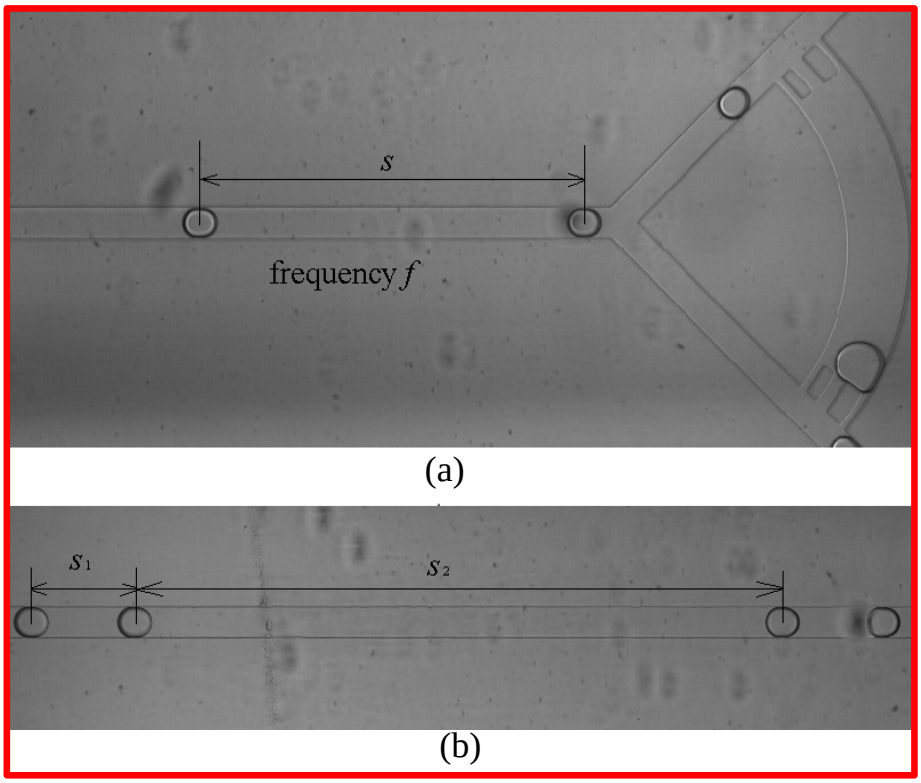

Figure 6.8 (a) Top view of the droplet sorting loop; (b) Droplet pairs are generated after the sorting loop. The pictures were captured from videos under experimental settings of $P_d = 945\text{mbar}$, $P_c = 960\text{mbar}$, and $P_{diluter1} = 860\text{mbar}$, where P_d is the pressure applied at the inlet of the dispersed phase, P_c is the pressure applied at the inlet of the continuous phase, and $P_{diluter1}$ is the pressure applied at the inlet of diluter 1. s is the initial spacing between droplets, f is droplet frequency, s_1 and s_2 is the spacing between two nearby droplets after the sorting loop, respectively.

6.3.4 Some Preliminary Results for Droplet Interaction Travelling in a Curved Microchannel

Jakiela *et al.* [309] experimentally verified that the speed of individual droplets in microfluidic channels is a function of the capillary number, droplet size and viscosity ratio of two phases. Muradoglu et al. numerically studied that the curvature of microchannel affects the lubrication thin film thickness and distribution, and hence affects the droplet speed. Moreover, Labrot *et al.* [268] presented that the initial spacing between droplets also has influence on the droplet resistance in a straight microchannel. Therefore, the observed spacing change of a droplet pair through a curved

microchannel can be caused by many factors, including channel curvature, viscosity contrast between two phases, capillary number, droplet length, and the initial spacing between two droplets. This project aims to study the influence of these parameters on the spacing of a droplet pair travelling in a curved microchannel by using the proposed droplet pair generator.

A curved channel was connected to the downstream channel of the droplet pair generator, as shown in Figure 6.9(a). The diameter of the curved channel ϕ was set to be $1000\,\mu m$, $2000\,\mu m$ and $3000\,\mu m$, respectively, in order to study the influence of channel curvature. The one shown in Figure 6.9 has a diameter of ϕ=2000μm. The channel width and height were measured ($w = 130\mu m$, $h = 52\mu m$) after swelling. In Figure 6.9(a), the picture was captured using $4\times$ objective, which has a large view of the curved channel. However, the measurement of droplet spacing has a larger error by using $4\times$ objective, because one pixel represents $5\mu m$ with an $4\times$ objective. The measurement has a random error of 1 ~ 2 pixels, leading to $\pm 10\mu m$ error with $4\times$ objective. Therefore, an $20\times$ objective was used to measure the spacing before a droplet pair enters the curved channel (s_{before}, see Figure 6.9(b)), and the spacing after the same droplet pair leaves the curved channel (s_{after}, see Figure 6.9(c)). The measurement has a random error within $\pm 2\mu m$, since one pixel represents $1\mu m$ by using $20\times$ objective.

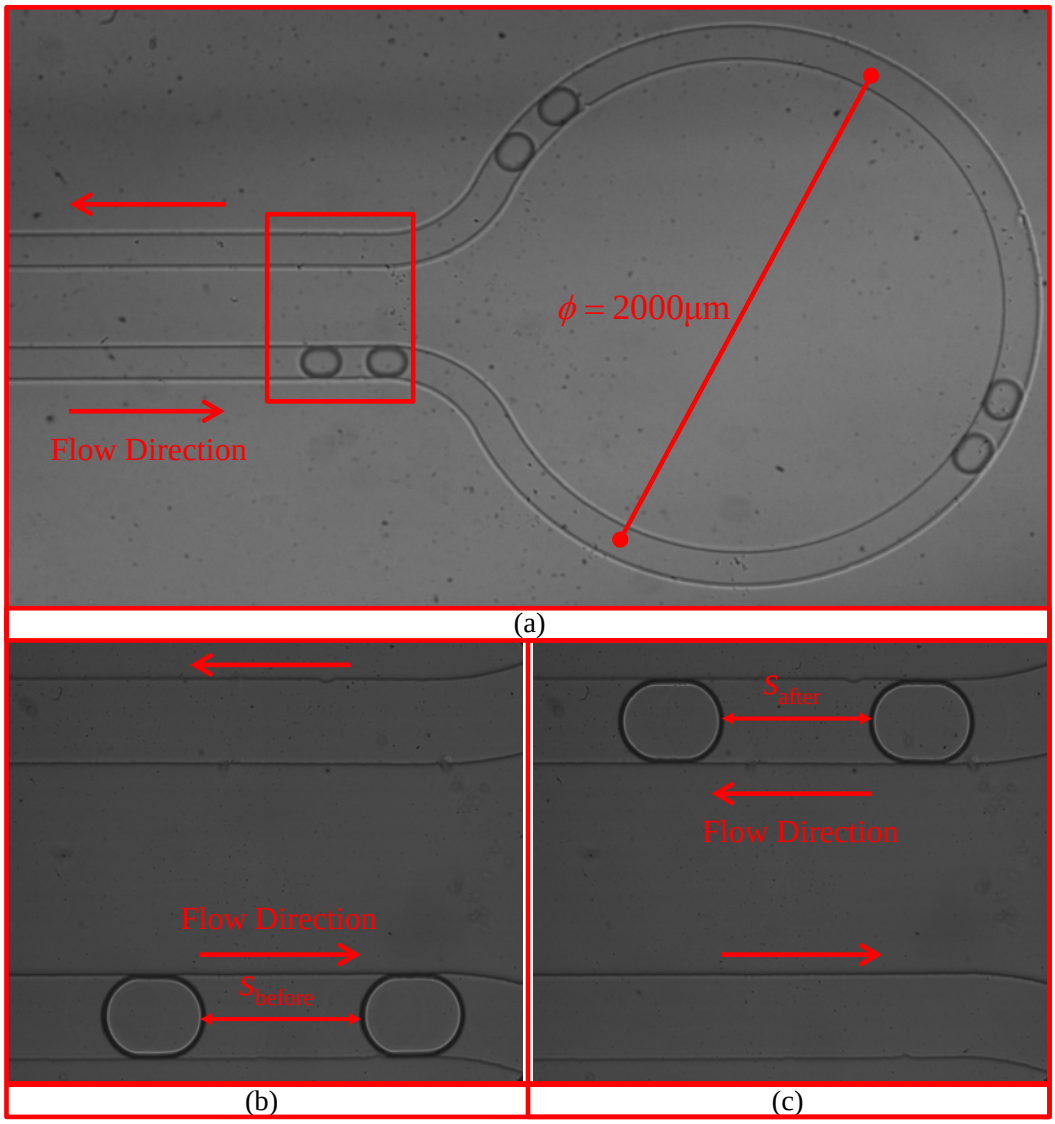

Figure 6.9 (a) Picture of a curved microchannel with a diameter of ϕ=2000μm connected to the downstream channel of the droplet pair generator. The picture is captured using $4\times$ objective, and the droplet pairs are different from the one shown in (b) and (c); (b) a droplet pair before entering the curved channel captured using $20\times$ objective. s_{before} is the spacing between two droplets before entering the curved channel; (c) the same droplet pair as in (b) after leaving the curved channel captured using $20\times$ objective. s_{after} is the spacing between two droplets after leaving the curved channel;

Some preliminary tests have been done by using 10%glycel/water mixture as the dispersed phase, and silicone oil (DC200, Sigma Aldrich, 10cSt) as the continuous phase, since the properties of these two types of liquid have been measured in other projects, including the viscosity and interfacial tension. Figure 6.10 shows the droplet spacing of 100 pairs of droplet before entering the curved channel and after leaving the curved channel under experimental settings of viscosity ratio of the dispersed phase to the continuous phase $\eta = 0.12$, capillary number $Ca = 0.81 \times 10^{-3}$, and non-dimensional droplet length $L_d / w = 1.18$. The spacing before entering the curved channel varies from $224\,\mu m$ ~$392\,\mu m$. From Figure 6.10, one can see that the droplet spacing decreases after a droplet pair passes through the curved microchannel.

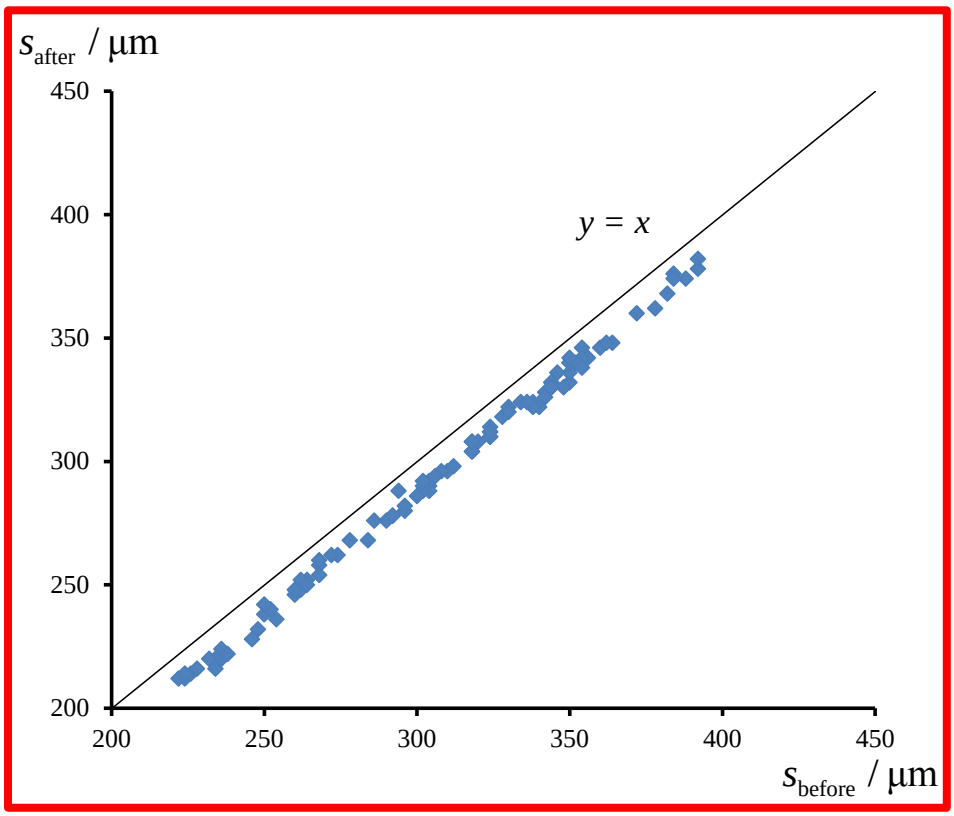

Figure 6.10 Droplet spacing before entering the curved channel (x – coordinate), and after leaving the curved channel (y – coordinate) under experimental settings of viscosity ratio $\eta = 0.12$, capillary number $Ca = 0.81 \times 10^{-3}$, non-dimensional droplet length $L_d / w = 1.18$. 100 Pairs of droplet were measured with an initial spacing range from $224\,\mu m$ ~$392\,\mu m$.

Although some preliminary results have been obtained and show that the droplet spacing decreases after a curved channel, extensive experiments need to be done by varying channel curvature, capillary number, droplet length, viscosity contrast, and initial spacing. After experiments are completed, a theoretical model is expected to be built to explain the phenomena, which will be continued as one of my postdoctor projects.

6.4 Droplet Merging Design for Controlled Reaction Volumes

The most basic forms of droplet manipulation are splitting, trapping, short and long term storage, and merging, which have been extensively discussed in Chapter 2. This section introduces a simple geometry for passively merging droplets with controlled number of merged droplets. I proposed this design, and verified the proof of concept. A master student in our lab, Alexander Brukson, performed the experiments. Both of us worked on the theoretical model for predicting the operation of the merging element.

6.4.1 Introduction

When performing chemical or biological reactions in droplet-based platforms, a critical step is to combine and mix the desired reagents. Some methods for introducing reagents into droplets include: co-flowing, where reagents are flowed in parallel prior to droplet generation [222]; direct injection [326, 386, 387], where a small amount of fluid from a perpendicular channel is allowed to merge with a passing droplet; and droplet merging [223, 226, 229, 239–241, 257], where two or more droplets are allowed to fuse together. Merging the droplets allows for a controlled method of combining reagents in a way that allows the contents to mix quickly and without the risk of cross-contamination.

In general, the different methods for merging droplets are divided into active methods and passive methods. Active methods are those which employ an external force such as electrical [236–238, 388], thermal [232], pneumatic controls [241, 389], optical [390] or acoustic [209, 239] while passive methods [223, 226, 227, 257] use the channel geometry to manipulate the flow in a particular manner. Active designs require external components such as power sources, valves, or control units which make the operation of the device increasingly complex as well as increasing the overall cost of the system. Although, passive designs have not been largely implemented in real applications, their simplicity of operation, minimal external equipment, no active control, coupled with potentially high throughput could be an excellent alternative for the reliable droplet-based microfluidic devices. Therefore, the following will focus on passive merging structures.

Some passive designs incorporate a channel expansion [189] to remove the oil separating the droplets. The channel expansion causes the distance between droplets to decrease so that the droplets can collide and merge. Similarly, other implementations have used cross junctions to partially remove the oil phase separating droplets in the channels [391]. These methods have been shown to be effective in merging droplets but require ensuring the droplets are within an appropriate spacing and designs which remove (instead of redirecting) the oil phase can cause pressure fluctuations downstream [226]. Other methods include forcing droplets together through the use of velocity gradients [248, 392, 393]. A long channel with increasing width creates a velocity gradient along the channel and different numbers of successive droplets have been shown to merge [248]. The difference in velocity between droplets of different sizes and viscosities has also been utilized to collide and merge droplets in microchannels [393]. The use of velocity gradients can be more effective than a straight channel expansion, however poses the risk of unwanted droplet coalescence or droplets not remaining in contact long enough to actually merge. Another common technique for merging droplets utilizes channel constrictions to generate a Laplace pressure difference across the downstream and the upstream ends of the droplet [226]. In combination with a bypass channel filled with the continuous phase (i.e. oil) the droplets are slowed or trapped, allowing other droplets to collide and merge [226, 394].

In particular, Niu *et al.* [226] were able to successfully trap, and merge droplets in a droplet train by using pillar structures to facilitate droplet trapping and oil bypass. This geometry allows droplets to be trapped for an extended period of time and does not have any observable effects on the inter-droplet spacing. Although the design has been shown to be highly effective in merging droplets, the generated difference in Laplace pressure is inversely proportional to the size of the interface; therefore by scaling the channel dimensions up, there will be a diminishing return on the Laplace pressure difference across the droplet. This makes it difficult to trap droplets when the channel dimensions are relatively larger. At the same time, although capable of merging droplets in a consistent manner it was not shown the conditions under which the chamber can merge different numbers of droplets.

In this work, a passive merging was proposed capable of merging variable numbers of droplets by designing a valve-type function in the merging chamber. The relationship between the numbers of droplets merged, the length of input droplets, and the length of output droplets is used to tune the design parameters according to the desired set of reactions. The reduced complexity of the design

allows for easier design and configuration to a desired purpose and low risk for failures due to fabrication and operation uncertainties. The single-input-single-output design minimizes pressure disturbances from propagating downstream [226], and reduces the complexity of integration into a larger LOC system. The specific geometry of the chamber allows for the operation of a valve-type function to force the droplet from the chamber thereby imposing a critical volume limit. The geometry can be scaled up with little to no observable effect on the mode of operation. And finally, the capability of having different numbers of mergers for a single chip allows for the diversity of application to be broadened without changing fabrication, or design.

6.4.2 Design of the Merging Chamber

Figure 6.11 shows the schematic of the proposed merging design. There are two columns of pillars that act to divide the merging chamber into three virtual channels – two bypass channels and one central channel where droplets are designed to merge. The dimensions labeled are: L, the chamber length; W_{by}, the width of the bypass channel; W_c, the width of the central chamber between the pillar arrays; W_s, the distance between each pillar; W_p, the width of each pillar; and L_p, the length of each pillar. Each dimension is normalized with the upstream channel width w, which is the same distance between the two pillar arrays.

$$L^* = \frac{L}{W},\ W_{by}^* = \frac{W_{by}}{W},\ W_p^* = \frac{W_p}{W},\ W_c^* = \frac{W_c}{W},\ W_s^* = \frac{W_s}{W},\ L_p^* = \frac{L_p}{W}$$

The design of the chamber is such that to allow the entering droplets to become trapped and force the oil to bypass the droplet via the bypass channels. Once the droplet has reached the volume limit threshold it will extend through the pillar array and block the exit of the bypass channel, preventing the oil from bypassing the droplet. The oil will push the droplet out of the chamber.

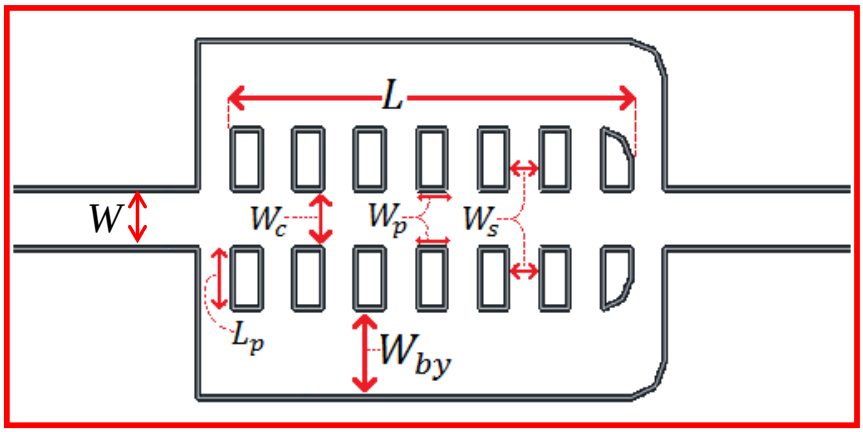

Figure 6.11 Schematic of the merging chamber. L, W_{by}, W_c, W_p, W_s, and L_p represent the chamber length, bypass channel width, width of the central chamber, width of the pillars, inter-pillar spacing, and pillar lengths, respectively.

6.4.3 Working Principle of Trapping and Merging

When the droplet width is less than the channel width which is also the same as the central path of the merging chamber (i.e. is not confined by the channel walls), it is able to pass directly through the merging chamber without being affected. In order to be merged, droplets need to have a width larger than the channel width. When such a 'large' droplet enters into the merging chamber, it will expand and consequently occupy some of the space between the pillars [395], because the surface tension tends to minimize its surface area making it as circular as possible. This is also observed in Figure 6.12, where the droplets within the pillar array have a small but noticeable extension into the inter-pillar spacing. The presence of the droplet coupled with the droplet curvature between the pillars increases the resistance along the central path and forces oil to bypass the droplet. This mechanism acts to slow the droplet and trap it between the pillars allowing the oil to bypass the droplet and the following droplets to catch up and merge together. The product droplet will remain trapped between the pillars until its volume reaches a critical threshold; the critical threshold is only determined by the chamber length, L^*. At this critical threshold the product droplet will block the exit of the bypass channel and generate a large pressure buildup near the entrance of the chamber causing the droplet to be forced out of the chamber by the continuous phase liquid.

Robustness has been one of the key issues with mergers which require optimization for each design parameter. For example, once within the chamber, the curving of the droplet between the pillars will

slightly reduce the length of the droplet which could alter the expected results for the merging device reducing its robustness. .Therefore the space between the pillars must be optimized to minimize the deformation of the droplet while maximizing the capacity of the oil to bypass the droplet. The spacing between the pillars (W_s^*) is set to a constant value of 0.625 in this study. It was determined as the optimal spacing in order to adequately prevent droplets from entering the chamber's bypass channel while still allowing sufficient oil to bypass through and providing the appropriate amount of space for the droplet to expand between the pillars. The length of the pillars (L_p^*) is set to be 1 to have the pillar length greater than 1.5 times W_p^*; this is to ensure that the pillar structures do not become deformed or incomplete during the fabrication procedure. The width of the central channel (W_c) is set to unity in order to minimize the alteration of the droplet length within the pillar array. Finally, the pillar width (W_p^*) is set to 0.5 which was determined as the minimal pillar width to ensure the quality of the microstructures after the fabrication process. The remaining, W_{by}^* and L^* are then calculated to the desired criteria of the device.

Figure 6.12 shows the procession of droplet merging from the time before the droplet enters the chamber, to the first droplet becoming trapped between the pillars, the sequential merging of droplets in the train, the blocking of the bypass channel exit and finally, the product droplet releases after reaching the critical volume threshold. This behavior is advantageous as it provides a passive on/off mechanism of operation which can be useful for predictable operation under different conditions. This function is most useful in preventing the undesired merging of reagents by ensuring the product droplet is released in synchrony with the following droplet entering the channel.

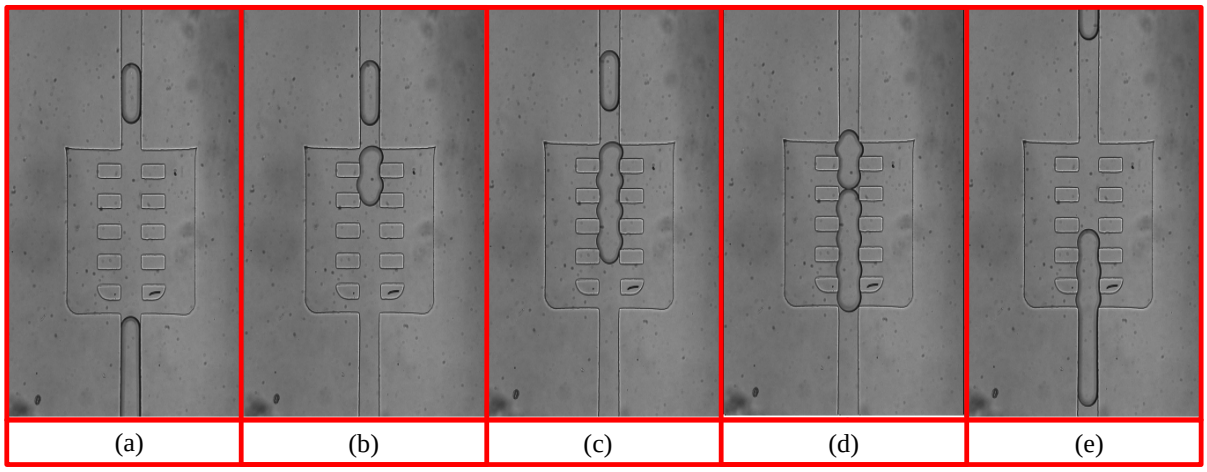

Figure 6.12 Sequential droplet merging captured using $10\times$ objective. (a) the first droplet enters the merging chamber, (b) the first droplet is trapped between the pillars allowing the next droplet to catch up, (c) the first two droplets merge and remain trapped within the pillar array and the length of the product droplet increases proportionally, (d) the product droplet blocks the exit of the bypass channel when the third droplet enters the central chamber, (e) the product droplet is fully merged and is forced out of the chamber by the continuous phase liquid.

6.4.4 Merging Performance

The extension of the product droplet length within the central pillar array is proportional to the individual droplets merged and is limited by the imposed critical volume limit. Therefore the length of the droplets entering the chamber will have a direct impact on the operation of the merging chamber. The geometry of the merging chamber will influence two key parameters: the critical volume limit, and the critical Capillary number. Changing the length of the merging chamber will proportionally change the critical volume threshold by altering the length which the product droplet can extend. And at the same time, changing the length of the chamber in combination with the bypass channel width will influence the capability of the oil to bypass the droplet through altering relative channel resistances. Then, due to the balance of the surface tension and viscous forces, there exists a regime where the surface tension force dominates in holding the droplet within the pillar array and allowing the product droplet to reach the critical volume threshold. Conversely there also exists a regime where the viscous forces of the oil overcome the capability of the droplet to become trapped and the merging cannot be predicted. The transition between these two regimes is the critical

Capillary number. Therefore the effects of the droplet length, geometry, inter-droplet spacing, and Capillary number are studied to characterize the modes of operation for the proposed merging design.

From the geometry, the critical volume threshold will occur at a volume between the N^{th} droplet and the $(N-1)^{\text{th}}$ droplet merged within the pillar array. Because the droplets are constricted by the channel height and width, any increase in volume will be reflected by an increase in the droplet length. Therefore it can be determined that the length of the droplet exiting the channel (L_{o}) should be a N multiple of the input droplet length (L_{d}), which will be larger than or equal to the length of the chamber (L), and the trapped droplet should have a length less than the chamber. This gives us the inequality equation,

$$(N-1)L_{\text{d}} < L < NL_{\text{d}} \tag{6.10}$$

Rearranging Equation (6.10), we can obtain the number of droplets that can be trapped in a chamber with a length of L,

$$\frac{L}{L_{\text{d}}} < N < \frac{L}{L_{\text{d}}} + 1 \tag{6.11}$$

By substituting $L_{\text{o}} = NL_{\text{d}}$ into Equation (6.11), we can obtain the range of output droplet length (L_{o}),

$$1 < \frac{L_{\text{o}}}{L} < 1 + \frac{L_{\text{d}}}{L} \tag{6.12}$$

The functionality of the merging chamber is dependent on the competition between viscous and surface tension forces. The ratio of these two forces is represented by the Capillary number. Surface tension force acts to prevent the droplet from easily passing through the pillar array and even trapping the droplet while viscous force tends to push the droplet through the pillar array without stopping. Therefore there exists a critical Capillary number (Ca_{crit}) at which the droplets can no longer be trapped because the pressure exerted on the droplet from the oil flow will exceed the maximum possible drag force the droplets experience in the pillar array.

The efficacy of the design is tested by varying the length of input droplets and comparing to the predicted results from equations (6.11) and (6.12). The designs were chosen such that for a fixed droplet length ($L_{\text{d}}^{*} = 2$) the chamber would merge 2, 3, 4, and 6 droplets with chamber length L^{*}

equal to 4, 6.25, 8.5, and 13 respectively, and bypass channel width W_{by}^{*} equal to 1.5 and 3, respectively. Alexander Brukson performed the experiments by using pure water as the dispersed phase, and silicone oil l (DC200, Sigma Aldrich, 10cSt) as the continuous phase. The microfluidic chips were fabricated by standard soft lithography technique. Experimental results verified that the number of merged droplets follows the rule describing in Inequation (6.11), and the output droplet length L_o falls into the range describing in Inequation (6.12). The largest critical Capillary number is found to be 2.5×10^{-3} when $L^{*}=4$ and $W_{by}^{*}=3$, and the critical Capillary number is found to decrease with the increase of the hydrodynamic resistance of the bypass channel. Detailed Experimental results can be found in Alexander Brukson's thesis.

The effect of initial droplet spacing was tested by adding a diluting stream to increase the volume of oil between each pair of droplets. Droplets were generated with comparable sizes between each trial. It was observed that the functionality of the merging chamber was not affected by the initial droplet spacing and the merging adhered to the inequalities previously discussed, as long as the Capillary number is smaller than the critical Capillary number. Therefore, the droplet spacing does not have a considerable effect on the operation of the merging device while operating underneath the critical Capillary number.

6.5 Design of a Microfluidic Device for Trapping and Releasing Droplets on Demand

This section reports a microfluidic device capable of trapping and releasing droplets on demand for drug screening. The whole project was worked in collaboration with the Drug Design and Discovery Research Group at School of Pharmacy, University of Waterloo. Tarek Mohamed, a PhD candidate and Dr. Praveen P. Nekkar Rao, a professor from the Drug Design and Discovery Research Group provided their expertise on how to screen for potential drug candidates that treat Alzheimer's disease. Our lab's contribution is to provide a droplet based microfluidic device for screening drugs instead of using 96-well plates. The microfluidic design was done by collaborating with an undergraduate student, Matthew Courtney, who worked as a co-op student in the University of Waterloo Microfluidics Laboratory. I provided the design and verified the proof of concept, and Matthew Courtney performed most of the experiments under my instructions to optimize the design.

6.5.1 Introduction

Traditional drug screening efforts rely on the use of 96- or 384-well plates to assess the efficacy of various drug candidates against key biological targets [396]. While the setup is generally straightforward, these platforms require large aliquots of the biological components and long operation times, adding to the overall costs of the screening process. Droplet microfluidics that utilizes nanoliter-sized, uniform droplets generated in microchannel networks at kHz rates as reaction vessels offers significant advantages over well plate format, including orders of magnitude reduction in reagents use and reaction time and orders of magnitude increase in throughput.

In this work, a droplet-based microfluidic device that is equipped with functions such as rapid mixing and trapping and releasing droplets on demand has been developed for screening drugs that inhibit the tau-hexapeptide (AcPHF6) aggregation relatable to Alzheimer's disease. With the ability to trap and release droplets on demand, this device allows stable droplet generation and mixing prior to droplet storage. The on-chip mixing function allows for AcPHF6 aggregation feedback immediately after the process begins. During the tests, the AcPHF6 hexapeptide (Ac-VQIVYK-NH2) was used to replicate the full-length tau protein aggregation. The AcPHF6 solution is mixed on-chip with a solution of MOPS buffer, a fluorescent indicator dye (Thioflavin-S or ThS), and a tau-aggregation inhibitor. Droplets are generated from these combined aqueous streams, and then mixed, trapped, and stored within seconds. While being stored, ThS was used to monitor the tau-aggregation in the presence of three inhibitors including Orange G, tolcapone, and methylbenzophenone. The fluorescence intensity data was compared to the results obtained using the 96-well plate provided by Mohamed *et al.* [396]. It is demonstrated that droplet microfluidic platform is a powerful alternative to traditional well plate methods for screening drugs towards Alzheimer's disease because it offers comparable sensitivity and accuracy for assays while significantly reducing reaction time (10minutes vs. 2 hours) and reagent use by four orders of magnitude (10nL vs. 200uL).

6.5.2 Design of the Trapping and Releasing Droplets on Demand System

When considering the design specifications for this microfluidic device, the on-chip mixing function is important because it allows for fast chemical reactions to be monitored immediately after the process begins. During the on-chip mixing process, droplets generated at the beginning have unknown concentrations because it takes time to reach stable flow conditions. Therefore, it is beneficial to have an on demand method for trapping so that these droplets can avoid the traps. Once

stable flow rates have been reached, the concentration of reagents within the droplets can be calculated and then these droplets can be trapped on demand. These droplets can remain stationary in the trap for a long period of time so that they can easily be monitored. Afterwards, the droplets will be released so that the traps can be reused, or so that the products within the droplets can be collected.

The microfluidic design is shown in Figure 6.13, which consists of three main functions, i.e. droplet generator (Figure 6.13(b)), droplet mixer (Figure 6.13(c)), and droplet trapping and releasing wells (Figure 6.13(d)). The droplet generator is a simple flow focusing device, and the mixer utilizes a serpentine type channel. As shown in Figure 6.13(d), the trapping design consists of a bypass channel, and a trapping well that is connected to a diluting stream. The droplets will always go into the branch that has a larger flow rate. When a high pressure is applied to the diluting stream, the flow rate in the trapping well is smaller than that in the bypass channel ($Q_T < Q_B$), keeping droplets from going into the trapping well. When the pressure in the diluting stream is stopped, the flow rate in the trapping well becomes larger than that in the bypass channel ($Q_T > Q_B$), because the hydrodynamic resistance of the trapping well is smaller than that of the bypass channel. Therefore, the droplets starting go into the trapping wells. After the droplets go into the trapping well, they can remain stationary in the trapping well due to the interfacial tension and increase the hydrodynamic resistance of the trapping well, leading to $Q_T < Q_B$ again. Therefore, the other droplets will continue flowing through the bypass channel and go to the downstream trapping wells. The trapped droplets can be released by reapplying a high pressure to the diluting stream.

Since the reaction has already started once the two reagents are injected into the channel in a co-flowing stream, it is important to trap the droplets as fast as possible. Therefore, it is required to trap droplet with a large flow rate. However, if the capillary number of the continuous phase is too large, the droplet cannot remain inside the trapping welling and will be pushed through the gap into the main channel. Therefore, there exists a maximum flow rate that ensures the trapping design works. In order to maximize the working flow rate, silicone oil with very low viscosity can be used as the continuous phase ((DC200, Sigma Aldrich, 5cSt)

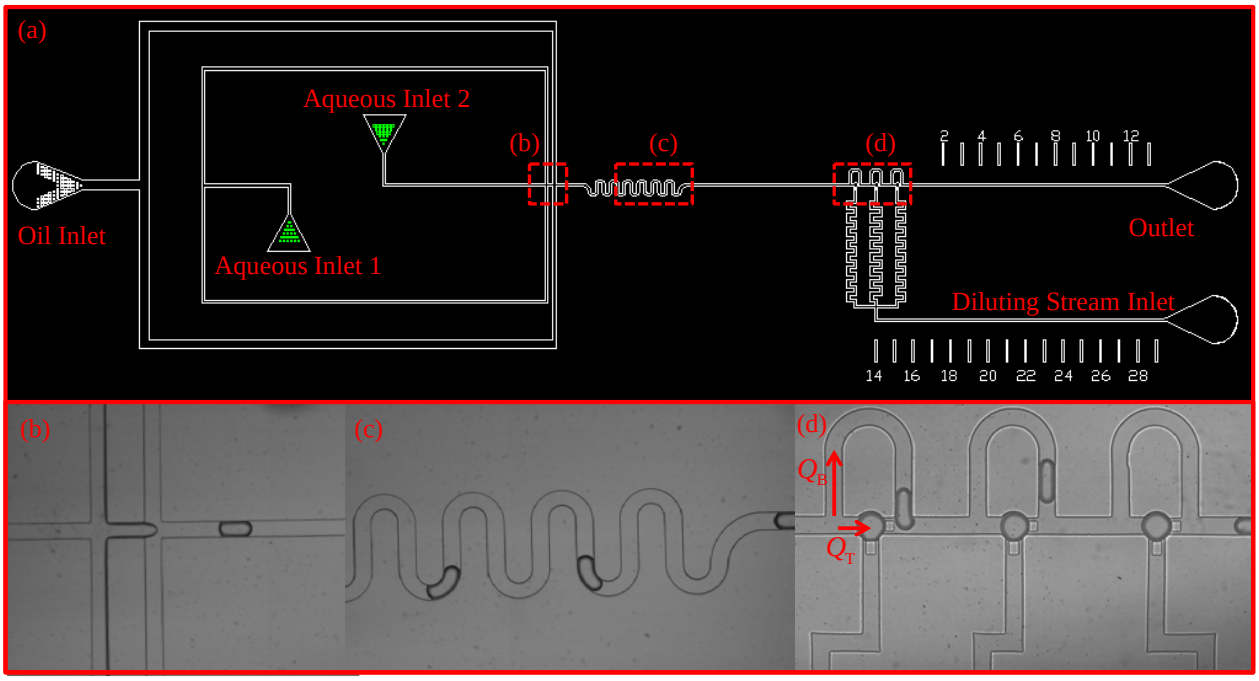

Figure 6.13 (a) Microfluidic circuit design of the droplet trapping and releasing on demand system; (b) Flow focusing device for droplet generation; (c) Serpentine type channel for droplet mixing; (d) Design for droplet trapping and releasing on demand, where Q_B is the flow rate in the bypass channel and Q_T is the flow rate in the trapping well.

6.5.3 Performance of the Design

Matthew tested this design with a low viscosity silicone oil ((DC200, Sigma Aldrich, 5cSt) as the continuous phase, and pure water as the dispersed phase. Figure 6.14 shows one example of droplet trapping process with a relatively high droplet velocity U_d=18.4mm/s. Experimental results show that the trapping process can be finished in $t_1 = 1.87$s. The microchannel length between the droplet generator and the first trapping well is set to around 25.2mm. Hence, the travelling time of a preformed droplet from the droplet generator to the trapping well is estimated as $t_2 = 25.2/18.4$s=1.37s. The reaction time is counted after the droplets are trapped, since the microscope objective focuses on the trapping well area. However, the reaction has already started once the two aqueous reagents are mixed together. The total reaction time that is not counted can be estimated as $t_{delay} = t_1 + t_2 = 3.24$s, which can be ignored compared to the total reaction time 10min. Therefore, this design can be used for screening drugs that inhibit the tau-hexapeptide (AcPHF6)

aggregation relatable to Alzheimer's disease. This design is not applicable for a biological or chemical reaction with a fast reaction rate.

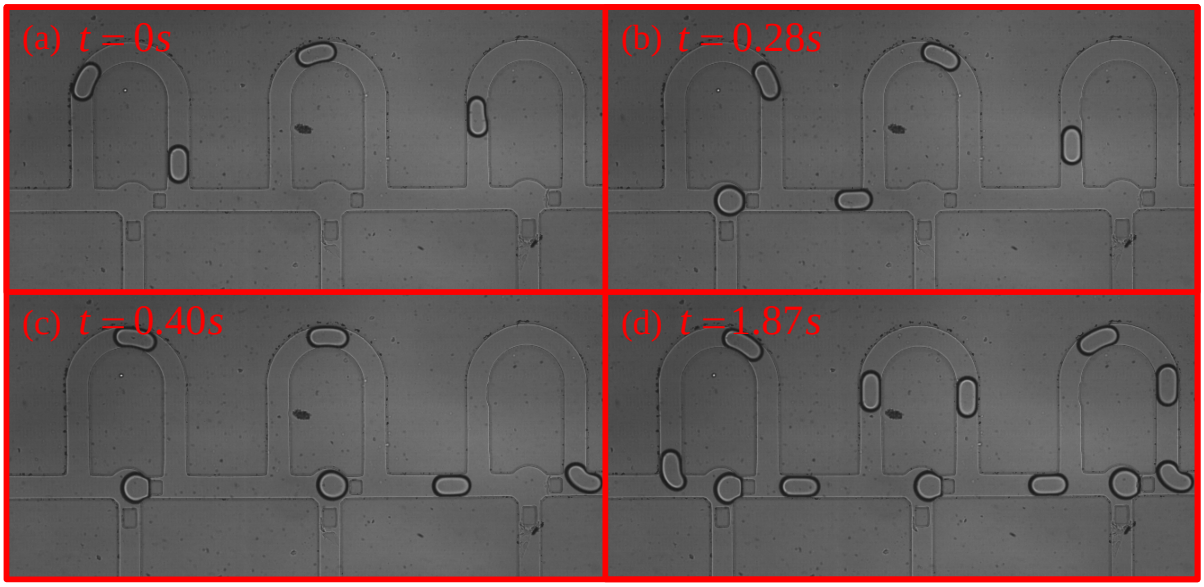

Figure 6.14 One example of droplet trapping sequence captured using $4\times$objective with droplet velocity U_d =18.4mm/s. (a) Droplet trapping is triggered by stopping the pressure applied in the diluting stream; (b) A droplet is trapped in the first trapping well at time $t = 0.28\text{s}$;(c) A droplet is trapped in the second trapping well at time $t = 0.40\text{s}$;(d) A droplet is trapped in the third trapping well at time $t = 1.87\text{s}$.

6.6 Conclusion

This chapter presents several microfluidic designs for generating and manipulating droplets, including a flow focusing device with different angles to generate monodispersed droplets, a droplet on demand system using off-the-shelf solenoid valves and a microcontroller, a droplet pair generator with uniform droplet size and controlled spacing, a droplet merging design for controlled reagent volume, and a droplet trapping and releasing on demand system for screening drugs. These designs are shown to have prospective applications in chemical and biomedical reactions. Each proposed design has its own function to generate or manipulate droplets, but they are not integrated into a microfluidic chip to fulfill multi-steps of reactions. The next chapter will introduce a microfluidic system that integrates multiple functions.

6.7 List of Symbols

AcPHF6	Tau-hexapeptide
Ca	Capillary number
Ca_{crit}	Critical capillary number
f	Droplet generation frequency
h	Channel height
L	Chamber length of the merging design
$L_1 \sim L_7$	Channel lengths of branches 1 ~ 7
L_d	Droplet length
L_o	Output droplet length
$L_{effdrop}$	Equivalent droplet length
L_p	Length of each pillar
N	Number of droplets
PDMS	Polydimethylsiloxane
P_{b1}	Pressure at the end of branch 1
ΔP_{b1}	Pressure drop in branch 1
P_{b2}	Pressure at the end of branch 2
ΔP_{b2}	Pressure drop in branch 2
P_c	Pressure applied at the inlet of the continuous phase
P_d	Pressure applied at the inlet of the dispersed phase
$P_{diluter1}$	Pressure applied at the inlet of diluter 1
P_D	Pressure at the end of down branch
P_{in}	Pressure at the inlet of the sorting loop
P_{j1}	Pressure at beginning junction of the loop
P_{j2}	Pressure at end junction of the loop
P_{out}	Pressure at the outlet of the sorting loop
P_U	Pressure at the end of up branch
P_Y	Pressure at the Y-junction

Q	Flow rate
Q_{b1}	Flow rate of branch 1
Q_{b2}	Flow rate of branch 2
Q_B	Flow rate in the bypass channel
Q_T	Flow rate in the trapping well
r_1	Length of branch 1
r_2	Length of branch 2
$R_1 \sim R_7$	Hydrodynamic resistances of branches 1 ~ 7
R_{b1}	Hydrodynamic resistance of branches 1
R_{b2}	Hydrodynamic resistance of branches 2
R_c	Hydrodynamic resistance of the continuous phase liquid
R_{drop}	Hydrodynamic resistance of a droplet
R_{eqv}	Equivalent hydrodynamic resistance of the sorting loop
s	Droplet spacing
s_1	Spacing between two droplets in a pair
s_2	Spacing between two droplet pairs
s_{after}	Droplet spacing after a droplet pair leaves the curved channel
s_{before}	Droplet spacing before a droplet pair enters the curved channel
s_{c5}	Droplet spacing in channel 5
s_{c6}	Droplet spacing in channel 6
t	Time sequence
Δt	Valve opening time
t_1	Trapping process time
t_2	Travelling time of a preformed droplet from the droplet generator to the trapping well
t_{delay}	The total reaction time that is not counted
ThS	Fluorescent indicator dye Thioflavin-S
U_d	Droplet average velocity
U_{d1}	Droplet average velocity before entering the sorting loop

U_{d7}	Droplet average velocity after leaving the sorting loop
V_d	Droplet Volume
Voh	High level output voltage
Vol	Low level output voltage
w	Channel width
W_{by}	Width of the bypass channel
W_c	Width of the central chamber between the pillar arrays
W_p	**W**idth of each pillar
W_s	Distance between each pillar

Greek symbols

α	Slip factor
ϕ	Diameter of the curved channel
η	Viscosity ratio of the dispersed phase to the continuous phase
μ	Fluid viscosity
θ	The angle between the inlet of the dispersed phase and the continuous phase

Subscripts

c	Continuous phase
d	Dispersed phase

Superscripts

*	Dimensionless form of variables

Chapter 7
A Microfluidic Chip Design Integrated Droplet Generating, Pairing, Trapping, Merging, Mixing and Releasing

A typical chemical or biomedical reaction requires multiple steps of droplet generation and manipulation. Although droplet generation and manipulation have been extensively studied, it is still strongly required to develop a microfluidic chip that integrates multiple functions. This chapter describes a microfluidic chip design that integrates droplet generating, pairing, trapping, merging, mixing and releasing, aiming to be used in drug screening.

7.1 Introduction

As reviewed in Chapter 2, numerous studies have been done on droplet generation [93, 96, 124, 153], transportation [156, 253, 397], pairing [249], trapping [273, 275, 276, 279], merging [226, 230, 239, 240], mixing [266], and sorting [187, 190, 195] etc., either actively or passively. However, it is still very challenging to integrate multiple functions into one microfluidic chip due to the complexity of flow inside microfluidic chips.

Some groups have reported several microfluidic structures integrated with trapping and releasing droplet functions for cell incubation [273–275] and nanoparticle synthesis [281]. However, many reactions such as drug screening, diagnostics require the development of a system to enable two different types of sample to be trapped and merged on demand in order to control the reaction starting time or observe cell-cell interaction. The reported microfluidic structures add two types of reagents into one channel before droplet generation, where the reaction has already started before droplets get trapped. Therefore, these designs cannot control the reaction starting time. Several other methods reported to add one reagent into the other include: direct injection [387], where a small amount of reagent from a branch is injected into a passing droplet; and droplet merging [226], where a second droplet stream containing the new reagent is merged with the original droplet stream. However, direct injection method could cause cross-contamination between each droplet reactor, and droplet merging method requires generating two droplet streams alternatively with the same frequency, which needs additional droplet synchronization structure.

In this chapter, a microfluidic design that can generate, pair, trap, merge, mix and release two streams of droplet with two different types of reagents is demonstrated. This design is controlled

entirely by liquid flow involving no electrodes, magnets or any other moving parts, and doesn't require synchronized droplet generation with a rapid mixing process within several seconds. Moreover, this design can perform reactions with different reagent concentrations by varying droplet size. This microfluidic structure has a potential application for screening the best drug concentration values.

7.2 Working Principle and Design Criterion

7.2.1 Working Principle and Channel Structures

The designed microfluidic chip mainly consists of two parts: one is droplet generator, which can generate two streams of droplet with different reagents; and the other trapping wells, where two droplets from different streams get trapped and merged, and the reagents of the two droplets start to mix in the merged droplet. If the chemical composites in the two droplets are the same but with difference in the concentration of a particular reagent, the concentration of the reagent in the merged droplet can be well controlled by varying the reagent concentration of the two droplets. Generation of droplet pairs has been demonstrated previously by Frenz *et al.* [249], which has been adopted in the first version design as shown in Figure 7.1. Although it was successful to generate droplet pairs and merge them after being trapped in the trapping well, this design is not robust due to the strong, dynamic coupling of two generators, the need for synchronization of droplet pairs that are generated in two channels for trapping and merging, and the lack of strategy to eliminate the non-uniform droplets that are generated at the beginning while the system is being stabilized to be trapped. Figure 7.1(D) shows the trapping wells. When a droplet from either of the two steams (for example, one droplet from reagent 1) goes to the front of the trapping well, it has two choices, either goes into the trapping well or into the bypass channel. The bypass channel is designed to have a higher resistance than that of the trapping well (Bypass channel length is set at 3200 μm based on some preliminary experimental test). Therefore, droplet 1 will go into the trapping well and increase the resistance of trapping well dramatically so that the following droplets will go through the bypass channel. The trapped droplet can stay inside the trapping well due to interfacial tension and wait for a droplet from reagent 2 getting trapped. The bypass channel and trapping well for reagent 2 have the same dimensions as for reagent 1. Therefore, when a droplet from reagent 2 goes to the front of the trapping well, it will get trapped. The trapping wells for droplet 1 and droplet 2 intersect with a gap so

that the trapped droplets can merge. The following droplets will go through bypass channel and follow the same rule in downstream trapping wells.

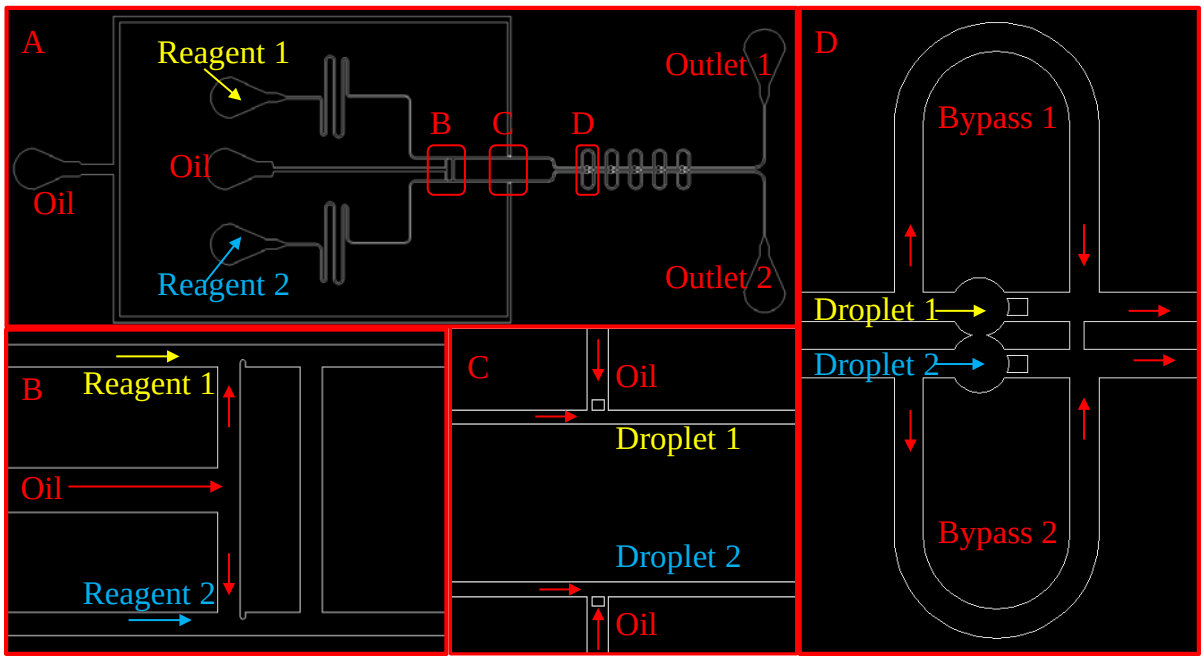

Figure 7.1 Sketch of the first version design for trapping two streams of droplets. A) Overview of the chip design. B) Droplet generator to generate two streams of droplets with channel height 60 μm , channel width of oil 240 μm , channel widths of reagent 1 and 2 120 μm . C) A regulator to adjust the spacing between two droplets. D) Trapping wells to trap two droplets from two different streams. An array of trapping wells can be integrated into the flow stream depending on requirements. Five trapping wells are integrated in this design to demonstrate the working principle.

Preliminary tests were performed to examine the functions of each part. The results show this generator can generate two streams of droplets and the trapping wells can trap and merge two droplets from two streams as anticipated. However, some problems were also found.

- The droplet generators affect each other because they share one oil channel. One cannot control the droplet sizes of each stream independently.
- At the beginning, droplet generation is not stable. Unstable droplets will go into the trapping wells and occupy all trapping wells. Therefore, when the flow is stable, good droplets cannot go into trapping wells.
- A channel for chemical waste should be added to release droplets after reaction.

- Some dust occasionally goes into the channel, which could affect the flow stream as shown in Figure 7.2

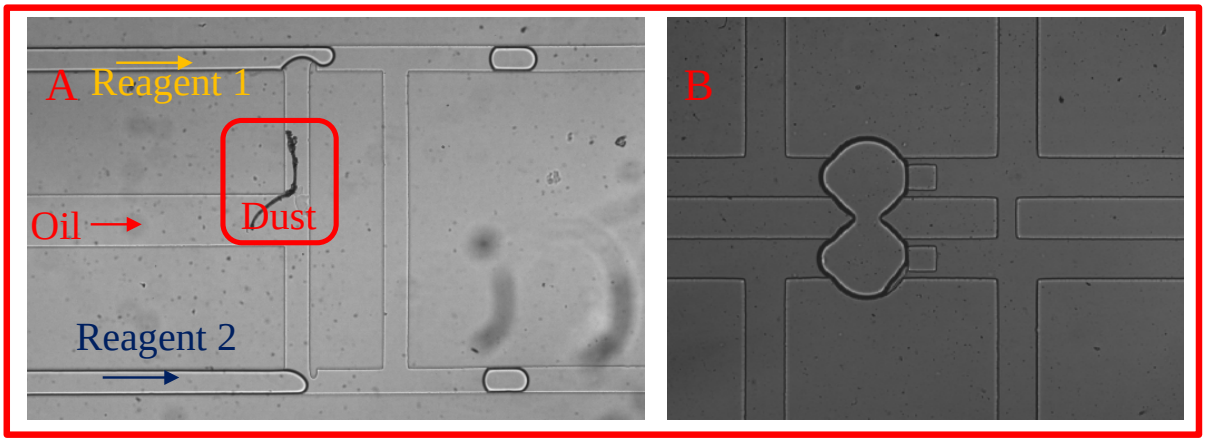

Figure 7.2 A. Picture of droplet generation captured using $4\times$ magnification. B. Picture of trapped droplets captured using $10\times$ magnification.

The second version design was proposed based on the preliminary tests of the first version as shown in Figure 7.3. In this design, the droplet generator can generate droplets from reagent 1 and reagent 2 alternatively [248]. Compared with the droplet generator in the first version, this droplet generator combines two droplet streams into one and simplifies the channel structure. The bypass channel also reduces to one. In addition, a channel branch is added to dispose chemical waste. At the beginning of droplet generation, the droplets are not uniform due to unstable flow rates. These droplets are not allowed to go into to the trapping wells. Therefore, a moderate pressure is applied in outlet 1at first, and unwanted droplets will go into the waste channel. When droplet generation is stable, a pressure with the same magnitude as applied in outlet 1 is applied in outlet 2, and set no pressure in outlet 1. Droplets start going to trapping wells. The dimensions of waste channel are set to the same as that of the trapping channel to minimize the flow fluctuation during the change of pressure. Droplets will go into the traps when the resistance of bypass channel is larger than the resistance of trapping wells. After droplets get trapped, the resistance of trapping wells will be larger than the resistance of bypass channel, so the rest of droplets will go through the bypass channel and repeat the same process in downstream trapping wells. Since the droplet generator can generator droplets from two reagents alternatively, the trapping wells can trap one droplet from reagent 1 and the other from reagent 2. After the reaction is finished, a high pressure is applied in outlet 1 and no

pressure is applied in outlet 2, the sample will be flushed into the waste channel. The microfluidic chip can be reused for other reactions.

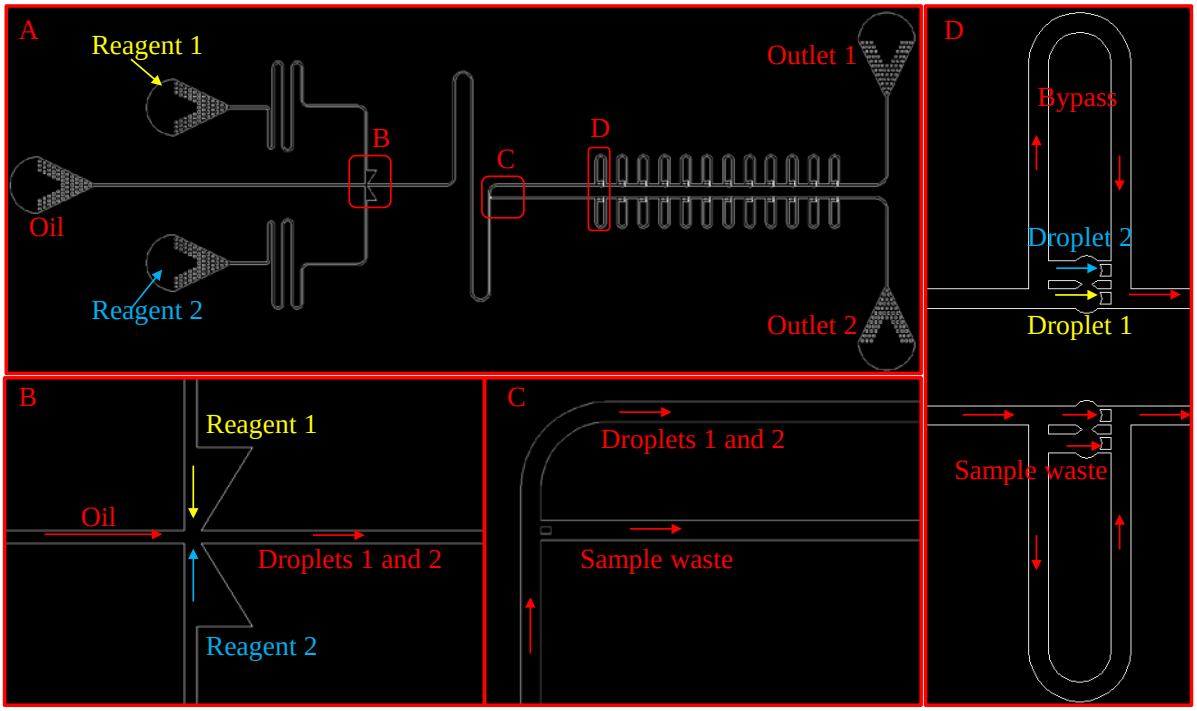

Figure 7.3 Sketch of the second version design for trapping two streams of droplets. A) Overview of the chip design. B) Droplet generator to generate two streams of droplets alternatively with channel height 60 μm , channel width of oil 120 μm , channel widths of reagent 1 and 2 120 μm with a triangle pressure oscillator. C) A channel is added beside the trapping channel to dispose the sample waste, which has a rectangular pillar at the inlet. D) Trapping wells to trap two droplets from upstream. The channel of sample waste has the same dimensions as the trapping channel. An array of trapping wells can be integrated into the flow stream depending on requirements.

Some preliminary experiments were performed to test the design as shown in Figure 7.4. Results show that the trapping wells can successfully trap and merge droplets. Although the second version combines two flow streams into one and thus has a much simpler structure, several problems were also found:

- It is difficult to adjust the flow rates of each fluid to ensure an alternative droplet generation with 1:1 ratio.

- The droplet generation mode is sensitive to the pressure fluctuation downstream. When switching the pressures in outlet 1 and outlet 2, a small flow fluctuation could break the droplet generation rule (from 1:1 ratio to other ratios).
- When some dust (e.g. a small piece of PDMS) occasionally goes into the channel, it is difficult to remove it to the sample waste channel due to the pillar in the waste channel inlet. Nevertheless, the pillar should be kept there in order to prevent droplets going inside the waste channel when droplet trapping is triggered.

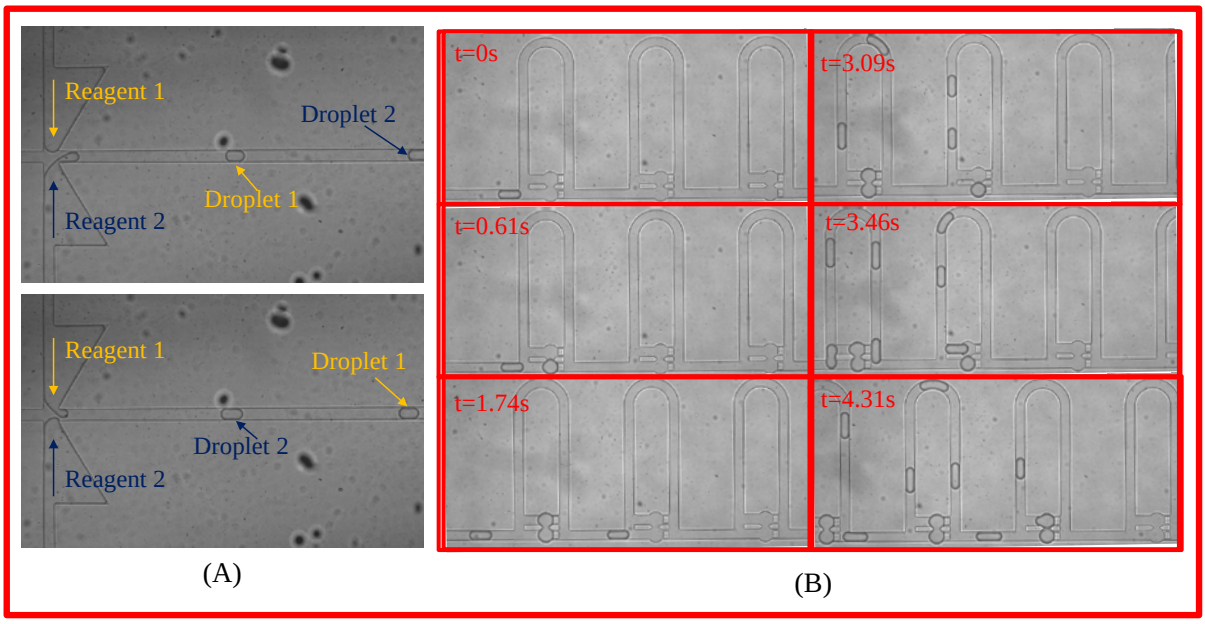

Figure 7.4 (A) Picture of droplet generation alternatively captured using $4\times$ magnification. B. Droplet trapping process captured using $4\times$ magnification.

Therefore, the third version design was proposed after many tests and optimization to overcome the above drawbacks. The sketch of the design is shown in Figure 7.5, which consists of two T-junction generators, a trapping channel, a waste channel and a channel for removing dust inside the chip. The two droplet streams are symmetric and have exactly the same channel dimensions. The T-junction as shown in Figure 7.5 (B), has a channel width of $120\,\mu m$, channel height $60\,\mu m$ (channel height is uniform in the whole chip). Robustness is particularly emphasized in the channel design. First, the performance of the two droplet generators must be decoupled which is achieved by designing a long channel after each of the T-junctions. If the channel after the T-junction is too short, a droplet going into or exiting it will lead to significant fluctuation of the channel resistance, which will affect the

droplet generation in the other T-junction path. Preliminary experimental testing indicated that the channel between the T-junction and trapping well on each side should be long enough to contain at least 40 ~ 50 droplets to damp the fluctuation, which is set to be 42 mm.This decoupling eliminates the need for synchronizing the two droplet generation processes as in the previously reported designs, which is quite challenging from the practical point of view. Second, an intersection is added before the trapping wells shown in Figure 7.5 (C) with the left branch for disposing waste and the right for removing dust. At the beginning of droplet generation, droplets are not uniform due to unstable flow conditions. These undesired droplets are disposed through the left branch, through which the waste in the trapping wells after each reaction is also released into the waste reservoir. A pillar is added at the entrance of the left branch to prevent droplets from entering it during the trapping time. The right branch is designed to remove any dust inside the chip. Although pillars are added in the entrance to filter the fluids, small pieces of PDMS inside the chip may still block the channel. High pressure is applied to remove the dust through this channel, where the channel width is set to be larger than the other three channels so that the dust can be easily removed (the right channel width is set to $150\,\mu m$, the others are set to $120\,\mu m$). The downstream channel is set to guide droplets into the trapping wells. The trapping design shown in Figure 7.5 (D) consists of two trapping wells and two bypass channels. Each bypass channel has a length of $4000\,\mu m$, and width $120\,\mu m$. The trapping well as shown in Figure 7.5(E), has a diameter of $85\,\mu m$, and the distance between two centers is $160\,\mu m$. Therefore, the two circles intersect and form a gap between them. The gap width at the intersection is $57.4\,\mu m$. The gap between each pillar is set to $25\,\mu m$.

When a droplet from either of the streams (e.g. a droplet from reagent 1) reaches the trapping channel, it will enter the trapping well because the resistance of the bypass channel is set to be higher than that of the trapping well. After being trapped, the droplet will stay inside the trapping well due to the interfacial tension and dramatically increase the resistance of the trapping well. The droplets behind the trapped one will enter the bypass channel then. When a droplet from the other stream (reagent 2) reaches the trapping channel, it will also enter the other trapping well and merge with the trapped droplet from reagent 1. Meanwhile, the reaction starts. The merged droplets mix fast within several seconds due to the disturbance induced by the droplets coming or leaving the bypass channel.

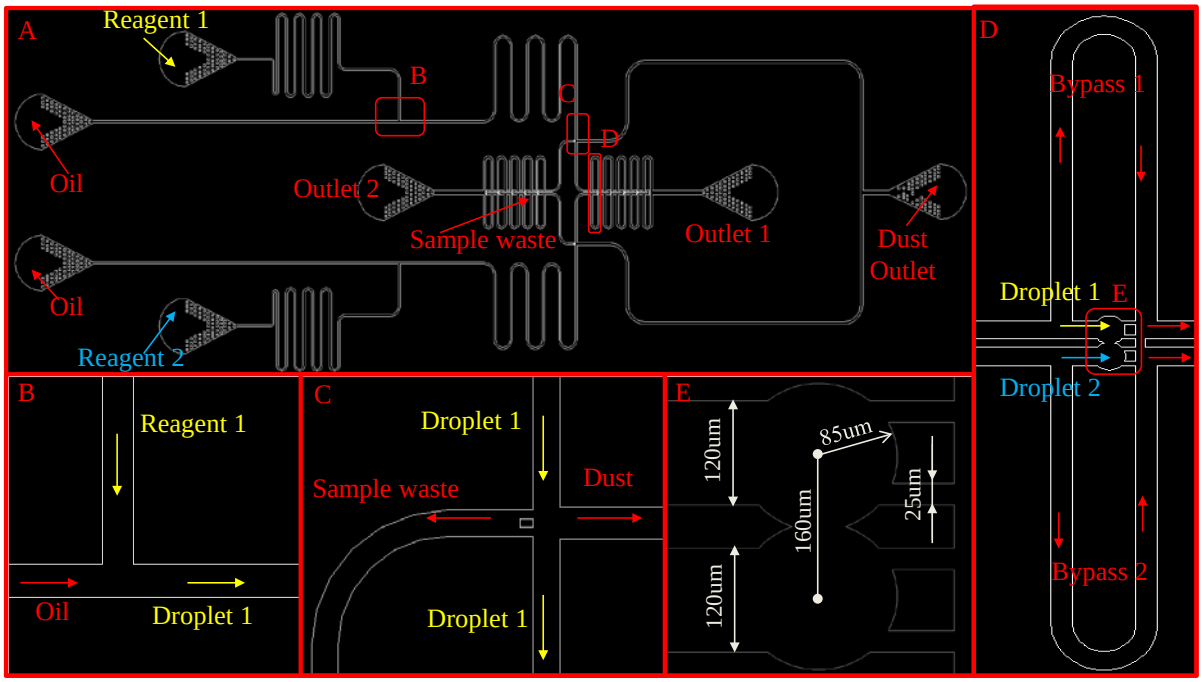

Figure 7.5 Sketch of the third version design for trapping two streams of droplets. A) Overview of the chip design. The design is symmetric and has two separate T-junction droplet generators with exactly the same channel dimensions. B) T-junction droplet generator for reagent 1 with channel height 60 μm , channel width of oil 120 μm , channel width of reagent 1 120 μm . C) An intersection: the left channel is used to dispose sample waste; the right channel is used to remove dust inside the microfluidic chip, the downstream channel is used to trap droplets. D) Trapping design for trapping droplets from two droplet streams. The channel of sample waste has the same dimensions as the trapping channel. An array of trapping wells can be integrated into the flow stream depending on requirements. E) Dimensions of two trapping wells. Inlet channel width keeps the same as upstream channel 120 μm ; trapping well diameter 85 μm ; Distance between two centers 160 μm ; gap width at the intersection of the two wells 57.4 μm ; gap width between each pillar 25 μm .

The operation procedures for a typical chemical or biological reaction are summarized as follows:

1. Remove all the dust inside the chip by pumping oil with high pressures (1bar in our experimental setup) from all of the inlets and outlets except the dust outlet, which will be blocked after checking the chip is clean.
2. Fill the sample inlets with reagent 1 and reagent 2, respectively and adjust pressures to generate droplets at the generators. In general, the system takes a bit time to stabilize and

generate uniform droplets. Non-uniform droplets should be eliminated for quantitative analysis which is realized in this design by adding a sample waste channel. By applying a moderate pressure from outlet 1 during the initial period of droplet generation, the unstable droplets can be pumped into the sample waste channel. The pressure in outlet 1 is adjusted to a threshold that can prevent the droplet from going into the trapping channel but not a significant back flow into the sample waste channel.

3. Once the droplets are uniform, the same amount of pressure as that applied in outlet 1 is applied in outlet 2 and no pressure in outlet 1. The droplets start going to the trapping channel.
4. Use a microscope and high speed camera to record the trapping and reaction process.
5. After the reaction is finished, apply a high pressure in outlet 1(1bar) and no pressure in outlet 2 to release the sample.
6. After releasing the sample in the trapping channel, repeat step 3~6 for a second reaction.

7.2.2 Design Criterion

First, the trapping wells must satisfy two flow conditions in order to trap droplets: i), when a droplet reaches the entrance of the trapping wells, it must enter the trapping well, and ii), after a droplet gets trapped, the droplet cannot be pushed through any gaps connected with the trapping well. To consider these criteria in the design, one-dimensional (1D) circuit analysis model is used as shown in Figure 7.6 (B), while Figure 7.6 (A) illustrates the design of the trapping well region and the definition of the associated parameters. To satisfy the first condition, the flow rate of the trapping well and the bypass channel should meet the criterion of $Q_{\text{trap}} > Q_{\text{bypass}}$ when a droplet reaches the entrance of the trapping well, since droplets always flow into the stream with a higher flow rate. When a droplet from one stream gets trapped, it will block half of the trapping well and increase its resistance. Therefore, the only concern is whether or not the droplet form the second stream will get trapped or not, that is the flow condition should satisfy $Q'_{\text{trap}} > Q_{\text{bypass}}$ (Q'_{trap} is the flow rate in the second half trapping well after a droplet gets trapped in the first half trapping well). If the droplet from the second stream can get trapped, the droplet from the first stream can get trapped as well due to $Q_{\text{trap}} > Q'_{\text{trap}}$ (Q_{trap} is the flow rate in the first half trapping well when no droplet gets inside the trapping well). When the first droplet gets trapped, the half of the trapping well can be considered as blocked due to small flow rate.

In a rectangular channel in which there are no droplets or obstructions, the resistance of a laminar flow can be approximately estimated as:

$$\Delta P = \frac{a\mu QL}{wh^3} \tag{7.1}$$

where μ is the viscosity of the fluid, Q the flow rate of the fluid, L, w and h are the length, width and height of the channel, respectively, and a is a dimensionless parameter that depends on height/width ratio, and is expressed in Equation(7.2) [398]:

$$a = 12\left[1 - \frac{192h}{\pi^5 w}\tanh\left(\frac{\pi w}{2h}\right)\right]^{-1} \tag{7.2}$$

Equation (7.1) is accurate to within 0.26% for any rectangular channel that has $h/w < 1$, when Reynolds number is below ~1000 [398]. Therefore, the pressure drop through the bypass channel can be calculated as:

$$P_{\mathrm{j}} - P_{\mathrm{down}} = \Delta P = \frac{a_{\mathrm{bypass}}\mu_{\mathrm{c}} Q_{\mathrm{bypass}} L_{\mathrm{bypass}}}{wh^3} \tag{7.3}$$

where a_{bypass} is a constant, μ_{c} is the viscosity of the continuous phase, Q_{bypass} is the flow rate of the continuous phase in the bypass channel, L_{bypass} is the bypass channel length.

The lower channel (trapping well) consists of the trapping well and two small gaps. The trapping well is circular in top view and rectangular in cross-section. We approximate the circular shape with the square that circumscribes it. This approximation does not input significant error in the calculation of the total hydrodynamic resistance, since the trapping well contributes only around 2% to the total hydrodynamic resistance of the lower channel ($R_{\mathrm{trap}} << R_{\mathrm{gap}}$), and we can estimate $P_{\mathrm{j}} \approx P_{\mathrm{trap}}$, and $P_{\mathrm{j}}^{'} \approx P_{\mathrm{trap}}^{'}$. Because the gap width is smaller than the gap height, we need to substitute gap width as h, and gap height as w into Equation (7.1) to calculate R_{gap}. Therefore, the pressure drop through the lower channel can be estimated as:

$$P_{\mathrm{j}} - P_{\mathrm{down}} = \Delta P = \frac{a_{\mathrm{trap}}\mu_{\mathrm{c}} Q_{\mathrm{trap}} L_1}{wh^3} + \frac{1}{2}\frac{a_{\mathrm{gap}}\mu_{\mathrm{c}} Q_{\mathrm{trap}} L_2}{hw_{\mathrm{gap}}^{\ 3}} \tag{7.4}$$

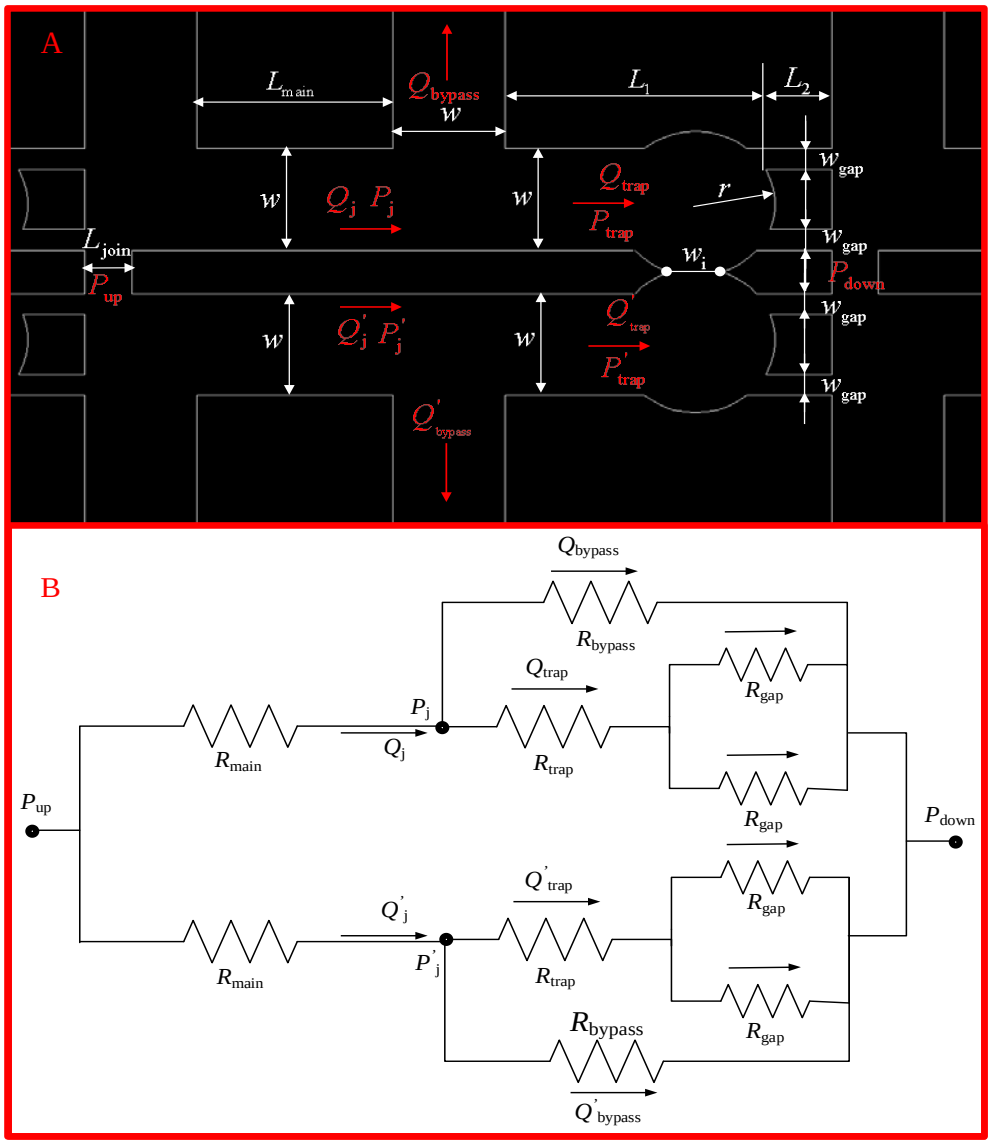

Figure 7.6 (a) Definition of parameters of a trapping well unit. P_{up} and P_{down} are the pressures at the inlet and outlet of a trapping well, respectively; P_j and $P_j^{'}$ are the pressures at the T-junctions of each stream, respectively; P_{trap} and $P_{trap}^{'}$ are the pressures at the back tip of trapped droplets; Q_j and $Q_j^{'}$ are the flow rates in the main channels of each stream, respectively. Q_{bypass} and $Q_{bypass}^{'}$ are the flow rates in each bypass channel; Q_{trap} and $Q_{trap}^{'}$ are the flow rates in each trapping well; w the channel width; w_i the width of the intersection gap between two trapping wells; w_{gap} the width between each pillar; r the radius of the trapping well; L_1 length of the trapping well; L_2 length of gap between each pillar; L_{join} length of the junction that connects the two main channels of the two streams; and L_{main} length of the main channel. (b) Equivalent fluidic circuit of a trapping well unit with fluidic resistors.

Combine Equation (7.3) and Equation (7.4), one can obtain,

$$\frac{Q_{\text{trap}}}{Q_{\text{bypass}}} = \frac{a_{\text{bypass}} L_{\text{bypass}}}{a_{\text{trap}} L_1 + \frac{wh^2}{2w_{\text{gap}}^3} a_{\text{gap}} L_2} \tag{7.5}$$

Define non-dimensional forms:

$$L^*_{\text{bypass}} = \frac{L_{\text{bypass}}}{w}, L^*_1 = \frac{L_1}{w}, L^*_2 = \frac{L_2}{w}, w^*_{\text{gap}} = \frac{w_{\text{gap}}}{w}, h^* = \frac{h}{w}, \text{ flow rate ratio } \varphi = \frac{Q_{\text{trap}}}{Q_{\text{bypass}}}$$

Then, Equation (7.5) can be rewritten into a non-dimensional form,

$$\varphi = \frac{a_{\text{bypass}} L^*_{\text{bypass}}}{a_{\text{trap}} L^*_1 + \frac{a_{\text{gap}} L^*_2 h^{*2}}{2w^{*3}_{\text{gap}}}} > 1 \tag{7.6}$$

The radius of the trapping well is set to be $r = 0.7w$ ($r = 85\mu\text{m}$) in order to allow the droplet to occupy most of the trapping well. L^*_1 is set to be $L^*_1 = 2.33$ ($L_1 = 279\mu\text{m}$) so that the following droplets don't contact with the trapped droplet (avoid droplet merging). L^*_2 is set to be $L^*_2 = 0.6$ ($L_2 = 71\mu\text{m}$), and w^*_{gap} is set to be $w^*_{\text{gap}} = 0.2$ ($w_{\text{gap}} = 25\mu\text{m}$) due to fabrication limitation (If the pillars after the trapping well are too small, they may be peeled off from the silicon wafer). The actual channel dimensions are smaller than the nominal channel dimensions since silicone oil swells PDMS channel. The actual channel dimensions are measured after silicone oil sufficiently swells PDMS channel and listed in Table 7.1.

Table 7.1 Channel dimensions of microfluidic trapping wells

Parameters	w (μm)	h (μm)	r (μm)	w_i (μm)	w_{gap} (μm)	L_1 (μm)	L_2 (μm)	L_{bypass} (μm)	L_{join} (μm)	L_{main} (μm)
Nominal Dimensions	120	60	85	57.4	25	279	71	4000	50	210
Actual Dimensions	100	53	75	66	15	291	74	4000	45	227

By substituting the actual channel dimensions into Equation (7.2), one can obtain: $a_{\text{bypass}} = 17.93$, $a_{\text{trap}} = 17.93$, $a_{\text{gap}} = 14.59$. Substitute all the parameters into Equation (7.6), we can get,

$$\varphi = 0.036 L^*_{\text{bypass}} > 1 \tag{7.7}$$

The final expression of flow rate ratio φ is proportional to the bypass channel length L^*_{bypass}. In order to trap a droplet in the trapping well, we must satisfy $\varphi = 0.036 L^*_{\text{bypass}} > 1$. Therefore, the first condition must satisfy $L^*_{\text{bypass}} > 27.8$.

In order to satisfy the second condition which is the trapped droplet cannot go through any gaps in the trapping well, the pressure drops over different components must be well designed. First, to ensure the droplet doesn't go through the gap in the intersection of the two circles, the pressure drop through the two circles ($\Delta P_{\text{i}} = P_{\text{trap}} - P'_{\text{trap}} \approx P_{\text{j}} - P'_{\text{j}}$) must be less than (or equal to) the Laplace pressure gradient across the intersection (ΔP_{Lap1}), which can be expressed as,

$$\Delta P_{\text{i}} \le \Delta P_{\text{Lap1}} = \gamma \left[\left(\frac{2}{w_{\text{i}}} + \frac{2}{h} \right) - \left(\frac{1}{r_{\text{d}}} + \frac{2}{h} \right) \right] = \gamma \left(\frac{2}{w_{\text{i}}} - \frac{1}{r_{\text{d}}} \right) \tag{7.8}$$

where the actual $w_{\text{i}} = 66\mu\text{m}$ (after swelling), interfacial tension $\gamma = 42\text{mN/m}$, and droplet radius $r_{\text{d}} \le 75\mu\text{m}$ (after swelling). By substituting these parameters into Equation (7.8), the pressure drop between two streams should satisfy,

$$\Delta P_{\text{i}} \le 713\text{Pa} \tag{7.9}$$

In order to minimize the pressure gradient between the two streams, the main channels of the two streams are connected through junctions after each trapping well. The length of the junction is set to be $L_{\text{join}} = 50\mu\text{m}$ in order to keep the droplets from going through it. When the droplets haven't gone into the trapping channel, the pressures (P_{j}, P'_{j}) and flow rates (Q_{j}, Q'_{j}) in the two steams are supposed to be the same due to the symmetric geometry, and there is no pressure gradient across the intersection of the two circles. When droplets come into the main channel and the number of droplets inside the main channels of the two streams are not the same (duo to non-synchronized droplet generation), the resistances of the main channels of the two streams are not equal, which cause the

pressure drop between two circles(ΔP_i). To reduce the resistance imbalance between the two main channels, the length of each main channel is set to much less than the spacing between two droplets ($L_{main} << \lambda_d$) so that the difference of number of droplets between two main channels is less than (or equal to) one. However, L_{main} should be set at least some distance to let the flow be fully developed. Here, L_{main} is set to $L_{main} = 210\mu m$.

Second, to ensure the trapped droplet doesn't go through the gap between the pillars, the fluid pressure drop through the trapping well and the pillars ($\Delta P_d = P_{trap} - P_{down} \approx P_j - P_{down}$) should be less than (or equal to) the Laplace pressure gradient across the trapped droplet (ΔP_{Lap2}), which can be expressed as:

$$\Delta P_d \le \Delta P_{Lap2} = \gamma\left[\left(\frac{2}{w_{gap}}+\frac{2}{h}\right)-\left(\frac{1}{r_d}+\frac{2}{h}\right)\right]=\gamma\left(\frac{2}{w_{gap}}-\frac{1}{r_d}\right) \quad \textbf{(7.10)}$$

Since $r_d >> \frac{w_{gap}}{2}$, Equation (7.10) can be simplified as,

$$\Delta P_d \le \Delta P_{Lap2} \approx \frac{2\gamma}{w_{gap}} \quad \textbf{(7.11)}$$

After a droplet gets trapped inside the trapping well, the following droplets will enter the bypass channel, which increase the hydrodynamic resistance of the bypass channel. The resistance of bypass channel with droplets can be estimated as,

$$R_{bypass+drop} = \frac{a_{bypass}\mu_c L_{bypass}}{wh^3} + n.R_d \quad \textbf{(7.12)}$$

where n is the number of droplets inside the bypass channel, R_d is the resistance of a droplet. The number of droplets can be calculated as,

$$n = \frac{L_{bypass}}{\lambda_d} \quad \textbf{(7.13)}$$

where λ_d is the spacing between two droplet centers. Therefore, the pressure drop $\Delta P_d = P_j - P_{down}$ can be calculated as,

$$\Delta P_{\mathrm{d}} = Q_{\mathrm{bypass}} \times R_{\mathrm{bypass+drop}} = Q_{\mathrm{bypass}} \left(\frac{a_{\mathrm{bypass}} \mu_{\mathrm{c}} L_{\mathrm{bypass}}}{wh^3} + \frac{L_{\mathrm{bypass}}}{\lambda_{\mathrm{d}}} . R_{\mathrm{d}} \right) \quad \textbf{(7.14)}$$

Droplet resistance is difficult to be accurately predicted without having some empirical data to work with, although several studies have experimentally studied the influence of the viscosity ratio, droplet speed, surface tension, droplet size and channel geometry on droplet resistance[268, 277, 399]. Glawdel *et al*. [367] proposed a suitable rule of thumb to estimate the droplet resistance, that is, each droplet will increase the resistance of the segment of channel it occupies by 2-5 times. Hence, one can estimate R_{d} (three times was used in this calculation) as,

$$R_{\mathrm{d}} = \frac{3 a_{\mathrm{bypass}} \mu_{\mathrm{c}} L_{\mathrm{d}}}{wh^3} \quad \textbf{(7.15)}$$

where L_{d} is the droplet length.

By substituting Equation (7.14) and Equation (7.15) into Equation (7.11), one can obtain,

$$Q_{\mathrm{bypass}} \le \frac{2\gamma wh^3}{\mu_{\mathrm{c}} a_{\mathrm{bypass}} L_{\mathrm{bypass}} w_{\mathrm{gap}} \left(1 + \frac{3L_{\mathrm{d}}}{\lambda_{\mathrm{d}}} \right)} \quad \textbf{(7.16)}$$

After a droplet gets trapped, $Q_{\mathrm{trap}} << Q_{\mathrm{bypass}}$, but a small amount of fluid can still go through the trapping well due to the thin film between the droplet and channel wall ($Q_{\mathrm{trap}} \neq 0$). Therefore, $Q_{\mathrm{j}} = Q_{\mathrm{bypass}} + Q_{\mathrm{trap}} > Q_{\mathrm{bypass}}$ is always true. In order to ensure the droplet can remain in the trapping well, we let:

$$Q_{\mathrm{j}} \le \frac{2\gamma wh^3}{\mu_{\mathrm{c}} a_{\mathrm{bypass}} L_{\mathrm{bypass}} w_{\mathrm{gap}} \left(1 + \frac{3L_{\mathrm{d}}}{\lambda_{\mathrm{d}}} \right)} \quad \textbf{(7.17)}$$

If we satisfy Equation (7.17), Equation (7.16) is also satisfied due to $Q_{\mathrm{j}} > Q_{\mathrm{bypass}}$.

Q_{j} can be expressed as,

$$Q_{\mathrm{j}} = U_{\mathrm{c}} wh \quad \textbf{(7.18)}$$

where U_c is the average velocity of the continuous phase in the main channel. By substituting Equation (7.18) into Equation (7.17), one can obtain the third flow condition:

$$Ca_{\mathrm{c}} \le \frac{2h^2}{a_{\mathrm{bypass}} L_{\mathrm{bypass}} w_{\mathrm{gap}} \left(1+\frac{3L_{\mathrm{d}}}{\lambda_{\mathrm{d}}}\right)} \tag{7.19}$$

where $Ca_{\mathrm{c}} = \frac{\mu_{\mathrm{c}} U_{\mathrm{c}}}{\gamma}$ is the capillary number of the continuous phase. The non-dimensional form of the third condition can be expressed as:

$$Ca_{\mathrm{c}} \le \frac{2h^{*2}}{a_{\mathrm{bypass}} L^*_{\mathrm{bypass}} w^*_{\mathrm{gap}} \left(1+\frac{3L^*_d}{\lambda^*_{\mathrm{d}}}\right)} \tag{7.20}$$

The design criteria are summarized as follows:

- The geometry of the two streams should be symmetric and the upstream channel length should be long enough to contain enough number of droplets (at least 50 droplets in each stream) in order to reduce the fluctuation of pressure when a droplet comes or leaves the channel, and decouple the influence of two droplet generators.
- The length of each main channel between two trapping well units should be much less than the droplet spacing to minimize the imbalance of the main channel resistances between two flow streams. The pressure unbalance between two main channels should satisfy:

$$\Delta P_{\mathrm{i}} \le \Delta P_{\mathrm{Lap1}} = \gamma\left[\left(\frac{2}{w_{\mathrm{i}}}+\frac{2}{h}\right)-\left(\frac{1}{r_{\mathrm{d}}}+\frac{2}{h}\right)\right] = \gamma\left(\frac{2}{w_{\mathrm{i}}}-\frac{1}{r_{\mathrm{d}}}\right) \tag{7.8}$$

- There exists a minimum bypass channel length that ensures the droplet can be trapped. The bypass channel length should satisfy:

$$\varphi = \frac{a_{\mathrm{bypass}} L^*_{\mathrm{bypass}}}{a_{\mathrm{trap}} L^*_1 + \frac{a_{\mathrm{gap}} L^*_2 h^{*2}}{2w^{*3}_{\mathrm{gap}}}} > 1$$

- The capillary number of the continuous phase should satisfy:

$$Ca_c \le \frac{2h^{*2}}{a_{\text{bypass}} L^*_{\text{bypass}} w^*_{\text{gap}} \left(1 + \frac{3L^*_d}{\lambda^*_d}\right)}$$

- Reducing the bypass channel length can expand a larger Capillary number range, but the bypass channel length should be larger than the minimum required value.
- Increasing the channel height or reducing the gap width can also expand a larger Capillary number range, but the ratio h^* / w^*_{gap} should be limited, it is hard to fabricate the gaps when $h^* / w^*_{\text{gap}} > 5$.
- Increasing the droplet spacing can also expand a larger capillary number range.

Considering some dust may partially block the gaps between each pillar, which increases the resistance of the trapping channel, it is suggested that L^*_{bypass} should be set at least 1.5 times larger than the minimum required value. In this design, L^*_{bypass} is set to $L^*_{\text{bypass}} = 40$ ($L_{\text{bypass}} = 4000\mu\text{m}$, ideal result based on calculation $L_{\text{bypass}} = 2500\mu\text{m}$) in order to make sure the droplet can directly go into the trapping well. By estimating the droplet length $L^*_d = 2$ and the spacing $\lambda^*_d \in (10,15)$, one can calculate the capillary number range that can let droplets remain inside the trapping wells $Ca < 0.0033$ when $\lambda^*_d = 10$, and $Ca < 0.0037$ when $\lambda^*_d = 15$.

7.3 Materials and Experimental Setup

For all experiments, two types of silicone oil (DC200, Sigma Aldric) with a viscosity of 5 cSt and 10 cSt, respectively were used as the continuous phase to consider the influence of the viscosity of the continuous phase. Ultrapure water was used as reagent 1, and Methylene Blue with a concentration of 1mg/ml (diluted in ultrapure water) was used as reagent 2 to create a phase contrast in order to demonstrate the merging and mixing processes. No surfactant was added to any of the fluids. Microfluidic chips were fabricated using polydimethylsiloxane (PDMS) by standard soft-lithography techniques.

The fluids were driven by a high precision microfluidic pressure control system (MSFC 8C, Fluigent). Droplet generating, trapping, mixing and releasing were visualized using an inverted epifluorescence microscope (Eclipse Ti, Nikon) with $4\times$ and $20\times$ objectives and a high speed camera

(Phantom v210, Vision Research). Different input pressures were applied to span a range of capillary number and flow rates. Instead of using multiple flow sensors to monitor the flow rate for each streams, the average velocity of droplets was measured when they reached the entrance of the trapping wells, based on which the average velocity of silicone oil was estimated by dividing droplet velocity with a slip factor. The slip factor is defined as:

$$\alpha = \frac{U_{\mathrm{d}}}{U_{\mathrm{c}}} \tag{7.21}$$

where U_{d} is the average velocity of the dispersed phase; U_{c} is the average velocity of the continuous phase.

Vanapalli *et al*. [399]found the slip factor $\alpha = 1.28$ for all droplets that tested under the following conditions: droplet length varies from 1.5~7.2w (w is the channel width), two viscosity ratios 0.03 and 0.88 (the dispersed phase to the continuous phase) and capillary number from 0.001~0.01 without surfactant. All of the flow conditions in this experiment fall in these ranges. Therefore, $\alpha = 1.28$ was used to estimate the velocity of the continuous phase in all experimental results. U_{d} can be directly measured from the captured videos.

7.4 Experiments

7.4.1 Droplet Generation

The two T-junctions (see Figure 7.7) can generate droplets independently. There is no need to synchronize the droplet generation frequency and spacing of the two droplet streams, which significantly simplifies the structure of the microfluidic chip. From Figure 7.7 we can see that the system performs robustly as the droplets are trapped as desired even the droplet generation frequency and spacing of the two droplet streams are quite different. Droplet sizes can be adjusted by varying the flow rate ratio of the two phases. By gradually increasing the pressure applied in the continuous phases, we can figure out the maximum capillary number that we can reach to keep the trapped droplets inside the trapping wells. Four pressures (400mbar, 500mbar, 600mbar and 700mbar) were applied to the continuous phases in both T-junctions when using 5cSt silicone oil, and two pressures (400mbar, 700mbar) were applied in both T-junctions respectively, when using 10cSt silicone oil as the continuous phases. For each pressure setting in the continuous phases, pressures applied in the

dispersed phases were adjusted to generate droplets with a droplet length around twice of the channel width.

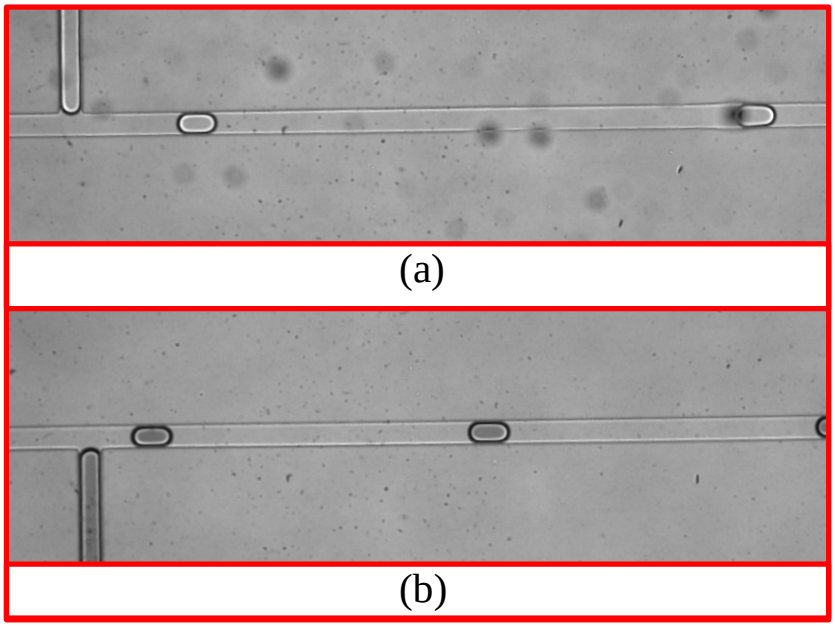

Figure 7.7 Two streams of droplet generation captured from high-speed camera with $4\times$ objective under the setting conditions: $P_{\text{oil1}} = 500\text{mbar}$, $P_{\text{oil2}} = 500\text{mbar}$, $P_{\text{water}} = 440\text{mbar}$, $P_{\text{dye}} = 440\text{mbar}$, $P_{\text{outlet1}} = 230\text{mbar}$, $P_{\text{outlet2}} = 0\text{mbar}$. Silicone oil with a viscosity of 5cSt was used as the continuous phase. (a) Water droplets with droplet length about $2w$ and spacing $28w$. (b) Methylene blue dye droplets with droplet length $2w$ and spacing $19w$.

7.4.2 Droplet pairing and Trapping

After the droplet generation is stable with uniform droplet size and spacing, the next step is to switch the pressure magnitude between outlet 1and outlet 2 (see Figure 7.5). The droplets from two separate streams started going to the trapping channel. The pairing and trapping processes are shown in Figure 7.8 with the capillary numbers $Ca_{\text{c\_dye}} = 0.00118$, and $Ca_{\text{c\_water}} = 0.00134$, respectively. From the experimental results, one can see that the trapping wells can robustly pair and trap droplets with one from the stream of dye droplets and the other water droplets. The microfluidic chip design was test with different pressure ranges until the trapped droplets couldn't remain inside the trapping wells (pushed through gaps due to high pressure). Experimental results showed that when the

capillary number of the continuous phase increased to 0.0034, the trapped droplet couldn't remain in the trapping wells, which agrees well with the theoretical calculation.

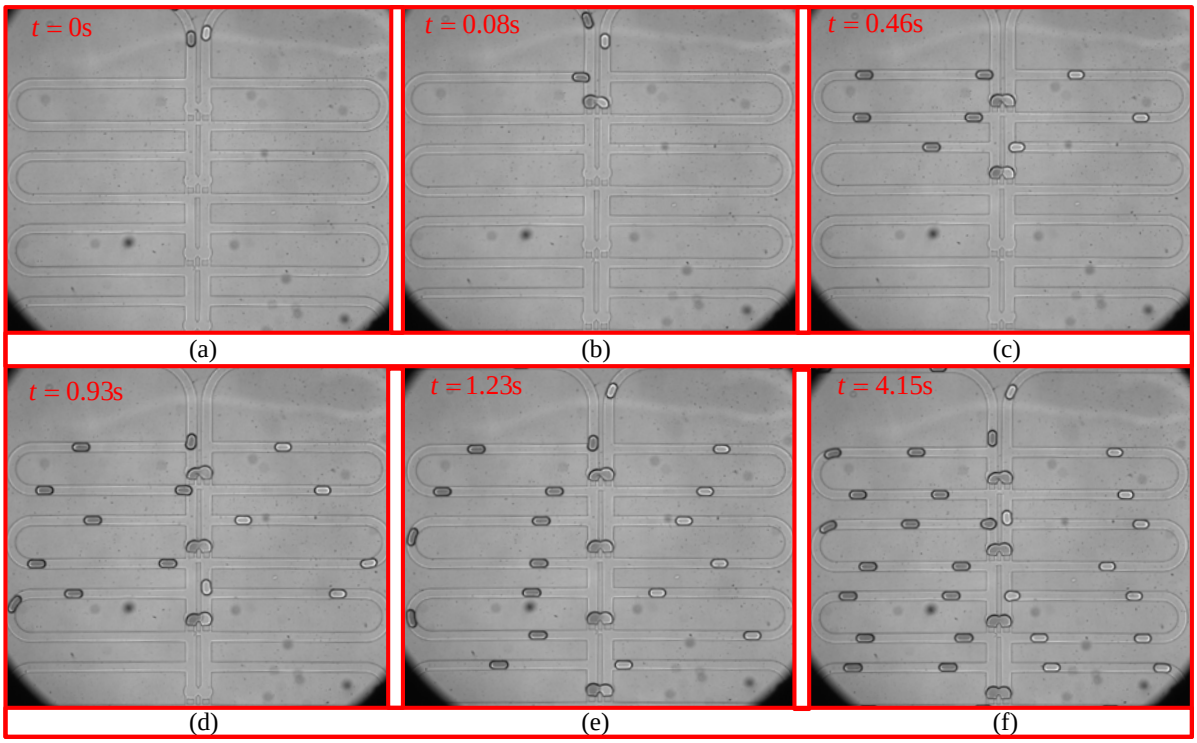

Figure 7.8 Droplet pairing and trapping process captured from high-speed camera using $4\times$ objective under the setting conditions: $P_{oil1} = 500\text{mbar}$, $P_{oil2} = 500\text{mbar}$, $P_{water} = 440\text{mbar}$, $P_{dye} = 440\text{mbar}$, $P_{outlet1} = 0\text{mbar}$, $P_{outlet2} = 230\text{mbar}$. Silicone oil with a viscosity of 5cSt (5cSt silicone oil density 0.913g/ml) was used as the continuous phase. Droplets containing Methylene blue dye are on the left side branch, and Droplets full of water are on the right side branch. (a) Droplets reached in front of the first trapping well. The methylene blue droplet had an average velocity of $U_{d\_dye} = 13.9\text{mm/s}$, and the water droplet had an average velocity of $U_{d\_water} = 15.8\text{mm/s}$ before they got trapped in the first trapping well. Capillary number of the continuous phase were estimated as $Ca_{c\_dye} = 0.00118$, $Ca_{c\_water} = 0.00134$; (b) the first pair of droplets got trapped; (c) the second pair of droplets got trapped; (d) the third pair of droplets got trapped; (e) the forth pair of droplets got trapped. (f) Four pairs of droplets are fully mixed after 4.15s.

7.4.3 Droplet Merging and Mixing

Mixing of the reagents flowing through microchannels is important in a variety of chemical or biological reactions. It is difficult to mix solutions in microchannels due to low Reynolds number. At low Reynolds number, pressure flows are laminar and uniaxial, so the mixing between streams in the flow is purely by diffusion[400]. The diffusion time in one dimensional diffusion can be estimated as,

$$t \approx \frac{x^2}{2D} \tag{7.22}$$

where t is the elapsed time since the diffusion begins; x is the mean distance travelled by the diffusing solute in one direction along one axis after the elapsed time t; D is the diffusion coefficient of a solute in free solution. The diffusion coefficient of methylene blue in water was assumed to be $D_{\mathrm{MB}} = 5 \times 10^{-10}\ \mathrm{m}^2/\mathrm{s}$ [401]. The travelling distance of the solute inside a trapping well is $300\mu\mathrm{m}$. Therefore the mixing time of methylene blue by pure diffusion is estimated about 90s, which is unacceptable in many chemical or biological reactions. However, in fact, this design can reach a fast fully mixing within several seconds as shown in Figure 7.9. In order to observe the detailed mixing process, $20\times$ objective was used to capture the video. From Figure 7.9, one can see that the droplet mixing was enhanced by a repeated droplet shape waving.

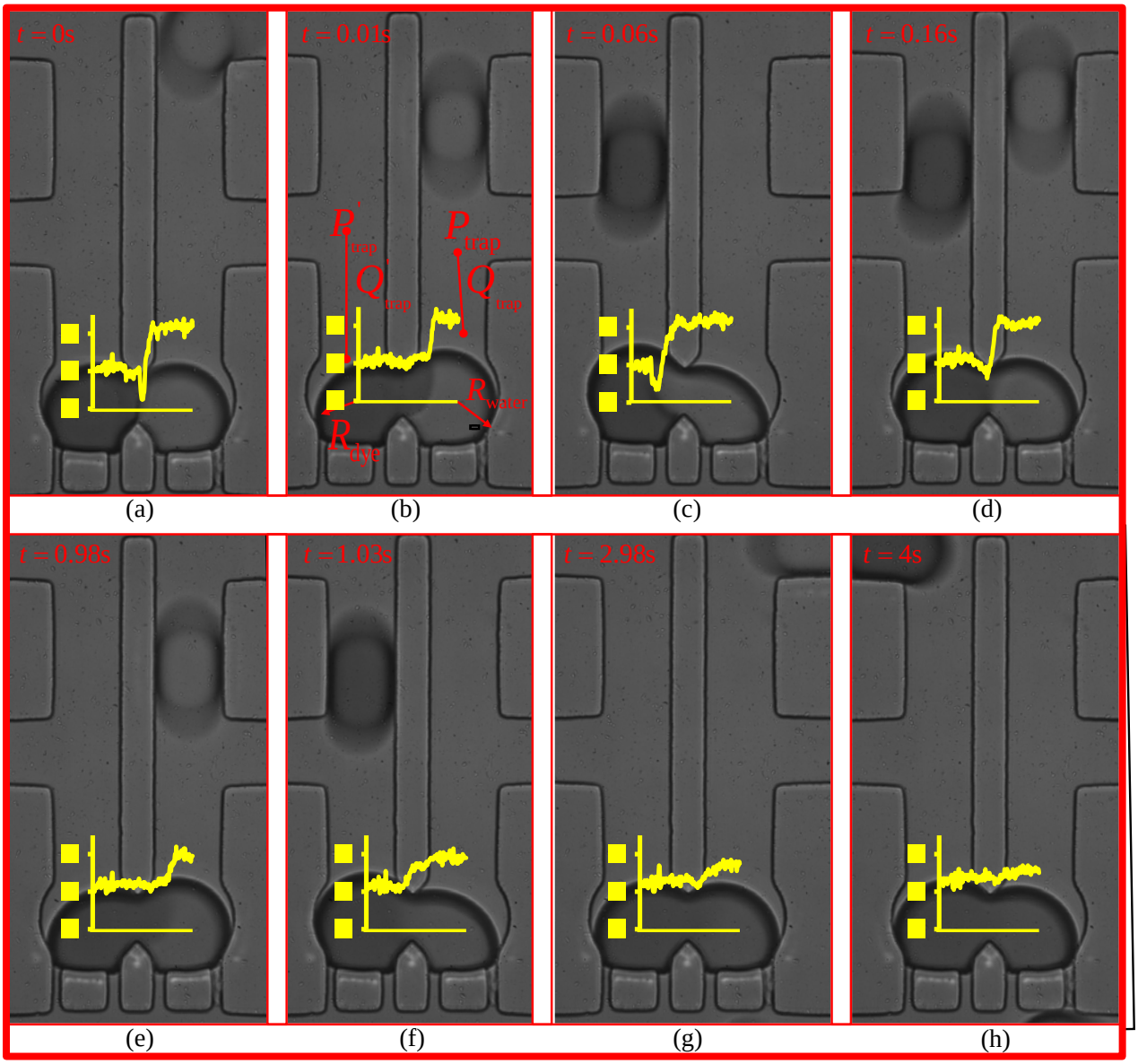

Figure 7.9 Droplet merging and mixing process in the second trapping well captured from high-speed camera using $20\times$ objective under the setting conditions: $P_{\text{oil1}} = 500\text{mbar}$, $P_{\text{oil2}} = 500\text{mbar}$, $P_{\text{water}} = 440\text{mbar}$, $P_{\text{dye}} = 440\text{mbar}$, $P_{\text{outlet1}} = 0\text{mbar}$, $P_{\text{outlet2}} = 230\text{mbar}$. Silicone oil with a viscosity of 5cSt (5cSt silicone oil density 0.913g/ml) was used as the continuous phase. The darker droplet is methylene blue, and the brighter droplet is pure water. (a) The two droplets start merging. (b ~ h) Droplet mixing process after merging. Line grayscale values (range 0-255) are plotted in each figure cross the center of the trapping well, which shows that the reagents are fully mixed after 4s.

After both of the droplets got trapped and merged, the Laplace pressure drop between the two droplets (see Figure 7.9(b)) can be calculated using Equation (7.23),

$$P_{\text{trap}} - P_{\text{trap}}^{'} = \gamma\left[\left(\frac{1}{R_{\text{dye}}} + \frac{2}{h}\right) - \left(\frac{1}{R_{\text{water}}} + \frac{2}{h}\right)\right] = \gamma\left(\frac{1}{R_{\text{dye}}} - \frac{1}{R_{\text{water}}}\right) \quad \textbf{(7.23)}$$

where R_{dye} is the radius of dye droplet after merging, and R_{water} is the radius of water droplet after merging.

When a water droplet enters the main channel of the water stream (i.e. Figure 7.9 (b) and (e)), it increases the main channel resistance of the water stream. Therefore, more silicone oil enters the dye stream ($Q_{\text{trap}}^{'} > Q_{\text{trap}}$), which leads to $P_{\text{trap}}^{'} > P_{\text{trap}}$. From Equation (7.23), we can obtain that the radius of the dye droplet is larger than the radius of the water droplet ($R_{\text{dye}} > R_{\text{water}}$), when $P_{\text{trap}}^{'} > P_{\text{trap}}$. Therefore, we can see that when a water droplet enters the main channel with water droplets, the trapped droplets will be slightly pushed into trapping well near the water side as shown in Figure 7.9 (b) and (e). On the other hand, when a dye droplet enters the main channel of the dye stream, leading to $P_{\text{trap}} > P_{\text{trap}}^{'}$, the trapped droplets will be slightly pushed into trapping well near the dye side as shown in Figure 7.9 (c) and (f). However, the main channel length is designed to contain no more than one droplet so that the pressure fluctuation is not large enough to push the merged droplets out of the trapping well. When both of the main channels contain one droplet (i.e. Figure 7.9 (d)) or no droplet (i.e. Figure 7.9 (g)), the resistances of the two main channels are balanced, and the two trapped droplets have almost the same shape. Therefore, the droplet shapes keep waving when the following droplets come into and leave the trapping channel, which greatly improves the mixing of solute inside the droplet.

In order to quantify the degree of mixing as a function of time, the mixing index of the captured cross-section images was experimentally measured, which is defined by $I_{\text{mix}} = 1 - I_{\text{s}}$, where I_{s} is the discrete intensity of segregation, which is defined by Danckwerts [402]:

$$I_{\text{s}} = \frac{\left\langle \left(N - \langle N \rangle\right)^2 \right\rangle}{\langle N \rangle \left(N_{\max} - \langle N \rangle\right)} \quad \textbf{(7.24)}$$

where N is the grayscale value (between 0 and 255) of a pixel, and $\langle\ \rangle$ means an average over all the pixels in the image, and $N_{\max}$ is the maximum grayscale value over all the pixels in the image. In a perfectly mixed droplet, $I_s = 0$ or the index of mixing $I_{mix} = 1$, while in a completely segregated droplet, $I_s = 1$ or $I_{mix} = 0$.

Because a droplet is 3D curved, the boundary of the trapped droplets is darker than the inside area, which could affect the measurement of grayscale values. Therefore, the boundary was excluded when measuring the grayscale value of each pixel inside the trapped droplets as shown in Figure 7.10(a). A Matlab code was written to identify the contour of the trapped droplet in each frame and measure the grayscale value of each pixel inside the red line. The mixing index I_m was measured along with time under three different incoming droplet velocities as shown in Figure 7.10(b). Experimental results indicate that the mixing index is a power function of time. When I_m reaches 0.98, the two reagents are considered to be fully mixed. Figure 7.10(b) shows that the reagents were well mixed at around $t = 3\text{s}$, when $U_d = 17.3\text{mm/s}$ and $U_d = 19.8\text{mm/s}$ .The reagents were well mixed at around $t = 6\text{s}$, when $U_d = 12.9\text{mm/s}$. Therefore, increasing the droplet velocity (or Capillary number) can improve the mixing process, because it increases the fluctuation speed of the droplet shape.

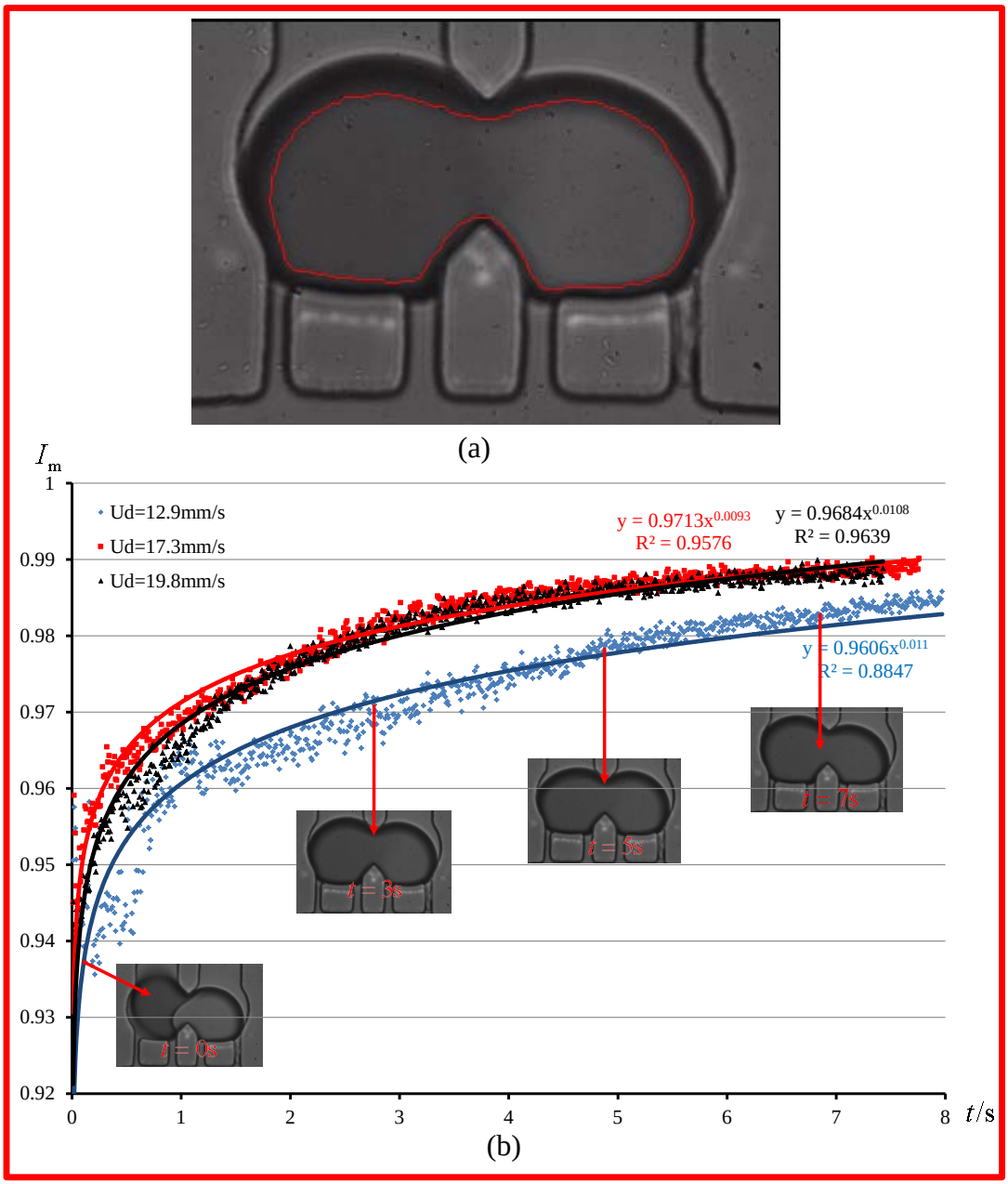

Figure 7.10 (a) Grayscale value measurement area, where the boundary was excluded. (b) Mixing index V.S. time under different droplet average velocities

7.4.4 Droplet Releasing

After all the trapping wells were full of droplets, the flow in the chip can be stopped allowing for the desired reaction completed. Figure 7.11(a) shows an image of the trapped droplets that were kept

in the trapping well for a period of time. After that, the trapping wells were rinsed by applying a high pressure at outlet 1, and the sample is washed out of the chip through outlet 2 (see Figure 7.11 (b)). Figure 7.11(c) shows the trapping wells after rinsed by silicone oil, which has no sample waste and ready for another trapping process.

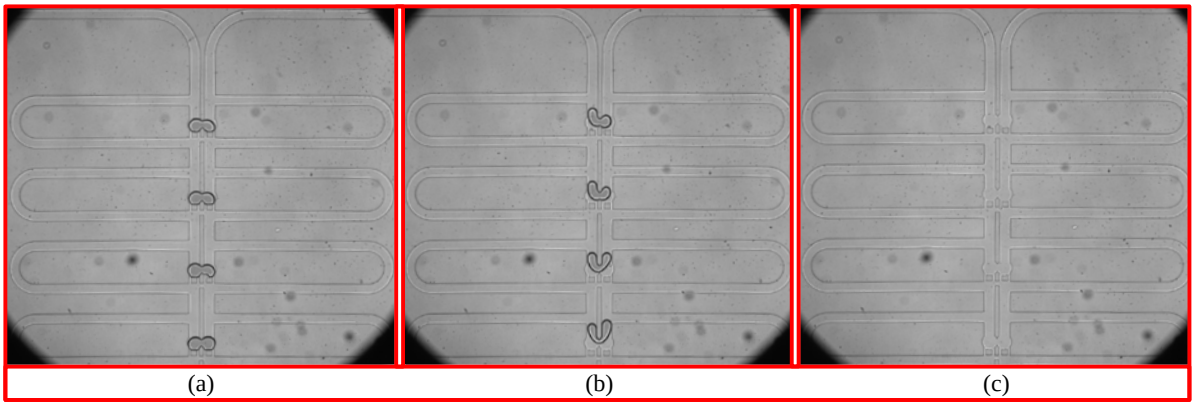

Figure 7.11 Droplet releasing process captured from high-speed camera using $4\times$ objective under the setting conditions: $P_{oil1} = 500\text{mbar}$, $P_{oil2} = 500\text{mbar}$, $P_{water} = 0\text{mbar}$, $P_{dye} = 0\text{mbar}$, $P_{outlet1} = 1000\text{mbar}$, $P_{outlet2} = 0\text{mbar}$. Silicone oil with a viscosity of 5cSt (5cSt silicone oil density 0.913g/ml) was used as the continuous phase. (a) Droplets trapped inside the trapping wells before releasing. (b) The trapped droplets were about to be washed out of the trapping wells. (c) The trapping wells after rinsed by silicone oil.

7.4.5 Generating Sample Concentration Gradient

It is very important to control the concentration ratio between two reagents in many applications, such as drug screening [403], nanoparticle synthesis [360], and cell analysis [359]. In this design, one can vary the concentration of each sample by simply adjusting the droplet sizes of each reagent. However, this method can only generate one concentration at each trapping process. During a trapping process, all the trapping wells have the same concentration due to the uniform size of droplets. If we need to switch to a different concentration, we have to release the trapped droplets and change the droplet size first. This method is acceptable in some applications which don't require high-throughput reactions. However, some applications need a concentration gradient of samples in one chip at the same time. To solve this problem, the droplet size was fixed at constant value, and the concentration of each sample was adjusted by changing the number of droplets that get trapped at each trapping well. The design of the trapping wells is shown in Figure 7.12. The number of trapped

droplets ratio in a trapping well varies from 1:3 to 3:1, which creates 5 different reagent concentrations.

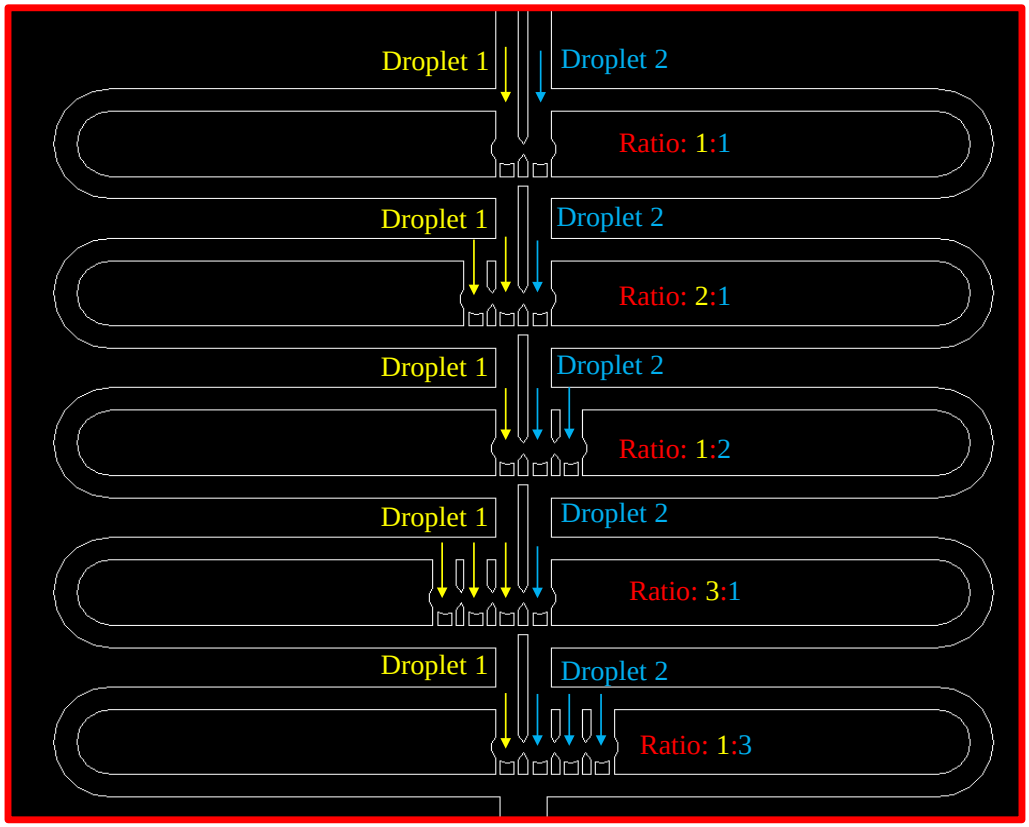

Figure 7.12 Sketch of the trapping well design for trapping multiple droplets with a concentration gradient of reagents. The number of trapped droplets ratio in a trapping well varies from 1:3 to 3:1, which creates 5 different reagent concentrations.

The experimental trapping process is shown in Figure 7.13(a) ~ (h). Figure 7.13(i) shows that the trapped droplets are fully mixed. The merged droplet has a final methylene blue dye concentration of 50%, 66.7%, 33.% and 75% of the original concentration in each trapping well from upstream to downstream, respectively. Figure 7.13(j) shows the droplets are being released from the trapping wells.

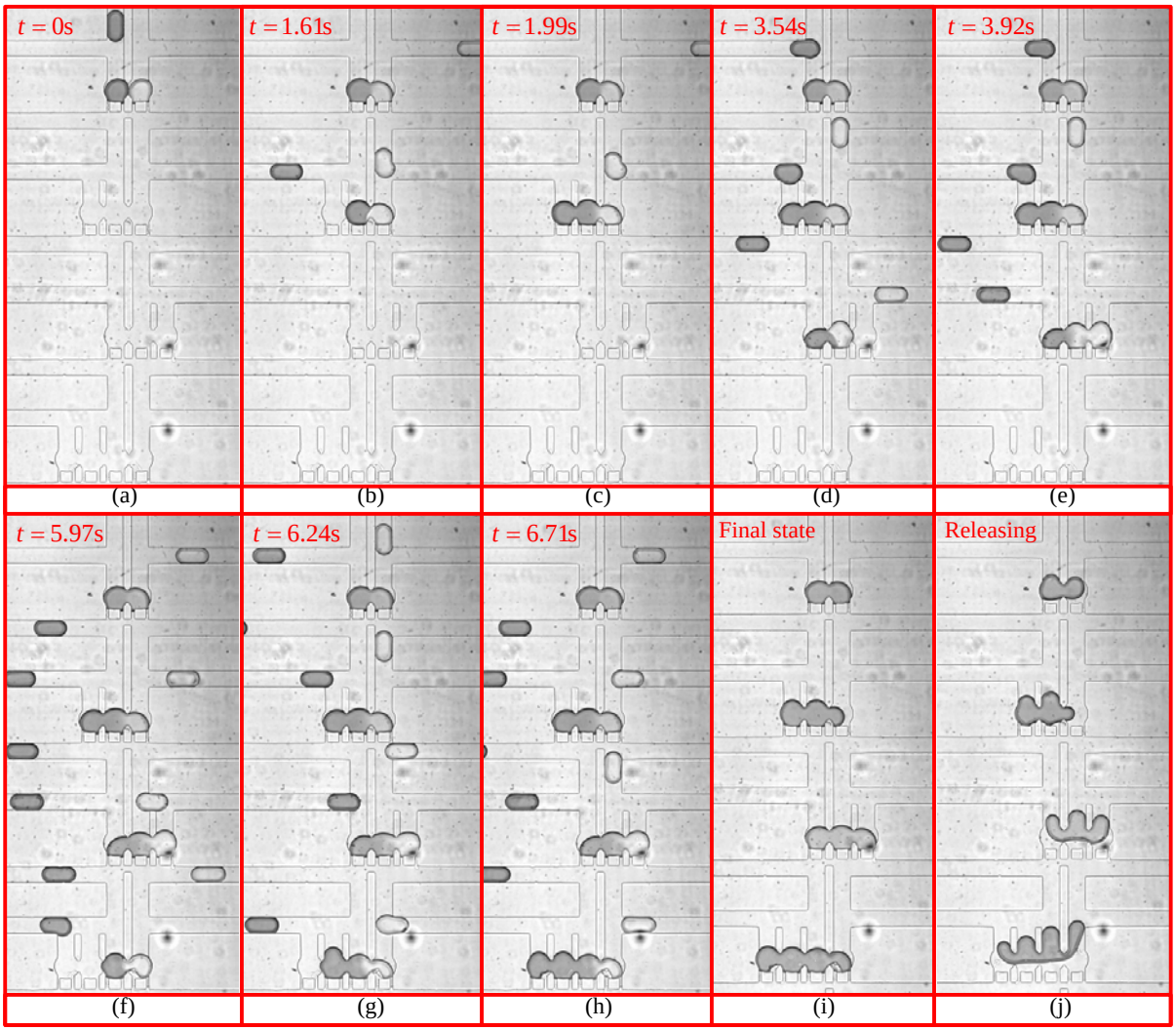

Figure 7.13 Droplet trapping and releasing process to generate a concentration gradient captured from high-speed camera using $4\times$ objective under the setting conditions: $P_{oil1} = 480\text{mbar}$, $P_{oil2} = 480\text{mbar}$, $P_{water} = 440\text{mbar}$, $P_{dye} = 450\text{mbar}$, $P_{outlet1} = 0\text{mbar}$, $P_{outlet2} = 170\text{mbar}$. (a) ~ (h) is droplet trapping process. (i) ~ (j) is droplet releasing process.

7.5 Conclusion

In this work, a microfluidic chip design that integrates droplet generation, pairing, trapping, merging, mixing, and releasing was proposed and experimentally demonstrated. The criterion of this design was analyzed and verified by experiments. This design doesn't require any synchronization of droplet frequency, spacing or velocity, which makes the microfluidic chip work robustly, and is

controlled entirely by liquid flow involving no electrodes, magnets or any other moving parts. This design can control the trapping starting time by simply applying a pressure in two outlets so that we can calculate the exact reaction time. Experiments also show that this design has a fast mixing within several seconds, which is caused by the fluctuation of droplet shape when a droplet comes or leaves the main channel. In addition, a modified trapping well design can trap multiple droplets, which can generate reagent concentration gradient. This design can be applied in many chemical or biological reactions, such as drug screening.

7.6 List of Symbols

2D	Two dimensional
3D	Three dimensional
a	Dimensionless parameter dependent on channel aspect ratio
Ca	Capillary number
Ca_{c_dye}	Capillary number of the continuous phase in the dye droplet stream
Ca_{c_water}	Capillary number of the continuous phase in the water droplet stream
D	Diffusion coefficient
D_{MB}	Diffusion coefficient of methylene blue in water
h	Channel height
I_{mix}	Mixing index
I_s	Discrete intensity of segregation
L	Channel length
L_1	Length of trapping well
L_2	Length of pillars
L_{bypass}	Length of bypass channel
L_d	Droplet length
L_{join}	Length of the junction that connects the two main channels of the two streams
L_{main}	Length of the main channel
n	Number of droplets inside the bypass channel
N	Grayscale value
N_{max}	Maximum grayscale value
PDMS	Polydimethylsiloxane
P_{down}	Pressure at the downstream
P_{dye}	Pressure applied at the inlet of methylene blue dye
P_j	Pressure at the up junction
$P_j^{'}$	Pressure at the down junction

P_{oil1}	Pressure applied at the inlet 1 of silicone oil
P_{oil2}	Pressure applied at the inlet 2 of silicone oil
$P_{outlet1}$	Pressure applied at outlet 1
$P_{outlet2}$	Pressure applied at outlet 2
P_{trap}	Pressure at the up trapping well
P'_{trap}	Pressure at the down trapping well
P_{up}	Pressure at the upstream
P_{water}	Pressure applied at the inlet of pure water
Q	Flow rate
Q_j	Flow rate in the up main channel
Q'_j	Flow rate in the down main channel
Q_{bypass}	Flow rate through the up bypass channel
Q'_{bypass}	Flow rate through the down bypass channel
Q_{trap}	Flow rate through the up trapping well
Q'_{trap}	Flow rate through the down trapping well
r	Radius of trapping well
r_d	Radius of droplets
$R_{bypass+drop}$	Hydrodynamic resistance of the bypass channel with droplets
R_d	Droplet resistance
R_{dye}	Radius of dye droplet after merging
R_{gap}	Hydrodynamic resistance of the gap between pillars
R_{trap}	Hydrodynamic resistance of the trapping well
R_{water}	Radius of water droplet after merging
t	Elapsed time
U_c	Average velocity of the continuous phase

U_{d}	Average velocity of droplets
$U_{\mathrm{d\_dye}}$	Average velocity of dye droplets
$U_{\mathrm{d\_water}}$	Average velocity of pure water droplets
w	Channel width
w_{i}	Width of the intersection gap between two trapping wells
w_{gap}	Gap width between pillars
x	Mean distance travelled by the diffusing solute in one direction along one axis

Greek symbols

α	Slip factor
λ	Spacing between two droplet centers
φ	Flow rate ratio of trapping well to bypass channel
γ	Interfacial tension
μ	Fluid viscosity

Subscripts

c	Continuous phase
d	Dispersed phase
bypass	Bypass channel

Superscripts

*	Dimensionless form of variables
'	Down trapping well

Chapter 8
Conclusions and Recommendations for Future Work

8.1 Conclusions of this Thesis

Droplet-based microfluidic devices are believed to be a viable tool for improving the performance of biomedical assays. Each droplet can be used as a movable micro-reactor and is fully compartmentalized by an immiscible liquid phase, which prevents precipitating of substances and cross contaminations between different droplets and channel walls. The volume of each droplet can reach the scale of femtoliter, which can minimize the consumption of samples and reduce reaction time. The droplet generation frequency can be as high as 20 KHz with small volume variations ranging only from 1-3%. Therefore, droplet-based microfluidics can also be used in high throughput applications. Moreover, compared to single phase microfluidic flow, mixing occurs very rapidly within the droplets due to the convective flow inside them, which is extremely important in microfluidics, where the Reynolds number is very small. With these merits, droplet-based microfluidic offers many possibilities to study fundamental and applied chemical and biomedical reactions.

Although extensive research effort has been reported in the study of droplet-based microfluidic over the past decades, this technique has not been commercialized, yet. One of the challenges that limit droplet microfluidic chips into commercialization is to integrate and scale up multiple functions effectively into a small chip to generate droplets with controlled volume and frequency, and precisely control and manipulating each individual droplet including droplet sorting, detecting, merging, splitting, pairing, mixing, trapping, releasing, long term and short term storing. Therefore, it is critical to investigate the droplet formation process and understand how to design microfluidic structures to manipulate each individual droplet effectively. In order to integrate and scale up multiple functions of manipulating droplets, the first step is to design some effective and easy to use techniques for each function of manipulating droplets.

The initial motivation of this thesis is to study the fundamental principles of liquid-liquid droplet generation in a flow focusing device (Chapter 4). This work presents a 3D physical model with less fitting parameters compared to others' work, describing the droplet formation process in flow focusing devices operating in the squeezing regime, where droplet size is usually larger than the channel width. This model incorporates an accurate geometric description of the 3D droplet shape

during the formation process, an estimation of the time period for the formation cycle based on the conservation of mass and a semi-analytical model predicting the pressure drop over the 3D corner gutter between the droplet curvature and channel walls, which allow an accurate determination of the droplet size, spacing and formation frequency. The model considers the influences of channel geometry (height to width ratio), viscosity contrast, flow rate ratio and capillary number with a wide variety.

Based on the understanding of droplet generation process described in Chapter 4 , the next phase of research experimentally investigated liquid-liquid droplet generation in a flow focusing device using stratified flow as the dispersed phase and its impact on single encapsulation, since most of chemical or biomedical reactions involve two or more reagents that are injected into the microchannel as a co-flowing stream before the droplet generation (Chapter 5). The co-flowing stream forms a stratified flow due to low Reynolds number, and sometimes involves single cell encapsulation into individual droplet in a biological reaction. The stratified flow with viscosity contrast has a significant impact on droplet formation process and single cell or particle encapsulation. This study employs a simple flow focusing device with two junctions in series and glycerol solutions with different concentrations which result in viscosity contrasts to form stratified flow in the first junction and thus droplets in the second junction. The droplet formation process was experimentally studied in the flow focusing generator by varying the flow rate ratio between fluids and the viscosity contrast while maintaining the operation is within the squeezing regime. To obtain a comprehensive understanding of the droplet formation dynamics involving stratified flow, five different scenarios were considered including two cases with pure 10%glycerol and pure 80%glycerol as the dispersed phase respectively and three other cases where these two fluids are either side by side or one is accompanied by the other. Droplet size and formation period for these cases were compared and analyzed considering the same geometric and flow conditions. It is found that stratified flow structure strongly influence droplet formation dynamics such as droplet size and formation frequency and the scenario with 80%glycerol surrounded by 10%glycerol in the first junction generates the largest droplet size. Each structure finds its own applications. For the purpose of single encapsulation, the scenario with 80%glycerol surrounded by 10%glycerol in the first junction provides the optimized means because high viscosity of 80%glycerol allows particles to be focused into a thin stream and spaced before entering droplets. The efficiency for single encapsulation was demonstrated up to 80% for $10\,\mu m$ polystyrene beads. However, the scenario with two fluids side by side in the first junction generates droplets with high

monodispersity for a larger range of flow ratios, which is useful for high throughput reactions involving different reagents.

After understanding the fundamentals of droplet generation process, several designs for practical use are proposed to generate or manipulate droplets (Chapter 6). These designs include: i) an improvement design of flow focusing device with different angles between the inlets of the dispersed and continuous phases in order to improve the uniformity of droplet size, ii) a droplet generation on demand system to control droplet generation on demand, iii) a droplet pair generation geometry with uniform droplet size and controlled droplet spacing to study the interaction between two nearby droplets, iv) a simple droplet merging chamber for controlled reagent volume, and v) a droplet trapping and releasing on demand system for drug screening.

First, droplet generation in flow focusing devices with three different angles between the inlets of the dispersed phase and the continuous phase $\theta = 45^{\circ}, 90^{\circ}$ and 135° was experimentally studied in order to synthesize monodispersed microbeads. Experimental results show that the size of drops produced in flow focusing devices depends on the velocity component of the continuous phase directed perpendicular to the main channel while the fluid is in the inlet. Thus, the angle between the inlets of two phases influences the drop size. Devices with $\theta = 90^{\circ}$ produce the smallest droplets because they have the largest velocity component perpendicular to the main channel. Moreover, this angle strongly impacts the robustness of the device operation: Devices with $\theta = 135^{\circ}$ operate more robustly and produce the most monodispersed drops.

Second, a droplet on demand system was presented by using off-the-shelf solenoid valves and a microcontroller. The microcontroller that has more than 100 digital I/O pins, can be pre-programmed to manipulate over 100 solenoid valves in parallel. Therefore, this droplet on demand system can be effectively scaled up to generate droplet on demand in a high throughput manner. The solenoid valves have fast response with a response time as low as 12ms, and can reach a maximum frequency of droplet generation up to 40Hz. In addition, droplet sizes linearly increase with the valve opening time, leading to easy control of droplet volume.

Third, a droplet pair generator was proposed to study the interaction between two nearby droplets when they travel in curved microchannels. Compared to other droplet pair generators, he uniqueness of this design is that it is capable of controlling the spacing between two droplets with only one

droplet generator, which eliminates the coupled effect of parallel droplet generators and hence, guarantees the uniformity of droplets.

Fourth, a passive merging design was proposed capable of merging variable numbers of droplets by designing a valve-type function in the merging chamber. The relationship between the numbers of droplets merged, the length of input droplets, and the length of output droplets is used to tune the design parameters according to the desired set of reactions. The reduced complexity of the design allows for easier design and configuration to a desired purpose and low risk for failures due to fabrication and operation uncertainties. The single-input-single-output design minimizes pressure disturbances from propagating downstream, and reduces the complexity of integration into a larger Lab-On-a-Chip system. The specific geometry of the chamber allows for the operation of a valve-type function to force the droplet from the chamber thereby imposing a critical volume limit. The geometry can be scaled up with little to no observable effect on the mode of operation. And finally, the capability of having different numbers of mergers for a single chip allows for the diversity of application to be broadened without changing fabrication, or design.

Last, a trapping and releasing droplet on demand design was presented for screening drugs that inhibit the tau-hexapeptide (AcPHF6) aggregation relatable to Alzheimer's disease. With the ability to trap and release droplets on demand, this device allows stable droplet generation and mixing prior to droplet storage. It is demonstrated that droplet microfluidic platform is a powerful alternative to traditional well plate methods for screening drugs towards Alzheimer's disease because it offers comparable sensitivity and accuracy for assays while significantly reducing reaction time (10minutes vs. 2 hours) and reagent use by four orders of magnitude (10nL vs. 200uL).

Although each proposed design in Chapter 6 has its own function to generate or manipulate droplets, but they are not integrated into a microfluidic chip to fulfill multi-steps of reactions. Therefore, the final project is to explore a microfluidic system that integrates multiple functions into one microfluidic chip to perform biomedical reactions, such as drug screen, and chemical synthesis (Chapter 7). This microfluidic device integrates droplet generation, pairing, trapping, merging, mixing, and releasing. The criterion of this design was analyzed and verified by experiments. This design doesn't require any synchronization of droplet frequency, spacing or velocity, which makes the microfluidic chip work robustly, and is controlled entirely by liquid flow involving no electrodes, magnets or any other moving parts. This design can control the trapping starting time by simply applying a pressure in two outlets so that we can calculate the exact reaction time. Experiments also

show that this design has a fast mixing within several seconds, which is caused by the fluctuation of droplet shape when a droplet comes or leaves the main channel. In addition, a modified trapping well design can trap multiple droplets, which can generate reagent concentration gradient. This design can be applied in many chemical or biological reactions, such as drug screening, chemical synthesis, and cell culture, etc.

8.2 Recommendations for Future Work

Several aspects for additional research in droplet-based microfluidic chip design are still required. For example, the assumption of 3D droplet shape in a rectangular channel is not very accurate as shown in Figure 4.5. It was hypothesized that the radius of droplet edge is half of the channel height, which could be varied with the contact angle. This could be examined by using a confocal micro Particle-Image_Velocimetry (μ-PIV) to measure the flow fields along the two-phase interface in order to scan the complete shape of the droplet.

The second effort is required to build a model to precisely describe the droplet resistance and slip factor inside microchannels. In this thesis, droplet resistance is assumed that each droplet will increase the resistance of the segment of channel it occupies by 2-5 times, and the slip factor is assumed to be a constant based on experimental measurements. In fact, the hydrodynamic resistance of moving droplets in microfluidic channels is dependent on many parameters, including droplet size, speed, spacing, viscosity ratio, surfactant concentration and confinement of channel geometry. The slip factor is relative to the hydrodynamic resistance of moving droplets. As far as I know, there have been no systematic studies of these effects.

The third effort is suggested to improve the microfluidic chip materials. PDMS swells most of the solvents, and shrink the channel geometries. In this thesis, the channel height is estimated by measuring the pressure and flow rate through the microfluidic channel. The actual channel dimensions are smaller than the nominal dimensions, and different solvents have different actual channel dimensions. Therefore, it is difficult to obtain precise channel dimensions by using PDMS. Silicon wafer and glass are hard materials and ideal for fabricating microfluidic chips, but the cost for the fabrication is high. Seeking for hard material and cheap fabrication method is still strongly required.

As mentioned in Section 6.3, several of our lab members observed that the spacing between a droplet pair changed when droplets passed through a curved microchannel. When droplets are transported

along a microchannel, they have significant influence on the hydrodynamic resistance of the flow streams. The velocity of the droplet may be different from that of the continuous phase depending on several factors such as channel geometry, viscosities of phases, flow rates, length of droplets and capillary number, which causes the spacing between two droplets to change. Studying the dynamics of interactions between droplets and the interactions between droplets and continuous phase can help to improve the control and manipulation of droplets in Lab-On-a-Chip devices such as sorting, merging, splitting etc. Therefore, the forth recommendation for future work was to study the droplet interaction between a droplet pair. Although some preliminary results have been obtained and show that the droplet spacing decreases after a curved channel, extensive experiments still need to be done by varying channel curvature, capillary number, droplet length, viscosity contrast, and initial spacing. After experiments are completed, a theoretical model is expected to be built to explain the phenomena, which will be continued as one of my postdoctoral projects.

Appendix A

Experimental Data Used in Chapter 4

Table A-1 Experimental data with dispersed phase: glyc/water 10% by wt., and channel height $h^* = 0.41$.

Q_c (μl/min)	Q_d (μl/min)	L^*_{fill}	L^*_{pinch}	W^*_{pinch}	V^*_d
2.83	2.13	0.865168539	2.820224719	0.269662921	2.660132781
2.93	1.85	0.831460674	2.775280899	0.247191011	2.462970774
2.97	1.66	0.797752809	2.797752809	0.280898876	2.292664269
3.07	1.44	0.775280899	2.786516854	0.247191011	2.169852828
3.15	1.21	0.730337079	2.797752809	0.247191011	2.045228822
3.26	1	0.730337079	2.741573034	0.258426966	1.880938568
3.53	0.83	0.707865169	2.797752809	0.258426966	1.745387419
3.65	0.66	0.674157303	2.786516854	0.235955056	1.682477783
2.69	1.66	0.831460674	2.876404494	0.235955056	2.400755823
2.79	1.36	0.786516854	2.786516854	0.269662921	2.177608282
2.93	1.08	0.730337079	2.752808989	0.280898876	2.009628288
3.05	0.83	0.696629213	2.764044944	0.258426966	1.828822968
2.36	1.35	0.842696629	2.808988764	0.247191011	2.476799494
2.48	1.06	0.786516854	2.797752809	0.247191011	2.177788858
2.61	0.8	0.730337079	2.786516854	0.269662921	1.940710294
2.75	0.59	0.685393258	2.786516854	0.235955056	1.819120735
2.04	1.01	0.820224719	2.831460674	0.247191011	2.345453524
2.18	0.76	0.775280899	2.831460674	0.235955056	2.092823263
2.31	0.55	0.741573034	2.865168539	0.224719101	1.927205814
1.82	0.58	0.808988764	2.797752809	0.224719101	2.117394956

Table A-2 Experimental data with dispersed phase: glyc/water 10% by wt., and channel height $h^* = 0.58$.

Q_c (μl/min)	Q_d (μl/min)	L^*_{fill}	L^*_{pinch}	W^*_{pinch}	V^*_d
3.58	3.19	0.987951807	2.759036145	0.385542169	2.754614093
3.65	3.03	0.987951807	2.734939759	0.409638554	2.679105004
3.74	2.87	0.963855422	2.686746988	0.385542169	2.565479265
3.84	2.72	0.927710843	2.722891566	0.385542169	2.501122775
3.9	2.53	0.927710843	2.686746988	0.385542169	2.388488719
3.98	2.37	0.879518072	2.734939759	0.397590361	2.312599774
4.06	2.21	0.843373494	2.759036145	0.397590361	2.230550117
4.15	2.04	0.855421687	2.710843373	0.397590361	2.146305135
4.23	1.88	0.819277108	2.686746988	0.385542169	2.082564503
4.34	1.66	0.819277108	2.65060241	0.397590361	1.990285667
3.14	2.42	1	2.686746988	0.385542169	2.648301481
3.24	2.25	0.951807229	2.710843373	0.385542169	2.561484865
3.32	2.09	0.915662651	2.734939759	0.409638554	2.440188152
3.41	1.92	0.903614458	2.746987952	0.373493976	2.35285124
3.49	1.77	0.879518072	2.722891566	0.409638554	2.270601396
3.58	1.61	0.819277108	2.662650602	0.385542169	2.171797686
3.67	1.45	0.807228916	2.65060241	0.385542169	2.104562686
2.6	1.89	1.072289157	2.746987952	0.397590361	2.754545889
2.68	1.71	1	2.734939759	0.397590361	2.605304052
2.78	1.58	0.951807229	2.771084337	0.385542169	2.462705623
2.89	1.44	0.891566265	2.722891566	0.385542169	2.376483213

Table A-3 Experimental data with dispersed phase: glyc/water 10% by wt., and channel height $h^* = 0.66$.

Q_c (µl/min)	Q_d (µl/min)	L^*_{fill}	L^*_{pinch}	W^*_{pinch}	V^*_d
3.43	2.7	1.202531646	2.481012658	0.430379747	2.724940716
3.59	2.34	1.126582278	2.53164557	0.46835443	2.531749556
3.7	2.08	1.063291139	2.455696203	0.455696203	2.397480245
3.81	1.83	0.987341772	2.430379747	0.455696203	2.264757919
3.96	1.59	0.936708861	2.455696203	0.443037975	2.123176649
4.11	1.35	0.886075949	2.443037975	0.455696203	1.999303542
4.29	1.12	0.835443038	2.455696203	0.443037975	1.895817451
4.46	0.9	0.82278481	2.430379747	0.430379747	1.772690876
4.63	0.7	0.810126582	2.443037975	0.46835443	1.608472707
2.69	2.04	1.278481013	2.53164557	0.430379747	2.923795385
2.8	1.75	1.202531646	2.46835443	0.443037975	2.654517434
2.91	1.51	1.113924051	2.481012658	0.443037975	2.504031986
3.08	1.27	1.075949367	2.493670886	0.455696203	2.366198391
3.23	1.06	0.987341772	2.46835443	0.430379747	2.157318614
3.4	0.87	0.924050633	2.493670886	0.430379747	2.016894415
3.61	0.66	0.835443038	2.455696203	0.430379747	1.832321583
3.79	0.48	0.784810127	2.455696203	0.430379747	1.699937798
1.99	1.36	1.392405063	2.569620253	0.443037975	3.087679188
2.09	1.13	1.316455696	2.493670886	0.430379747	2.805608839
2.21	0.92	1.227848101	2.53164557	0.417721519	2.579767773
1.65	1.06	1.481012658	2.544303797	0.405063291	3.287920491

Table A-4 Experimental data with dispersed phase: glyc/water 60% by wt., and channel height $h^* = 0.41$.

Q_c (μl/min)	Q_d (μl/min)	L^*_{fill}	L^*_{pinch}	W^*_{pinch}	V^*_d
2.54	1.83	0.806818182	3.136363636	0.295454545	2.197044262
2.66	1.71	0.795454545	3.056818182	0.295454545	2.067257046
2.76	1.57	0.75	3.011363636	0.306818182	1.930436847
2.9	1.44	0.772727273	2.920454545	0.284090909	1.821276779
3.03	1.32	0.727272727	2.852272727	0.284090909	1.734453359
2.29	1.78	0.829545455	3.113636364	0.306818182	2.296360068
2.39	1.62	0.818181818	3.079545455	0.295454545	2.100167038
2.52	1.5	0.795454545	2.920454545	0.318181818	1.978313606
2.63	1.37	0.806818182	2.863636364	0.306818182	1.851916969
2.72	1.23	0.75	2.863636364	0.295454545	1.737796087
1.96	1.67	0.852272727	3.102272727	0.284090909	2.431018615
2.05	1.53	0.829545455	3	0.295454545	2.251179083
2.16	1.4	0.806818182	2.977272727	0.284090909	2.093060248
2.25	1.25	0.795454545	2.931818182	0.295454545	1.928833138
2.36	1.1	0.715909091	2.875	0.295454545	1.767813818
2.47	0.99	0.715909091	2.852272727	0.306818182	1.683146597
1.73	1.35	0.875	3.090909091	0.295454545	2.376167783
1.86	1.17	0.806818182	2.988636364	0.284090909	2.111727605

Table A-5 Experimental data with dispersed phase: glyc/water 60% by wt., and channel height $h^* = 0.58$.

Q_c (µl/min)	Q_d (µl/min)	L^*_{fill}	L^*_{pinch}	W^*_{pinch}	V^*_d
3.21	3.04	0.987951807	2.963855422	0.385542169	2.545776827
3.31	2.97	0.915662651	2.987951807	0.409638554	2.4700761
3.47	2.79	0.891566265	2.939759036	0.385542169	2.321795363
3.63	2.6	0.879518072	2.86746988	0.409638554	2.183166375
3.81	2.4	0.855421687	2.807228916	0.397590361	2.050619495
4.02	2.2	0.831325301	2.734939759	0.385542169	1.917176323
2.81	2.53	0.987951807	3	0.385542169	2.553301357
2.99	2.31	0.86746988	2.927710843	0.385542169	2.358623771
3.18	2.09	0.86746988	2.879518072	0.385542169	2.173692987
3.36	1.88	0.819277108	2.807228916	0.409638554	2.003861234
3.59	1.69	0.78313253	2.78313253	0.385542169	1.863039974
3.84	1.49	0.746987952	2.795180723	0.409638554	1.742203523
2.38	2.01	0.963855422	2.963855422	0.373493976	2.571958502
2.57	1.77	0.951807229	2.831325301	0.397590361	2.319301032
2.78	1.55	0.86746988	2.831325301	0.373493976	2.097897964
2.98	1.35	0.819277108	2.807228916	0.397590361	1.920132659
3.21	1.15	0.795180723	2.710843373	0.385542169	1.772137495
1.83	1.57	1.13253012	3.012048193	0.373493976	2.752202777
2.02	1.36	1.024096386	2.951807229	0.373493976	2.414680487
4.24	3.58	0.86746988	2.86746988	0.397590361	2.197510853
4.43	3.32	0.831325301	2.831325301	0.373493976	2.065588765
4.62	3.07	0.795180723	2.795180723	0.397590361	1.948910137

Table A-6 Experimental data with dispersed phase: glyc/water 60% by wt., and channel height $h^* = 0.66$.

Q_c (μl/min)	Q_d (μl/min)	L^*_{fill}	L^*_{pinch}	W^*_{pinch}	V^*_d
2.58	2.4	1.2125	2.5	0.4125	2.708982858
2.81	2.13	1.075	2.4375	0.4125	2.423981423
3.09	1.87	0.9375	2.4375	0.4125	2.207884255
3.36	1.59	0.8875	2.4875	0.4125	1.997906566
3.69	1.32	0.8625	2.3875	0.4125	1.820392483
4.02	1.05	0.8	2.4125	0.4125	1.668997619
4.37	0.81	0.7875	2.4125	0.4	1.561657278
4.75	0.55	0.7625	2.4	0.425	1.425224167
2.3	1.63	1.1125	2.4375	0.4	2.590487303
2.59	1.32	1	2.4625	0.4	2.193728943
2.95	1.04	0.9125	2.4375	0.4125	1.940337436
3.31	0.78	0.825	2.3375	0.4	1.73650985
3.7	0.52	0.75	2.35	0.425	1.553667848
1.86	1.6	1.1875	2.675	0.3875	2.934795576
2.07	1.33	1.1375	2.4625	0.3875	2.536833392
2.33	1.11	1.05	2.425	0.3875	2.243975991
2.59	0.91	0.975	2.4375	0.3875	2.017141994
1.64	1.15	1.25	2.45	0.4	2.729517815
1.93	0.96	1.0875	2.425	0.4	2.400827043
2.2	0.74	0.975	2.425	0.4	2.098869595

Table A-7 Experimental data with dispersed phase: glyc/water 80% by wt., and channel height $h^* = 0.41$.

Q_c (µl/min)	Q_d (µl/min)	L^*_{fill}	L^*_{pinch}	W^*_{pinch}	V^*_d
2.08	0.95	0.715909091	3.761363636	0.284090909	1.551698943
2.03	0.85	0.727272727	3.613636364	0.295454545	1.633500586
2.11	0.82	0.704545455	3.556818182	0.284090909	1.553143323
2.2	0.8	0.704545455	3.511363636	0.295454545	1.5143926
2.3	0.77	0.659090909	3.420454545	0.306818182	1.464055621
1.73	0.78	0.738636364	3.636363636	0.306818182	1.666820784
1.81	0.75	0.727272727	3.556818182	0.295454545	1.606083601
1.88	0.71	0.715909091	3.477272727	0.295454545	1.536316337
1.98	0.68	0.681818182	3.443181818	0.295454545	1.481714821
1.33	0.74	0.761363636	3.852272727	0.295454545	1.848304867
1.41	0.7	0.75	3.693181818	0.306818182	1.75173941
1.5	0.66	0.727272727	3.556818182	0.295454545	1.654569885
1.57	0.63	0.738636364	3.443181818	0.295454545	1.585161252
2.41	0.78	0.704545455	3.306818182	0.295454545	1.40509907
2.51	0.74	0.659090909	3.295454545	0.306818182	1.351523227
2.1	0.66	0.681818182	3.318181818	0.295454545	1.39596618
1.12	0.62	0.795454545	3.806818182	0.295454545	1.906992269

Table A-8 Experimental data with dispersed phase: glyc/water 80% by wt., and channel height $h^* = 0.58$.

Q_c (μl/min)	Q_d (μl/min)	L^*_{fill}	L^*_{pinch}	W^*_{pinch}	V^*_d
2.44	1.66	0.869047619	3.30952381	0.380952381	2.055538099
2.62	1.6	0.869047619	3.19047619	0.392857143	1.941423504
2.83	1.53	0.80952381	3.095238095	0.380952381	1.822683482
3.13	1.48	0.821428571	2.952380952	0.404761905	1.707629865
3.36	1.39	0.785714286	2.928571429	0.392857143	1.6034369
3.6	1.29	0.785714286	2.928571429	0.392857143	1.504486262
3.78	1.22	0.75	2.857142857	0.392857143	1.437683726
2.31	1.37	0.869047619	3.095238095	0.380952381	1.940228718
2.49	1.31	0.833333333	3.071428571	0.404761905	1.825299953
2.65	1.25	0.80952381	3	0.392857143	1.727264302
2.84	1.18	0.797619048	2.94047619	0.392857143	1.631880502
3.04	1.12	0.761904762	2.928571429	0.380952381	1.559816103
3.22	1.04	0.773809524	2.904761905	0.380952381	1.468001885
3.41	0.98	0.761904762	2.916666667	0.404761905	1.410154668
1.78	1.21	0.964285714	3.095238095	0.380952381	2.176951876
1.96	1.14	0.916666667	3.095238095	0.392857143	1.995636748
2.14	1.07	0.857142857	3.023809524	0.369047619	1.840696797
2.32	0.99	0.869047619	2.928571429	0.404761905	1.704207611
2.5	0.93	0.785714286	2.857142857	0.392857143	1.611254674
2.7	0.85	0.773809524	2.857142857	0.380952381	1.49622061

Table A-9 Experimental data with dispersed phase: glyc/water 80% by wt., and channel height $h^* = 0.66$.

Q_c (µl/min)	Q_d (µl/min)	L^*_{fill}	L^*_{pinch}	W^*_{pinch}	V^*_d
2.29	1.31	0.975	2.725	0.4125	2.103877311
2.48	1.24	0.95	2.675	0.4125	1.97393417
2.68	1.16	0.875	2.675	0.4125	1.852964672
2.9	1.07	0.85	2.6125	0.3875	1.733339166
3.11	0.98	0.825	2.55	0.4	1.62674308
3.34	0.9	0.8	2.525	0.3875	1.552863374
3.57	0.81	0.75	2.4	0.425	1.476983647
3.77	0.72	0.7375	2.425	0.4125	1.41112925
4.02	0.64	0.6625	2.425	0.4125	1.374521119
4.26	0.54	0.6625	2.375	0.4375	1.306819581
1.89	1	1.0375	2.5625	0.4375	2.125706331
2.13	0.91	0.9375	2.5375	0.4125	1.939559009
2.38	0.82	0.8875	2.425	0.425	1.793137592
2.62	0.72	0.85	2.3875	0.425	1.65350871
2.88	0.62	0.825	2.3625	0.4	1.531539535
3.15	0.53	0.775	2.4	0.4125	1.45522014
1.5	0.69	1.0125	2.7	0.4	2.175504977
1.76	0.6	0.9375	2.66	0.3875	1.951330698
2.04	0.5	0.8875	2.4125	0.425	1.736728865
1.28	0.55	1.1125	2.6	0.425	2.2240593

Appendix B

Flow Rates Applied for Each Experiment in Chapter 5

Table A-10 Flow rate Settings for each experiment, where Q_{oil} is the flow rate of the continuous phase, $Q_{10\%}$ is the flow rate of 10%glyc, $Q_{80\%}$ is the flow rate of 80%glyc, $\frac{Q_{10\%}}{Q_{10\%}+Q_{80\%}}$ is the flow rate ratio of 10%glyc to total flow rate of the dispersed phase, and $\frac{Q_{10\%}+Q_{80\%}}{Q_{\text{oil}}}$ is the flow rate ratio of the dispersed phase to the continuous phase. Unit: (μl/min).

Exp #	Q_{oil}	$Q_{10\%}$	$Q_{80\%}$	$\frac{Q_{10\%}}{Q_{10\%}+Q_{80\%}}$	$\frac{Q_{10\%}+Q_{80\%}}{Q_{\text{oil}}}$	**Exp #**	Q_{oil}	$Q_{10\%}$	$Q_{80\%}$	$\frac{Q_{10\%}}{Q_{10\%}+Q_{80\%}}$	$\frac{Q_{10\%}+Q_{80\%}}{Q_{\text{oil}}}$
1	4	0.32	1.30	0.20	0.4	**20**	2.11	0.89	0.42	0.68	0.62
2	4	0.49	1.13	0.30	0.4	**21**	3.07	1.40	1.08	0.56	0.81
3	4	0.65	0.97	0.40	0.4	**22**	3.13	1.16	1.11	0.51	0.73
4	4	0.81	0.81	0.50	0.4	**23**	3.33	1.49	0.85	0.64	0.70
5	4	0.97	0.65	0.60	0.4	**24**	3.34	1.01	0.89	0.53	0.57
6	4	1.13	0.49	0.70	0.4	**25**	3.49	1.31	0.60	0.69	0.55
7	4	1.30	0.32	0.80	0.4	**26**	3.60	0.97	0.67	0.59	0.46
8	3.17	1.45	0.33	0.81	0.56	**27**	2.66	1.44	0.98	0.60	0.91
9	2.68	1.32	0.41	0.76	0.65	**28**	2.97	0.98	0.81	0.55	0.60
10	2.77	0.97	0.45	0.68	0.51	**29**	3.07	1.14	0.65	0.64	0.58
11	2.91	1.47	0.58	0.72	0.70	**30**	2.51	0.91	0.76	0.54	0.67
12	2.92	1.45	0.47	0.76	0.66	**31**	3.31	1.83	0.59	0.76	0.73
13	3.00	1.13	0.47	0.71	0.53	**32**	3.42	1.95	0.42	0.82	0.69
14	3.06	0.77	0.46	0.63	0.40	**33**	3.50	1.57	0.45	0.78	0.58
15	3.13	0.83	0.40	0.67	0.39	**34**	3.61	1.18	0.47	0.72	0.46
16	3.14	0.92	0.28	0.77	0.38	**35**	3.81	0.98	0.34	0.74	0.35
17	2.22	0.64	0.33	0.66	0.44	**36**	3.00	1.72	0.48	0.78	0.73
18	2.3	0.54	0.26	0.68	0.35	**37**	3.10	1.34	0.51	0.72	0.60
19	1.83	0.64	0.36	0.64	0.55						

Appendix C

Real Time Operating System (RTOS) Code for Microcontrollers in the Droplet on Demand System

```
/* rskM32C87def.h defines some common definitions and includes the sfr.h file*/
#include "rskM32C87def.h"
#include "sfr32c87.h"
#include "main.h"
#include "lcd.h"
#include "stdio.h"
#include "stdlib.h"
/* ************************* Global variables ********************************/
unsigned char data_display[8];
unsigned short led_status;
unsigned short led_count;
unsigned short led_period;
unsigned short p0_value[32];
unsigned short p1_value[32];
unsigned short p2_value[32];
unsigned short p3_value[32];
unsigned short old_value[32];
unsigned short new_value[32];
unsigned short          wave_1[16];
unsigned short          wave_2[16];
unsigned short          wave_3[16];
unsigned short          wave_4[16];
unsigned short  base_period;
unsigned short  timer_count;
unsigned short sequence_index;
/*****************************************************************************
Name:       Main
Parameters:  none
```

```
Returns:     none
Description: This is the main program
*******************************************************************************/
void main(void)
{
        unsigned short data_received;
        unsigned short test_byte;
        unsigned short mode;

        unsigned short temp_id;
        unsigned short temp_ON;
        unsigned short i;
        unsigned short j;
        pump_block pumps[8];
        pump_block temp_pump_block;
        unsigned short valves[32];

        // Initialization of constants
        wave_1[0] = 13;
        wave_1[1] = 14;
        wave_1[2] = 13;
        wave_1[3] = 13;
        wave_1[4] = 14;
        wave_1[5] = 14;
        wave_1[6] = 13;
        wave_1[7] = 13;
        wave_1[8] = 13;
        wave_1[9] = 13;
        wave_1[10] = 14;
        wave_1[11] = 14;
        wave_1[12] = 14;
        wave_1[13] = 14;
```

```
wave_1[14] = 14;
wave_1[15] = 14;

wave_2[0] = 13;
wave_2[1] = 14;
wave_2[2] = 14;
wave_2[3] = 13;
wave_2[4] = 13;
wave_2[5] = 14;
wave_2[6] = 14;
wave_2[7] = 13;
wave_2[8] = 13;
wave_2[9] = 13;
wave_2[10] = 13;
wave_2[11] = 14;
wave_2[12] = 14;
wave_2[13] = 13;
wave_2[14] = 14;
wave_2[15] = 14;

wave_3[0] = 13;
wave_3[1] = 13;
wave_3[2] = 14;
wave_3[3] = 14;
wave_3[4] = 13;
wave_3[5] = 13;
wave_3[6] = 14;
wave_3[7] = 14;
wave_3[8] = 14;
wave_3[9] = 14;
wave_3[10] = 14;
wave_3[11] = 14;
```

```
	wave_3[12] = 14;
	wave_3[13] = 14;
	wave_3[14] = 14;
	wave_3[15] = 14;

	wave_4[0] = 13;
	wave_4[1] = 14;
	wave_4[2] = 13;
	wave_4[3] = 14;
	wave_4[4] = 13;
	wave_4[5] = 14;
	wave_4[6] = 13;
	wave_4[7] = 14;
	wave_4[8] = 13;
	wave_4[9] = 14;
	wave_4[10] = 13;
	wave_4[11] = 14;
	wave_4[12] = 13;
	wave_4[13] = 14;
	wave_4[14] = 13;
	wave_4[15] = 14;
	timer_count = 0;
	// Set port value and initial valve states to zero
	for (i=0;i<32;i++)
	{
		p0_value[i]=p1_value[i]=p2_value[i]=p3_value[i]=0xFF;
		valves[i] = OFF;
	}
	p0=p1=p2=p3=0xFF;
	uart_init();
//	InitialiseDisplay();
	base_period = 50;
```

```
        led_period = 1; // default value
        led_count = 0;
        led_status = 0;
        LED2 = LED_OFF;
        LED2_DDR = 1;
        sequence_index = 0;
        timer_init();
        test_byte = 0b10001000;
        if ((test_byte & 0x0080) == 128) // MSB = 1 -> pump
                {
                        temp_id = (test_byte & 0b01110000)/0b00010000;
                        temp_pump_block.speed = test_byte & 0b00000111;
                        temp_pump_block.is_ON = (test_byte & 0b00001000)/0b00001000;
                        update_pumps(temp_id, pumps[temp_id], temp_pump_block);
                        pumps[temp_id].speed = temp_pump_block.speed;
                        pumps[temp_id].is_ON = temp_pump_block.is_ON;
                }
        else // update base period
                        base_period = 10*test_byte;
/*************** MAIN PROGRAM LOOP ************************/
  for(;;)
  {
        if (ri_u0c1 == 1)
        {
                data_received = u0rb;
                test_byte = data_received & 0x00FF;
//              sprintf(data_display, "%d      ", test_byte);
//              DisplayString(LCD_LINE2,data_display);
                if ((test_byte & 0x0080) == 128) // MSB = 1 -> pump
                {
                        temp_id = (test_byte & 0b01110000)/0b00010000;
                        temp_pump_block.speed = test_byte & 0b00000111;
```

```
                    temp_pump_block.is_ON = (test_byte & 0b00001000)/0b00001000;

                    update_pumps(temp_id, pumps[temp_id], temp_pump_block);
                    pumps[temp_id].speed = temp_pump_block.speed;
                    pumps[temp_id].is_ON = temp_pump_block.is_ON;
            }
            else // update base period
                    base_period = 10*test_byte;
      }
 }
}
/*****************************************************************************
Name:  timer_init()
Parameters: none
Returns:  nothing
Description: Initializes Timer TA2 to event counter mode. An interrupt is
                    generated after it has counted the number of events specified on
                    ta2 (i.e. 100).  In this module TA2 is counting underflows on TA3
                    This init also starts TA3 in timer mode with a 5 mSec period
***************************************************************************** */
void timer_init()
{
            /*timer mode, f2n divided by 30 output*/
      ta2 = (unsigned short) (((f1_CLK_SPEED/30)*.005)-1);
      /*ta2 mode register */
      ta2mr = 0x80;
                    /*  00000001
                b1:b0     TMOD1:TMOD0                    EVENT COUNTER MODE
                b2        MR0                  NO PULSE OUTPUT
                b3        MR1                  COUNT FALLING EDGES
                b4        MR2                  USE UP/DOWN FLAG
```

```
                    b5      MR3                     Set to 0 IN EVENT COUNTER
MODE
                    b6      TCK0            Reload Type
                    b7      TCK1            Normal Type (not two phase counting)
                            */
        /* set the prescaler so n = 15 divide will be 30 (2*15) */
        tcspr = 0x0f;
        /* enable prescaler*/
        cst =1;
        /* disable irqs before setting interrupt registers to prevent unwanted interrupt */
    DISABLE_IRQ
        ta2ic = 0x03;
    ENABLE_IRQ
        /* start timers */
        ta2s = 1;
}
/***********************************************************************************
Name: ta2_irq()
Parameters: none
Returns:        nothing
Description: Timer A2 Interrupt Service Routine. Interrupts every 100 falling
            edges on the TA2in pin or it this example every 100 undeflows of
                    TA3.  The ISR flashes the LED and increments 'count'

                    The compiler option is selected in HEW which will automatically create
                    the correct interrupt vector table
*********************************************************************************** */
void ta2_irq(void)
{
        timer_count ++;
        if (timer_count >= base_period)
        {
```

```
            timer_count = 0;
            if (sequence_index >=32)
            {
                  sequence_index = 0;
            }
            p0 = p0_value[sequence_index];
            p1 = p1_value[sequence_index];
            p2 = p2_value[sequence_index];
            p3 = p3_value[sequence_index];
            sequence_index++;
            led_status = !led_status;
            if (led_status == 0)
                  LED2 = LED_ON;
            else
                  LED2 = LED_OFF;
      }
}
/*****************************************************************************
Name:    UART0 Receive Interrupt Routine
Parameters:  none
Returns:     none
Description: Interrupt routine for UART0 receive
                        Reads character received from keyboard and stores U0_in variable
/*****************************************************************************
Name:                  uart_init
Parameters:   None
Returns:      None
Description: Uart0 initialization - 19200 baud, 8 data bits, 1 stop bit, no parity.
*****************************************************************************/
void uart_init(void) {
      /* set UART0 bit rate generator */
      u0brg = (unsigned char)(((f1_CLK_SPEED/16)/BAUD_RATE)-1);
```

```
                /*
                 bit rate can be calculated by:
                 bit rate = ((BRG count source / 16)/baud rate) - 1
                 ** the value of BCLK does not affect BRG count source */
        u0mr = 0x05;
    /* 00000101        8 bit mode, internal clock, one stop, no parity, no polarity inversion
      b2:b0     SMD2:0          SELECTS UART MODE, 8 BIT DATA TRANSFER
        b3              CKDIR           INTERNAL CLOCK SELECTED
        b4              STPS            ONE STOP BIT
        b5              PRY             ODD PARITY (parity is disabled using b6)
        b6              PRYE            DISABLE PARITY
        b7              IOPOL           TRANSMITTER RECEIVER OUTPUT NOT INVERSED
*/
        u0c0 = 0x10;
        /* 00010000        MSB first, n channel output, CTS/RTS enabled, f1 clock source
        b1:b0   CLK1:0                  COUNT SOURCE DIVIDED BY 1
                b2              CRS         CTS RTS ENABLED WHEN CRD=0
                b3              TXEPT           TRANSMIT REGISTER EMPTY FLAG
                b4              CRD                     CTS/RTS FUNCTION DISABLED
                b5              NCH         DATA OUTPUT SELECT BIT
                b6              CKPOL                   CLOCK POLARITY SELECTED,TX
FALLING EDGE,RX RISING EDGE
                b7              UFORM                   MSB FIRST */
        /* clear UART0 receive buffer by reading then clear UART0 transmit buffer */
        u0tb = u0rb;
        u0tb = 0;
        /* disable irqs before setting interrupt registers then set priority level to 4 which
        also enables interrupt */
  //    DISABLE_IRQ
  //      s0ric = 0x04;
  //      ENABLE_IRQ
        /* pin settings for making pin p6_3 as transmitter pin of Uart 0 */
```

```
//      ps0_3=1;
   /* pin settings for making pin p6_2 as receiver pin of Uart 0 */
        ps0_2=0;
        pd6_2=0;
        u0c1 = 0x05;
                 /* 00000101    UART0 receive control register 1
                b0              TE                  Transmit Enable Bit
                b1              TI                  Transmit buffer empty flag,
                b2              RE                  Receive enable bit,
                b3      RI                  Receive complete flag,
                b5:b4                       Reserved, set to 0
                b6              U0LCH       Data logic select bit,
                b7              U0ERE       Error signal output enable bit,  */
}
void update_pumps(unsigned short id, pump_block old_block, pump_block new_block)
{
        unsigned short i;
        unsigned short j;
//      unsigned short k;
//      unsigned short repeat;
        unsigned short mod;
//      repeat = 1;
        if(old_block.is_ON == new_block.is_ON && old_block.speed == new_block.speed)
        {
//              sprintf(data_display, "%s%d ", "No ch p", id);
//              DisplayString(LCD_LINE2,data_display);
        }
        else
        {
                j = 0;
                i = 0;
                // compute the pin values of the old pump status
```

```
if (old_block.is_ON == ON)
{
        while (i<32)
        {
                if (old_block.speed == WAVEONE)
                {
                        if (j==16)// wrap around
                        {
                                j = 0;
                        }
                        old_value[i] = wave_1[j];
                        i++;
                        j++;
                }
                else if (old_block.speed == WAVETWO)
                {
                        if (j==16)// wrap around
                        {
                                j = 0;
                        }
                        old_value[i] = wave_2[j];
                        i++;
                        j++;
                }
                else if (old_block.speed == WAVETHREE)
                {
                        if (j==16)// wrap around
                        {
                                j = 0;
                        }

                        old_value[i] = wave_3[j];
```

```
                    i++;
                    j++;
                }
                else
                {
                    if (j==16)// wrap around
                    {
                        j = 0;
                    }
                    old_value[i] = wave_4[j];
                    i++;
                    j++;
                }
            }
        }
        else
        {
            for (i = 0; i<32; i++)
                old_value[i] = 0;
        }
/************* compute the pin values ********************/
        j = 0;
        i = 0;
        if (new_block.is_ON == ON)
        {
            while (i<32)
            {
                if (new_block.speed == WAVEONE)
                {
                    if (j==16)// wrap around
                    {
                        j = 0;
```

```
            }
            new_value[i] = wave_1[j];
            i++;
            j++;
    }
    else if (new_block.speed == WAVETWO)
    {
            if (j==16)// wrap around
            {
                    j = 0;
            }
            new_value[i] = wave_2[j];
            i++;
            j++;
    }
    else if (new_block.speed == WAVETHREE)
    {
            if (j==16)// wrap around
            {
                    j = 0;
            }
            new_value[i] = wave_3[j];
            i++;
            j++;
    }
    else
    {
            if (j==16)// wrap around
            {
                    j = 0;
            }
            new_value[i] = wave_4[j];
```

```
                                        i++;
                                        j++;
                                }
                        }
                }
                else
                {
                        for (i = 0; i<32; i++)
                                new_value[i] = 0;
                }
  /****************end of new block sequence calculation****************/
        // subtract old value from the proper port value and add the new value
                if (id == 0)
                {
                        DISABLE_IRQ
                        for (i = 0; i<32; i++)
                                p0_value[i] = 0xff - ((0xff - p0_value[i]) -old_value[i] +
new_value[i]);
                        ENABLE_IRQ
                }
                else if (id == 1)
                {
                        DISABLE_IRQ
                        for (i = 0; i<32; i++)
                                p1_value[i] = 0xff - ((0xff - p1_value[i]) - old_value[i] +
new_value[i]);
                        ENABLE_IRQ
                }
                else if (id == 2)
                {
                        DISABLE_IRQ
                        for (i = 0; i<32; i++)
```

```
                        p2_value[i] = 0xff - ((0xff - p2_value[i]) - old_value[i] +
new_value[i]);
                ENABLE_IRQ
            }
            else
            {
                DISABLE_IRQ
                for (i = 0; i<32; i++)
                        p3_value[i] = 0xff - ((0xff - p3_value[i]) - old_value[i] +
new_value[i]);
                ENABLE_IRQ
            }
        }
    }
```

Appendix D

Matlab Code for Simulating Droplet Travelling in a Bypass Loop

```
clc
clear all, close all
freq=6.506;
Droplet_period=1/freq;
w=140; %channel width unit um
h=51;  %channel height unit um
A=w*h; %channel cross-section unit um
L1=53160; % Length of channel 1 unit um
L2=1150; % Length of channel 2 unit um
L3=1300; % Length of channel 3 unit um
L4=1806; % Length of channel 4 unit um
L5=15888; % Length of channel 5 unit um
L6=15520; % Length of channel 6 unit um
L7=45944; % Length of channel 7 unit um
L=[L1,L2,L3,L4,L5,L6,L7];
Pin=900;
Pout=0; %Inlet and outlet pressures
visc=10; % continuous phase viscosity mPa.s
beta=1.1; % Assume the slip factor is constant 1.1. But it should be a function of Q, droplet size and channel geometry
% Calculate Hydrodynamic Resistance of Channels

Trunc1=1/1^5*tanh(1*pi*w/(2*h));
Trunc2=1/3^5*tanh(3*pi*w/(2*h));
Trunc5=1/5^5*tanh(5*pi*w/(2*h));
Trunc=1-h/w*192/pi^5*(Trunc1+Trunc2+Trunc5);
Rc=12*visc/(w*h^3*Trunc)*10000/60;  % multiply by 10000/60 to match units. P in mbar. Q in uL/min
R_channels=Rc*L;
```

```
% Calculate Hydrodynamic Resistance of a single droplet
Leff_drop=450; % Estimated effective drop length
R_droplet=Leff_drop*Rc;
%Define a matrix which contains the position of droplets in each channel.
%The starting position is 0, '-1'means no droplet
max_droplet=1000;
C=-1*ones(length(L),max_droplet);
% Set intial droplet distribution to create different start up conditions
%%%%%%%%%%%%%%%%%%%%%%%%%%%%%%%%%%%%%%%%%%%%%%%%%%%%%%%%%%%%%%%%%%%%%%%%%%%%
 %CODE FOR SOLVING THE DROPLET MOTION IN THE NETWORK
 %%%%%%%%%%%%%%%%%%%%%%%
 % simulation parameters
 totalTime = 0;   %Time that the averaging value will be integrated over set to 0
 %t=0;
 tNewDrop=Droplet_period;
%Use x as the number of droplet generation events that occurs,
%simulation will run for xlim drop generations.
x=1;
xlim=10000;
while x<=xlim
%calculates the flow rate of each branch using a node analysis
%find number of droplets in each channel
for i=1:size(C,1);
   if (C(i,1)==-1)
      n_droplets(i)=0;  %if the first element is "-1", no droplets in the channel
   else
      n_droplets(i) = find(C(i,:)~=-1,1,'last');
   end
end
%displays an error message if the size of C matrix is not large enough to hold all the droplets.
for i=1:size(C,1);
   if (n_droplets(i)==size(C,2))
```

```
        disp('ERROR!!! increase the size of C matrix. There are too many droplets. (press Ctrl+C)')
        pause(1);
      end
    end
    %calculate resistance of each branch
    for i=1:size(R_channels,2);
      R(i) = R_channels(i) + n_droplets(i)*R_droplet;
    end

    % Calculate Reqv of the bridge channels
    Reff=(R(2)*R(3)*(1/R(2)+1/R(4)+1/R(5))*(1/R(3)+1/R(4)+1/R(6))-
R(2)*R(3)/(R(4)^2))/(R(3)*(1/R(3)+1/R(4)+1/R(6))/R(5)+R(2)*(1/R(2)+1/R(4)+1/R(5))/R(6)+R(2)/(
R(4)*R(5))+R(3)/(R(4)*R(6)));
    Q1=(Pin-Pout)/(R(1)+Reff+R(7));
    Q7=Q1;
    %calculate pressures at 4 junctions, respectly
    Pj1=Pin-Q1*R(1);
    Pj4=Q7*R(7);
    Pj2=(R(4)*(1+R(4)/R(3)+R(4)/R(6)+R(2)/R(3))/R(2)*Pj1+R(4)*(1+R(4)/R(3)+R(4)/R(6)+R(5)/R(
6))/R(5)*Pj4)/((1+R(4)/R(2)+R(4)/R(5))*(1+R(4)/R(3)+R(4)/R(6))-1);
    Pj3=(R(4)*(1+R(4)/R(2)+R(4)/R(5)+R(3)/R(2))/R(3)*Pj1+R(4)*(1+R(4)/R(2)+R(4)/R(5)+R(6)/R(
5))/R(6)*Pj4)/((1+R(4)/R(2)+R(4)/R(5))*(1+R(4)/R(3)+R(4)/R(6))-1);
    % Calculat flow rates
    Q2=(Pj1-Pj2)/R(2);
    Q3=(Pj1-Pj3)/R(3);
    Q4=(Pj2-Pj3)/R(4);
    Q5=(Pj2-Pj4)/R(5);
    Q6=(Pj3-Pj4)/R(6);
    Q=[Q1,Q2,Q3,Q4,Q5,Q6,Q7];
    %Calculating droplet speed
    S=(beta/A*1e9/60).*Q;
    %Find how long for each event: 1. Exit of a droplet, 2. a new droplet comes
```

```
%in
% Calculate the time required for the last droplet in each branch to
% leave that branch.
%find the position of last droplet in each channel,
for i=1:size(C,1);
   if (max(C(i,:)) > -1)    %check if the channel is empty or not
      ind=find(C(i,:)>-1,1,'last');
      last=C(i,ind);
      tExit(i)=(L(i)-last)/S(i);      % tExit in [s]. L in [um].  S in [um/s]
   else
      tExit(i)=999999;     % no droplets in the channel
   end
end

%find the timeStep and triggering droplet action for the next iteration
[tStep,trigger] = min([tNewDrop,tExit]);
totalTime =tStep+totalTime;
%%%%%%%%%%%%%%%%%%%%%%%%%%%%%%%%%%%%%%%%%%%%%%%%%%%%%%%%%%%%%%%%%%%%%%%
%Move the droplets in each branch by the velocity and timestep
%%%%%%%%%%%%%%%%%%%%%%%%%%%%%%%%%%%%
      for i=1:size(C,1);
         for j=1:size(C,2)
            if (C(i,j) ~= -1)        %"-1" denotes no droplet, keep it unchanged.
               C(i,j) = C(i,j) + S(i)*tStep;
            end
         end
      end

if trigger==1
C(1,:)=addDroplet(C(1,:)); %new droplet is generated
tNewDrop=Droplet_period;
   elseif trigger==2
```

```
        if(Q2>Q3)
            C(2,:)=addDroplet(C(2,:));
        else
            C(3,:)=addDroplet(C(3,:));
        end
        tNewDrop=tNewDrop-tStep;
    elseif trigger==3
        C(5,:)=addDroplet(C(5,:));
        tNewDrop=tNewDrop-tStep;
    elseif trigger==4
        C(6,:)=addDroplet(C(6,:));
        tNewDrop=tNewDrop-tStep;
    elseif trigger==6
        C(7,:)=addDroplet(C(7,:));
        tNewDrop=tNewDrop-tStep;
    elseif trigger==7
        C(7,:)=addDroplet(C(7,:));
        tNewDrop=tNewDrop-tStep;
else
        C(7,:)=removeDroplet(C(7,:));
        tNewDrop=tNewDrop-tStep;
end
%  Count the total number of droplets now that the switch has happend
         for i=1:size(C,1);
           if (C(i,1)==-1)
               n_droplets(i)=0;  %if the first element is "-1", no droplets in the channel
            else
               n_droplets(i) = find(C(i,:)~=-1,1,'last');
            end
         end
%%%%%%%%%%%%%%%%%%%%%%%%%%%%%%%%%%%%%%%%%%%%%%%%%%%%%%%%%%%%%%%%%%%%%%%
%Remove droplets if they are past the channel length
```

```
%%%%%%%%%%%%%%%%%%%%%%%%%%%%%%%%%%%%
      for i=1:size(C,1);
          if (max(C(i,:)) > -1)    %check if the channel is empty or not
             ind=find(C(i,:)>-1,1,'last');
             last=C(i,ind);
             if last>=L(i)
                C(i,:)=removeDroplet(C(i,:));
             end
          end
       end
x=x+1;
end   %
%Calculate spacing between droplets in each branch
% for i=1:length(C(7,:))-1
%         spacing(i)=C(7,i+1)-C(7,i);     %in micrometer
%     end
for i=1:length(C(1,:))-1
        spacing1(i)=C(1,i+1)-C(1,i);     %in micrometer
end
    for i=1:length(C(2,:))-1
        spacing2(i)=C(2,i+1)-C(2,i);     %in micrometer
    end
for i=1:length(C(3,:))-1
        spacing3(i)=C(3,i+1)-C(3,i);     %in micrometer
end
for i=1:length(C(5,:))-1
        spacing5(i)=C(5,i+1)-C(5,i);     %in micrometer
end
for i=1:length(C(6,:))-1
        spacing6(i)=C(6,i+1)-C(6,i);     %in micrometer
end
for i=1:length(C(7,:))-1
```

```
        spacing7(i)=C(7,i+1)-C(7,i);     %in micrometer
end
disp('All Done')

% removes the last droplet from the given channel.
function c = removeDroplet(c)
last = find(c<0,1,'first')-1;
c(last)=-1;
end
% adds a new droplet to the given channel.
function c = addDroplet(c)
c(length(c))=[];    %deletes the last element (which must be -1)
c=[0,c];            %add a new element at distance=0
end
```

Appendix E

Experimental Results V.S. Calculated Results of a Droplet Pairs Generation Design Discussed in Chapter 6

The compared parameters include the initial spacing between droplets s, droplet spacing in channel 5 (s_{c5}) and in channel 6(s_{c6}), droplet velocities before entering the loop (U_{d1}) and after leaving the loop (U_{d7}), spacing between two nearby droplets after the loop, s_1 and s_2

Table A-11 Experimental results V.S. Calculated results under the condition of input pressure $P_{in} = 920\text{mbar}$, droplet frequency $f = 6.576\text{Hz}$, slip factor $\alpha = 1.1$, equivalent droplet length $L_{effdrop} = 450\mu\text{m}$

Parameters	s (μm)	s_{c5} (μm)	s_{c6} (μm)	s_1 (μm)	s_2 (μm)	U_{d1} (mm/s)	U_{d7} (mm/s)
Experimental	2065	2105	2005	960	2965	13.48	13.38
Calculated	1938	1962	1917	957	2922	12.72	12.72
Error	6.15%	6.79%	4.39%	0.31%	1.45	5.64%	4.93%

Table A-12 Experimental results V.S. Calculated results under the condition of input pressure $P_{in} = 900\text{mbar}$, droplet frequency $f = 6.506\text{Hz}$, slip factor $\alpha = 1.1$, equivalent droplet length $L_{effdrop} = 450\mu\text{m}$

Parameters	s (μm)	s_{c5} (μm)	s_{c6} (μm)	s_1 (μm)	s_2 (μm)	U_{d1} (mm/s)	U_{d7} (mm/s)
Experimental	2055	2082	1930	895	2980	13.37	12.93
Calculated	1913	1935	1890	927	2898	12.43	12.43
Error	6.91%	7.06%	2.07%	3.57%	2.75%	7.03%	3.87%

Table A-13 Experimental results V.S. Calculated results under the condition of input pressure $P_{in} = 880\text{mbar}$, droplet frequency $f = 6.581\text{Hz}$, slip factor $\alpha = 1.1$, equivalent droplet length $L_{effdrop} = 450\mu\text{m}$

Parameters	s (μm)	s_{c5} (μm)	s_{c6} (μm)	s_1 (μm)	s_2 (μm)	U_{d1} (mm/s)	U_{d7} (mm/s)
Experimental	2015	1905	2043	870	3025	13.26	12.75
Calculated	1837	1812	1855	840	2828	12.06	12.06
Error	8.83%	4.88%	9.20%	3.45%	6.51%	9.05%	5.41%

Table A-14 Experimental results V.S. Calculated results under the condition of input pressure $P_{in} = 860\text{mbar}$, droplet frequency $f = 7.484\text{Hz}$, slip factor $\alpha = 1.1$, equivalent droplet length $L_{effdrop} = 450\mu\text{m}$

Parameters	s (μm)	s_{c5} (μm)	s_{c6} (μm)	s_1 (μm)	s_2 (μm)	U_{d1} (mm/s)	U_{d7} (mm/s)
Experimental	1705	1619	1740	445	2830	12.76	12.25
Calculated	1514	1494	1539	479	2546	11.34	11.34
Error	11.2%	7.72%	11.55%	7.64%	10.03%	11.13%	7.43%

Table A-15 Experimental results V.S. Calculated results under the condition of input pressure $P_{in} = 500\text{mbar}$, droplet frequency $f = 4.477\text{Hz}$, slip factor $\alpha = 1.1$, equivalent droplet length $L_{effdrop} = 450\mu\text{m}$

Parameters	s (μm)	s_{c5} (μm)	s_{c6} (μm)	s_1 (μm)	s_2 (μm)	U_{d1} (mm/s)	U_{d7} (mm/s)
Experimental	1490	1407	1540	285	2555	6.67	6.38
Calculated	1372	1354	1388	318	2423	6.14	6.14
Error	7.92%	3.77%	9.87%	11.58%	5.17%	7.95%	3.76%

Table A-16 Experimental results V.S. Calculated results under the condition of input pressure $P_{in} = 280\text{mbar}$, droplet frequency $f = 2.401\text{Hz}$, slip factor $\alpha = 1.1$, equivalent droplet length $L_{effdrop} = 450\mu\text{m}$

Parameters	s (μm)	s_{c5} (μm)	s_{c6} (μm)	s_1 (μm)	s_2 (μm)	U_{d1} (mm/s)	U_{d7} (mm/s)
Experimental	1570	1435	1560	585	2240	3.77	3.47
Calculated	1542	1523	1560	514	2570	3.71	3.71
Error	1.81%	6.13%	0%	12.14%	14.73%	1.59%	6.92%

Bibliography

[1] H. a. Stone, a. D. Stroock, and a. Ajdari, "Engineering Flows in Small Devices," *Annu. Rev. Fluid Mech.*, vol. 36, no. 1, pp. 381–411, Jan. 2004.

[2] D. B. Weibel and G. M. Whitesides, "Applications of microfluidics in chemical biology.," *Curr. Opin. Chem. Biol.*, vol. 10, no. 6, pp. 584–91, Dec. 2006.

[3] S. Haeberle and R. Zengerle, "Microfluidic platforms for lab-on-a-chip applications.," *Lab Chip*, vol. 7, pp. 1094–1110, Sep. 2007.

[4] G. M. Whitesides, "Cool, or simple and cheap? Why not both?," *Lab Chip*, pp. 11–13, 2013.

[5] P. Abgrall and a-M. Gué, "Lab-on-chip technologies: making a microfluidic network and coupling it into a complete microsystem—a review," *J. Micromechanics Microengineering*, vol. 17, no. 5, pp. R15–R49, May 2007.

[6] C. T. Culbertson, T. G. Mickleburgh, S. a Stewart-James, K. a Sellens, and M. Pressnall, "Micro total analysis systems: fundamental advances and biological applications.," *Anal. Chem.*, vol. 86, no. 1, pp. 95–118, Jan. 2014.

[7] M. Madou, J. Zoval, G. Jia, H. Kido, J. Kim, and N. Kim, "Lab on a CD.," *Annu. Rev. Biomed. Eng.*, vol. 8, pp. 601–28, Jan. 2006.

[8] R. Gorkin, J. Park, J. Siegrist, M. Amasia, B. S. Lee, J.-M. Park, J. Kim, H. Kim, M. Madou, and Y.-K. Cho, "Centrifugal microfluidics for biomedical applications.," *Lab Chip*, vol. 10, no. 14, pp. 1758–73, Jul. 2010.

[9] S. K. Sia and G. M. Whitesides, "Microfluidic devices fabricated in poly(dimethylsiloxane) for biological studies.," *Electrophoresis*, vol. 24, no. 21, pp. 3563–76, Nov. 2003.

[10] R. Seemann, M. Brinkmann, T. Pfohl, and S. Herminghaus, "Droplet based microfluidics," *Reports Prog. Phys.*, vol. 75, no. 1, p. 016601, Jan. 2012.

[11] B. Ziaie, A. Baldi, M. Lei, Y. Gu, and S. A. Ronald, "Hard and soft micromachining for BioMEMS: review of techniques and examples of applications in microfluidics and drug delivery," *Adv. Drug Deliv. Rev.*, vol. 56, no. 2, pp. 145–172, Feb. 2004.

[12] S. R. Quake and A. Scherer, “From Micro- to Nanofabrication with Soft Materials,” *Science (80-.).*, vol. 290, no. 5496, pp. 1536–1540, Nov. 2000.

[13] M. Heckele and W. K. Schomburg, “Review on micro molding of thermoplastic polymers,” *J. Micromechanics Microengineering*, vol. 14, no. 3, pp. R1–R14, Mar. 2004.

[14] D. B. Weibel, W. R. Diluzio, and G. M. Whitesides, “Microfabrication meets microbiology.,” *Nat. Rev. Microbiol.*, vol. 5, no. 3, pp. 209–18, Mar. 2007.

[15] V. Hessel, H. Lowe, and F. Schonfeld, “Micromixers - a review on passive and active mixing principles,” *Chem. Eng. Sci.*, vol. 60, no. 8–9, pp. 2479–2501, May 2005.

[16] N.-T. Nguyen and Z. Wu, “Micromixers—a review,” *J. Micromechanics Microengineering*, vol. 15, no. 2, pp. R1–R16, Feb. 2005.

[17] A. Ajdari, N. Bontoux, and H. a Stone, “Hydrodynamic dispersion in shallow microchannels: the effect of cross-sectional shape.,” *Anal. Chem.*, vol. 78, no. 2, pp. 387–92, Jan. 2006.

[18] P. Tabeling, “Investigating slippage, droplet breakup, and synthesizing microcapsules in microfluidic systems,” *Phys. Fluids*, vol. 22, no. 2, p. 021302, 2010.

[19] G. F. Christopher and S. L. Anna, “Microfluidic methods for generating continuous droplet streams,” *J. Phys. D. Appl. Phys.*, vol. 40, no. 19, pp. R319–R336, Oct. 2007.

[20] H. Song, M. R. Bringer, J. D. Tice, C. J. Gerdts, and R. F. Ismagilov, “Experimental test of scaling of mixing by chaotic advection in droplets moving through microfluidic channels,” *Appl. Phys. Lett.*, vol. 83, no. 12, pp. 4664–4666, 2003.

[21] R. Chabreyrie, D. Vainchtein, C. Chandre, P. Singh, and N. Aubry, “Tailored mixing inside a translating droplet,” *Phys. Rev. E*, vol. 77, no. 3, pp. 2–5, Mar. 2008.

[22] J. D. Tice, A. D. Lyon, and R. F. Ismagilov, “Effects of viscosity on droplet formation and mixing in microfluidic channels.,” *Anal. Chim. Acta*, vol. 507, no. 1, pp. 73–77, Apr. 2004.

[23] A. Accardo, F. Mecarini, M. Leoncini, F. Brandi, E. Di Cola, M. Burghammer, C. Riekel, and E. Di Fabrizio, “Fast, active droplet interaction: coalescence and reactive mixing controlled by electrowetting on a superhydrophobic surface,” *Lab Chip*, 2013.

[24] P. Paik, V. K. Pamula, and R. B. Fair, “Rapid droplet mixers for digital microfluidic

systems.,” *Lab Chip*, vol. 3, no. 4, pp. 253–9, Nov. 2003.

[25] T. P. Lagus and J. F. Edd, “A review of the theory, methods and recent applications of high-throughput single-cell droplet microfluidics,” *J. Phys. D. Appl. Phys.*, vol. 46, no. 11, p. 114005, Mar. 2013.

[26] M. Leman, F. Abouakil, A. D. Griffiths, and P. Tabeling, “Droplet-based microfluidics at the femtolitre scale,” *Lab Chip*, Nov. 2014.

[27] X. Casadevall i Solvas and A. DeMello, “Droplet microfluidics: recent developments and future applications.,” *Chem. Commun. (Camb).*, vol. 47, no. 7, pp. 1936–1942, Feb. 2011.

[28] L. Shui, S. Pennathur, J. C. T. Eijkel, and A. van den Berg, “Multiphase flow in lab on chip devices: a real tool for the future?,” *Lab Chip*, vol. 8, no. 7, pp. 1010–4, Jul. 2008.

[29] E. K. Sackmann, A. L. Fulton, and D. J. Beebe, “The present and future role of microfluidics in biomedical research,” *Nature*, vol. 507, no. 7491, pp. 181–189, Mar. 2014.

[30] Y. Zhu and Q. Fang, “Analytical detection techniques for droplet microfluidics-A review,” *Anal. Chim. Acta*, vol. 787, pp. 24–35, 2013.

[31] R. Samy, T. Glawdel, and C. L. Ren, “Method for microfluidic whole-chip temperature measurement using thin-film poly(dimethylsiloxane)/rhodamine B.,” *Anal. Chem.*, vol. 80, no. 2, pp. 369–75, Jan. 2008.

[32] P. Jankowski, D. Ogończyk, L. Derzsi, W. Lisowski, and P. Garstecki, “Hydrophilic polycarbonate chips for generation of oil-in-water (O/W) and water-in-oil-in-water (W/O/W) emulsions,” *Microfluid. Nanofluidics*, Nov. 2012.

[33] T. Fu, Y. Ma, D. Funfschilling, and H. Z. Li, “Gas–liquid flow stability and bubble formation in non-Newtonian fluids in microfluidic flow-focusing devices,” *Microfluid. Nanofluidics*, vol. 10, no. 5, pp. 1135–1140, Dec. 2010.

[34] K. Takahashi, Y. Sugii, K. Mawatari, and T. Kitamori, “Experimental investigation of droplet acceleration and collision in the gas phase in a microchannel,” *Lab Chip*, pp. 3098–3105, 2011.

[35] M. Hashimoto, S. S. Shevkoplyas, B. Zasońska, T. Szymborski, P. Garstecki, and G. M. Whitesides, “Formation of bubbles and droplets in parallel, coupled flow-focusing

geometries.,” *Small*, vol. 4, no. 10, pp. 1795–805, Oct. 2008.

[36] P. Garstecki, M. J. Fuerstman, H. a Stone, and G. M. Whitesides, “Formation of droplets and bubbles in a microfluidic T-junction-scaling and mechanism of break-up.,” *Lab Chip*, vol. 6, no. 3, pp. 437–46, Mar. 2006.

[37] A. R. Abate and D. a Weitz, “Air-bubble-triggered drop formation in microfluidics.,” *Lab Chip*, vol. 11, no. 10, pp. 1713–6, May 2011.

[38] T. Fu, Y. Ma, D. Funfschilling, and H. Z. Li, “Bubble formation and breakup mechanism in a microfluidic flow-focusing device,” *Chem. Eng. Sci.*, vol. 64, no. 10, pp. 2392–2400, May 2009.

[39] A. Utada, A. Fernandez-Nieves, H. Stone, and D. Weitz, “Dripping to Jetting Transitions in Coflowing Liquid Streams,” *Phys. Rev. Lett.*, vol. 99, no. 9, pp. 1–4, Aug. 2007.

[40] P. P. Bhat, O. a. Basaran, and M. Pasquali, “Dynamics of viscoelastic liquid filaments: Low capillary number flows,” *J. Nonnewton. Fluid Mech.*, vol. 150, no. 2–3, pp. 211–225, Apr. 2008.

[41] X. Feng, Y. Yi, X. Yu, D.-W. Pang, and Z.-L. Zhang, “Generation of water-ionic liquid droplet pairs in soybean oil on microfluidic chip.,” *Lab Chip*, vol. 10, no. 3, pp. 313–9, Feb. 2010.

[42] W. Wang and T. B. Jones, “Microfluidic actuation of insulating liquid droplets in a parallel-plate device,” *J. Phys. Conf. Ser.*, vol. 301, p. 012057, Jun. 2011.

[43] S.-Y. Teh, R. Lin, L.-H. Hung, and A. P. Lee, “Droplet microfluidics.,” *Lab Chip*, vol. 8, no. 2, pp. 198–220, Feb. 2008.

[44] C. X. Zhao and A. P. J. Middelberg, “Two-phase microfluidic flows.pdf.” Chemical Engineering Science, pp. 1394–1411, 2011.

[45] R. B. Fair, “Digital microfluidics: is a true lab-on-a-chip possible?,” *Microfluid. Nanofluidics*, vol. 3, no. 3, pp. 245–281, Mar. 2007.

[46] V. Cristini and Y.-C. C. Tan, “Theory and numerical simulation of droplet dynamics in complex flows--a review.,” *Lab Chip*, vol. 4, no. 4, pp. 257–64, Aug. 2004.

[47] A. Günther and K. F. Jensen, “Multiphase microfluidics: from flow characteristics to chemical and materials synthesis.,” *Lab Chip*, vol. 6, no. 12, pp. 1487–503, Dec. 2006.

[48] C.-H. Choi, J. Kim, J.-O. Nam, S.-M. Kang, S.-G. Jeong, and C.-S. Lee, “Microfluidic design of complex emulsions.,” *Chemphyschem*, vol. 15, no. 1, pp. 21–9, Jan. 2014.

[49] D. J. Collins, A. Neild, A. deMello, A.-Q. Liu, and Y. Ai, “The Poisson distribution and beyond: methods for microfluidic droplet production and single cell encapsulation,” *Lab Chip*, 2015.

[50] L. Rosenfeld, T. Lin, R. Derda, and S. K. Y. Tang, “Review and analysis of performance metrics of droplet microfluidics systems,” *Microfluid. Nanofluidics*, vol. 16, no. 5, pp. 921–939, Jan. 2014.

[51] K. V. I. S. Kaler and R. Prakash, “Droplet Microfluidics for Chip-Based Diagnostics.,” *Sensors (Basel).*, vol. 14, no. 12, pp. 23283–23306, Jan. 2014.

[52] A. Huerre, V. Miralles, and M.-C. Jullien, “Bubbles and foams in microfluidics.,” *Soft Matter*, Jun. 2014.

[53] J. C. Baret, “Surfactants in droplet-based microfluidics.pdf,” *Lab on a chip*, no. 12. Lab on a Chip, p. 422, 2012.

[54] W. C. Griffin, “Classification of surface active agents by ‘HLB,’” *J. Soc. Cosmet. Chem.*, vol. 1, pp. 311–326, 1949.

[55] L. Shui, A. van den Berg, and J. C. T. Eijkel, “Interfacial tension controlled W/O and O/W 2-phase flows in microchannel.,” *Lab Chip*, vol. 9, no. 6, pp. 795–801, Mar. 2009.

[56] J. Lacava, A.-A. Ouali, B. Raillard, and T. Kraus, “On the behaviour of nanoparticles in oil-in-water emulsions with different surfactants.,” *Soft Matter*, vol. 10, no. 11, pp. 1696–704, Feb. 2014.

[57] W. Lee, L. M. Walker, and S. L. Anna, “Competition Between Viscoelasticity and Surfactant Dynamics in Flow Focusing Microfluidics,” *Macromol. Mater. Eng.*, vol. 296, no. 3–4, pp. 203–213, Mar. 2011.

[58] T. Glawdel and C. L. Ren, “Droplet formation in microfluidic T-junction generators operating in the transitional regime. III. Dynamic surfactant effects,” *Phys. Rev. E - Stat. Nonlinear, Soft*

Matter Phys., vol. 86, no. 2, pp. 1–12, 2012.

[59] J. H. Xu, P. F. Dong, H. Zhao, C. P. Tostado, and G. S. Luo, "The Dynamic Effects of Surfactants on Droplet Formation in Coaxial Microfluidic Devices," *Langmuir*, 2012.

[60] B. Dai and L. G. Leal, "The mechanism of surfactant effects on drop coalescence," *Phys. Fluids*, vol. 20, no. 4, p. 040802, 2008.

[61] J.-C. Baret, F. Kleinschmidt, A. El Harrak, and A. D. Griffiths, "Kinetic aspects of emulsion stabilization by surfactants: a microfluidic analysis.," *Langmuir*, vol. 25, no. 11, pp. 6088–93, Jun. 2009.

[62] M. Roché, M. Aytouna, D. Bonn, and H. Kellay, "Effect of Surface Tension Variations on the Pinch-Off Behavior of Small Fluid Drops in the Presence of Surfactants," *Phys. Rev. Lett.*, vol. 103, no. 26, pp. 1–4, Dec. 2009.

[63] Y. Chen, G.-T. Liu, J.-H. Xu, and G.-S. Luo, "The dynamic mass transfer of Surfactants upon droplet formation in coaxial microfluidic devices," *Chem. Eng. Sci.*, vol. 132, pp. 1–8, 2015.

[64] L. E. Scriven and C. V. Sternling, "The Marangoni Effects," *Nature*, vol. 187, no. 4733, pp. 186–188, 1960.

[65] T. Ward, M. Faivre, and H. a Stone, "Drop production and tip-streaming phenomenon in a microfluidic flow-focusing device via an interfacial chemical reaction.," *Langmuir*, vol. 26, no. 12, pp. 9233–9, Jun. 2010.

[66] A. a. Darhuber and S. M. Troian, "Principles of Microfluidic Actuation By Modulation of Surface Stresses," *Annu. Rev. Fluid Mech.*, vol. 37, no. 1, pp. 425–455, Jan. 2005.

[67] P. Fischer and P. Erni, "Emulsion drops in external flow fields — The role of liquid interfaces," *Curr. Opin. Colloid Interface Sci.*, vol. 12, no. 4–5, pp. 196–205, Oct. 2007.

[68] C. Holtze, a C. Rowat, J. J. Agresti, J. B. Hutchison, F. E. Angilè, C. H. J. Schmitz, S. Köster, H. Duan, K. J. Humphry, R. a Scanga, J. S. Johnson, D. Pisignano, and D. a Weitz, "Biocompatible surfactants for water-in-fluorocarbon emulsions.," *Lab Chip*, vol. 8, no. 10, pp. 1632–9, Oct. 2008.

[69] M. Hashimoto, S. S. Shevkoplyas, B. Zasońska, T. Szymborski, P. Garstecki, and G. M. Whitesides, "Formation of bubbles and droplets in parallel, coupled flow-focusing

geometries.,” *Small*, vol. 4, no. 10, pp. 1795–805, Oct. 2008.

[70] M. M. Norton, T. Brugarolas, J. Chou, D. Lee, and H. H. Bau, “Ellipsoidal particles encapsulated in droplets.,” *Soft Matter*, vol. i, May 2014.

[71] J. Guzowski, P. M. Korczyk, S. Jakiela, and P. Garstecki, “Automated high-throughput generation of droplets,” *Lab Chip*, vol. 1, pp. 3593–3595, 2011.

[72] J. Clausell-Tormos, D. Lieber, J.-C. Baret, A. El-Harrak, O. J. Miller, L. Frenz, J. Blouwolff, K. J. Humphry, S. Köster, H. Duan, C. Holtze, D. a Weitz, A. D. Griffiths, and C. a Merten, “Droplet-based microfluidic platforms for the encapsulation and screening of Mammalian cells and multicellular organisms.,” *Chem. Biol.*, vol. 15, no. 5, pp. 427–37, May 2008.

[73] R. Dangla, F. Gallaire, and C. N. Baroud, “Microchannel deformations due to solvent-induced PDMS swelling.,” *Lab Chip*, vol. 10, no. 21, pp. 2972–8, Nov. 2010.

[74] D. F. Farson and H. W. Chou, “Femtosecond laser bulk micromachining of microfluid channels in poly (methylmethacrylate),” *J. Laser Appl.*, vol. 18, no. 3, pp. 210–215, 2006.

[75] R. Suriano, A. Kuznetsov, S. M. Eaton, R. Kiyan, G. Cerullo, R. Osellame, B. N. Chichkov, M. Levi, and S. Turri, “Femtosecond laser ablation of polymeric substrates for the fabrication of microfluidic channels,” *Appl. Surf. Sci.*, vol. 257, no. 14, pp. 6243–6250, Feb. 2011.

[76] N. Wu, Y. Zhu, S. Brown, J. Oakeshott, T. S. Peat, R. Surjadi, C. Easton, P. W. Leech, and B. a Sexton, “A PMMA microfluidic droplet platform for in vitro protein expression using crude E. coli S30 extract.,” *Lab Chip*, vol. 9, no. 23, pp. 3391–8, Dec. 2009.

[77] L. Derzsi, P. Jankowski, W. Lisowski, and P. Garstecki, “Hydrophilic polycarbonate for generation of oil in water emulsions in microfluidic devices.,” *Lab Chip*, vol. 11, no. 6, pp. 1151–6, Mar. 2011.

[78] B. Subramanian, N. Kim, W. Lee, D. a Spivak, D. E. Nikitopoulos, R. L. McCarley, and S. a Soper, “Surface modification of droplet polymeric microfluidic devices for the stable and continuous generation of aqueous droplets.,” *Langmuir*, vol. 27, no. 12, pp. 7949–57, Jun. 2011.

[79] C. De Marco, S. M. Eaton, R. Suriano, S. Turri, M. Levi, R. Ramponi, G. Cerullo, and R. Osellame, “Surface properties of femtosecond laser ablated PMMA.,” *ACS Appl. Mater. Interfaces*, vol. 2, no. 8, pp. 2377–84, Aug. 2010.

[80] M. Muluneh and D. Issadore, “Hybrid soft-lithography/laser machined microchips for the parallel generation of droplets.,” *Lab Chip*, vol. 80, no. 512, Oct. 2013.

[81] D. Ogończyk, J. Wegrzyn, P. Jankowski, B. Dabrowski, and P. Garstecki, “Bonding of microfluidic devices fabricated in polycarbonate.,” *Lab Chip*, vol. 10, no. 10, pp. 1324–1327, 2010.

[82] P. P. Shiu, G. K. Knopf, M. Ostojic, and S. Nikumb, “Rapid fabrication of tooling for microfluidic devices via laser micromachining and hot embossing,” *J. Micromechanics Microengineering*, vol. 18, no. 2, p. 025012, Feb. 2008.

[83] H. Becker and C. Gärtner, “Polymer microfabrication technologies for microfluidic systems.,” *Anal. Bioanal. Chem.*, vol. 390, no. 1, pp. 89–111, Jan. 2008.

[84] C.-W. Tsao and D. L. DeVoe, “Bonding of thermoplastic polymer microfluidics,” *Microfluid. Nanofluidics*, vol. 6, no. 1, pp. 1–16, Nov. 2008.

[85] T. Glawdel, C. Elbuken, and C. Ren, “Droplet formation in microfluidic T-junction generators operating in the transitional regime. I. Experimental observations,” *Phys. Rev. E*, vol. 85, no. 1, pp. 1–9, Jan. 2012.

[86] A. W. Martinez, S. T. Phillips, M. J. Butte, and G. M. Whitesides, “Patterned paper as a platform for inexpensive, low-volume, portable bioassays,” *Angew. Chemie - Int. Ed.*, vol. 46, no. 8, pp. 1318–1320, 2007.

[87] X. Li, D. R. Ballerini, and W. Shen, “A perspective on paper-based microfluidics: Current status and future trends.,” *Biomicrofluidics*, vol. 6, no. 1, pp. 11301–1130113, Mar. 2012.

[88] R. Dreyfus, P. Tabeling, and H. Willaime, “Ordered and Disordered Patterns in Two-Phase Flows in Microchannels,” *Phys. Rev. Lett.*, vol. 90, no. 14, pp. 1–4, Apr. 2003.

[89] V. Barbier, M. Tatoulian, H. Li, F. Arefi-Khonsari, A. Ajdari, and P. Tabeling, “Stable modification of PDMS surface properties by plasma polymerization: application to the formation of double emulsions in microfluidic systems.,” *Langmuir : the ACS journal of surfaces and colloids*, vol. 22, no. 12. pp. 5230–2, 06-Jun-2006.

[90] C. C. Roberts, R. R. Rao, M. Loewenberg, C. F. Brooks, P. Galambos, A. M. Grillet, and M. B. Nemer, “Comparison of monodisperse droplet generation in flow-focusing devices with hydrophilic and hydrophobic surfaces.,” *Lab Chip*, vol. 12, no. 8, pp. 1540–7, Apr. 2012.

[91] D. Bodas and C. Khan-Malek, “Hydrophilization and hydrophobic recovery of PDMS by oxygen plasma and chemical treatment—An SEM investigation,” *Sensors Actuators B Chem.*, vol. 123, no. 1, pp. 368–373, Apr. 2007.

[92] K. Ren, J. Zhou, and H. Wu, “Materials for microfluidic chip fabrication.,” *Acc. Chem. Res.*, vol. 46, no. 11, pp. 2396–406, Nov. 2013.

[93] T. Thorsen, R. W. Roberts, F. H. Arnold, and S. R. Quake, “Dynamic Pattern Formation in a Vesicle-Generating Microfluidic Device,” *Phys. Rev. Lett.*, vol. 86, no. 18, pp. 4163–4166, Apr. 2001.

[94] M. L. J. Steegmans, K. G. P. H. Schroën, and R. M. Boom, “Characterization of emulsification at flat microchannel Y junctions.,” *Langmuir*, vol. 25, no. 6, pp. 3396–401, Apr. 2009.

[95] M. L. J. Steegmans, J. De Ruiter, and K. G. P. H. Schroe, “A Descriptive Force-Balance Model for Droplet Formation at Microfluidic Y-Junctions,” *AIChE J.*, vol. 56, no. 10, pp. 2641–2649, 2010.

[96] Y. Ding, X. Casadevall I Solvas, and A. deMello, “‘V-junction’: a novel structure for high-speed generation of bespoke droplet flows.,” *Analyst*, vol. 00, pp. 1–8, Nov. 2014.

[97] M.-C. Jullien, M.-J. Tsang Mui Ching, C. Cohen, L. Menetrier, and P. Tabeling, “Droplet breakup in microfluidic T-junctions at small capillary numbers,” *Phys. Fluids*, vol. 21, no. 7, p. 072001, 2009.

[98] A. R. Abate, P. Mary, V. van Steijn, and D. a. Weitz, “Experimental validation of plugging during drop formation in a T-junction,” *Lab Chip*, pp. 1516–1521, 2012.

[99] D. Qian and A. Lawal, “Numerical study on gas and liquid slugs for Taylor flow in a T-junction microchannel,” *Chem. Eng. Sci.*, vol. 61, no. 23, pp. 7609–7625, Dec. 2006.

[100] Y. Yan, D. Guo, and S. Z. Wen, “Numerical simulation of junction point pressure during droplet formation in a microfluidic T-junction,” *Chem. Eng. Sci.*, vol. 84, pp. 591–601, Dec. 2012.

[101] M. Wörner, “Numerical modeling of multiphase flows in microfluidics and micro process engineering: a review of methods and applications,” *Microfluid. Nanofluidics*, vol. 12, no. 6, pp. 841–886, Mar. 2012.

[102] L. Sang, Y. Hong, and F. Wang, “Investigation of viscosity effect on droplet formation in T-shaped microchannels by numerical and analytical methods,” *Microfluid. Nanofluidics*, vol. 6, no. 5, pp. 621–635, Aug. 2008.

[103] T. Glawdel, C. Elbuken, and C. Ren, “Droplet formation in microfluidic T-junction generators operating in the transitional regime. II. Modeling,” *Phys. Rev. E*, vol. 85, no. 1, pp. 1–12, Jan. 2012.

[104] V. van Steijn, C. R. Kleijn, and M. T. Kreutzer, “Predictive model for the size of bubbles and droplets created in microfluidic T-junctions.,” *Lab Chip*, vol. 10, no. 19, pp. 2513–8, Oct. 2010.

[105] T. Fu, Y. Ma, D. Funfschilling, C. Zhu, and H. Z. Li, “Squeezing-to-dripping transition for bubble formation in a microfluidic T-junction,” *Chem. Eng. Sci.*, vol. 65, no. 12, pp. 3739–3748, Jun. 2010.

[106] L. Ménétrier-Deremble and P. Tabeling, “Droplet breakup in microfluidic junctions of arbitrary angles,” *Phys. Rev. E*, vol. 74, no. 3, pp. 1–4, Sep. 2006.

[107] G. F. Christopher, N. N. Noharuddin, J. a. Taylor, and S. L. Anna, “Experimental observations of the squeezing-to-dripping transition in T-shaped microfluidic junctions,” *Phys. Rev. E*, vol. 78, no. 3, pp. 1–12, Sep. 2008.

[108] D. Malsch, N. Gleichmann, M. Kielpinski, G. Mayer, T. Henkel, D. Mueller, V. Steijn, C. R. Kleijn, and M. T. Kreutzer, “Dynamics of droplet formation at T-shaped nozzles with elastic feed lines,” *Microfluid. Nanofluidics*, vol. 8, no. 4, pp. 497–507, Aug. 2009.

[109] P. Guillot and A. Colin, “Stability of parallel flows in a microchannel after a T junction,” *Phys. Rev. E*, vol. 72, no. 6, pp. 1–4, Dec. 2005.

[110] J. H. Xu, S. W. Li, J. Tan, and G. S. Luo, “Correlations of droplet formation in T-junction microfluidic devices: from squeezing to dripping,” *Microfluid. Nanofluidics*, vol. 5, no. 6, pp. 711–717, May 2008.

[111] J. H. Xu, G. S. Luo, S. W. Li, and G. G. Chen, “Shear force induced monodisperse droplet formation in a microfluidic device by controlling wetting properties.,” *Lab Chip*, vol. 6, no. 1, pp. 131–6, Jan. 2006.

[112] K. Wang, Y. C. Lu, J. H. Xu, and G. S. Luo, “Determination of dynamic interfacial tension and its effect on droplet formation in the T-shaped microdispersion process.,” *Langmuir*, vol.

25, no. 4, pp. 2153–8, Feb. 2009.

[113] G. F. Christopher, N. N. Noharuddin, J. a. Taylor, and S. L. Anna, “Experimental observations of the squeezing-to-dripping transition in T-shaped microfluidic junctions,” *Phys. Rev. E*, vol. 78, no. 3, pp. 1–12, Sep. 2008.

[114] M. De Menech, P. Garstecki, F. Jousse, and H. a. Stone, “Transition from squeezing to dripping in a microfluidic T-shaped junction,” *J. Fluid Mech.*, vol. 595, pp. 141–161, Jan. 2008.

[115] S. Afkhami, a. M. Leshansky, and Y. Renardy, “Numerical investigation of elongated drops in a microfluidic T-junction,” *Phys. Fluids*, vol. 23, no. 2, p. 022002, 2011.

[116] A. Gupta, S. M. S. Murshed, and R. Kumar, “Droplet formation and stability of flows in a microfluidic T-junction,” *Appl. Phys. Lett.*, vol. 94, no. 16, p. 164107, 2009.

[117] A. Gupta and R. Kumar, “Effect of geometry on droplet formation in the squeezing regime in a microfluidic T-junction,” *Microfluid. Nanofluidics*, vol. 8, no. 6, pp. 799–812, Oct. 2009.

[118] V. Barbier, H. Willaime, P. Tabeling, and F. Jousse, “Producing droplets in parallel microfluidic systems,” *Phys. Rev. E*, vol. 74, no. 4, p. 046306, Oct. 2006.

[119] P. B. Umbanhowar, V. Prasad, and D. a. Weitz, “Monodisperse Emulsion Generation via Drop Break Off in a Coflowing Stream,” *Langmuir*, vol. 16, no. 2, pp. 347–351, Jan. 2000.

[120] W. van Hoeve, B. Dollet, J. M. Gordillo, M. Versluis, L. van Wijngaarden, and D. Lohse, “Bubble size prediction in co-flowing streams,” *EPL (Europhysics Lett.*, vol. 94, no. 6, p. 64001, Jun. 2011.

[121] E. Castro-Hernández, W. van Hoeve, D. Lohse, and J. M. Gordillo, “Microbubble generation in a co-flow device operated in a new regime.,” *Lab Chip*, vol. 11, no. 12, pp. 2023–9, Jun. 2011.

[122] C. Cramer, S. Studer, E. J. Windhab, and P. Fischer, “Periodic dripping dynamics in a co-flowing liquid-liquid system,” *Phys. Fluids*, vol. 24, no. 9, p. 093101, 2012.

[123] K. Xu, C. Tostado, J. Xu, Y. Lu, and G. Luo, “Direct measurement of the differential pressure during drop formation in a co-flow microfluidic device,” *Lab Chip*, 2014.

[124] S. L. Anna, N. Bontoux, and H. a. Stone, “Formation of dispersions using ‘flow focusing’ in microchannels,” *Appl. Phys. Lett.*, vol. 82, no. 3, p. 364, 2003.

[125] S.-H. Huang, W.-H. Tan, F.-G. Tseng, and S. Takeuchi, “A monolithically three-dimensional flow-focusing device for formation of single/double emulsions in closed/open microfluidic systems,” *J. Micromechanics Microengineering*, vol. 16, no. 11, pp. 2336–2344, Nov. 2006.

[126] a S. Utada, E. Lorenceau, D. R. Link, P. D. Kaplan, H. a Stone, and D. a Weitz, “Monodisperse double emulsions generated from a microcapillary device.,” *Science*, vol. 308, no. 5721, pp. 537–41, Apr. 2005.

[127] L.-Y. Chu, A. S. Utada, R. K. Shah, J.-W. Kim, and D. a Weitz, “Controllable monodisperse multiple emulsions.,” *Angew. Chem. Int. Ed. Engl.*, vol. 46, no. 47, pp. 8970–4, Jan. 2007.

[128] W. Lee, L. M. Walker, and S. L. Anna, “Role of geometry and fluid properties in droplet and thread formation processes in planar flow focusing,” *Phys. Fluids*, vol. 21, no. 3, p. 032103, 2009.

[129] T. Cubaud and T. G. Mason, “Capillary threads and viscous droplets in square microchannels,” *Phys. Fluids*, vol. 20, no. 5, p. 053302, 2008.

[130] P. a Romero and A. R. Abate, “Flow focusing geometry generates droplets through a plug and squeeze mechanism.,” *Lab Chip*, pp. 5130–5132, Nov. 2012.

[131] P. A. Romero and A. R. Abate, “Flow focusing geometry generates droplets through a plug and squeeze mechanism,” *Lab Chip*, vol. 12, no. 24, pp. 5130–5132, Nov. 2012.

[132] Z. Nie, M. Seo, S. Xu, P. C. Lewis, M. Mok, E. Kumacheva, G. M. Whitesides, P. Garstecki, and H. a. Stone, “Emulsification in a microfluidic flow-focusing device: effect of the viscosities of the liquids,” *Microfluid. Nanofluidics*, pp. 585–594, Mar. 2008.

[133] W. Li, Z. Nie, H. Zhang, C. Paquet, M. Seo, P. Garstecki, and E. Kumacheva, “Screening of the effect of surface energy of microchannels on microfluidic emulsification.,” *Langmuir*, vol. 23, no. 15, pp. 8010–4, Jul. 2007.

[134] S. L. Anna and H. C. Mayer, “Microscale tipstreaming in a microfluidic flow focusing device,” *Phys. Fluids*, vol. 18, no. 12, p. 121512, 2006.

[135] T. Fu, Y. Wu, Y. Ma, and H. Z. Li, “Droplet formation and breakup dynamics in microfluidic

flow-focusing devices: From dripping to jetting," *Chem. Eng. Sci.*, vol. 84, pp. 207–217, Dec. 2012.

[136] Y.-C. Tan, V. Cristini, and A. P. Lee, "Monodispersed microfluidic droplet generation by shear focusing microfluidic device," *Sensors Actuators B Chem.*, vol. 114, no. 1, pp. 350–356, Mar. 2006.

[137] P. K. Notz, A. U. Chen, and O. a. Basaran, "Satellite drops: Unexpected dynamics and change of scaling during pinch-off," *Phys. Fluids*, vol. 13, no. 3, p. 549, 2001.

[138] T. Ward, M. Faivre, M. Abkarian, and H. a Stone, "Microfluidic flow focusing: drop size and scaling in pressure versus flow-rate-driven pumping.," *Electrophoresis*, vol. 26, no. 19, pp. 3716–24, Oct. 2005.

[139] W.-L. Ong, J. Hua, B. Zhang, T.-Y. Teo, J. Zhuo, N.-T. Nguyen, N. Ranganathan, and L. Yobas, "Experimental and computational analysis of droplet formation in a high-performance flow-focusing geometry," *Sensors Actuators A Phys.*, vol. 138, no. 1, pp. 203–212, Jul. 2007.

[140] J. M. Park and P. D. Anderson, "A ternary model for double-emulsion formation in a capillary microfluidic device.," *Lab Chip*, vol. 12, no. 15, pp. 2672–7, Aug. 2012.

[141] M. J. Jensen, H. a. Stone, and H. Bruus, "A numerical study of two-phase Stokes flow in an axisymmetric flow-focusing device," *Phys. Fluids*, vol. 18, no. 7, p. 077103, 2006.

[142] M. Dupin, I. Halliday, and C. Care, "Simulation of a microfluidic flow-focusing device," *Phys. Rev. E*, vol. 73, no. 5, p. 055701, May 2006.

[143] L. S. Kim, H. K. Jeong, M. Y. Ha, and K. C. Kim, "Numerical simulation of droplet formation in a micro-channel using the lattice Boltzmann method," *J. Mech. Sci. Technol.*, vol. 22, no. 4, pp. 770–779, May 2008.

[144] W. Li, E. W. K. Young, M. Seo, Z. Nie, P. Garstecki, C. a. Simmons, and E. Kumacheva, "Simultaneous generation of droplets with different dimensions in parallel integrated microfluidic droplet generators," *Soft Matter*, vol. 4, no. 2, pp. 258–262, 2008.

[145] M. K. Mulligan and J. P. Rothstein, "Scale-up and control of droplet production in coupled microfluidic flow-focusing geometries," *Microfluid. Nanofluidics*, vol. 13, no. 1, pp. 65–73, Feb. 2012.

[146] M. T. Sullivan and H. a Stone, “The role of feedback in microfluidic flow-focusing devices.,” *Philos. Trans. A. Math. Phys. Eng. Sci.*, vol. 366, no. 1873, pp. 2131–43, Jun. 2008.

[147] E. Miller, M. Rotea, and J. P. Rothstein, “Microfluidic device incorporating closed loop feedback control for uniform and tunable production of micro-droplets.,” *Lab Chip*, vol. 10, no. 10, pp. 1293–301, May 2010.

[148] C. Priest, S. Herminghaus, and R. Seemann, “Generation of monodisperse gel emulsions in a microfluidic device,” *Appl. Phys. Lett.*, vol. 88, no. 2, p. 024106, 2006.

[149] D. Saeki, S. Sugiura, T. Kanamori, S. Sato, S. Mukataka, and S. Ichikawa, “Highly productive droplet formation by anisotropic elongation of a thread flow in a microchannel.,” *Langmuir*, vol. 24, no. 23, pp. 13809–13, Dec. 2008.

[150] K. Humphry, A. Ajdari, A. Fernández-Nieves, H. Stone, and D. Weitz, “Suppression of instabilities in multiphase flow by geometric confinement,” *Phys. Rev. E*, vol. 79, no. 5, p. 056310, May 2009.

[151] F. Malloggi, N. Pannacci, R. Attia, F. Monti, P. Mary, H. Willaime, P. Tabeling, B. Cabane, and P. Poncet, “Monodisperse colloids synthesized with nanofluidic technology.,” *Langmuir*, vol. 26, no. 4, pp. 2369–73, Feb. 2010.

[152] R. Dangla, E. Fradet, Y. Lopez, and C. N. Baroud, “The physical mechanisms of step emulsification,” *J. Phys. D. Appl. Phys.*, vol. 46, no. 11, p. 114003, Mar. 2013.

[153] Z. Li, a. M. Leshansky, L. M. Pismen, and P. Tabeling, “Step-emulsification in a microfluidic device,” *Lab Chip*, Nov. 2014.

[154] D. Link, S. Anna, D. Weitz, and H. Stone, “Geometrically Mediated Breakup of Drops in Microfluidic Devices,” *Phys. Rev. Lett.*, vol. 92, no. 5, pp. 1–4, Feb. 2004.

[155] A. R. Abate and D. a Weitz, “Faster multiple emulsification with drop splitting.,” *Lab Chip*, vol. 11, no. 11, pp. 1911–5, Jun. 2011.

[156] V. Chokkalingam, S. Herminghaus, and R. Seemann, “Self-synchronizing pairwise production of monodisperse droplets by microfluidic step emulsification,” *Appl. Phys. Lett.*, vol. 93, no. 25, p. 254101, 2008.

[157] A. R. Abate, M. B. Romanowsky, J. J. Agresti, and D. a. Weitz, “Valve-based flow focusing

for drop formation," *Appl. Phys. Lett.*, vol. 94, no. 2, p. 023503, 2009.

[158] C.-Y. Lee, Y.-H. Lin, and G.-B. Lee, "A droplet-based microfluidic system capable of droplet formation and manipulation," *Microfluid. Nanofluidics*, vol. 6, no. 5, pp. 599–610, Aug. 2008.

[159] J.-H. Choi, S.-K. Lee, J.-M. Lim, S.-M. Yang, and G.-R. Yi, "Designed pneumatic valve actuators for controlled droplet breakup and generation.," *Lab Chip*, vol. 10, no. 4, pp. 456–61, Feb. 2010.

[160] S. Zeng, B. Li, X. Su, J. Qin, and B. Lin, "Microvalve-actuated precise control of individual droplets in microfluidic devices.," *Lab Chip*, vol. 9, no. 10, pp. 1340–3, May 2009.

[161] a. Amirzadeh and S. Chandra, "Small droplet formation in a pneumatic drop-on-demand generator: Experiments and analysis," *Exp. Therm. Fluid Sci.*, vol. 34, no. 8, pp. 1488–1497, Nov. 2010.

[162] Y. Zeng, M. Shin, and T. Wang, "Programmable active droplet generation enabled by integrated pneumatic micropumps.," *Lab Chip*, Nov. 2012.

[163] K. Churski, J. Michalski, and P. Garstecki, "Droplet on demand system utilizing a computer controlled microvalve integrated into a stiff polymeric microfluidic device.," *Lab Chip*, vol. 10, no. 4, pp. 512–8, Feb. 2010.

[164] F. Guo, K. Liu, X.-H. Ji, H.-J. Ding, M. Zhang, Q. Zeng, W. Liu, S.-S. Guo, and X.-Z. Zhao, "Valve-based microfluidic device for droplet on-demand operation and static assay," *Appl. Phys. Lett.*, vol. 97, no. 23, p. 233701, 2010.

[165] C. Baroud, J.-P. Delville, F. Gallaire, and R. Wunenburger, "Thermocapillary valve for droplet production and sorting," *Phys. Rev. E*, vol. 75, no. 4, pp. 1–5, Apr. 2007.

[166] K. Churski, P. Korczyk, and P. Garstecki, "High-throughput automated droplet microfluidic system for screening of reaction conditions.," *Lab Chip*, vol. 10, no. 7, pp. 816–8, Apr. 2010.

[167] S.-H. Tan, S. M. Sohel Murshed, N.-T. Nguyen, T. N. Wong, and L. Yobas, "Thermally controlled droplet formation in flow focusing geometry: formation regimes and effect of nanoparticle suspension," *J. Phys. D. Appl. Phys.*, vol. 41, no. 16, p. 165501, Aug. 2008.

[168] C. a Stan, S. K. Y. Tang, and G. M. Whitesides, "Independent control of drop size and velocity in microfluidic flow-focusing generators using variable temperature and flow rate.,"

Anal. Chem., vol. 81, no. 6, pp. 2399–402, Mar. 2009.

[169] M. He, J. S. Kuo, and D. T. Chiu, "Electro-generation of single femtoliter- and picoliter-volume aqueous droplets in microfluidic systems," *Appl. Phys. Lett.*, vol. 87, no. 3, p. 031916, 2005.

[170] M. He, J. S. Kuo, and D. T. Chiu, "Effects of ultrasmall orifices on the electrogeneration of femtoliter-volume aqueous droplets.," *Langmuir*, vol. 22, no. 14, pp. 6408–13, Jul. 2006.

[171] H. Kim, D. Luo, D. Link, D. a. Weitz, M. Marquez, and Z. Cheng, "Controlled production of emulsion drops using an electric field in a flow-focusing microfluidic device," *Appl. Phys. Lett.*, vol. 91, no. 13, p. 133106, 2007.

[172] S. J. Kim, Y.-A. Song, P. L. Skipper, and J. Han, "Electrohydrodynamic generation and delivery of monodisperse picoliter droplets using a poly(dimethylsiloxane) microchip.," *Anal. Chem.*, vol. 78, no. 23, pp. 8011–9, Dec. 2006.

[173] A. Bransky, N. Korin, M. Khoury, and S. Levenberg, "A microfluidic droplet generator based on a piezoelectric actuator.," *Lab Chip*, vol. 9, no. 4, pp. 516–20, Feb. 2009.

[174] K.-C. Fan, J.-Y. Chen, C.-H. Wang, and W.-C. Pan, "Development of a drop-on-demand droplet generator for one-drop-fill technology," *Sensors Actuators A Phys.*, vol. 147, no. 2, pp. 649–655, Oct. 2008.

[175] X. Niu, M. Zhang, J. Wu, W. Wen, and P. Sheng, "Generation and manipulation of 'smart' droplets," *Soft Matter*, vol. 5, no. 3, p. 576, 2009.

[176] M. Zhang, J. Wu, X. Niu, W. Wen, and P. Sheng, "Manipulations of microfluidic droplets using electrorheological carrier fluid," *Phys. Rev. E*, vol. 78, no. 6, pp. 1–5, Dec. 2008.

[177] F. Malloggi, S. a Vanapalli, H. Gu, D. van den Ende, and F. Mugele, "Electrowetting-controlled droplet generation in a microfluidic flow-focusing device," *J. Phys. Condens. Matter*, vol. 19, no. 46, p. 462101, Nov. 2007.

[178] J. Gong and C.-J. C. J. Kim, "All-electronic droplet generation on-chip with real-time feedback control for EWOD digital microfluidics.," *Lab Chip*, vol. 8, no. 6, pp. 898–906, Jun. 2008.

[179] J. Liu, S.-H. Tan, Y. F. Yap, M. Y. Ng, and N.-T. Nguyen, "Numerical and experimental

investigations of the formation process of ferrofluid droplets," *Microfluid. Nanofluidics*, vol. 11, no. 2, pp. 177–187, Mar. 2011.

[180] S. H. Tan and N.-T. Nguyen, "Generation and manipulation of monodispersed ferrofluid emulsions: The effect of a uniform magnetic field in flow-focusing and T-junction configurations," *Phys. Rev. E*, vol. 84, no. 3, pp. 1–7, Sep. 2011.

[181] S.-H. Tan, N.-T. Nguyen, L. Yobas, and T. G. Kang, "Formation and manipulation of ferrofluid droplets at a microfluidic T -junction," *J. Micromechanics Microengineering*, vol. 20, no. 4, p. 045004, Apr. 2010.

[182] J. Liu, Y. F. Yap, and N.-T. Nguyen, "Numerical study of the formation process of ferrofluid droplets," *Phys. Fluids*, vol. 23, no. 7, p. 072008, 2011.

[183] S.-Y. Park, T.-H. Wu, Y. Chen, M. a Teitell, and P.-Y. Chiou, "High-speed droplet generation on demand driven by pulse laser-induced cavitation.," *Lab Chip*, vol. 11, no. 6, pp. 1010–2, Mar. 2011.

[184] Y.-C. Tan and A. P. Lee, "Microfluidic separation of satellite droplets as the basis of a monodispersed micron and submicron emulsification system.," *Lab Chip*, vol. 5, no. 10, pp. 1178–83, Oct. 2005.

[185] Y.-C. Tan, Y. L. Ho, and A. P. Lee, "Microfluidic sorting of droplets by size," *Microfluid. Nanofluidics*, vol. 4, no. 4, pp. 343–348, Jun. 2007.

[186] L. Mazutis and A. D. Griffiths, "Preparation of monodisperse emulsions by hydrodynamic size fractionation," *Appl. Phys. Lett.*, vol. 95, no. 20, p. 204103, 2009.

[187] A. C. Hatch, A. Patel, N. R. Beer, and A. P. Lee, "Passive droplet sorting using viscoelastic flow focusing.," *Lab Chip*, vol. 13, no. 7, pp. 1308–15, 2013.

[188] J. Kim, J. Erath, A. Rodriguez, and C. Yang, "A high-efficiency microfluidic device for size-selective trapping and sorting.," *Lab Chip*, May 2014.

[189] Y.-C. Tan, J. S. Fisher, A. I. Lee, V. Cristini, and A. P. Lee, "Design of microfluidic channel geometries for the control of droplet volume, chemical concentration, and sorting.," *Lab Chip*, vol. 4, no. 4, pp. 292–298, 2004.

[190] K. Ahn, C. Kerbage, T. P. Hunt, R. M. Westervelt, D. R. Link, and D. a. Weitz,

"Dielectrophoretic manipulation of drops for high-speed microfluidic sorting devices," *Appl. Phys. Lett.*, vol. 88, no. 2, p. 024104, 2006.

[191] P. Y. Chiou, A. T. Ohta, and M. C. Wu, "Massively parallel manipulation of single cells and microparticles using optical images.," *Nature*, vol. 436, no. 7049, pp. 370–2, Jul. 2005.

[192] H. Tae, C. James, R. B. Edward, A. T. Ohta, S. Member, P. Chiou, T. H. Han, J. C. Liao, and U. Bhardwaj, "Dynamic Cell and Microparticle Control via Optoelectronic Tweezers," *J. microelectromechanical Syst.*, 2007.

[193] D.-H. Lee, H. Hwang, and J.-K. Park, "Generation and manipulation of droplets in an optoelectrofluidic device integrated with microfluidic channels," *Appl. Phys. Lett.*, vol. 95, no. 16, p. 164102, 2009.

[194] S.-Y. Park, S. Kalim, C. Callahan, M. a Teitell, and E. P. Y. Chiou, "A light-induced dielectrophoretic droplet manipulation platform.," *Lab Chip*, vol. 9, no. 22, pp. 3228–35, Dec. 2009.

[195] A. Sciambi and A. R. Abate, "Accurate microfluidic sorting of droplets at 30 kHz," *Lab Chip*, Oct. 2014.

[196] M. J. Fulwyler, R. B. Glascock, R. D. Hiebert, and N. M. Johnson, "Device which separates minute particles according to electronically sensed volume," *Rev. Sci. Instrum.*, vol. 40, no. 1, pp. 42–48, 1969.

[197] J. Kr$uuml$ger, K. Singh, A. O$apos$Neill, C. Jackson, A. Morrison, and P. O$apos$Brien, "Development of a microfluidic device for fluorescence activated cell sorting," *J. Micromechanics Microengineering*, vol. 12, no. 4, pp. 486–494, Jul. 2002.

[198] S. W. Lim and A. R. Abate, "Ultrahigh-throughput sorting of microfluidic drops with flow cytometry.," *Lab Chip*, vol. 13, no. 23, pp. 4563–72, 2013.

[199] A. Zinchenko, S. R. a Devenish, B. Kintses, P. Y. Colin, M. Fischlechner, and F. Hollfelder, "One in a million: Flow cytometric sorting of single cell-lysate assays in monodisperse picolitre double emulsion droplets for directed evolution," *Anal. Chem.*, vol. 86, no. 5, pp. 2526–2533, 2014.

[200] N. R. Beer, K. A. Rose, and I. M. Kennedy, "Monodisperse droplet generation and rapid trapping for single molecule detection and reaction kinetics measurement.," *Lab Chip*, vol. 9, no. 6, pp. 841–4, Mar. 2009.

[201] S.-Y. Yang, S.-K. Hsiung, Y.-C. Hung, C.-M. Chang, T.-L. Liao, and G.-B. Lee, "A cell counting/sorting system incorporated with a microfabricated flow cytometer chip," *Meas. Sci. Technol.*, vol. 17, no. 7, pp. 2001–2009, Jul. 2006.

[202] A. a. Darhuber and S. M. Troian, "Principles of Microfluidic Actuation By Modulation of Surface Stresses," *Annu. Rev. Fluid Mech.*, vol. 37, no. 1, pp. 425–455, Jan. 2005.

[203] K. Zhang, Q. Liang, S. Ma, X. Mu, P. Hu, Y. Wang, and G. Luo, "On-chip manipulation of continuous picoliter-volume superparamagnetic droplets using a magnetic force.," *Lab Chip*, vol. 9, no. 20, pp. 2992–9, Oct. 2009.

[204] E. Surenjav, C. Priest, S. Herminghaus, and R. Seemann, "Manipulation of gel emulsions by variable microchannel geometry.," *Lab Chip*, vol. 9, no. 2, pp. 325–30, Jan. 2009.

[205] O. Manneberg, S. Melker Hagsäter, J. Svennebring, H. M. Hertz, J. P. Kutter, H. Bruus, and M. Wiklund, "Spatial confinement of ultrasonic force fields in microfluidic channels.," *Ultrasonics*, vol. 49, no. 1, pp. 112–9, Jan. 2009.

[206] T. Franke, A. R. Abate, D. a Weitz, and A. Wixforth, "Surface acoustic wave (SAW) directed droplet flow in microfluidics for PDMS devices.," *Lab Chip*, vol. 9, no. 18, pp. 2625–7, Sep. 2009.

[207] T. Franke, S. Braunmüller, L. Schmid, a Wixforth, and D. a Weitz, "Surface acoustic wave actuated cell sorting (SAWACS).," *Lab Chip*, vol. 10, no. 6, pp. 789–94, Mar. 2010.

[208] Z. Wang and J. Zhe, "Recent advances in particle and droplet manipulation for lab-on-a-chip devices based on surface acoustic waves.," *Lab Chip*, vol. 11, no. 7, pp. 1280–5, Apr. 2011.

[209] M. Sesen, T. Alan, and A. Neild, "Microfluidic plug steering using surface acoustic waves," *Lab Chip*, vol. 15, pp. 3030–3038, 2015.

[210] J.-W. Choi, K. W. Oh, J. H. Thomas, W. R. Heineman, H. B. Halsall, J. H. Nevin, A. J. Helmicki, H. T. Henderson, and C. H. Ahn, "An integrated microfluidic biochemical detection system for protein analysis with magnetic bead-based sampling capabilities.," *Lab Chip*, vol. 2, no. 1, pp. 27–30, Feb. 2002.

[211] S. Liu, Y. Gu, R. B. Le Roux, S. M. Matthews, D. Bratton, K. Yunus, A. C. Fisher, and W. T. S. Huck, "The electrochemical detection of droplets in microfluidic devices.," *Lab Chip*, vol.

8, no. 11, pp. 1937–42, Nov. 2008.

[212] N. Srivastava and M. a Burns, “Electronic drop sensing in microfluidic devices: automated operation of a nanoliter viscometer.,” *Lab Chip*, vol. 6, no. 6, pp. 744–51, Jun. 2006.

[213] X. Niu, M. Zhang, S. Peng, W. Wen, and P. Sheng, “Real-time detection, control, and sorting of microfluidic droplets.,” *Biomicrofluidics*, vol. 1, no. 4, p. 44101, Jan. 2007.

[214] C. Elbuken, T. Glawdel, D. Chan, and C. L. Ren, “Detection of microdroplet size and speed using capacitive sensors,” *Sensors Actuators A Phys.*, vol. 171, no. 2, pp. 55–62, Nov. 2011.

[215] P. K. Isgor, M. Marcali, M. Keser, and C. Elbuken, “Microfluidic droplet content detection using integrated capacitive sensors,” *Sensors Actuators B Chem.*, vol. 210, pp. 669–675, 2015.

[216] M. S. Boybay, A. Jiao, T. Glawdel, and C. L. Ren, “Microwave sensing and heating of individual droplets in microfluidic devices,” *Lab Chip*, vol. 13, no. 19, pp. 3840–6, 2013.

[217] J.-C. Baret, O. J. Miller, V. Taly, M. Ryckelynck, A. El-Harrak, L. Frenz, C. Rick, M. L. Samuels, J. B. Hutchison, J. J. Agresti, D. R. Link, D. a Weitz, and A. D. Griffiths, “Fluorescence-activated droplet sorting (FADS): efficient microfluidic cell sorting based on enzymatic activity.,” *Lab Chip*, vol. 9, no. 13, pp. 1850–8, Jul. 2009.

[218] X. Casadevall i Solvas, X. Niu, K. Leeper, S. Cho, S.-I. Chang, J. B. Edel, and A. J. deMello, “Fluorescence detection methods for microfluidic droplet platforms.,” *J. Vis. Exp.*, no. 58, pp. 1–9, Jan. 2011.

[219] M. Bercovici, G. V Kaigala, C. J. Backhouse, and J. G. Santiago, “Fluorescent carrier ampholytes assay for portable, label-free detection of chemical toxins in tap water.,” *Anal. Chem.*, vol. 82, no. 5, pp. 1858–66, Mar. 2010.

[220] B. Jung, Y. Zhu, and J. G. Santiago, “Detection of 100 aM fluorophores using a high-sensitivity on-chip CE system and transient isotachophoresis.,” *Anal. Chem.*, vol. 79, no. 1, pp. 345–9, Jan. 2007.

[221] N. Yi, B. K. Park, D. Kim, and J. Park, “Micro-droplet detection and characterization using thermal responses,” *Lab Chip*, pp. 2378–2384, 2011.

[222] H. Song, J. D. Tice, and R. F. Ismagilov, “A Microfluidic System for Controlling Reaction Networks in Time,” *Angew. Chemie*, vol. 115, pp. 791–796, 2003.

[223] N. Bremond, A. Thiam, and J. Bibette, “Decompressing Emulsion Droplets Favors Coalescence,” *Phys. Rev. Lett.*, vol. 100, no. 2, pp. 1–4, Jan. 2008.

[224] A. Lai, N. Bremond, and H. a. Stone, “Separation-driven coalescence of droplets: an analytical criterion for the approach to contact,” *J. Fluid Mech.*, vol. 632, p. 97, Jul. 2009.

[225] B. M. Jose and T. Cubaud, “Droplet arrangement and coalescence in diverging/converging microchannels,” *Microfluid. Nanofluidics*, vol. 12, no. 5, pp. 687–696, Nov. 2011.

[226] X. Niu, S. Gulati, J. B. Edel, and A. J. deMello, “Pillar-induced droplet merging in microfluidic circuits.,” *Lab Chip*, vol. 8, no. 11, pp. 1837–41, Nov. 2008.

[227] G. F. Christopher, J. Bergstein, N. B. End, M. Poon, C. Nguyen, and S. L. Anna, “Coalescence and splitting of confined droplets at microfluidic junctions.,” *Lab Chip*, vol. 9, no. 8, pp. 1102–9, Apr. 2009.

[228] L. Yang, K. Wang, J. Tan, Y. Lu, and G. Luo, “Experimental study of microbubble coalescence in a T-junction microfluidic device,” *Microfluid. Nanofluidics*, vol. 12, no. 5, pp. 715–722, Nov. 2011.

[229] L. Mazutis, J.-C. Baret, and A. D. Griffiths, “A fast and efficient microfluidic system for highly selective one-to-one droplet fusion.,” *Lab Chip*, vol. 9, no. 18, pp. 2665–72, Sep. 2009.

[230] L. Mazutis and A. D. Griffiths, “Selective droplet coalescence using microfluidic systems,” *Lab Chip*, vol. 12, no. 10, p. 1800, 2012.

[231] N.-N. Deng, S.-X. Sun, W. Wang, X.-J. Ju, R. Xie, and L.-Y. Chu, “A novel surgery-like strategy for droplet coalescence in microchannels.,” *Lab Chip*, vol. 13, no. 18, pp. 3653–7, Sep. 2013.

[232] T.-D. Luong, N.-T. Nguyen, and A. Sposito, “Thermocoalescence of microdroplets in a microfluidic chamber,” *Appl. Phys. Lett.*, vol. 100, no. 25, p. 254105, 2012.

[233] M. Zagnoni and J. M. Cooper, “On-chip electrocoalescence of microdroplets as a function of voltage, frequency and droplet size.,” *Lab Chip*, vol. 9, no. 18, pp. 2652–8, Sep. 2009.

[234] C. Priest, S. Herminghaus, and R. Seemann, “Controlled electrocoalescence in microfluidics: Targeting a single lamella,” *Appl. Phys. Lett.*, vol. 89, no. 13, p. 134101, 2006.

[235] D. R. Link, E. Grasland-Mongrain, A. Duri, F. Sarrazin, Z. Cheng, G. Cristobal, M. Marquez, and D. a. Weitz, "Electric Control of Droplets in Microfluidic Devices," *Angew. Chemie*, vol. 118, no. 16, pp. 2618–2622, Apr. 2006.

[236] M. Zagnoni, C. Baroud, and J. Cooper, "Electrically initiated upstream coalescence cascade of droplets in a microfluidic flow," *Phys. Rev. E*, vol. 80, no. 4, p. 046303, Oct. 2009.

[237] M. Chabert, K. D. Dorfman, and J.-L. Viovy, "Droplet fusion by alternating current (AC) field electrocoalescence in microchannels.," *Electrophoresis*, vol. 26, no. 19, pp. 3706–15, Oct. 2005.

[238] K. Ahn, J. Agresti, H. Chong, M. Marquez, and D. a. Weitz, "Electrocoalescence of drops synchronized by size-dependent flow in microfluidic channels," *Appl. Phys. Lett.*, vol. 88, no. 26, p. 264105, 2006.

[239] M. Sesen, T. Alan, and A. Neild, "Microfluidic on-demand droplet merging using surface acoustic waves.," *Lab Chip*, vol. 14, no. 17, pp. 3325–33, Sep. 2014.

[240] Akartuna, Ilke, D. M. Aubrecht, T. E. Kodger, and D. A. Weitz, "Chemically induced coalescence in droplet-based microfluidics," *Lab Chip*, vol. 15, pp. 1140–1144, 2015.

[241] D. H. Yoon, A. Jamshaid, J. Ito, A. Nakahara, D. Tanaka, T. Akitsu, T. Sekiguchi, and S. Shoji, "Active microdroplet merging by hydrodynamic flow control using a pneumatic actuator-assisted pillar structure.," *Lab Chip*, vol. 14, no. 16, pp. 3050–5, Aug. 2014.

[242] a. M. Leshansky and L. M. Pismen, "Breakup of drops in a microfluidic T junction," *Physics of Fluids*, vol. 21, no. 2. p. 023303, 2009.

[243] M. De Menech, "Modeling of droplet breakup in a microfluidic T-shaped junction with a phase-field model," *Phys. Rev. E*, vol. 73, no. 3, pp. 1–9, Mar. 2006.

[244] A. Bedram and A. Moosavi, "Droplet breakup in an asymmetric microfluidic T junction.," *Eur. Phys. J. E. Soft Matter*, vol. 34, no. 8, p. 78, Aug. 2011.

[245] D. a. Hoang, L. M. Portela, C. R. Kleijn, M. T. Kreutzer, and V. van Steijn, "Dynamics of droplet breakup in a T-junction," *J. Fluid Mech.*, vol. 717, p. R4, Feb. 2013.

[246] M. Samie, A. Salari, and M. B. Shafii, "Breakup of microdroplets in asymmetric T junctions,"

Phys. Rev. E, vol. 87, no. 5, p. 053003, May 2013.

[247] B. Zheng, J. D. Tice, and R. F. Ismagilov, "Formation of droplets of alternating composition in microfluidic channels and applications to indexing of concentrations in droplet-based assays," *Anal. Chem.*, vol. 76, no. 17, pp. 4977–4982, 2004.

[248] L.-H. Hung, K. M. Choi, W.-Y. Tseng, Y.-C. Tan, K. J. Shea, and A. P. Lee, "Alternating droplet generation and controlled dynamic droplet fusion in microfluidic device for CdS nanoparticle synthesis.," *Lab Chip*, vol. 6, no. 2, pp. 174–8, Feb. 2006.

[249] L. Frenz, J. Blouwolff, A. D. Griffiths, and J.-C. Baret, "Microfluidic production of droplet pairs.," *Langmuir*, vol. 24, no. 20, pp. 12073–12076, Oct. 2008.

[250] J. Hong, M. Choi, J. B. Edel, and A. J. DeMello, "Passive self-synchronized two-droplet generation.," *Lab Chip*, vol. 10, no. 20, pp. 2702–2709, Oct. 2010.

[251] R. M. Schoeman, E. W. M. Kemna, F. Wolbers, and A. van den Berg, "High-throughput deterministic single-cell encapsulation and droplet pairing, fusion, and shrinkage in a single microfluidic device," *Electrophoresis*, vol. 35, no. 2–3, pp. 385–392, 2014.

[252] M. Prakash and N. Gershenfeld, "Microfluidic bubble logic.," *Science*, vol. 315, no. 5813, pp. 832–5, Feb. 2007.

[253] B. Ahn, K. Lee, H. Lee, R. Panchapakesan, and K. W. Oh, "Parallel synchronization of two trains of droplets using a railroad-like channel network.," *Lab Chip*, vol. 11, no. 23, Oct. 2011.

[254] K. Song, L. Zhang, and G. Hu, "Modeling of droplet traffic in interconnected microfluidic ladder devices.," *Electrophoresis*, vol. 33, no. 3, pp. 411–8, Feb. 2012.

[255] J. Maddala, W. S. Wang, S. a. Vanapalli, and R. Rengaswamy, "Traffic of pairs of drops in microfluidic ladder networks with fore-aft structural asymmetry," *Microfluid. Nanofluidics*, vol. 14, no. 1–2, pp. 337–344, Oct. 2012.

[256] A. M. Skelley, O. Kirak, H. Suh, R. Jaenisch, and J. Voldman, "Microfluidic control of cell pairing and fusion," *Nat. Methods*, vol. 6, no. 2, pp. 147–152, 2009.

[257] B. Dura, Y. Liu, and J. Voldman, "Deformability-based microfluidic cell pairing and fusion.," *Lab Chip*, Jun. 2014.

[258] A. M. Huebner, C. Abell, W. T. S. Huck, C. N. Baroud, and F. Hollfelder, “Monitoring a reaction at submillisecond resolution in picoliter volumes,” *Anal. Chem.*, vol. 83, no. 4, pp. 1462–1468, 2011.

[259] J. D. Tice, H. Song, A. D. Lyon, and R. F. Ismagilov, “Formation of Droplets and Mixing in Multiphase Microfluidics at Low Values of the Reynolds and the Capillary Numbers,” *Langmuir*, vol. 19, no. 22, pp. 9127–9133, Oct. 2003.

[260] V. Steijn, M. T. Kreutzer, and C. R. Kleijn, “μ-PIV study of the formation of segmented flow in microfluidic T-junctions,” *Chem. Eng. Sci.*, vol. 62, pp. 7505–7514, 2007.

[261] H. Kinoshita, S. Kaneda, T. Fujii, and M. Oshima, “Three-dimensional measurement and visualization of internal flow of a moving droplet using confocal micro-PIV.,” *Lab Chip*, vol. 7, no. 3, pp. 338–46, Mar. 2007.

[262] R. Lindken, M. Rossi, S. Grosse, and J. Westerweel, “Micro-Particle Image Velocimetry (microPIV): recent developments, applications, and guidelines.,” *Lab Chip*, vol. 9, no. 17, pp. 2551–67, Sep. 2009.

[263] H. Song, Z. Cai, H. M. Noh, and D. J. Bennett, “Chaotic mixing in microchannels via low frequency switching transverse electroosmotic flow generated on integrated microelectrodes.,” *Lab Chip*, vol. 10, no. 6, pp. 734–40, Mar. 2010.

[264] S. Verguet, C. Duan, A. Liau, V. Berk, J. H. D. Cate, A. Majumdar, and A. J. Szeri, “Mechanics of liquid–liquid interfaces and mixing enhancement in microscale flows,” *J. Fluid Mech.*, vol. 652, pp. 207–240, May 2010.

[265] Z. B. Stone and H. a. Stone, “Imaging and quantifying mixing in a model droplet micromixer,” *Phys. Fluids*, vol. 17, no. 6, p. 063103, 2005.

[266] A. Liau, R. Karnik, A. Majumdar, and J. H. D. Cate, “Mixing crowded biological solutions in milliseconds.,” *Anal. Chem.*, vol. 77, no. 23, pp. 7618–25, Dec. 2005.

[267] S. Verguet, C. Duan, A. Liau, V. Berk, J. H. D. Cate, A. Majumdar, and A. J. Szeri, “Mechanics of liquid–liquid interfaces and mixing enhancement in microscale flows,” *J. Fluid Mech.*, vol. 652, pp. 207–240, May 2010.

[268] V. Labrot, M. Schindler, P. Guillot, A. Colin, and M. Joanicot, “Extracting the hydrodynamic resistance of droplets from their behavior in microchannel networks.,” *Biomicrofluidics*, vol. 3, no. 1, p. 12804, Jan. 2009.

[269] M. L. Cordero, H. O. Rolfsnes, D. R. Burnham, P. a Campbell, D. McGloin, and C. N. Baroud, “Mixing via thermocapillary generation of flow patterns inside a microfluidic drop,” *New J. Phys.*, vol. 11, no. 7, p. 075033, Jul. 2009.

[270] J. Avesar, T. Ben Arye, and S. Levenberg, “Frontier microfluidic techniques for short and long-term single cell analysis,” *Lab Chip*, 2014.

[271] L. Frenz, K. Blank, E. Brouzes, and A. D. Griffiths, “Reliable microfluidic on-chip incubation of droplets in delay-lines.,” *Lab Chip*, vol. 9, no. 10, pp. 1344–8, May 2009.

[272] W.-H. Tan and S. Takeuchi, “A trap-and-release integrated microfluidic system for dynamic microarray applications.,” *Proc. Natl. Acad. Sci. U. S. A.*, vol. 104, no. 4, pp. 1146–51, Jan. 2007.

[273] W. Shi, J. Qin, N. Ye, and B. Lin, “Droplet-based microfluidic system for individual Caenorhabditis elegans assay.,” *Lab Chip*, vol. 8, no. 9, pp. 1432–5, Sep. 2008.

[274] A. Dewan, J. Kim, R. H. McLean, S. a Vanapalli, and M. N. Karim, “Growth kinetics of microalgae in microfluidic static droplet arrays.,” *Biotechnol. Bioeng.*, vol. 109, no. 12, pp. 2987–96, Dec. 2012.

[275] A. Huebner, D. Bratton, G. Whyte, M. Yang, A. J. Demello, C. Abell, and F. Hollfelder, “Static microdroplet arrays: a microfluidic device for droplet trapping, incubation and release for enzymatic and cell-based assays.,” *Lab Chip*, vol. 9, no. 5, pp. 692–8, Mar. 2009.

[276] P. M. Korczyk, L. Derzsi, S. Jakieła, and P. Garstecki, “Microfluidic traps for hard-wired operations on droplets.,” *Lab Chip*, vol. 13, no. 20, pp. 4096–102, Oct. 2013.

[277] S. S. Bithi and S. a Vanapalli, “Behavior of a train of droplets in a fluidic network with hydrodynamic traps.,” *Biomicrofluidics*, vol. 4, no. 4, p. 44110, Jan. 2010.

[278] D. Di Carlo, N. Aghdam, and L. P. Lee, “Single-Cell Enzyme Concentrations , Kinetics , and Inhibition Analysis Using High-Density Hydrodynamic Cell Isolation Arrays Single-Cell Enzyme Concentrations , Kinetics , and Inhibition Analysis Using High-Density Hydrodynamic Cell Isolation Arrays,” *Anal. Chem.*, vol. 78, no. 14, pp. 4925–4930, 2006.

[279] Y. Bai, X. He, D. Liu, S. N. Patil, D. Bratton, A. Huebner, F. Hollfelder, C. Abell, and W. T. S. Huck, “A double droplet trap system for studying mass transport across a droplet-droplet

interface.," *Lab Chip*, vol. 10, no. 10, pp. 1281–5, May 2010.

[280] P. Abbyad, R. Dangla, A. Alexandrou, and C. N. Baroud, "Rails and anchors: guiding and trapping droplet microreactors in two dimensions.," *Lab Chip*, vol. 11, no. 5, pp. 813–21, Mar. 2011.

[281] I. Doh, E. Y. Erdem, and a. P. Pisano, "Trapping and collection of uniform size droplets for nanoparticle synthesis," *Appl. Phys. Lett.*, vol. 100, no. 7, p. 074106, 2012.

[282] M. G. Simon, R. Lin, J. S. Fisher, and A. P. Lee, "A Laplace pressure based microfluidic trap for passive droplet trapping and controlled release.," *Biomicrofluidics*, vol. 6, no. 1, pp. 14110–1411013, Mar. 2012.

[283] S. H. Jin, H.-H. Jeong, B. Lee, S. S. Lee, and C.-S. Lee, "A programmable microfluidic static droplet array for droplet generation, transportation, fusion, storage, and retrieval," *Lab Chip*, 2015.

[284] W. Wang, C. Yang, and C. M. Li, "On-demand microfluidic droplet trapping and fusion for on-chip static droplet assays.," *Lab Chip*, vol. 9, no. 11, pp. 1504–6, Jun. 2009.

[285] W. Wang, C. Yang, Y. Liu, and C. M. Li, "On-demand droplet release for droplet-based microfluidic system.," *Lab Chip*, vol. 10, no. 5, pp. 559–62, Mar. 2010.

[286] V. Trivedi, A. Doshi, G. K. Kurup, E. Ereifej, P. J. Vandevord, and A. S. Basu, "A modular approach for the generation, storage, mixing, and detection of droplet libraries for high throughput screening.," *Lab Chip*, vol. 10, no. 18, pp. 2433–42, Sep. 2010.

[287] C. N. Baroud, F. Gallaire, and R. Dangla, "Dynamics of microfluidic droplets.," *Lab Chip*, vol. 10, no. 16, pp. 2032–45, Aug. 2010.

[288] P. Sobieszuk, J. Aubin, and R. Pohorecki, "Hydrodynamics and Mass Transfer in Gas-Liquid Flows in Microreactors," *Chem. Eng. Technol.*, vol. 35, no. 8, pp. 1346–1358, Aug. 2012.

[289] F. Fairbrother and A. E. Stubbs, "Studies in Electro-endosmosis," *J. chem. Soc.*, vol. 1, pp. 527–529, 1935.

[290] G. I. Taylor, "Deposition of a viscous fluid on a plane surface," *J. Fluid Mech.*, vol. 9, no. 02, p. 218, 1960.

[291] B. G. Cox, “An experimental investigation of the streamlines in viscous fluid expelled from a tube,” *J. Fluid Mech.*, vol. 20, no. 02, p. 193, 1964.

[292] J. Chen, “Measuring the Film Thickness Surrounding a Bubble inside a Capillary,” *J. Colloid Interface Sci.*, vol. 109, no. 2, pp. 341–349, 1986.

[293] T. C. Thulasidas, M. a. Abraham, and R. L. Cerro, “Flow patterns in liquid slugs during bubble-train flow inside capillaries,” *Chem. Eng. Sci.*, vol. 52, no. 17, pp. 2947–2962, 1997.

[294] P. Aussillous, D. Que, and T. B. Regimes, “Quick deposition of a fluid on the wall of a tube,” *Phys. Fluids*, vol. 12, no. 10, pp. 2367–2371, 2000.

[295] F. P. Bretherton, “The motion of long bubbles in tubes,” *J. Fluid Mech.*, vol. 10, no. 02, pp. 166–188, 1961.

[296] W. B. Kolb and R. L. Cerro, “Coating the inside of a capillary of square cross section,” *Chem. Eng. Sci.*, vol. 46, no. 9, pp. 2181–2195, Jan. 1991.

[297] W. B. Kolb and R. L. Cerro, “Film Flow in the Space between a Circular Bubble and a Square Tube,” *J. Colloid Interface Sci.*, 1993.

[298] H. Wong, C. J. Radke, and S. Morris, “The motion of long bubbles in polygonal capillaries. Part 1. Thin films,” *J. Fluid Mech.*, vol. 292, no. -1, p. 71, Apr. 1995.

[299] H. Wong, C. J. Radke, and S. Morris, “The motion of long bubbles in polygonal capillaries. Part 2. Drag, fluid pressure and fluid flow,” *J. Fluid Mech.*, vol. 292, pp. 95–110, Apr. 1995.

[300] T. Taha and Z. F. Cui, “Hydrodynamics of slug flow inside capillaries,” *Chem. Eng. Sci.*, vol. 59, no. 6, pp. 1181–1190, Mar. 2004.

[301] D. Eskin and F. Mostowfi, “A model of a bubble train flow accompanied with mass transfer through a long microchannel,” *Int. J. Heat Fluid Flow*, vol. 33, no. 1, pp. 147–155, Feb. 2012.

[302] E. Klaseboer, R. Gupta, and R. Manica, “An extended Bretherton model for long Taylor bubbles at moderate capillary numbers,” *Phys. Fluids*, vol. 26, no. 3, p. 032107, Mar. 2014.

[303] a. C. DeVoria and K. Mohseni, “Droplets in an axisymmetric microtube: Effects of aspect ratio and fluid interfaces,” *Phys. Fluids*, vol. 27, no. 1, p. 012002, 2015.

[304] S. R. Hodges, O. E. Jensen, and J. M. Rallison, “The motion of a viscous drop through a cylindrical tube,” *J. Fluid Mech.*, vol. 501, pp. 279–301, Feb. 2004.

[305] M. Muradoglu and H. a. Stone, “Motion of large bubbles in curved channels,” *J. Fluid Mech.*, vol. 570, p. 455, Jan. 2007.

[306] M. Muradoglu, “Axial dispersion in segmented gas-liquid flow: Effects of alternating channel curvature,” *Phys. Fluids*, vol. 22, no. 12, p. 122106, 2010.

[307] M. J. Fuerstman, A. Lai, M. E. Thurlow, S. S. Shevkoplyas, H. a Stone, and G. M. Whitesides, “The pressure drop along rectangular microchannels containing bubbles.,” *Lab Chip*, vol. 7, no. 11, pp. 1479–89, Nov. 2007.

[308] M. Schindler and A. Ajdari, “Droplet Traffic in Microfluidic Networks: A Simple Model for Understanding and Designing,” *Phys. Rev. Lett.*, vol. 100, no. 4, pp. 1–4, Jan. 2008.

[309] S. Jakiela, S. Makulska, P. M. Korczyk, and P. Garstecki, “Speed of flow of individual droplets in microfluidic channels as a function of the capillary number, volume of droplets and contrast of viscosities,” *Lab Chip*, no. 207890, 2011.

[310] F. Jousse, G. Lian, R. Janes, and J. Melrose, “Compact model for multi-phase liquid-liquid flows in micro-fluidic devices.,” *Lab Chip*, vol. 5, no. 6, pp. 646–56, Jun. 2005.

[311] D. Sessoms, M. Belloul, W. Engl, M. Roche, L. Courbin, and P. Panizza, “Droplet motion in microfluidic networks: Hydrodynamic interactions and pressure-drop measurements,” *Phys. Rev. E*, vol. 80, no. 1, pp. 1–10, Jul. 2009.

[312] B. J. Adzima and S. S. Velankar, “Pressure drops for droplet flows in microfluidic channels,” *J. Micromechanics Microengineering*, vol. 16, no. 8, pp. 1504–1510, Aug. 2006.

[313] S. a Vanapalli, A. G. Banpurkar, D. van den Ende, M. H. G. Duits, and F. Mugele, “Hydrodynamic resistance of single confined moving drops in rectangular microchannels.,” *Lab on a chip*, vol. 9, no. 7. pp. 982–90, 07-Apr-2009.

[314] A. Huebner, S. Sharma, M. Srisa-Art, F. Hollfelder, J. B. Edel, and A. J. Demello, “Microdroplets: a sea of applications?,” *Lab Chip*, vol. 8, no. 8, pp. 1244–54, Aug. 2008.

[315] M. J. Jebrail, M. S. Bartsch, and K. D. Patel, “Digital microfluidics: a versatile tool for applications in chemistry, biology and medicine.,” *Lab Chip*, vol. 12, no. 14, pp. 2452–2463,

Jul. 2012.

[316] K. S. Elvira, X. Casadevall, R. C. R. Wootton, and J. Andrew, “The past, Present and Potential For microfluidic reactor technology in chemical synthesis,” *Nat. Chem.*, vol. 5, pp. 905–915, 2013.

[317] J. K. Nunes, S. S. H. Tsai, J. Wan, and H. a Stone, “Dripping and jetting in microfluidic multiphase flows applied to particle and fibre synthesis,” *J. Phys. D. Appl. Phys.*, vol. 46, no. 11, p. 114002, Mar. 2013.

[318] P. H. Hoang, C. T. Nguyen, J. Perumal, and D.-P. Kim, “Droplet synthesis of well-defined block copolymers using solvent-resistant microfluidic device.,” *Lab Chip*, vol. 11, no. 2, pp. 329–35, Jan. 2011.

[319] N. J. Carroll, S. B. Rathod, E. Derbins, S. Mendez, D. a Weitz, and D. N. Petsev, “Droplet-based microfluidics for emulsion and solvent evaporation synthesis of monodisperse mesoporous silica microspheres.,” *Langmuir*, vol. 24, no. 3, pp. 658–61, Feb. 2008.

[320] J. Kim, Y. Song, H. Lee, W. Park, H. Kim, and S. Kwon, “MICROFLUIDIC SYNTHESIS OF MAGNETOCHROMATIC MICROSPHERES UTILIZING MAGNETIC SELF-ASSEMBLY AND PHOTOPOLYMERIZATION PROCESS,” *Electr. Eng.*, no. October, pp. 1361–1363, 2010.

[321] J. R. Millman, K. H. Bhatt, B. G. Prevo, and O. D. Velev, “Anisotropic particle synthesis in dielectrophoretically controlled microdroplet reactors.,” *Nat. Mater.*, vol. 4, no. 1, pp. 98–102, Jan. 2005.

[322] P. Y. Keng, S. Chen, H. Ding, S. Sadeghi, G. J. Shah, A. Dooraghi, M. E. Phelps, N. Satyamurthy, A. F. Chatziioannou, C.-J. Kim, and R. M. van Dam, “Micro-chemical synthesis of molecular probes on an electronic microfluidic device.,” *Proc. Natl. Acad. Sci. U. S. A.*, vol. 109, no. 3, pp. 690–695, Jan. 2012.

[323] B. F. Cottam, S. Krishnadasan, A. J. Demello, J. C. Demello, and M. S. P. Shaffer, “Accelerated synthesis of titanium oxide nanostructures using microfluidic chips.,” *Lab Chip*, vol. 7, no. 2, pp. 167–9, Mar. 2007.

[324] Y. H. Kim, L. Zhang, T. Yu, M. Jin, D. Qin, and Y. Xia, “Droplet-Based Microreactors for Continuous Production of Palladium Nanocrystals with Controlled Sizes and Shapes.,” *Small*, pp. 1–6, Apr. 2013.

[325] M. Lade, H. Mays, J. Schmidt, R. Willumeit, and R. Schomacker, “On the nanoparticle synthesis in microemulsions : detailed characterization of an applied reaction mixture,” *Colloids Surfaces A Physicochem. Eng. Asp.*, vol. 163, pp. 3–15, 2000.

[326] I. Shestopalov, J. D. Tice, and R. F. Ismagilov, “Multi-step synthesis of nanoparticles performed on millisecond time scale in a microfluidic droplet-based system.,” *Lab Chip*, vol. 4, no. 4, pp. 316–21, Aug. 2004.

[327] J. B. Wacker, I. Lignos, V. K. Parashar, and M. a M. Gijs, “Controlled synthesis of fluorescent silica nanoparticles inside microfluidic droplets.,” *Lab Chip*, vol. 12, no. 17, pp. 3111–6, Sep. 2012.

[328] Y. Shu, P. Jiang, D.-W. Pang, and Z.-L. Zhang, “Droplet-based microreactor for synthesis of water-soluble Ag_2S quantum dots,” *Nanotechnology*, vol. 26, no. 27, p. 275701, 2015.

[329] R. F. Shepherd, J. C. Conrad, S. K. Rhodes, D. R. Link, M. Marquez, D. A. Weitz, J. A. Lewis, P. Program, V. Di, and C. Road, “Microfluidic Assembly of Homogeneous and Janus Colloid-Filled Hydrogel Granules,” *Langmuir*, vol. 18, no. 9, pp. 8618–8622, 2006.

[330] T. Rossow, J. a Heyman, A. J. Ehrlicher, A. Langhoff, D. a Weitz, R. Haag, and S. Seiffert, “Controlled synthesis of cell-laden microgels by radical-free gelation in droplet microfluidics.,” *J. Am. Chem. Soc.*, vol. 134, no. 10, pp. 4983–9, Mar. 2012.

[331] M. Marquis, J. Davy, B. Cathala, a Fang, and D. Renard, “Microfluidics assisted generation of innovative polysaccharide hydrogel microparticles.,” *Carbohydr. Polym.*, vol. 116, pp. 189–99, Feb. 2015.

[332] M. J. Jebrail, A. H. C. Ng, V. Rai, R. Hili, A. K. Yudin, and A. R. Wheeler, “Synchronized synthesis of peptide-based macrocycles by digital microfluidics.,” *Angew. Chem. Int. Ed. Engl.*, vol. 49, no. 46, pp. 8625–9, Nov. 2010.

[333] Y. Zhang and P. Ozdemir, “Microfluidic DNA amplification--a review.,” *Anal. Chim. Acta*, vol. 638, no. 2, pp. 115–25, Apr. 2009.

[334] Y.-H. Chang, G.-B. Lee, F.-C. Huang, Y.-Y. Chen, and J.-L. Lin, “Integrated polymerase chain reaction chips utilizing digital microfluidics.,” *Biomed. Microdevices*, vol. 8, no. 3, pp. 215–25, Sep. 2006.

[335] R. Tewhey, J. B. Warner, M. Nakano, B. Libby, M. Medkova, P. H. David, S. K. Kotsopoulos, M. L. Samuels, J. B. Hutchison, J. W. Larson, E. J. Topol, M. P. Weiner, O. Harismendy, J.

Olson, D. R. Link, and K. a Frazer, “Microdroplet-based PCR enrichment for large-scale targeted sequencing.,” *Nat. Biotechnol.*, vol. 27, no. 11, pp. 1025–31, Nov. 2009.

[336] E. M. Miller, A. H. C. Ng, U. Uddayasankar, and A. R. Wheeler, “A digital microfluidic approach to heterogeneous immunoassays.,” *Anal. Bioanal. Chem.*, vol. 399, no. 1, pp. 337–45, Jan. 2011.

[337] J. Q. Boedicker, L. Li, T. R. Kline, and R. F. Ismagilov, “Detecting bacteria and determining their susceptibility to antibiotics by stochastic confinement in nanoliter droplets using plug-based microfluidics.,” *Lab Chip*, vol. 8, no. 8, pp. 1265–72, Aug. 2008.

[338] a Huebner, M. Srisa-Art, D. Holt, C. Abell, F. Hollfelder, a J. deMello, and J. B. Edel, “Quantitative detection of protein expression in single cells using droplet microfluidics.,” *Chem. Commun. (Camb).*, vol. 2, no. 12, pp. 1218–20, Mar. 2007.

[339] C. H. J. Schmitz, A. C. Rowat, S. Köster, and D. a Weitz, “Dropspots: a picoliter array in a microfluidic device.,” *Lab Chip*, vol. 9, no. 1, pp. 44–9, Jan. 2009.

[340] L. Boitard, D. Cottinet, C. Kleinschmitt, N. Bremond, J. Baudry, G. Yvert, and J. Bibette, “Monitoring single-cell bioenergetics via the coarsening of emulsion droplets.,” *Proc. Natl. Acad. Sci. U. S. A.*, vol. 109, no. 19, pp. 7181–6, May 2012.

[341] P. Mary, A. Chen, I. Chen, A. R. Abate, and D. a Weitz, “On-chip background noise reduction for cell-based assays in droplets.,” *Lab Chip*, vol. 11, no. 12, pp. 2066–70, Jun. 2011.

[342] S. Köster, F. E. Angilè, H. Duan, J. J. Agresti, A. Wintner, C. Schmitz, A. C. Rowat, C. a Merten, D. Pisignano, A. D. Griffiths, and D. a Weitz, “Drop-based microfluidic devices for encapsulation of single cells.,” *Lab Chip*, vol. 8, no. 7, pp. 1110–5, Jul. 2008.

[343] E. Brouzes, M. Medkova, N. Savenelli, D. Marran, M. Twardowski, J. B. Hutchison, J. M. Rothberg, D. R. Link, N. Perrimon, and M. L. Samuels, “Droplet microfluidic technology for single-cell high-throughput screening.,” *Proc. Natl. Acad. Sci. U. S. A.*, vol. 106, no. 34, pp. 14195–200, Aug. 2009.

[344] M. Chabert and J.-L. Viovy, “Microfluidic high-throughput encapsulation and hydrodynamic self-sorting of single cells.,” *Proc. Natl. Acad. Sci. U. S. A.*, vol. 105, no. 9, pp. 3191–6, Mar. 2008.

[345] E. Um, S.-G. Lee, and J.-K. Park, “Random breakup of microdroplets for single-cell encapsulation,” *Appl. Phys. Lett.*, vol. 97, no. 15, p. 153703, 2010.

[346] L. Wu, P. Chen, Y. Dong, X. Feng, and B.-F. Liu, “Encapsulation of single cells on a microfluidic device integrating droplet generation with fluorescence-activated droplet sorting.,” *Biomed. Microdevices*, vol. 15, no. 3, pp. 553–60, Jun. 2013.

[347] T. Jing, R. Ramji, M. E. Warkiani, J. Han, C. T. Lim, and C.-H. Chen, “Jetting microfluidics with size-sorting capability for single-cell protease detection,” *Biosens. Bioelectron.*, vol. 66, pp. 19–23, 2015.

[348] J. F. Edd, D. Di Carlo, K. J. Humphry, S. Köster, D. Irimia, D. a Weitz, and M. Toner, “Controlled encapsulation of single-cells into monodisperse picolitre drops.,” *Lab Chip*, vol. 8, no. 8, pp. 1262–4, Aug. 2008.

[349] A. R. Abate, C. Chen, J. Agresti, and D. A. Weitz, “Beating Poisson encapsulation statistics using close-packed ordering †,” *Lab Chip*, vol. 9, pp. 2628–2631, 2009.

[350] E. W. M. Kemna, R. M. Schoeman, F. Wolbers, I. Vermes, D. a Weitz, and A. van den Berg, “High-yield cell ordering and deterministic cell-in-droplet encapsulation using Dean flow in a curved microchannel.,” *Lab Chip*, vol. 12, no. 16, pp. 2881–7, Aug. 2012.

[351] V. Srinivasan, V. K. Pamula, and R. B. Fair, “An integrated digital microfluidic lab-on-a-chip for clinical diagnostics on human physiological fluids.,” *Lab Chip*, vol. 4, no. 4, pp. 310–5, Aug. 2004.

[352] N. a Mousa, M. J. Jebrail, H. Yang, M. Abdelgawad, P. Metalnikov, J. Chen, A. R. Wheeler, and R. F. Casper, “Droplet-scale estrogen assays in breast tissue, blood, and serum.,” *Sci. Transl. Med.*, vol. 1, no. 1, p. 1ra2, Oct. 2009.

[353] M. J. Jebrail, H. Yang, J. M. Mudrik, N. M. Lafrenière, C. McRoberts, O. Y. Al-Dirbashi, L. Fisher, P. Chakraborty, and A. R. Wheeler, “A digital microfluidic method for dried blood spot analysis.,” *Lab Chip*, vol. 11, no. 19, pp. 3218–24, Oct. 2011.

[354] O. J. Miller, A. El Harrak, T. Mangeat, J.-C. Baret, L. Frenz, B. El Debs, E. Mayot, M. L. Samuels, E. K. Rooney, P. Dieu, M. Galvan, D. R. Link, and A. D. Griffiths, “High-resolution dose-response screening using droplet-based microfluidics.,” *Proc. Natl. Acad. Sci. U. S. A.*, vol. 109, no. 2, pp. 378–83, Jan. 2012.

[355] E. Berthier and D. J. Beebe, “Gradient generation platforms: new directions for an established microfluidic technology.,” *Lab Chip*, vol. 14, pp. 3241–3247, Jul. 2014.

[356] A. B. Theberge, G. Whyte, and W. T. S. Huck, “Generation of Picoliter Droplets with Defined Contents and Concentration Gradients from the Separation of Chemical Mixtures,” *Anal. Chem.*, vol. 82, no. 9, pp. 3449–3453, 2010.

[357] S. Jambovane, D. J. Kim, E. C. Duin, S. Kim, and J. W. Hong, “Creation of Stepwise Concentration Gradient in Picoliter Droplets for Parallel Reactions of Matrix Metalloproteinase II and IX,” *Anal. Chem.*, vol. 83, pp. 3358–3364, 2011.

[358] C.-H. Yeh and Y.-C. Lin, “Use of an adjustable microfluidic droplet generator to produce uniform emulsions with different concentrations,” *J. Micromechanics Microengineering*, vol. 23, no. 12, p. 125025, Dec. 2013.

[359] C.-G. Yang, Y.-F. Wu, Z.-R. Xu, and J.-H. Wang, “A radial microfluidic concentration gradient generator with high-density channels for cell apoptosis assay.,” *Lab Chip*, vol. 11, no. 19, pp. 3305–12, Oct. 2011.

[360] C.-G. Yang, Z.-R. Xu, A. P. Lee, and J.-H. Wang, “A microfluidic concentration-gradient droplet array generator for the production of multi-color nanoparticles.,” *Lab Chip*, vol. 13, no. 14, pp. 2815–20, Jul. 2013.

[361] M.-P. N. Bui, C. A. Li, K. N. Han, J. Choo, E. K. Lee, and G. H. Seong, “Enzyme kinetic measurements using a droplet-based microfluidic system with a concentration gradient.,” *Anal. Chem.*, vol. 83, no. 5, pp. 1603–8, Mar. 2011.

[362] C.-H. Yeh, Y.-C. Chen, and Y.-C. Lin, “Generation of droplets with different concentrations using gradient-microfluidic droplet generator,” *Microfluid. Nanofluidics*, vol. 11, no. 3, pp. 245–253, Mar. 2011.

[363] K. Leung, H. Zahn, T. Leaver, K. M. Konwar, N. W. Hanson, a. P. Page, C.-C. Lo, P. S. Chain, S. J. Hallam, and C. L. Hansen, “A programmable droplet-based microfluidic device applied to multiparameter analysis of single microbes and microbial communities,” *Proc. Natl. Acad. Sci.*, vol. 109, no. 20, pp. 7665–7670, 2012.

[364] K. Churski, T. S. Kaminski, S. Jakiela, W. Kamysz, W. Baranska-Rybak, D. B. Weibel, and P. Garstecki, “Rapid screening of antibiotic toxicity in an automated microdroplet system,” *Lab Chip*, vol. 12, no. 9, pp. 1629–1637, May 2012.

[365] E. Um, M. E. Rogers, and H. a. Stone, “Combinatorial generation of droplets by controlled assembly and coalescence,” *Lab Chip*, 2013.

[366] M. Sun and S. a Vanapalli, “Generation of chemical concentration gradients in mobile droplet arrays via fragmentation of long immiscible diluting plugs.,” *Anal. Chem.*, vol. 85, no. 4, pp. 2044–8, Feb. 2013.

[367] T. Glawdel and C. L. Ren, “Global network design for robust operation of microfluidic droplet generators with pressure-driven flow,” *Microfluid. Nanofluidics*, vol. 13, no. 3, pp. 469–480, 2012.

[368] P. M. Korczyk, O. Cybulski, S. Makulska, and P. Garstecki, “Effects of unsteadiness of the rates of flow on the dynamics of formation of droplets in microfluidic systems.,” *Lab Chip*, vol. 11, no. 1, pp. 173–175, Jan. 2011.

[369] F. M. White, *Viscous fluid flow*, 2nd ed. New York: McGraw-Hill, 1991.

[370] P. Garstecki, I. Gitlin, W. DiLuzio, G. M. Whitesides, E. Kumacheva, and H. a. Stone, “Formation of monodisperse bubbles in a microfluidic flow-focusing device,” *Appl. Phys. Lett.*, vol. 85, no. 13, p. 2649, 2004.

[371] D. Bardin, T. D. Martz, P. S. Sheeran, R. Shih, P. a Dayton, and A. P. Lee, “High-speed, clinical-scale microfluidic generation of stable phase-change droplets for gas embolotherapy.,” *Lab Chip*, vol. 11, no. 23, pp. 3990–8, Dec. 2011.

[372] H. Liu and Y. Zhang, “Droplet formation in microfluidic cross-junctions,” *Phys. Fluids*, vol. 23, no. 8, p. 082101, 2011.

[373] P. Garstecki, H. Stone, and G. Whitesides, “Mechanism for Flow-Rate Controlled Breakup in Confined Geometries: A Route to Monodisperse Emulsions,” *Phys. Rev. Lett.*, vol. 94, no. 16, pp. 1–4, Apr. 2005.

[374] W. van Hoeve, B. Dollet, M. Versluis, and D. Lohse, “Microbubble formation and pinch-off scaling exponent in flow-focusing devices,” *Phys. Fluids*, vol. 23, no. 9, p. 092001, 2011.

[375] S. W. Tchikanda, R. H. Nilson, and S. K. Griffiths, “Modeling of pressure and shear-driven flows in open rectangular microchannels,” *Int. J. Heat Mass Transf.*, vol. 47, no. 3, pp. 527–538, Jan. 2004.

[376] Y. Schaerli, R. C. Wootton, T. Robinson, V. Stein, C. Dunsby, M. a a Neil, P. M. W. French, A. J. Demello, C. Abell, and F. Hollfelder, “Continuous-flow polymerase chain reaction of single-copy DNA in microfluidic microdroplets.,” *Anal. Chem.*, vol. 81, no. 1, pp. 302–6, Jan. 2009.

[377] K. Kwapiszewska, a Michalczuk, M. Rybka, R. Kwapiszewski, and Z. Brzózka, “A microfluidic-based platform for tumour spheroid culture, monitoring and drug screening.,” *Lab Chip*, May 2014.

[378] D. Velasco, E. Tumarkin, and E. Kumacheva, “Microfluidic encapsulation of cells in polymer microgels,” *Small*, vol. 8, no. 11, pp. 1633–1642, 2012.

[379] J. Berthier, S. Le Vot, P. Tiquet, N. David, D. Lauro, P. Y. Benhamou, and F. Rivera, “Highly viscous fluids in pressure actuated flow focusing devices,” *Sensors Actuators A Phys.*, vol. 158, no. 1, pp. 140–148, Mar. 2010.

[380] A. Jouyban, “Review of the cosolvency models for predicting solubility of drugs in water-cosolvent mixtures,” *J. Pharm. Pharm. Sci.*, vol. 11, no. 1, pp. 32–58, 2008.

[381] B. Y. Yu, “Microfluidic Large Scale Integration and its Application in Image Based Microflow Cytometry,” 2010.

[382] M. J. Fuerstman, P. Garstecki, and G. M. Whitesides, “Coding/decoding and reversibility of droplet trains in microfluidic networks.,” *Science*, vol. 315, no. 5813, pp. 828–32, Feb. 2007.

[383] T. Glawdel, C. Elbuken, and C. Ren, “Passive droplet trafficking at microfluidic junctions under geometric and flow asymmetries.,” *Lab Chip*, vol. 11, no. 22, pp. 3774–84, Nov. 2011.

[384] G. Cristobal, J.-P. Benoit, M. Joanicot, and A. Ajdari, “Microfluidic bypass for efficient passive regulation of droplet traffic at a junction,” *Appl. Phys. Lett.*, vol. 89, no. 3, p. 034104, 2006.

[385] K. W. Oh, K. Lee, B. Ahn, and E. P. Furlani, “Design of pressure-driven microfluidic networks using electric circuit analogy,” *Lab Chip*, 2011.

[386] A. M. Nightingale, T. W. Phillips, J. H. Bannock, and J. C. de Mello, “Controlled multistep synthesis in a three-phase droplet reactor.,” *Nat. Commun.*, vol. 5, no. May, p. 3777, Jan. 2014.

[387] Y. Wang, E. Tumarkin, D. Velasco, M. Abolhasani, W. Lau, and E. Kumacheva, “Exploring a direct injection method for microfluidic generation of polymer microgels.,” *Lab Chip*, vol. 13, no. 13, pp. 2547–53, 2013.

[388] M. Lee, J. W. Collins, D. M. Aubrecht, R. a. Sperling, L. Solomon, J.-W. Ha, G.-R. Yi, D. a. Weitz, and V. N. Manoharan, "Synchronized reinjection and coalescence of droplets in microfluidics," *Lab Chip*, vol. 14, no. 3, pp. 509–513, 2014.

[389] A. R. Wheeler, W. R. Throndset, R. J. Whelan, A. M. Leach, R. N. Zare, Y. H. Liao, K. Farrell, I. D. Manger, and A. Daridon, "Microfluidic device for single-cell analysis.," *Anal. Chem.*, vol. 75, no. 14, pp. 3581–6, Jul. 2003.

[390] Z. G. Li, K. Ando, J. Q. Yu, a Q. Liu, J. B. Zhang, and C. D. Ohl, "Fast on-demand droplet fusion using transient cavitation bubbles.," *Lab Chip*, vol. 11, no. 11, pp. 1879–85, Jun. 2011.

[391] Y.-C. Tan, Y. L. Ho, and A. P. Lee, "Droplet coalescence by geometrically mediated flow in microfluidic channels," *Microfluid. Nanofluidics*, vol. 3, no. 4, pp. 495–499, 2007.

[392] K. Liu, H. Ding, Y. Chen, and X.-Z. Zhao, "Droplet-based synthetic method using microflow focusing and droplet fusion," *Microfluid. Nanofluidics*, vol. 3, no. 2, pp. 239–243, 2007.

[393] B.-J. Jin, Y. W. Kim, Y. Lee, and J. Y. Yoo, "Droplet merging in a straight microchannel using droplet size or viscosity difference," *J. Micromechanics Microengineering*, vol. 20, no. 3, p. 035003, 2010.

[394] V. Chokkalingam, B. Weidenhof, M. Krämer, W. F. Maier, S. Herminghaus, and R. Seemann, "Optimized droplet-based microfluidics scheme for sol–gel reactions," *Lab Chip*, vol. 10, no. 13, p. 1700, 2010.

[395] H. Gu, M. H. G. Duits, and F. Mugele, "Droplets formation and merging in two-phase flow microfluidics.," *Int. J. Mol. Sci.*, vol. 12, no. 4, pp. 2572–97, Jan. 2011.

[396] T. Mohamed, T. Hoang, M. Jelokhani-Niaraki, and P. P. N. Rao, "Tau-Derived-Hexapeptide (306)VQIVYK(311) Aggregation Inhibitors: Nitrocatechol Moiety as A Pharmacophore In Drug Design.," *ACS Chem. Neurosci.*, vol. 4, no. 12, pp. 1559–70, Dec. 2013.

[397] T. Glawdel, C. Elbuken, and C. Ren, "Passive droplet trafficking at microfluidic junctions under geometric and flow asymmetries.," *Lab Chip*, vol. 11, no. 22, pp. 3774–84, Nov. 2011.

[398] C. J. Morris and F. K. Forster, "Oscillatory flow in microchannels: Comparison of exact and approximate impedance models with experiments," *Exp. Fluids*, vol. 36, no. 6, pp. 928–937, 2004.

[399] S. a Vanapalli, A. G. Banpurkar, D. van den Ende, M. H. G. Duits, and F. Mugele, “Hydrodynamic resistance of single confined moving drops in rectangular microchannels.,” *Lab Chip*, vol. 9, no. 7, pp. 982–90, Apr. 2009.

[400] A. D. Stroock, S. K. W. Dertinger, A. Ajdari, I. Mezic, H. a Stone, and G. M. Whitesides, “Chaotic mixer for microchannels.,” *Science*, vol. 295, no. 5555, pp. 647–651, 2002.

[401] C. De Loubens, R. G. Lentle, C. Hulls, P. W. M. Janssen, R. J. Love, and J. P. Chambers, “Characterisation of mixing in the proximal duodenum of the rat during longitudinal contractions and comparison with a fluid mechanical model based on spatiotemporal motility data,” *PLoS One*, vol. 9, no. 4, pp. 2–7, 2014.

[402] P. V. Danckwerts, “The definition and measurement of some characteristics of mixtures,” *Appl. Sci. Res. Sect. A*, vol. 3, no. 4, pp. 279–296, 1952.

[403] O. J. Miller, A. El, T. Mangeat, J. Baret, L. Frenz, B. El, E. Mayot, M. L. Samuels, E. K. Rooney, P. Dieu, M. Galvan, D. R. Link, and A. D. Griffiths, “High-resolution dose-response screening using droplet-based microfluidics,” *PNAS*, vol. 109, no. 2, pp. 378–383, 2012.